FLOW PATTERNS IN FLAT-BOTTOMED SILOS

by

Graham Redpath Watson

Thesis presented for the degree of
Doctor of Philosophy

University of Edinburgh

August 1993

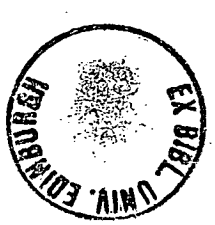

ABSTRACT

The work in this thesis is directed towards the measurement and prediction of the shape of the flow channel in granular solids as they discharge from flat-bottomed silos. It is widely believed that the flow pattern affects the pressure distribution against the walls and so also the stresses in the silo structure. Thus, a reliable means of predicting the shape of the flow channel has important design implications.

Kinematic analysis is used as the basis for the theoretical work. The governing partial differential equation contains one unknown empirical parameter: the kinematic parameter. Finite element formulations are developed and implemented to solve for the steady-state vertical velocity field in flowing granular solids for a range of conjectured kinematic parameters. The formulations are applied to the analysis of flow from flat-bottomed silos with planar or axisymmetric geometries. Criteria are proposed to define the boundary between flowing and near-stationary solid. The resultant flow channel boundaries are roughly paraboloidal in section. The flexibility of the finite element method allows many original kinematic analyses to be carried out *e.g.* the analysis of silos with more than one outlet; the analysis of planar silos with eccentrically-positioned orifices; the analysis of the effect of a spatially-varying kinematic parameter and the modelling of the top surface displacement are all claimed to be original.

Experiments are carried out in a half-cylindrical flat-bottomed silo. A rigid transparent sheet is used to form the front wall. The bisection of the flow in this way allows direct observation of flow mechanics to be made and the shape of the flow channel boundary can also be traced. Two solids are tested: a rough, frictional solid (sand) and a smooth, free-flowing solid (polypropylene pellets). The experiments entail the measurement of the residence times of tracer particles with known initial positions. From these residence times, the shape of the flow channel boundary is deduced. Measurements of the empirical kinematic parameter are also made.

It is shown that the numerical formulation accurately predicts the shape of the flow channel boundary. The correlation between the values of the kinematic parameter calculated from five different methods is reasonable.

PREFACE

This thesis is submitted to the University of Edinburgh, Scotland, for the degree of Doctor of Philosophy. The work described in this thesis was carried out by the candidate during the years 1989-1993 under the supervision of Professor J. M. Rotter. All the work was carried out in the Department of Civil Engineering and Building Science at the University of Edinburgh, Scotland.

In accordance with Regulation 3.4.7 of the University of Edinburgh governing the requirements for the degree of Doctor of Philosophy, the candidate submits that the thesis has been composed by himself and that the work described herein is his own unless otherwise stated in the text.

The paper 'A Finite Element Kinematic Analysis of Planar Granular Solids Flow', Watson, G. R. and Rotter, J. M. which is based on the work presented in this thesis has been accepted for publication in Chemical Engineering Science.

Graham Redpath Watson

ACKNOWLEDGEMENTS

The author was financially supported by the Science and Engineering Research Council through a studentship. The author is grateful for this support.

A debt of thanks is due to British Petroleum, Grangemouth who generously donated the polypropylene pellets for use in the experiments.

The author would like to thank his supervisor, Professor J. Michael Rotter for his guidance, friendship and inspiration.

I would like to thank my friends and colleagues from the University of Edinburgh: in particular, Niall McWilliam for his meticulous preparation of the diagrams; Jim Hutcheson and Ian Fowler for their innovative technical skills in the construction of the test rig; Ron O' Donnell for taking the photographs; and Betty McWilliam for her habitual help. I would also like to thank Computing Services at the University of Edinburgh for their help in finding a way through my computational hold-ups.

The author is also indebted to Dr. Jin Ooi of the University of Edinburgh, Professor Andrew Drescher of the University of Minnesota, Professor Peter Arnold of the University of Wollongong, Dr. Jorgen Nielsen of the Building Research Institute, Denmark and Dr. Andrew Chan of the University of Glasgow for many valuable comments and suggestions and for their enthusiastic interest in this work.

Thanks also go to Lex and Michele, Jenny and Ian for many happy memories and intense experiences over the past years. I wish them happy and safe futures.

Thanks are also due to my sisters Sally, Emma and Jane, who knew the answer all along: 'it moves faster in the middle than at the outsides'. And a special mention goes to my mother and father for their financial support in the latter stages of this thesis but mostly for their continuing love and guidance. To them, I dedicate this thesis.

CONTENTS

CHAPTER 7 COMPARISON OF EXPERIMENTAL RESULTS WITH PREDICTIONS OF THE KINEMATIC THEORY

CHAPTER 8 CONCLUSIONS

NOTATION

Roman

a	arbitrary expansion coefficient; constant in Eq. 3.17
A	radial flow constant (L^3T^{-1})
b,c,d	constants in Eq. 3.17
B	kinematic parameter (L)
c	void concentration (L^{-3})
D	silo diameter (L)
e	eccentricity
f	ratio defined in Section 6.3.2.3
H	height of silo (L)
[H]	matrix in Eqs 3.14 and 4.14
k	constant
[K]	matrix in Eqs 3.14 and 4.14
L	differential operator
n	direction cosine
{N}	shape function
P	probability that a particle will leave its cage
[P]	boundary flux matrix
Q	total volumetric flow rate ($L^3\ T^{-1}$)
r	horizontal co-ordinate in axisymmetric geometries (L)
r_o	orifice radius in axisymmetric geometries (L)
r*	radial co-ordinate as defined in Fig. 6.27 (L)
r^*_1	distance from silo floor to virtual apex of radial flow field (L)
R	silo radius in axisymmetric geometries (L)
S	non-overlapping summation
t	time (T)
T	residence time (T)
u	horizontal velocity (LT^{-1})
v	vertical velocity (LT^{-1})

$\{v\}$	nodal vertical velocity vector
v_o	maximum value of prescribed exit velocity (LT^{-1})
v_{exit}	prescribed exit velocities at nodes across orifice (LT^{-1})
w	weighting function set
x	horizontal co-ordinate in planar geometries (L)
x_o	orifice width in planar geometries (L)
X	silo width in planar geometries (L)
y	vertical co-ordinate in planar geometries (L)
z	vertical co-ordinate in axisymmetric geometries (L)

Greek

α	included hopper half-angle
β	angle of the flow channel boundary near the orifice to the vertical; ratio x/y
δ	angle between the plane perpendicular to the x-direction and the major principal plane
ϕ_i	arbitrary known spatial function set; angle of internal friction
ϕ_{ws}	angle of friction between bulk solid and steel wall
ϕ_{wg}	angle of friction between bulk solid and glass wall
Γ	domain boundary
η	$\pi/4 - \phi_i/2$
κ	arbitrary function of x and y in Eq. 3.9
λ	arbitrary function of x and y in Eq. 3.9
θ	angle the flow channel boundary makes with the vertical if the boundary is extended to the centreline
θ_1	radial flow channel angle
Ψ	stream function (L^2T^{-1})
Ω	domain
ζ	$\pi - \delta$
ζ_o	the value of ζ at $x = x_o$
ζ_X	the value of ζ at $x = X$

Subscripts

e	element
i	i^{th} term of an expansion; initial

k number of nodal unknowns per element (k = 4 linear; k = 8 parabolic; k = 12 cubic)

n node

o orifice

Superscripts

h indicates a discretization has occurred

N an N-termed approximation

t time station

CHAPTER 1

INTRODUCTION

1.1 General

Millions of tons of granular solids are stored and handled throughout the world in such industries as agriculture, mining, food processing and chemical process engineering. The safe design of containment structures involves a sound understanding of three interlinked phenomena: granular solids behaviour (static and dynamic), wall pressures and structural requirements. The flow of solids through a silo creates a complex pattern of pressures on the silo wall (see, for example, Munch-Andersen and Nielsen, 1990). These pressures manifest in the structure, usually made of steel or reinforced concrete, as particular stress states. The wall pressures are frequently asymmetric, even when the silo has been filled symmetrically and possesses geometrical symmetry (Ooi *et al*, 1990). Large horizontal pressures, or overpressures, often occur that exceed those pressures predicted from simple design theory. The prevalence of these seemingly-unpredictable wall pressures can only be understood by investigating the flow patterns that cause them. Reliable standards for the structural design of silos can only be produced if the wall pressures are known. It is thought, therefore, that of the three principal interlinked aspects (flow, pressures and structural design), solids flow mechanics is the most significant. Paradoxically, solids flow mechanics is also the least-well comprehended, possibly because the flow of granular solids does not fit snugly into any one established analytical field. In this thesis, a numerical kinematic theory is developed, implemented and tested to analyse granular solids flow.

There are two widely-recognised flow pattern forms that can exist during the discharge of granular media from silos: mass flow and funnel flow (Fig. 1.1). Mass flow is the flow mode that prevails in a silo/hopper system where every grain of solid is moving. Funnel flow is generally defined as any pattern which is not mass flow, and can be sub-divided into internal (or pipe) flow and semi-mass flow. The flow channel boundary (FCB) is defined as the interface between flowing and

stationary solid. The point at which this boundary strikes the silo wall is known as the 'effective transition'. If the FCB stretches from the edge of the orifice right up to the free surface of the solid, the flow is termed pipe or internal flow and there is no effective transition. Semi-mass flow is typified by mass flow in the upper part of the silo whilst converging internal flow takes over nearer the orifice, forming an 'effective hopper' which is surrounded by stagnant zones of stationary solid (Fig. 1.1).

It is widely believed that the overpressures mentioned above principally occur either near where the FCB intersects the silo wall (the effective transition) or where a sloping mass flow hopper meets the vertical bin wall (Jenike *et al*, 1973a,b). In many industrial applications mass flow is highly desirable as this has a 'first-in-first-out' operation and a more predictable discharge rate. However, where the solid is abrasive and non-degradable or where space restrictions constrain the geometry, funnel flow is often used. Funnel flow occurs in flat-bottomed or shallow-hoppered silos. The type of funnel flow depends upon the aspect ratio of the silo: in very squat silos internal flow will occur, whereas semi-mass flow is more likely in tall, slender silos. However, other factors such as the material properties, filling method and particle shape and size (Munch-Andersen and Nielsen, 1990 and Carson *et al*, 1991) also affect the flow mode.

Semi-mass flow is usually immediately preceded, at the start of discharge, by internal flow: after filling an empty silo and opening the orifice, a vertical pipe of flowing solid of the same diameter as the orifice rapidly extends upwards to the free surface and then swells laterally (*e.g.* Lenczner, 1963; Bransby *et al*, 1973 and Arteaga and Tuzun, 1990). This stage of discharge is not the chief goal of flow analysis, and is not considered in the present theoretical development. Most analyses of flow assume a steady-state condition, corresponding to the silo being essentially full, but with a fully-initiated pattern of flow. A number of dynamic and steady-state analyses described by Drescher (1990) indicate that this steady-state assumption is a good engineering approximation for most practical purposes.

Steady-state flow analyses include those based on soil mechanics plasticity theory (*e.g.* Deutsch and Clyde, 1967; Giunta, 1969; Jenike *et al*, 1973b; McCabe, 1974; Van Zanten *et al*, 1977; Murfitt *et al*, 1981 and Kuznetsov, 1984). These analyses were based on the assumption of a linear FCB (*i.e.* a wedge-shaped flow channel in planar silos and a conical channel in cylindrical silos). By contrast, experimental

observations of the FCB (*e.g.* Lenczner, 1963; Brown and Richards, 1965; Gardner, 1966; Bransby *et al*, 1973; Nguyen *et al*, 1980 and Tuzun and Nedderman, 1982) have generally described the FCB as non-linear, usually becoming steeper away from the orifice. There is a considerable mis-match between most theoretical predictions and experimental observations. The observations recently made by Carson *et al* (1991) on eccentric discharge flow patterns also indicate that it is not clear which material parameters should be used in attempting to predict flow channel geometries, since a wide range of flow channel shapes can be found within free-flowing solids with the same internal frictional properties. In this context, the current theoretical analysis represents an attempt to devise a simple but effective predictive tool applicable to a wide range of geometries.

Of the possible approaches to the analysis of flowing granular solid, perhaps the two most promising are plasticity theory and kinematic modelling. Unfortunately, the plastic behaviour of dilated, free-flowing granular solids is not yet fully defined, yet the suitability of purely kinematic models for very frictional, consolidated, incipient flows is questionable. A universal description of all flow regimes is not yet available and it is certainly a considerable challenge to try to produce one. Different approaches for the various flow configurations may be required until a better understanding is achieved.

The aim of the research work presented in this thesis is to develop a deeper understanding of the flow of dry bulk granular solids from silos and similar containment structures. The specific objectives are to investigate experimentally the formation of the FCB and to develop a numerical formulation to analyse the flow of granular solids. Experimental techniques to measure the FCB are developed and implemented. The geometries of the resulting FCBs are compared with theoretical predictions. Experimental measurements are also made of the kinematic parameter.

1.2 Review of topics covered in this thesis

Chapter 2 constitutes a detailed review of the work carried out to date in the field of granular solids flow and flow channel geometries. The previous research into granular solids is divided into five fields according to the method of approach: analytical soil mechanics, computational soil mechanics, fluid mechanics, discrete

elements and kinematic theory. A critique of each approach and of the work carried out in that field are presented.

In Chapter 3, a finite element method for the kinematic analysis of the flow of granular solids in planar geometries is developed. Flow channel boundary predictions are made. A short parametric study is also included. This study analyses the effect on the flow pattern as the kinematic parameter is varied.

Chapter 4 includes an analogous formulation to Chapter 3 which is applicable to axisymmetric geometries. The structure of this chapter follows that of Chapter 3.

In Chapter 5, a major parametric study is undertaken to demonstrate the power of the numerical formulations developed in the previous two chapters. A number of topics are investigated: eccentric flow patterns; flow in double-outlet silos; the successive displacement of the top surface; the effect of scaling the silo on the flow patterns; the trajectories of individual particles; and the application of the kinematic model to flow in hoppers. Many of these extensions are made possible only by the adaptable nature of the numerical formulation. They are beyond the scope of current analytical kinematic solutions and have therefore previously been left unexamined. With the numerical solution developed in this thesis, it was possible to analyse them fully.

In Chapter 6, the experimental apparatus and its method of operation are described. Details of specific experiments are given and various interpretations of the experimental data are made. The experiments include the observation of the flow channel boundary, the measurement of residence times, the tracing of particle trajectories and the determination of the value of the kinematic parameter.

In Chapter 7, the experimental results are compared with predictions from the axisymmetric version of the kinematic model described in Chapter 4. A critique of each of the methods used to estimate the kinematic parameter is also given.

Finally in Chapter 8, the conclusions of the findings of the previous chapters are presented and recommendations are made for future work.

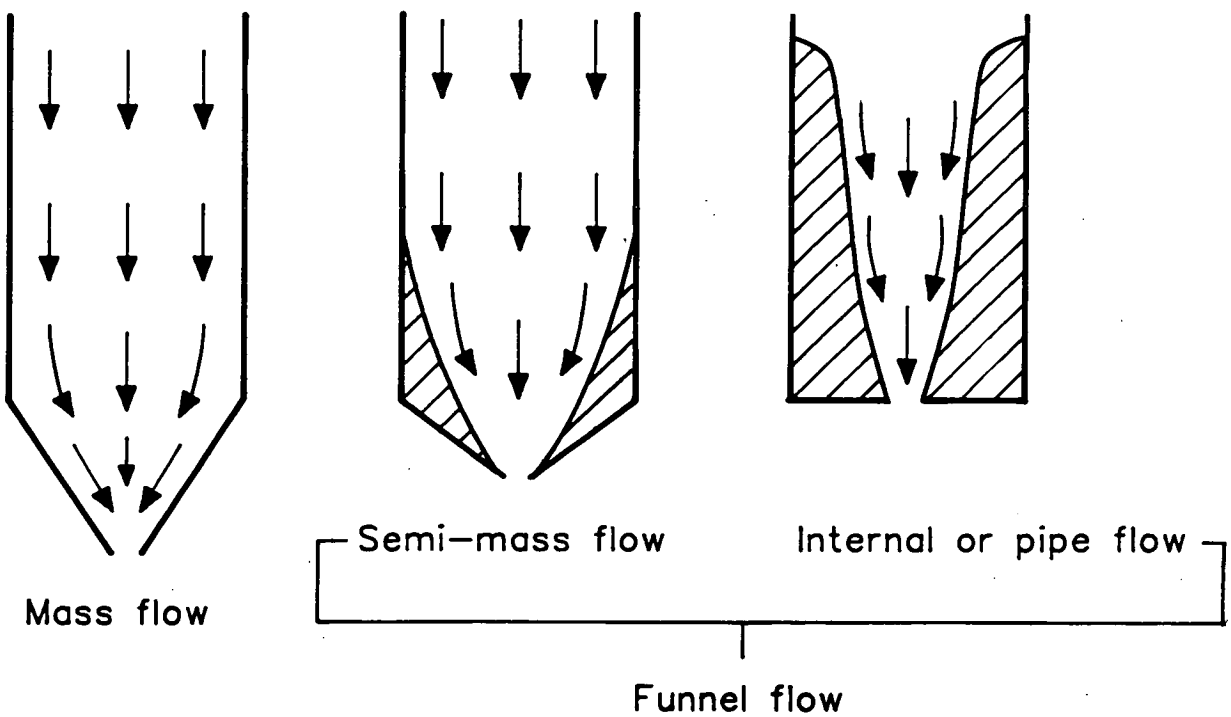

Fig. 1.1 Classification of flow patterns in silos

CHAPTER 2

A REVIEW OF PREVIOUS EXPERIMENTAL AND THEORETICAL TECHNIQUES EMPLOYED TO STUDY FLOW PATTERNS IN SILOS

2.1 Introduction

In Chapter 1, the scope and objectives of this thesis were stated. The first task of this chapter is to illustrate the complexity of the problems involved in devising an accurate description of the mechanics of granular solids flow. Various experimental methods that have been previously employed to determine the flow patterns in silos are then reviewed. The experimental methods discussed are:

(a) direct visual observation of horizontal layers of dyed solid
(b) photographic techniques
(c) radiographic techniques
(d) techniques using radio-transmitting pills
(e) bed splitting techniques
(f) residence time measurements

Next, detailed descriptions are presented of previous theoretical research carried out in the field of granular solids flow. This theoretical research is grouped under subject headings that relate to the field of study used to analyse the phenomena thought to occur in granular solids flow. Although not mutually exclusive, various theoretical backgrounds to the treatments can be identified:

(a) analytical soil mechanics
(b) computational soil mechanics
(c) fluid mechanics
(d) discrete element mechanics
(e) kinematic analysis

The experimental and theoretical reviews are not intended to be exhaustively comprehensive. Instead, a careful selection of the extensive literature published on granular solids flow is surveyed. The selection of studies for comment is made on the basis of research material that is of direct relevance to the task of predicting the position of the flow channel boundary. Although it is important to be aware of work in related topics, such as the theoretical prediction of the discharge rate from silos or the measurement of pressures on silo walls, a detailed review of such work is beyond the scope of this thesis.

2.2 The complexity of discharging bulk solids

It has been observed by many (*e.g.* Walker, 1966; Walker and Blanchard, 1967; Deutsch and Schmidt, 1969; Pieper, 1969; Blair-Fish and Bransby, 1973; Richards, 1977; van Zanten and Mooij, 1977 and Munch-Andersen and Nielsen, 1990) that overpressures occur during the discharge of dry bulk granular solids from silos. In extreme cases, these pressures have been reported to be up to five times the Janssen (1895) filling pressure at the same position. The overpressures are typically largest shortly after the start of discharge, when a flow channel has fully developed but the silo is still virtually full to capacity. For this reason, most time domain analyses concentrate on the earliest stages of discharge (*e.g.* Haussler and Eibl, 1984; Runesson and Nilsson, 1986; Eibl and Rombach, 1988 and Wu, 1990). The form of the flow channel is widely acknowledged to influence the pressures on the wall strongly, so reliable prediction of the flow pattern is an important research goal.

Recently, Munch-Andersen and Nielsen (1990) reported that the boundary conditions for incipient discharge depend strongly upon the way in which the silo has been filled. They reported the following main points.

Firstly, the method of filling has a profound effect on the behaviour during discharge. The granular solid was filled concentrically (with a vertical trajectory), in an inclined manner (down a chute), or in a uniformly-distributed form over the entire cross section of the silo. The filling method influences the packing orientation of the grains and thus the voids ratio and the shearing strength. These, in turn, may be responsible for the differences in measured static pressures after filling and in observed discharge patterns when comparing tests which differ only in

the technique of filling. Sugden (1980) also reported that different filling techniques produce different initial densities that strongly influence the flow pattern.

Secondly, it was noted that when a single stream of particles is used during filling, the grains pile up in two different ways. The grains may gather at the peak of a conical pile for a while before tumbling down the sides. Alternatively, they may behave as a plastic mass, with horizontal layers thinning out sideways. The former sliding-layers mechanism tends to give higher at-rest lateral pressures but lower unit weights, presumably due to a kinetic loosening effect. The mechanism which a given grain type would display was not predictable though it was repeatable. It may depend upon particle shape, particle surface roughness and the ratio of silo diameter to grain diameter, but a clear explanation of the mechanisms has not yet been presented.

Another factor that will effect the flow properties of a bulk solid is the height through which the grains free-fall before impacting in the silo. Although this was not touched upon by Munch-Andersen and Nielsen (1990), the energy of impact is likely to influence the particle packing and thus both the flow patterns and the wall pressures.

Thus, the manner in which particles are introduced into a silo is of paramount significance.

Munch-Andersen and Nielsen (1990) and Ooi *et al* (1990) also reported an asymmetric lateral pressure distribution around constant-height circumferences (for symmetrical filling). This suggests perhaps variations in wall roughness or anisotropic behaviour of the particulate solid. For the latter suggestion, the incorporation of a statistical element may be useful in future particulate solids flow research (Ooi and Rotter, 1991).

2.3 Experimental methods employed to investigate flow patterns

2.3.1 General

The study of the flow patterns in discharging silos presents several fundamental problems to the experimenter. Firstly, the majority of granular solids are opaque in

nature, so the experimenter cannot look into the bed of solid. Very little information can be gained from direct visual observation of the free surface. Even if the silo is made of a transparent material, only the flow adjacent to the walls can be studied. This technique is discussed in more detail below. Secondly, the method in which the silo has been filled affects the subsequent flow pattern. If it is necessary for the free surface to be levelled, in order to position marker particles, for example, it may affect the flow pattern. Thirdly, effects such as vibration and time of storage may also influence the flow pattern. The study of the internal flow fields in silos is seldom a simple affair. Many ingenious methods have been devised to chart the internal events in a discharging silo. These were listed in the introduction to this chapter and are discussed in turn below. The objective of this section is not to review all the experimental work that has been carried out, but to identify the commonest and most successful methods and highlight the advantages and disadvantages of each.

2.3.2 Direct visual observation techniques

2.3.2.1 Observation of displacements of horizontal layers of dyed solid

In this technique, horizontal layers of visually-detectable solid are placed adjacent to a transparent front wall of a plane-strain apparatus during filling. The subsequent deformation of these layers is then observed. Unless the silo is filled in a distributed manner, some levelling of the free surface is necessary. Munch-Andersen and Nielsen (1990) have shown that the packing arrangement affects the flow patterns and so this levelling may have an influence. The visually-detectable solid is usually either a sample of the granular solid that has been dyed or a similar granular solid of a different colour. In either case, the layers contain grains that have essentially the same properties as the bulk solid. In this experimental technique, the problems associated with the retarding effect of the front wall are pertinent. Jenike and Johanson (1962), Litwiniszyn (1963) and Gardner (1966) are amongst many who have utilised this technique. The results obtained are generally of a qualitative nature since it is not possible to determine the trajectory of any particles except those adjacent to the transparent front wall.

2.3.2.2 Observation through transparent walls of an axisymmetric silo

Another visual observation technique was employed by Carson *et al* (1991). They carried out flow experiments on flat-bottomed, cylindrical model silos. The walls were made of transparent plexiglass, so they could visually determine the boundary between flowing and stationary solid. By assuming a linear zone of stationary solid, they plotted the flow channel angle against the circumferential angle. Their experiments were carried out on full, two-thirds full and one third full silos discharging concentrically and eccentrically. They found that the flow channel closely followed a radial path from the outlet to the cylinder wall. The flow channel boundary, as observed through the wall, however, was neither distinct nor stable for most of the solids they tested. They also reported an unexpected lack of correlation between the flow channel angle and measured material properties such as the angle of internal friction.

2.3.3 Photographic techniques

Photographic techniques are one of the commonest methods used to study the behaviour of flowing granular solids and are often used in conjunction with the previous technique *i.e.* that of observing the movement of horizontal layers of dyed solid. Photographic techniques have been employed by many researchers (*e.g.* Bosley *et al*, 1969; Pariseau, 1970; and Tuzun and Nedderman, 1979a,b, 1982) using transparent plane-strain silos. Either high-speed photography (cine filming) or long exposures are taken.

It is assumed that the flow behaviour observed adjacent to the front wall is representative of the behaviour throughout the bed. However, several researchers (*e.g.* Brown and Richards, 1965 and Cleaver, 1991) have reported that the front wall exerts a retarding force on the flow. This must be taken into account somehow when velocities are calculated, as these velocities will almost certainly be less than those occurring at similar positions within the bed. However, it is not easy to devise satisfactory techniques to account for the retardation caused by the transparent wall.

Brown and Richards (1965) and Gardner took (1966) photographs of the flow through the transparent front walls of their plane-strain model silos. Careful

scrutiny of these photographs reveals a surprising point of contraflexure in the flow channel boundary. It seems possible that the stationary zones start to curve into the flow field near the outlet. This phenomenon could, however, be caused by frictional effects against the front wall.

Laohakul (1978) and Tuzun and Nedderman (1979a) are amongst those to have used cine filming to determine particle trajectories. Polynomials describing the position of a tracer particle with time were then fitted to the tracer trajectories. On differentiation, these polynomials yielded the horizontal and vertical velocities at any point at any time on the trajectory.

Long time exposures were used by Gardner (1966) and Tuzun and Nedderman (1982) to determine the position of the flow channel boundary. Gardner laid horizontal layers of dyed solid in the silo during filling. Flow was allowed to proceed until steady-state conditions were achieved. The flow channel boundary was defined in this study as the edge of the stationary solid, and its location was assessed by measuring the extent of the remaining horizontal layers of dyed solid.

By using an exposure time of 0.5 secs whilst photographing their discharging planar silo, Tuzun and Nedderman (1982) observed that some particles appear blurred whilst others (those that moved at less than one particle diameter per exposure time) were in focus. In this way, they could determine a flow channel boundary based on a similar but slightly different definition. With a longer exposure time of 1 sec, the flow channel boundary altered giving the appearance of a larger flowing region. They reported that these boundaries were also velocity contours. They further suggested that no clear-cut interface could be experimentally observed between flowing and stagnant solid since the velocity appears to decrease asymptotically towards zero at points further and further from the orifice horizontally. They did not, however, increase the exposure time beyond 1 sec to investigate further shifts in the observed flow channel boundary.

2.3.4 Radiographic techniques

In the radiographic technique, lead shot tracer particles are seeded into a silo bed during filling. This technique can only be used in small non-metallic plain-strain

models. It is therefore very susceptible to errors caused by friction on the 'side' walls, through which the observations must be made.

The flow is halted at frequent intervals during the discharge and the apparatus exposed to an X-ray source. The resulting X-ray photograph shows the positions of the tracer particles. By comparing successive X-rays, velocities can be calculated. This method is relatively rarely employed, presumably because of the expensive equipment required and the restricted size of the apparatus. Cutress and Pulfer (1967), Bransby *et al* (1973), Lee *et al* (1974), and Drescher *et al* (1978) are amongst those to have used this technique. Voidage changes, which often coincide with rupture surfaces, are more important phenomena which can be detected on the X-ray exposure.

2.3.5 Radio pill tracking technique

The radio pill tracking technique involves following the fate of a miniature radio-transmitter (a radio pill) as it passes through a model silo. Handley and Perry (1965, 1967), Rao and Venkateswarlu (1973) and Perry *et al* (1975, 1976) are amongst those to have employed this technique. Perry and his co-workers carried out the most comprehensive study using cylindrical radio pills of length 25 mm and diameter 8.8 mm. In an attempt to measure the stresses in the granular solid, some pills were fitted with a pressure-sensitive diaphragm. The pills were placed within axisymmetric model silos filled with fine sand. The signals from the radio pills were received by an aerial adjacent to the wall.

Since the radio pills were much larger than the mean particle diameter, the problem of segregation must be addressed when analysing the results. Arteaga and Tuzun (1990) later published their findings on flow of binary mixtures from silos. They defined a coarse-continuous bed as one in which the particle lattice is made up of coarse particles, with fines filling the interstitial spaces and a fines-continuous bed as one in which the microstructure is dominated by fines in which coarse particles are retained in relatively few numbers. They reported that segregation of fine particles occurs in a coarse-continuous bed whereas no segregation of coarse particles occurs in a fines-continuous bed. It can be concluded, therefore, that the results of Perry *et al* would not have been influenced by segregation problems. The major drawback in the work of Perry *et al* is the short range over which the radio

pills can be detected. For reliable detection, the radio pills must never be more than about 50 mm from the wall, so the technique is restricted to very small models.

2.3.6 Bed splitting techniques

In the bed-splitting technique, horizontal layers of dyed granular solid are included into the silo during filling. After an appropriate period of flow, the discharge is halted. The bed of granular solid is then immobilised. The commonest immobilization technique is to pour in a fixing medium which fills the interstices between the granular particles and then solidifies, rendering the particulate solid rigid. Brown and Richards (1965) and Novosad and Surapati (1968) used molten paraffin wax and Chatlynne and Resnick (1973) used a polyester resin as the fixing medium. The solidified granular solid can then be sliced up to reveal the internal deformation of the coloured layers.

In their experiments with sand in a plane-strain mass-flow hopper, Brown and Richards (1965) reported that the velocity profiles were unsymmetrical about the vertical centreline and that the flow rate generally increased with distance from the end face. However, the maximum flow rate did not occur in the central section of the hopper.

Brown and Richards also made measurements of the 'angle of approach'. This angle was defined as the angle the flow channel boundary, near the exit, made with the vertical. In plain-strain silos, the angle of approach was measured from direct observation through the end face. In axisymmetric silos, large numbers of tracer particles were initially seeded in layers into the silo at known positions. From a study of the particles that were left in the silo after a few seconds of discharge, an estimate of the angle of approach could be made. The angles of approach were measured for different solids in three flat-bottomed silos of different geometries:

(a) discharge through an edge slot adjacent to a side wall in a planar silo (this angle of approach was designated β_e).
(b) discharge through a central slot, parallel to the side walls, in a planar silo (β_c).
(c) discharge through a central circular orifice in the base of a cylindrical silo (β_3).

They found that all these angles fluctuated but in general $\beta_e \geq \beta_c > \beta_3$. They thus showed that the geometry of the silo has an influence on the angle of approach.

Giunta (1969) investigated the position of the flow channel boundary in an axisymmetric model silo. By continuously replenishing the top surface, steady-state conditions were allowed to develop. A different method to the fixing technique described above was then used to split the flow field. After fitting a semi-circular lid, the silo was rotated through 90° about the horizontal axis. A vacuum shovel was then used to remove the uppermost half-cylindrical section, thus exposing the longitudinal plane of symmetry. Although it was Giunta's intention to study the flow channel boundary in only flat-bottomed silos, his apparatus included a conical hopper of a smaller diameter than the cylindrical silo and so a reliable comparison with other results from flat-bottomed silos perhaps cannot be made.

Takahashi and Yanai (1973) used a technique similar to Giunta's to measure the flow pattern and void fraction of 4 mm diameter glass, silica and alumina spheres during flow through a vertical pipe. They reported a central constant-velocity region and a peripheral shear region where the velocities fell abruptly.

Although bed splitting techniques allow the flow patterns in true three-dimensional silos to be investigated, the results are generally only of a quantitative nature since trajectories are unknown. A further disadvantage of the fixing technique is that it is both time-consuming and labour-intensive.

2.3.7 Residence time measurements

In this technique, the time taken for a tracer particle to travel through the bulk from an initial known starting position to the outlet (*i.e.* its residence time) is measured. This technique lends itself very conveniently to the analysis of flow in true three-dimensional systems. The resources needed to implement this technique are few and inexpensive and the method is simple, if time-consuming.

In particular circumstances, streamlines and velocity fields can be assessed from residence times. A stream function analysis is used. Velocity distributions can only be calculated if either the trajectory of the particle or a constant bulk density is assumed. With the latter assumption, contours of equal time (isochrones) are fitted

to the residence time data and stream function values are then evaluated. Streamlines are calculated by numerically differentiating these stream functions (Cleaver, 1991). Smallwood and Thorpe (1980) continued the analysis to calculate velocity fields. Cleaver (1991) reported that stream function analysis was very sensitive to errors in the experimental results from his mass-flow silo. In the experiments described in the present thesis (see Chapter 6), it will be seen that many tracer particles remained stationary for a considerable period until the flow front reached them. Therefore, the measured residence times of these tracers do not represent the time the tracer was in motion. This phenomenon renders such residence time data unsuitable for stream function analysis. Furthermore, for stream function analysis to be reliable, a constant flowing bulk density must be assumed. The technique is also long-winded. For these reasons, and the fact that the main objective of this thesis is to determine the position of the flow channel boundary and not to calculate streamlines or velocity distributions, stream function analysis was not undertaken in the present work.

Different methods of placing the tracer particles into the silo have been employed. Smallwood and Thorpe (1980), Murfitt (1980), Graham *et al* (1987), Nedderman (1988) and Cleaver (1991) used positioning tubes to introduce tracer particles into discharging silos. Cleaver (1991) showed that the presence of a positioning tube in the flow field causes the subsequent movement of the tracer particle to be impeded. For the most accurate results, therefore, the tubes must be retracted after positioning a tracer particle. Tracer particles were dropped from marked positions at the top of the silo onto a pre-flattened free surface by van Zanten *et al* (1977). The accuracy of this method of positioning the tracer particles is in doubt because the degree of burrowing of the tracers is unknown.

From the literature, it can be seen that the residence time technique is a commonly adopted approach. A drawback of the technique is that the positioning of tubes and the recovery of tracer particles in full scale silos may be hampered by problems of access.

2.4 Theoretical techniques employed to analyse flow behaviour

2.4.1 General

Five theoretical techniques for the analysis of the behaviour of flowing granular solids were identified in the introduction to this chapter. A brief description of each technique and a critique of selected previous research is presented here.

2.4.2 Analytical soil mechanics or bulk solids mechanics approach

2.4.2.1 General

Soil mechanics is concerned with the engineering properties of soils in association with structures. Little, if any, interest is vested in the condition of a soil after failure. Large strains are generally exempt from the soil mechanicist's gaze.

Bulk solids mechanics has grown out of soil mechanics in more recent times, and has tried to address the problems of dry granular solids flow.

Soils and bulk solids can transfer considerable shear stresses through their mass. These are usually taken to depend on the local normal stress and the shear strain but are generally assumed to be independent of the rate of shearing. Many researchers further ignore the shear strain in the solid, and assume that bulk solids are always in a plastic state. For example, Arnold *et al* (1981) use this criterion to define the bulk granular solid as a plastic material.

Previous research undertaken that treats the material as plastic can be split into three categories:

(a) mass flow hoppers, in which blocks of rigid or plastic material are separated by discrete rupture surfaces.

(b) funnel flow hoppers, with stagnant zones separated from the flowing material by a linear flow channel boundary.

(c) funnel flow hoppers, with stagnant zones separated from the flowing material by a curved flow channel boundary.

2.4.2.2 Rigid blocks and rupture surfaces in a mass flow hopper

Many researchers (Johanson, 1964; Deutsch and Clyde, 1967; Blair-Fish and Bransby, 1973; Bransby *et al*, 1973 and Drescher *et al*, 1978) have noted the existence of what have been termed discrete rupture surfaces. These are formed between a 'feed zone' and a 'central pipe flow zone' (Fig. 2.1). A feed zone is a region of dense solid above the rupture surface which has not yet undergone shearing. The central pipe zone lies below the rupture surface and contains solid which has already been sheared and thus has a lower density.

Johanson (1964) employed the method of characteristics to solve the equations of plasticity, which were adapted to the steady flow of frictional cohesive solids by Jenike and Shield (1959), for a Mohr-Coulomb solid. He showed experimentally that the stress fields in his axisymmetric and plain-strain hoppers closely approximated the radial stress fields of Jenike (1964) (*i.e.* the orientation of the principal stresses is very nearly constant along any radial line). He observed rigid feed zones, a central pipe flow zone and lines of rapid velocity change. Since all his experiments involved only mass flow hoppers, he made no attempt to predict flow channel boundaries.

Drescher *et al* (1978) assumed that each feed zone behaves as a perfectly plastic rigid block sliding parallel to the hopper wall, and that all dilation of the solid occurs as it crosses the discrete rupture surfaces between these blocks and a radial flow zone (Fig. 2.1). Thereafter, radial flow is assumed. They analysed the velocity discontinuities that occur across the rupture surfaces using a velocity hodograph. This is a graphical technique which correlates the magnitudes and directions of the different velocities. Drescher *et al* succeeded in producing an analytical solution for the velocity field, although the theoretical results show a poor correlation with experimental observations. To explain this discrepancy, it was suggested that the flow pattern had been over-simplified.

2.4.2.3 Linear stagnant zones in funnel flow

Stagnant or dead zones of stationary solid are a characteristic of funnel-flow. Flowing solid slides past stationary solid which forms an 'effective hopper'. A large body of research has been conducted into the prediction of wall pressures during discharge of silos (*e.g.* Morrison 1977; Richards, 1977; and van Zanten *et al*, 1977). It is typical in this work to assume that the flow channel boundary (the division between flowing and stationary solid) takes up a simple geometrical shape. This is commonly linear: the surface between moving solid and static solid forms a cone in a cylindrical silo and a wedge in a plane-strain silo (both the conical and wedge surfaces are slightly truncated due to the finite size of the outlet). The reason for the assumption of a linear flow channel boundary is partly to simplify theoretical models, allowing closed-form solutions to be obtained, and partly because no reliable theoretical description currently exists that accurately describes the funnel flow boundary.

Deutsch and Clyde (1967) demonstrated that the rigid block/rupture surface flow pattern can also occur in funnel flow silos. They believed that it is a fundamental mechanism as it occurs across a wide range of test vessel to material diameter ratios. They also proposed, following Johanson (1964), that these flow patterns represent a steady-state phenomenon for much of the period of discharge from the silo.

In their general guidelines for safe economic bulk solids management, Arnold *et al* (1981) included design criteria, such as the conditions necessary to prevent flow obstructions from forming. Much of their theory was based on the work of Jenike (*e.g.* 1964). Here the emphasis was on practical results and proposals that can be directly exploited in the design of bins and silos. Therefore, serviceable, conservative analytical solutions were sought. As a result, they adopted simple assumptions, such as incompressible flow and an isotropic homogeneous elastic solid.

2.4.2.4 Curved stagnant zones in funnel flow

Several authors (*e.g.* Lenczner, 1963; Brown and Richards, 1965 and Gardner, 1966) observed the presence of a curved flow channel boundary (of the general form shown in Fig. 1.1) taking shape in model tests during discharge.

Brown and Richards (1965) proposed a radial velocity field for mass-flow hoppers and used a molten wax fixing technique to investigate the internal events in a wedge hopper. They found that radial flow was approximated near the orifice.

Gardner (1966) assumed that the solid in the flow channel was in a state of plastic equilibrium, obeying the Mohr-Coulomb failure criterion. He used the method of characteristics to solve numerically the equilibrium and plasticity equations for a continuum. He also assumed that the stresses in the plane of observation were not influenced by the stresses parallel or normal to this plane. Gardner had previously given (1964) a theoretical justification for this assumption. He reported that in circumstances where the flow tends to diverge very slightly rather than to converge in planes normal to the one of interest, the stresses parallel and normal to this plane can be ignored. For this reason, the model silo of Gardner (1966) was tapered from top to bottom, with a thickness of 83 mm at the base and 76 mm at the top (the silo height was 1.22 m and its width was 152 mm). Gardner (1966) obtained a theoretical prediction of the flow channel boundary and had consistent, but only moderate, success when the predictions were compared with his experimental observations.

Takahashi and Yanai (1974) developed an analysis for solids flow in flat-bottomed concentrically-discharging planar silos. Like Gardner (1966), Takahashi and Yanai used the method of characteristics and assumed a Mohr-Coulomb solid. By further assuming that the flow channel boundary coincides with a slip-line and that the mean compressive stress on this boundary was constant, they were able to produce an analytical solution to describe the shape of the flow channel boundary:

$$x/X = \left(\frac{(\zeta_o - \zeta) - \tan 2\eta \ln\left|\frac{\cos(\zeta - \eta)}{\cos(\zeta_o - \eta)}\right|}{(\zeta_o - \zeta_X) - \tan 2\eta \ln\left|\frac{\cos(\zeta_X - \eta)}{\cos(\zeta_o - \eta)}\right|} \right)\left(1 - \frac{x_o}{X}\right) + \frac{x_o}{X} \qquad (2.1)$$

$$y/X = \left(\frac{(\zeta_o - \zeta)\tan 2\eta + \ln\left|\frac{\cos(\zeta - \eta)}{\cos(\zeta_o - \eta)}\right|}{(\zeta_o - \zeta_X) - \tan 2\eta \ln\left|\frac{\cos(\zeta_X - \eta)}{\cos(\zeta_o - \eta)}\right|} \right)\left(1 - \frac{x_o}{X}\right) + \frac{x_o}{X}\cot\theta \qquad (2.2)$$

where, in planar geometries, x is the horizontal co-ordinate, y is the vertical co-ordinate and X is the silo half-width; $\zeta = \pi - \delta$ and δ is the angle between the plane perpendicular to the x-direction and the major principal plane; ζ_o and ζ_X are the values of ζ at $x = x_o$ (the edge of the orifice) and $x = X$ respectively; $\eta = \pi/4 - \phi_i/2$, the angle between the slip-line and the minor principal plane; ϕ_i is the angle of internal friction; and θ is defined in their Fig. 1 as the angle the flow channel boundary (FCB) makes with the vertical if this boundary is extended to the centreline.

Tuzun and Nedderman (1982) demonstrated that Eqs 2.1 and 2.2 give geometrically-similar flow channel boundaries as the silo width is varied. In Chapter 5, this finding is compared with the theoretical predictions of the current work.

2.4.3 Computational soil mechanics or bulk solids mechanics approach

2.4.3.1 General

Another area of knowledge which researchers have used in attempts to analyse granular solids flow is computational bulk solids mechanics. In this, it is assumed that the granular solid can be treated as a continuum and follows some well-defined behavioural laws based upon classical mechanics combined with generally quite complex constitutive models. This approach requires powerful computing facilities.

2.4.3.2 Previous research

Haussler and Eibl (1984), Runesson and Nilsson (1986), Eibl and Rombach (1987a,b, 1988) and Schmidt and Wu (1989) all worked from a viscous elastic-plastic model using the numerical finite element technique. Others that have utilised the technique of finite elements to analyse the behaviour of bulk solids in silos

include Bishara and Mahmoud (1976), Mahmoud and Abel-Sayed (1981), Link and Elwi (1987) and Ooi (1990). This technique is a relatively recent development. Typically, conservation of mass, the momentum equation and kinematic relations are employed, in conjunction with a constitutive law for stress-strain relations. This produces a series of non-linear partial differential equations. The forming of these equations into numerical algorithms suitable for programming is a complex task much divorced from the practicality and visualisation of bulk solids behaviour. It is perhaps because this method is so rigorous, requiring vast computing capacities, that the desired global perspective on the flow pattern is not always easily extracted. Although the work is certainly auspicious, a degree of distillation is needed before the flow patterns can be reliably traced.

2.4.4 Fluid-mechanical approach

2.4.4.1 General

Fluid mechanics is a vast field. Fluids can be classed as Newtonian or non-Newtonian. A Newtonian fluid is one in which the shear stress at a point is directly proportional to the velocity gradient at that point. Non-Newtonian fluids generally have non-linear relationships between shear stress and velocity gradient. The behaviour is generally independent of the internal pressure. Broadly speaking, this is the reverse of the case for soils. An ideal fluid responds to an applied shear stress with a shear strain which depends on the time the stress has been applied. Fluids, unlike granular solids or soils, cannot be piled up. Thus there are many difficulties in trying to apply fluid mechanical concepts to granular solids flow.

2.4.4.2 Previous research

During experiments into the shearing of neutrally-buoyant spherical particles, Bagnold (1954) discovered two response regions. At low shear rates his 'granular fluid' behaved in a Newtonian manner. This he termed the macro-viscous region. At higher shear rates, the stresses were found to vary with the square of the velocity gradient (*i.e.* as a non-Newtonian fluid). This he termed the grain-inertia region. He also found normal stresses to be acting, a feature reminiscent of a Coulomb soil. These findings suggest that it may be possible to analyse the discharge of granular

solids from silos either as a fluid-mechanical or a soil-mechanical phenomenon, or even as an integration of the two.

A further example of the fluid nature of granular solids, especially noted in the flow of smooth tiny spheres, was given by Savage (1979). He observed an interesting feature which could be called a 'granular jump' which was of an analogous form to the well-known hydraulic jump phenomenon.

In Savage's (1979) paper, a three-dimensional constitutive equation was presented which satisfies the Mohr-Coulomb failure criterion. In this investigation, the material response was found to be highly sensitive to the volume fraction of solids. The character of the constitutive equation is such that a large array of unknown parameters appears. By substituting conjectured approximations into the equations, two simple flows are solved analytically: flow down an inclined chute and flow in a vertical channel. However, this approach would probably become extremely complex if assumptions required to represent the conditions in a converging-flow silo were attempted.

Haff (1983) initiated a new line of research in applying the Navier-Stokes relations and the hydrodynamic equations for conservation of energy (both kernels of the theory of fluid mechanics) to the subject of granular solids flow. He used the continuum hypothesis: that the variation of properties across a grain diameter is negligible. He sought to maintain analyticality and gain a qualitative understanding of simple flows. An important dependent variable in his formulation, in addition to the flow velocity, was the mean random fluctuation velocity of an individual grain (which he termed the 'thermal' velocity). This 'thermal' velocity describes the local state of the medium and facilitates a self-consistent definition of the equations' coefficients. These coefficients were found not to be constants but functions of the local state of the medium. By the very nature of these equations, however, only elementary flows, with strictly-limited contingencies, can be analytically solved. Non-Newtonian flow was postulated (in line with Bagnold, 1954 and Savage, 1979) and the inelastic nature of collisions was found to have a profound effect on the grain system response.

Hui and Haff (1986) followed-up Haff's (1983) groundwork with a numerical treatment of grain flow in a vertical channel. The velocity profiles obtained are encouraging but the reader gains the impression that the complexity of this analysis

would increase unreasonably if converging flow were considered, as is the case in a silo. The flow velocity profiles of Haff (1983) and Hui and Haff (1986) show a good qualitative match to those of Savage (1979).

2.4.5 Discrete element approach

The discrete element approach is concerned with the microscopic features of individual particles and their mutual interactions. To analyse the mechanical behaviour of a granular solid from the viewpoint of individual (but reciprocal) particle-particle interactions, is, in theory, a promising venture. If it is possible to authentically model the details of inter-particle interactions, it should be possible to extrapolate trends and make any appropriate approximations for groups of particles that exhibit near-identical behaviour. In this way, a core of precise knowledge could be developed, and in principle, could be modified to solve many macroscopic granular solids flow situations.

However, it is necessary to make rather radical assumptions in developing any model of this kind. As a consequence, an essentially fictitious material is created, even when viewed from a very simplified stand-point. For example, Cundall and Strack (1979) worked with the numerical modelling of a limited number of two-dimensional discs and Thornton (1979) studied the strength of a face-centred cubic array of uniform rigid spheres. The realistic application of the discrete element technique, still in its infancy, to the discharge of full-scale silos, with their billions of irregular particles and complex packing assemblies, appears to be a very long way off.

2.4.6 Kinematic analysis

2.4.6.1 General

Kinematic analysis of granular solids flow begins with radically-elementary assumptions in an attempt to extract the key elements of the behaviour. Complete stress independence is assumed and any effects which interparticle friction or wall friction might have are excluded. These are weighty assumptions but the outcomes indicate that they are not unreasonable and that this approach is certainly viable

when applied to the free flow of dilated, smooth granular solids. For the analysis of incipient flows of very frictional, consolidated, granular solids, a soil-mechanical approach may be more appropriate. In the kinematic approach, the emphasis is on solving for velocities and fluxes (a flux in this sense is defined as a flow rate through a unit area normal to the direction of flow) in the granular solid mass rather than for pressures and stresses.

The kinematic modelling of granular solids flow has been carried out by a number of researchers. All those reviewed here have arrived at essentially the same governing differential equation which is shown below. This equation contains a single unknown parameter (here described by B) which is termed the kinematic constant. The governing differential equation, being similar to those for two-dimensional diffusion or heat flow, has standard solutions and these were exploited by some researchers.

2.4.6.2 Previous research

The first known work in this field was by Litwiniszyn (1963). In his analysis of a random 'walk' of particles, the granular particles were considered to be resident in hypothetical cages. The techniques of stochastic mechanics were used to find the probability P that a particle would leave its cage, centred on (x,z), where x is the horizontal co-ordinate and z is the vertical co-ordinate measured vertically upwards. The resulting partial differential equation was

$$\frac{\partial P(x,z)}{\partial z} + B\frac{\partial^2 P(x,z)}{\partial x^2} = 0 \qquad (2.3)$$

Litwiniszyn's original goal was to determine the deformed shape on the ground surface when an underground tunnel was excavated, so only planar geometries of unrestricted width were considered. The displacement profiles for these boundary conditions look plausible, although Mullins (1979) later showed that this subsidence theory contained inconsistencies. However, these inconsistencies could be remedied by applying Litwiniszyn's (1963) derivation to the vertical flux (the vertical flow rate through a unit horizontal area) rather than to the subsidence.

Mullins (1972), who also used the methods of stochastic mechanics, assumed that the downward flow of particles was equivalent to the upward flow of voids that

entered the system through the orifice. He solved for the void concentration c which, although closely related to the density, is not of direct use to the silo designer. He considered axisymmetric geometries and his governing differential equation was

$$\frac{\partial^2 c}{\partial x^2} + \frac{\partial^2 c}{\partial y^2} = \frac{1}{B}\frac{\partial c}{\partial z} \qquad (2.4)$$

where x and y are perpendicular horizontal co-ordinates and z is the vertical co-ordinate which is positive upwards. He hypothesised that the kinematic constant B (which has the dimensions of length) should be of the same order of magnitude as the diameter of a particle. By introducing such concepts as a semi-infinite bed and a point orifice, he was able to solve the resulting equations and produced plausible flow predictions.

Graham *et al* (1987) exploited a standard series solution to solve the basic kinematic (diffusion-type) differential equation (identical to Eq. 2.4) for discharge through a point orifice in the centre of an axisymmetric silo. They thus obtained a theoretical prediction of the vertical velocity field. Integrating down a particle trajectory, they calculated the residence time of each particle. They used fixed vertical tubes to introduce marker particles into their discharging axisymmetric silo. The time taken for a marker to exit the silo, the residence time, was measured. Steady state conditions were ensured by recycling two vessel volumes before placing any marker particles into the test silo. The analytically-predicted residence times were found to fit their experimental data remarkably well.

Graham *et al* produced a unique theoretical plot of dimensionless initial height on the centreline against a dimensionless residence time. This plot has an asymptotic gradient of unity and intercepts the vertical axis at $z_i B/R^2 = 0.14$, where z_i is the initial height on the centreline and R is the silo radius. This intercept value was used to find a value for the kinematic constant from experimental plots of z_i against the residence time T. They tested two solids: coke (rough, with a particle diameter 0.1 mm to 12.5 mm) and epoxy spheres (smooth, with a particle diameter 1.6 mm to 6.4 mm). They found the kinematic constant to be 15 mm for coke and 26 mm for epoxy spheres. Using these values, flow fronts were predicted which showed that the flow channel was much wider for the epoxy spheres than it was for the coke. They concluded that the kinematic model could predict residence time distributions for both solids in axisymmetric flow. The retarding effects of the

positioning tubes (Cleaver, 1991) and the implications for flow of their rather unusually-shaped silo were, however, ignored.

Tuzun and Nedderman's (1979a) theoretical model proposed that, as one particle falls out of the orifice, its space is taken by a particle free-falling from the layer above. The gravity flow of particles, producing voids in this manner, propagates upwards and outwards from the orifice. Tuzun and Nedderman put forward the very simple proposition that the horizontal velocity is a linear function of the horizontal gradient of the vertical velocity. Applying the condition of continuity in incompressible flow to this proposition led to their governing partial differential equation:

$$L(v) = B\left(\frac{\partial^2 v}{\partial x^2}\right) - \frac{\partial v}{\partial y} = 0 \qquad (2.5)$$

in which v is the vertical velocity. Equation 2.5 is directly analogous to the equation derived by Litwiniszyn (1963) (Eq. 2.3) and is slightly simpler than that of Mullins (1972) (Eq. 2.4) and Graham *et al* (1987) (Eq. 2.4), the latter two being formulated to analyse flow in axisymmetric geometries. Tuzun and Nedderman (1979a) exploited a similarity solution, which is only valid in the converging flow zone, and a more general product solution to solve for their independent variable, the vertical velocity v, in a plane-strain, flat-bottomed silo.

Using filming techniques, Tuzun and Nedderman (1979a) calculated the experimental horizontal and vertical velocities for their solid: glass ballotini with diameters between 1.5 and 2 mm. On the whole, the experimental velocities showed excellent correlation with the analytical predictions. By considering the variation of the vertical velocity down the centreline, Tuzun and Nedderman were able to extrapolate a value for the kinematic constant B. This they found to be in the region of 5 mm and fairly constant; it only increased slightly towards the top of the silo. They also reported that the kinematic constant was independent of silo width and orifice size. They proposed that the value of the kinematic constant may be related to the particle diameter and that it may be possible in the future to deduce its value from a simple material test when an appropriate test is developed.

Tuzun and Nedderman (1979b) extended their previous work by conducting a series of experiments to investigate the effect of varying the particle size on the kinematic

constant. They found a linear relationship between the kinematic constant and the particle diameter d, *i.e.*

$$B = kd \tag{2.6}$$

The proportionality constant k was about two for their material, glass ballotini. However, the number of eligible pairs of data points on their graph of B against d was only three so the findings are rather tenuous. It was proposed that the new dimensionless material constant k is primarily dependent on particle shape. They also reported that the kinematic model gives poor predictions for solids composed of particles with a mean diameter below 0.6 mm, due to the increasing importance of interstitial air effects.

Continuing their research into the discharge of glass ballotini from plane-strain silos, Tuzun and Nedderman (1982) directed their work towards an investigation of the flow channel boundary. Long time exposures were used to measure the extent of the flowing region of solid. They found that the flow channel boundary as assessed from the experiments corresponded closely with the theoretical velocity contour of 1 particle diameter per second and with the streamline that bounded 99% of the total flow.

The thorough series of experiments conducted by Tuzun and Nedderman (1982) showed that the silo width, the orifice width and the existence of a fully-rough wedge-shaped hopper had marginal effects on the apparent flow channel boundary provided that the hopper was always covered by 'stationary' solid. However, the particle diameter did affect the size of the fast-flowing core; the core being larger for larger particles. They therefore proposed that, for a given solid, there is a characteristic curve which describes the flow channel boundary and that this only depends upon the material properties, such as the particle diameter. However, they also noted that the flow channel boundary is affected by a smooth-walled hopper: both the volume of fast-flowing solid and the discharge rate are increased.

2.5 Summary

A review has been given of both the experimental and theoretical techniques used to study the flow behaviour of discharging silos. From the many methods discussed,

the focus of this thesis was chosen to be experiments involving a semi-circular silo with a transparent diametral wall, together with residence time measurements, and the kinematic model for numerical studies.

The semi-circular silo has the advantages of

(a) addressing the commonest geometry in service;

(b) permitting the effects of the transparent wall to be assessed by comparing radial lines close to and distant from the wall; and

(c) giving a substantial body of solid in the silo which is unaffected by the presence of the wall.

The technique of residence time measurements was adopted because of its simplicity and its suitability to studying the flow patterns in three-dimensional systems of reasonable size. It is shown in Chapter 6 that residence time data can be used in a number of ways to determine the position of the flow channel boundary.

The kinematic model was selected, from the possible theoretical approaches, because of its appealing simplicity and developmental potential. Smallwood and Thorpe (1980) and Graham *et al* (1987) have both coupled the experimental method of residence time measurements with the theoretical method of kinematic analysis and found favourable agreements.

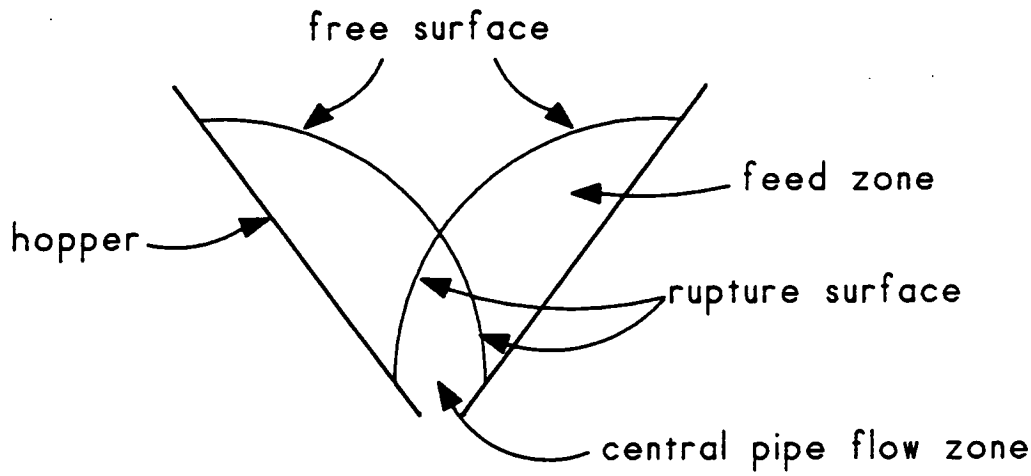

Fig. 2.1 Rigid blocks and rupture surfaces in a mass flow hopper

CHAPTER 3

A FINITE ELEMENT KINEMATIC ANALYSIS OF PLANAR GRANULAR SOLIDS FLOW

3.1 Introduction

In this chapter, a finite element analysis is presented to calculate the steady-state velocity fields in a cohesionless granular solid discharging from a planar flat-bottomed silo. The work expands and generalises Tuzun and Nedderman's (1979a) theory to treat a wide range of geometries, material properties and boundary conditions. The approach is kinematic and gravity-based, solving for the velocity field and assuming complete stress-independence.

Tuzun and Nedderman's (1979a) work was based on a purely kinematic approach and involved only one material property. This simplification, and the straight-forward geometries of their model silos, restricted the system sufficiently for it to be susceptible to algebraic analysis. They found remarkably close correlations between the theoretical and experimental results in their tests using glass ballotini.

Tuzun and Nedderman's (1979a) governing partial differential equation is generalised and solved using the finite element method. The inherent flexibility of this method allows the silo geometry to be varied, realistic boundary conditions to be prescribed and spatial variations in the kinematic constant to be made, creating a 'kinematic parameter'.

3.2 Theoretical formulation

3.2.1 Development of theory

The underlying assumptions of the kinematic theory presented here are identical to those of Tuzun and Nedderman (1979a). This theory is based on a kinematic model which proposes that as one particle falls out of the orifice, its space is taken by a

particle free-falling from the layer above (see Fig. 3.1). This gravity flow of particles propagates upwards and outwards from the orifice. Tuzun and Nedderman's (1979a) model is very similar to the stochastic mechanics models of Mullins (1972) and Litwiniszyn (1963). The former speaks of an upward flow of voids that enter the silo through the orifice whilst the latter offers a particle cage hypothesis with unknown particle motion probabilities. These three models arrive at essentially the same governing differential equation. Tuzun and Nedderman (1979a) solve for the vertical velocity field, Mullins (1972) solves for void concentration and Litwiniszyn (1963) solves for the probability that a particle will leave its cage.

Tuzun and Nedderman (1979a) assumed that the horizontal velocity, u, was a linear function of the horizontal gradient of the vertical velocity

$$u = -B(x,y)\frac{\partial v}{\partial x} \tag{3.1}$$

in which v was the vertical velocity and B was constant throughout the domain and was called the 'kinematic constant'. In the present work, B may vary spatially in any prescribed manner and is therefore called the 'kinematic parameter'. This assumption is intuitively reasonable, as it follows that if an entire horizontal layer is descending vertically at the same velocity, the horizontal velocity will be zero. As the horizontal gradient of the vertical velocity grows, the horizontal velocity also progressively increases: that is, high shear strain rates in the solid lead to high horizontal velocities. The model assumes incompressibility and steady state conditions.

Assuming that the flow is incompressible, continuity requires that

$$\frac{\partial u}{\partial x} + \frac{\partial v}{\partial y} = 0 \tag{3.2}$$

Substituting Eq. 3.1 into Eq. 3.2, the governing partial differential equation becomes

$$L(v) = \frac{\partial}{\partial x}\left(B(x,y)\frac{\partial v}{\partial x} \right) - \frac{\partial v}{\partial y} = 0 \tag{3.3}$$

Several researchers (*e.g.* Graham *et al*, 1987 and Mullins, 1972) have proceeded from this point, or an analogous one, by recognising the similarity of Eq. 3.3 to diffusion equations and exploiting existing diffusion solutions. However, this severely limits the scope of the analysis in terms of geometries, parameters and boundary conditions to the few analytically-tractable cases. Instead, a numerical solution technique is adopted here which exploits the finite element method, using the general philosophy for the solution of partial differential equations outlined by Baker and Pepper (1991).

The finite element method assumes that the unknown, dependent variable, here taken to be the vertical velocity v, can be approximated throughout the domain by a Taylor series of known spatial functions, ϕ_i, multiplied by an unknown expansion coefficient set, a_i. Thus, the result converges to the correct solution only as more terms of the series are used. So the value of v at any point may be written

$$v^N(x,y) = \sum_{i=1}^{N} a_i \, \phi_i(x,y) \tag{3.4}$$

where the superscript ^{N} denotes an N-termed approximation.

The global minimum for the approximation error is obtained using the method of weighted residuals

$$\iint_{\Omega} w_i(x,y) \, L(v^N) \, d\Omega = 0 \tag{3.5}$$

where Ω denotes the problem statement domain and $w_i(x,y)$ is an arbitrary weighting function set. The weighted residual technique used here is the Galerkin criterion which is chosen for its all-round applicability and guarantee of error minimisation. The Galerkin criterion stipulates that the weighting function set should be equal to the spatial function set:

$$w_i(x,y) = \phi_i(x,y) \tag{3.6}$$

Thus Eq. 3.5 becomes

$$\int\int_{\Omega} \phi_i(x,y)\, L(v^N)\, d\Omega \;=\; 0 \tag{3.7}$$

or, adopting Eq. 3.3

$$\int\int_{\Omega} \phi_i(x,y) \left(\frac{\partial}{\partial x}\left(B(x,y) \frac{\partial v}{\partial x} \right) - \frac{\partial v}{\partial y} \right) d\Omega \;=\; 0 \tag{3.8}$$

Green's First Identity states that

$$\int\int_{\Omega} \kappa \frac{\partial \lambda}{\partial x}\, dxdy \;=\; -\int\int_{\Omega} \lambda \frac{\partial \kappa}{\partial x}\, dxdy \;+\; \int_{\Gamma} \kappa\, \lambda\, n_x\, d\Gamma \tag{3.9}$$

where κ and λ are arbitrary functions of x and y with continuous first derivatives, Γ is the boundary of the domain Ω and n_x is the outward-pointing x-direction cosine.

Using Eq. 3.9 on Eq. 3.8 leads to

$$-\int\int_{\Omega} \frac{\partial \phi_i}{\partial x} B(x,y) \frac{\partial v^N}{\partial x}\, d\Omega \;+\; \int_{\Gamma} \phi_i\, B(x,y) \frac{\partial v^N}{\partial x}\, n_x\, d\Gamma \;-\; \int\int_{\Omega} \phi_i \frac{\partial v^N}{\partial y}\, d\Omega \;=\; 0 \tag{3.10}$$

where $d\Omega$ is an elemental area and $d\Gamma$ an elemental boundary segment. Equation 3.10 is termed the Galerkin Weak Statement (Baker and Pepper, 1991) because the differentiability that the approximation v^N must support has been weakened (from second to first order).

The finite element method may now be implemented by constructing a domain discretization. This divides the solution domain into discrete finite-sized elements. Elements are generally described in terms of the polynomial power of the assumed variation of the dependent variable within each element. The elements used here are

taken from the serendipity family (Zienkiewicz, 1971). The linear element has a node at each of its four corners, the quadratic element has an additional four midside nodes and the cubic element has four corner nodes plus two midside nodes per side. The present formulation employs 12-noded cubic isoparametric elements which have the same functional description for geometry as for the dependent variable (Zienkiewicz, 1971).

In the following, one generic element is examined. The spatial function set $\phi_i(x,y)$ now becomes the shape function set $\{N_k(x,y)\}$ and the expansion coefficient set a_i is the vector of nodal vertical velocity unknowns $\{v\}_e$. Thus, the vertical velocity distribution within a generic element, v_e, is approximated as

$$v_e(x,y) = \{ N_k(x,y) \}^T \{v\}_e \tag{3.11}$$

where k is the shape function degree and also indicates the number of terms in $\{N\}$, *i.e.* the number of nodal unknowns in the element. Hence, $k = 4$ for the linear element, $k = 8$ for the quadratic element and $k = 12$ for the cubic element. The vertical velocity throughout the entire domain is given as

$$v^h(x,y) = \cup_e v_e(x,y) \tag{3.12}$$

Upon discretization of the domain into elements, the Galerkin weak statement becomes

$$WS^h = S_e \left(\iint_{\Omega_e} \frac{\partial \{N_k\}}{\partial x} B(x,y) \frac{\partial \{N_k\}^T}{\partial x} d\Omega \{v\}_e - \int_{\Gamma_e} \{N_k\} B(x,y) \frac{\partial \{N_k\}^T}{\partial x} n_x d\Gamma \{v\}_e + \iint_{\Omega_e} \{N_k\} \frac{\partial \{N_k\}^T}{\partial y} d\Omega \{v\}_e \right) \equiv 0 \tag{3.13}$$

where S_e is the non-overlapping sum (or union, $\cup$) taken over all domain elements and the superscript ^{h} is used to signify that a discretization has occurred.

Equation 3.13 may be written in abbreviated form as

$$S_e([K + H - P]_e\{v\}_e) = \{0\} \tag{3.14}$$

with

$$[K]_e = \iint_{\Omega_e} \frac{\partial\{N_k\}}{\partial x} B(x,y) \frac{\partial\{N_k\}^T}{\partial x} \, d\Omega$$

$$[H]_e = \iint_{\Omega_e} \{N_k\} \frac{\partial\{N_k\}^T}{\partial y} \, d\Omega$$

and

$$[P]_e = \int_{\Gamma_e} \{N_k\} B(x,y) \frac{\partial\{N_k\}^T}{\partial x} n_x \, d\Gamma$$

In the above (and in subsequent) equations, curly brackets ({}) represent a column vector (a 1D array) and square brackets ([]) a matrix (an array of dimension two or above).

The first two terms in Eq. 3.14 involve integrals only over the generic individual finite element domain which, once the shape function degree k has been chosen, are evaluated quite simply using Gaussian Quadrature. The symmetrical matrix $[K]_e$ may be recognised as analogous to the element stiffness matrix which arises when the finite element method is applied to the theory of elasticity. $[P]_e$ is a term describing a flux along an element boundary (a Neumann boundary condition) whilst the matrix $[H]_e$ is a term characteristic of this governing partial differential equation.

3.2.2 Computational procedure

The versatility and unrestrictive generality of the finite element method allows attention to be concentrated on a characteristic element. The three arrays $[K]_e$, $[H]_e$ and $[P]_e$ in Eq. 3.14 are calculated for each element and are summed into the corresponding global system matrices [K], [H] and [P] by the process of assembly. This is continued for all elements of the domain. It may be noted that only those elements which both lie on domain boundaries and have Neumann boundary conditions specified on them will make a contribution to the global matrix [P]. The global matrix statement may then be written:

$$[K + H - P]\{v\} = \{0\} \tag{3.15}$$

Equation 3.15 can be completed by inserting any prescribed nodal vertical velocities (Dirichlet data) into the global vector of vertical velocity unknowns {v}. This results in an explicit system of simultaneous equations which are soluble. The unsymmetrical matrices [H] and [P] render the (banded) matrix [K+H-P] unsymmetrical. The counterpart of this matrix in elasticity, the global stiffness matrix, is banded and symmetrical and therefore yields to efficient symmetrical matrix solution techniques. To facilitate the evaluation of the boundary integral in the matrix [P], it is seen from Fig. 3.2 that $n_x = \cos\theta = dy/d\Gamma$ and so the product $n_x d\Gamma$ can be replaced with dy. Examples of the matrices $[K]_e$, $[H]_e$ and $[P]_e$ are given in Appendix 3.1.

3.2.3 Boundary conditions

The complete domain boundary Γ can be broken up into five boundary sectors as in Fig. 3.3. The matrix $[P]_e$ must be calculated for all elements on whose boundaries a flux is applied. The nature of $[P]_e$ will depend upon the domain boundary conditions on the side or sides of the element. The contributions from all elements may then be placed in the global matrix [P] by assembly.

Vertical Boundaries

Since the horizontal velocity u normal to a vertical silo wall or a vertical plane of symmetry must be zero at the boundary, u must be zero on the vertical boundaries Γ_2 and Γ_5 (Fig. 3.3). Using Eq. 3.1, $\partial v/\partial x$ must also be zero on these boundaries. Thus $[P]_e$ along these domain perimeters is identically zero. Thus those elements with edges that lie on these two boundary sectors will make no contribution to the global matrix [P].

Horizontal Boundaries

Considering next the boundaries Γ_1, Γ_3 and Γ_4 (which are taken to be horizontal in this steady-state analysis), the angle between the outward normal and the positive x-direction is either $\pi/2$ or $3\pi/2$. Thus the direction cosine n_x is also zero and the matrix $[P]_e$ associated with an element contiguous with any of these three boundaries also vanishes.

For simply geometries with only horizontal and vertical boundaries, the global matrix statement (in discrete form) is thus reduced to

$$S_e([K + H]_e\{v\}_e) = \{0\} \tag{3.16}$$

Since, in general, [K+H] is not singular, Eq. 3.16 leads to the trivial solution of identically zero velocities unless some boundary velocities are imposed. Thus, for the problem statement to be non-trivial, there must be some fixed Dirichlet boundary data. These take the form of prescribed values of the dependent variable v at particular nodes. Since the original differential equation (Eq. 3.3) contained no forcing function, this is to be expected.

In the present implementation, the vertical velocity v is prescribed as zero on Γ_3. A suitable vertical velocity distribution is prescribed along Γ_4 which is the stipulated exit velocity profile, v_{exit}.

3.2.4 Verification

The analysis was first applied to the experiments conducted by Tuzun and Nedderman (1979a). The experiment which Tuzun and Nedderman (1979a) termed Run No. 4 is presented first to explain some aspects of the modelling. In Run No. 4, the geometry of the planar model silo had a half-width of 101.5 mm, a half-orifice width of 11 mm and a height of 1500 mm, as shown in Fig. 3.4. Following Tuzun and Nedderman's (1979a) experimental observations, alternative values for B of 4 mm, 5 mm and 6 mm were used. Symmetry was exploited to analyse only the right hand half of the silo. Initially, the exit velocity profile was assumed to be invariant with x (constant velocity) and dimensioned to produce the required volumetric flow rate Q. This was calculated from their Eq. 3.7 (which is an approximation valid only in the converging flow zone) and at a height y of 220 mm, using a value of B of 5 mm and a value of vertical velocity on the centreline of 41 mm/s (from their Fig. 3.10), this equation gives Q = 4820 mm^2/s. The results of the present numerical prediction, together with the approximate analytical solution of Tuzun and Nedderman (1979a) are presented in Fig. 3.5.

The match between the present predictions and the experiment is good everywhere except at an x-co-ordinate corresponding to the edge of the orifice. This may be attributed to the discontinuity in the imposed exit velocity profile at this ordinate, which creates the dramatic fluctuation. Upon mesh refinement in this region, the fluctuation became more confined but increased in magnitude. Alternative profiles of imposed exit velocities were then substituted. First a parabolic exit velocity profile was used to give continuity in the imposed values of v, but the discontinuity in $\partial v/\partial x$, which implies a discontinuity in the horizontal velocity u, still caused some disturbance at the orifice edge co-ordinate. A cubic exit velocity was therefore implemented which satisfies the conditions of symmetry at the centreline and continuous vertical and horizontal velocity fields at the edge of the orifice. This adjustment of the exit velocity profile seems reasonable since the velocity distribution throughout most of the silo is effectively independent of the exit velocity profile. Only very close to the orifice is the distribution sensitive to the assumed exit profile (Tuzun and Nedderman, 1979a).

Thus the exit velocity profile was chosen as

$$v_{exit} = ax^3 + bx^2 + cx + d \qquad 0 \le x \le x_o \qquad (3.17)$$

in which a, b, c and d are constants and x_o is the orifice width. The above local boundary conditions can then be expressed as

$$v_{exit}\Big|_{x=x_o} = 0 \tag{3.18a}$$

$$\frac{dv_{exit}}{dx}\Big|_{x=x_o} = 0 \tag{3.18b}$$

$$u\Big|_{x=0} = 0 \qquad \text{or} \qquad \frac{dv_{exit}}{dx}\Big|_{x=0} = 0 \tag{3.18c}$$

and

$$Q = 2\int_0^{x_o} v_{exit}\, dx \tag{3.18d}$$

where Q is the defined volumetric flow rate per unit depth of the complete planar silo. Since the flow is in the negative y-direction, all vertical velocities should strictly be negative, but they are taken as positive here to match Tuzun and Nedderman's (1979a) convention.

Applying these conditions, Eq. 3.17 is solved for a, b, c and d yielding

$$v_{exit} = 2v_o\left(\frac{x}{x_o}\right)^3 - 3v_o\left(\frac{x}{x_o}\right)^2 + v_o \qquad 0 \le x \le x_o \tag{3.19}$$

where v_o, the largest value in the entire domain, is the vertical velocity at x = y = 0 and is given by

$$v_o = \frac{Q}{x_o} \tag{3.20}$$

In the present example (Run No. 4, B = 5 mm), the value of v_o is 438 mm/s.

3.2.5 Results

With the imposed exit velocity varying cubically with x, the vertical velocity variation at the height of 220 mm was calculated and is shown, along with the experimental data points and the analytical solution of Tuzun and Nedderman (1979a), in Fig. 3.6. Horizontal profiles of vertical velocity were plotted at other heights above the silo base. The results are presented in Figs 3.7 and 3.8. The velocity profile down the vertical centreline of the silo is shown in Fig. 3.9 and three further vertical profiles at different constant distances from the centreline are shown in Fig. 3.10.

Substituting Eq. 3.11 into Eq. 3.1, it is possible to calculate the horizontal velocity u at Gauss points throughout the domain as

$$u = -B(x,y) \frac{\partial \{N_k\}^T}{\partial x} \{v\}_e \tag{3.21}$$

Horizontal profiles of horizontal velocity, calculated at three different heights, are shown in Fig. 3.11. The sign convention used in these figures is that horizontal velocities towards the centreline are taken as positive.

The comparisons with two other reported experimental results of Tuzun and Nedderman (1979a) are shown in Figs 3.12 and 3.13. Figure 3.12 shows a horizontal profile of vertical velocity in a slightly wider silo (with a half-width of 152.5 mm) and Fig. 3.13 shows a horizontal profile of horizontal velocity in a silo of half-width 101.5 mm as before.

It would appear that Tuzun and Nedderman's (1979a) Figures 3.8, 3.9, 3.10 and 3.11 contain errors. In each of these figures, horizontal profiles of vertical velocity are given for three different values of the kinematic constant. From the current work, it is expected that these profiles should cross one another at some value of the horizontal co-ordinate x and continuity considerations applied at a given level require that this must occur. In the figures of Tuzun and Nedderman (1979a) however, the profiles appear to have no intersection. It is thought that these errors probably arose during the tracing process.

All of Tuzun and Nedderman's (1979a) test results show a similar correlation with the present predictions when the above errors are taken into account.

3.2.6 Discussion

From Fig. 3.6, it can be seen that the finite element method accurately reproduces the analytical solution of Tuzun and Nedderman (1979a) and that both correlate quite well with the experimental observations.

In Fig. 3.13, there is a dramatic and very narrow fluctuation in the horizontal velocity at an x co-ordinate that corresponds to the edge of the orifice ($x = x_0$). This arises from the very small elements required in this region to represent the change in vertical velocity. Even with a smooth cubically-varying exit velocity profile there is still a slight fluctuation in the vertical velocity along $x = x_0$. The calculation of the horizontal velocity is very sensitive to local variations in the vertical velocity. The small elements used ensure that the fluctuation is constrained to a narrow band in the x-direction but unfortunately this leads to a higher peak. Apart from this very local fluctuation, the match between the analytical solution of Tuzun and Nedderman (1979a) and the present formulation is very nearly exact, even though the assumed exit velocity distributions are quite different. It can therefore be concluded that the present finite element analysis has been correctly formulated and implemented.

From Figs 3.7 and 3.8, it can be seen that as one ascends the silo the plug of flowing solid becomes wider and the centreline velocity is reduced. This reduction is required to satisfy the assumption of incompressible flow as the channel becomes wider. The horizontal gradient of the vertical velocity $\partial v/\partial x$ is seen to approach zero at $x = 0$ and at $x = X$ (the silo half-width), satisfying the $u = 0$ boundary condition at these points.

Figure 3.9 shows how the centreline vertical velocity rapidly declines with height up the silo, approximately as $1/y^{1/2}$. This is as predicted by Tuzun and Nedderman (1979a) in their Eq. 7. This implies that the width of the flow channel must be opening out approximately as $y^{1/2}$.

Figure 3.10 shows that the vertical velocity approaches a constant value towards the top of the silo and that this value (about 23.8 mm/s) is quite uniform across the width, and may be compared with the centreline exit velocity of v_o = 438 mm/s. It may be noted that the product of this constant top surface velocity and the silo half-width accurately matches the value Q/2, demonstrating that the continuity condition is being globally satisfied. In the top part of the silo, the granular solid is mass flowing and, since $\partial v/\partial x = u = 0$ here, is moving as a rigid body. The behaviour at the bottom of the silo is quite different: at x co-ordinates outside the orifice, the vertical velocity is zero at y = 0, but rapidly increases with increasing height. In the small zone near the silo floor, the solid is essentially stationary and lies in what was earlier referred to as the stagnant zone.

Figure 3.11, which shows the horizontal velocity profile at different levels, indicates that u reaches a peak roughly in the middle of the fast-moving flow zone and decays towards the side wall. These profiles also flatten out with height as the flow zone expands.

The above features of the predicted flow pattern qualitatively match many of the characteristics of experimentally-observed flow patterns. The match with Tuzun and Nedderman's (1979a) experiments is thus also supported by many other aspects of these predictions.

3.3 Parametric study

3.3.1 Introduction

A parametric study was next conducted to investigate the range of flow channel predictions which this analysis can give as various parameters are changed. The geometry of the silo used in the parametric study is shown in Fig. 3.14.

The parametric study was undertaken in three parts to explore:

(a) the effect of the parameter B on the flow pattern with a homogeneous material (constant B throughout the silo).

(b) the interpretation of the flow pattern predictions in terms of a flow channel and stationary solid.

(c) the effect of material inhomogeneity on the flow pattern.

3.3.2 Vertical velocity distributions for different values of B

The kinematic constant was varied between B = 0.001 m and B = 0.1 m. These produced a range of realistic results. The vertical velocity profiles at y/X = 1 and y/X = 5 for different values of B are shown in Figs 3.15 and 3.16. All the vertical velocities have been normalised by dividing them by the modulus of the value of the vertical velocity at x = y = 0 (outlet centreline). This produces a maximum value of vertical velocity in the entire domain of -1.

It is evident that the flow channel widens out more rapidly as the value of B is increased. Because the flow is assumed to be incompressible, this means that the centreline velocity in the upper part of the silo is also reduced by increasing B. When B is only 0.001 m, a pipe flow with almost vertical sides is produced, whilst a B of 0.1 m leads to a semi-mass flow with a very uniform velocity at the surface.

3.3.3 Flow channel boundary (FCB) predictions

In common with most other comparable numerical analyses (*e.g.* Haussler and Eibl, 1984 and Eibl and Rombach, 1988), the current analysis produces a complete and continuous velocity field throughout the silo. This part of the parametric study examines appropriate ways of defining the 'flow channel boundary' (FCB) when such continuous velocity fields are obtained.

A sharp discontinuity in velocity cannot be predicted by the present formulation because the founding equations are parabolic in nature. In practice, however, it may be that there is often not a real discontinuity in the mean velocity over a finite period at the edge of the flow channel but a high (finite) mean velocity gradient: the mean vertical velocity falls from a high value of perhaps several hundred particle diameters per second to a very much smaller value, which is experimentally indistinguishable from zero, over a distance of several particle diameters. As mentioned in Section 2.3.3, Tuzun and Nedderman (1982) reported no clear cut boundary between flowing and stationary solid in their experiments. Therefore in certain flow situations, it is perhaps incorrect to assume that there is a discontinuity in the local velocity. It is necessary, therefore, to postulate some criterion which

defines what is chosen to be the flow channel boundary. In the present investigation, this was chosen as the position where the vertical velocity at a given height falls below a given proportion of the centreline velocity at that height (see Fig. 3.17). In Chapter 5, it is demonstrated that this definition results in a boundary that has the property of being everywhere tangential to the local velocity vector. In other words, no flow takes place across the FCB as defined in this thesis *i.e.* the FCB is a streamline.

3.3.3.1 Definition of the Flow Channel Boundary

Taking the case with B = 0.01 m, Fig. 3.18 shows contours of points at which the vertical velocity has fallen to a given proportion of the centreline velocity at the same height. These contours are deemed to provide a useful criterion from which the flow channel boundary may be drawn.

A wide range of conceivable FCB definitions is shown in Fig. 3.18 to indicate the insensitivity of the criterion to the adopted proportion: that is, to demonstrate that this continuum model does result in a FCB which is reasonably well defined. It is unlikely that an observer would judge that solid flowing at 10% of the centreline velocity was at rest. However, solid moving at 1% of this value would appear to be barely in motion and that at 0.1% would have indiscernible movement within the time scales and variabilities involved here.

As a result of this discussion, the FCB was chosen somewhat arbitrarily to be defined by the criterion of the locus of points at which the vertical velocity is equal to 1% of the centreline vertical velocity at the same height. However, as can be seen from Fig. 3.18, the choice of this criterion does not make a great difference to the predicted channel geometry.

It can also be seen that the FCB found using a criterion of this kind is not a conical surface (which would be given by a linear relationship between x and y) but that it is curved. It may be fortuitous and only valid for special geometries, but a parabola fits the data remarkably well.

3.3.3.2 Variation of the flow channel boundary with B

The above criterion for the FCB was applied to calculations using the same geometry but several different values of the kinematic parameter B. As the value of the kinematic parameter B is increased, the flow channel becomes wider and more sharply curved near the outlet. The increased volume of flowing solid at a given height naturally has lower relative velocities associated with it. In Fig. 3.19, a whole range of different flow patterns are exhibited, from a fast-moving narrow central pipe (B = 0.001 m) to a wide-spreading enlarged flow regime (B = 0.1 m). These correspond well to the familiar definitions of pipe flow and semi-mass flow respectively. The point at which the FCB intersects the silo wall (the effective transition) is evidently strongly dependent on the kinematic parameter B, though it is only weakly dependent on the criterion used to define the FCB.

3.3.4 Spatial variation of the kinematic parameter

Tuzun and Nedderman (1979a) reported that the kinematic 'constant' increased slightly with height in their experiments. In the present formulation, the kinematic parameter B(x,y) can be appointed to be any chosen function of x and y.

To investigate the effect of allowing B to vary in (x,y) space, the following four variations were examined:

(a) $B = 0.005$ m
(b) $B = 0.005 + 0.01x/X$ m
(c) $B = 0.005 + 0.002y/X$ m
(d) $B = 0.005 + 0.01x/X + 0.002y/X$ m

The variations were chosen to give the same range of B from the centreline to the wall in Case (b) and from the base to the surface in Case (c), with Case (d) being these two variations superimposed. All four patterns had the same value of B at the centre of the outlet.

Velocity profiles at $y/X = 2$ and $y/X = 5$ are presented in Figs 3.20 and 3.21 respectively and the 1% flow channel boundaries for the four cases are plotted in Fig. 3.22. From Figs 3.20, 3.21 and 3.22, it can be seen that as B increases with x

and/or y, the flow channel widens out, producing flatter vertical velocity profiles that have lower centreline velocities but higher velocities as the side wall is approached. It can also be seen that Cases (b) and (c) produce very similar widening effects on the FCB. If B is specified to vary with respect to both x and y, as in Case (d), the effects are compounded and the FCB becomes even wider.

3.4 Conclusions

A theoretical formulation that predicts velocity fields in a flowing granular solid has been developed and implemented using the finite element method. The theory is based upon a simple postulated relationship between the horizontal velocity and the horizontal gradient of the vertical velocity, which has its foundations in statistical mechanics. The relationship depends on only one empirical material parameter, B, which has the dimension of length. Unfortunately at present the value of B can only be established from silo flow experiments. The work accurately reproduces the experimental and theoretical results of Tuzun and Nedderman (1979a). The kinematic parameter B may be varied spatially throughout the solid. Flow channel boundary criteria have been proposed and the resulting flow channel geometries have been illustrated.

Appendix 3.1 Element matrices

$$[K]_e = \int_{\Omega_e} \int \int \begin{pmatrix} \frac{\partial N_1}{\partial x} B(x,y) \frac{\partial N_1}{\partial x} & \frac{\partial N_1}{\partial x} B(x,y) \frac{\partial N_2}{\partial x} & . & . & \frac{\partial N_1}{\partial x} B(x,y) \frac{\partial N_k}{\partial x} \\ \frac{\partial N_2}{\partial x} B(x,y) \frac{\partial N_1}{\partial x} & \frac{\partial N_2}{\partial x} B(x,y) \frac{\partial N_2}{\partial x} & . & . & \frac{\partial N_2}{\partial x} B(x,y) \frac{\partial N_k}{\partial x} \\ . & . & . & . & . \\ . & . & . & . & . \\ \frac{\partial N_k}{\partial x} B(x,y) \frac{\partial N_1}{\partial x} & \frac{\partial N_k}{\partial x} B(x,y) \frac{\partial N_2}{\partial x} & . & . & \frac{\partial N_k}{\partial x} B(x,y) \frac{\partial N_k}{\partial x} \end{pmatrix} d\Omega$$

$$[H]_e = \int_{\Omega_e} \int \int \begin{pmatrix} N_1 \frac{\partial N_1}{\partial y} & N_1 \frac{\partial N_2}{\partial y} & . & . & N_1 \frac{\partial N_k}{\partial y} \\ N_2 \frac{\partial N_1}{\partial y} & N_2 \frac{\partial N_2}{\partial y} & . & . & N_2 \frac{\partial N_k}{\partial y} \\ . & . & . & . & . \\ . & . & . & . & . \\ N_k \frac{\partial N_1}{\partial y} & N_k \frac{\partial N_2}{\partial y} & . & . & N_k \frac{\partial N_k}{\partial y} \end{pmatrix} d\Omega$$

$$[P]_e = \int_{\Gamma_e} n_x \begin{pmatrix} N_1 B(x,y) \frac{\partial N_1}{\partial x} & N_1 B(x,y) \frac{\partial N_2}{\partial x} & . & . & N_1 B(x,y) \frac{\partial N_k}{\partial x} \\ N_2 B(x,y) \frac{\partial N_1}{\partial x} & N_2 B(x,y) \frac{\partial N_2}{\partial x} & . & . & N_2 B(x,y) \frac{\partial N_k}{\partial x} \\ . & . & . & . & . \\ . & . & . & . & . \\ N_k B(x,y) \frac{\partial N_1}{\partial x} & N_k B(x,y) \frac{\partial N_2}{\partial x} & . & . & N_k B(x,y) \frac{\partial N_k}{\partial x} \end{pmatrix} d\Gamma$$

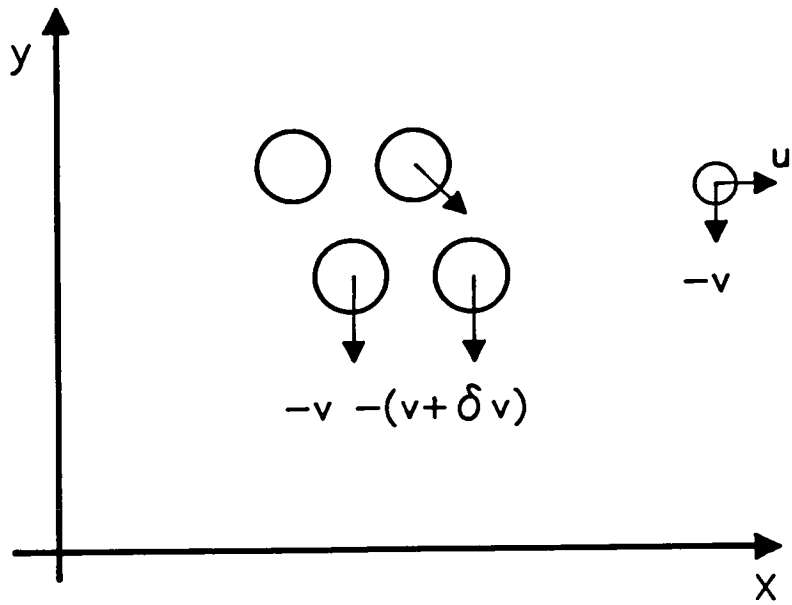

Fig. 3.1 Proposed kinematic model

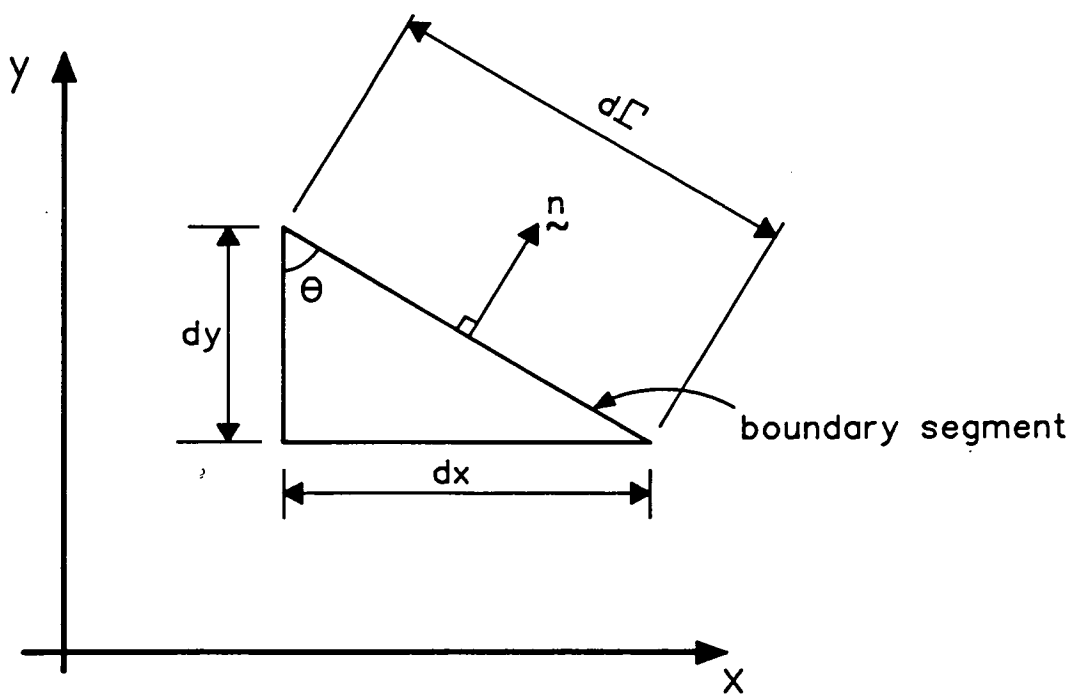

Fig. 3.2 Geometry of a boundary segment

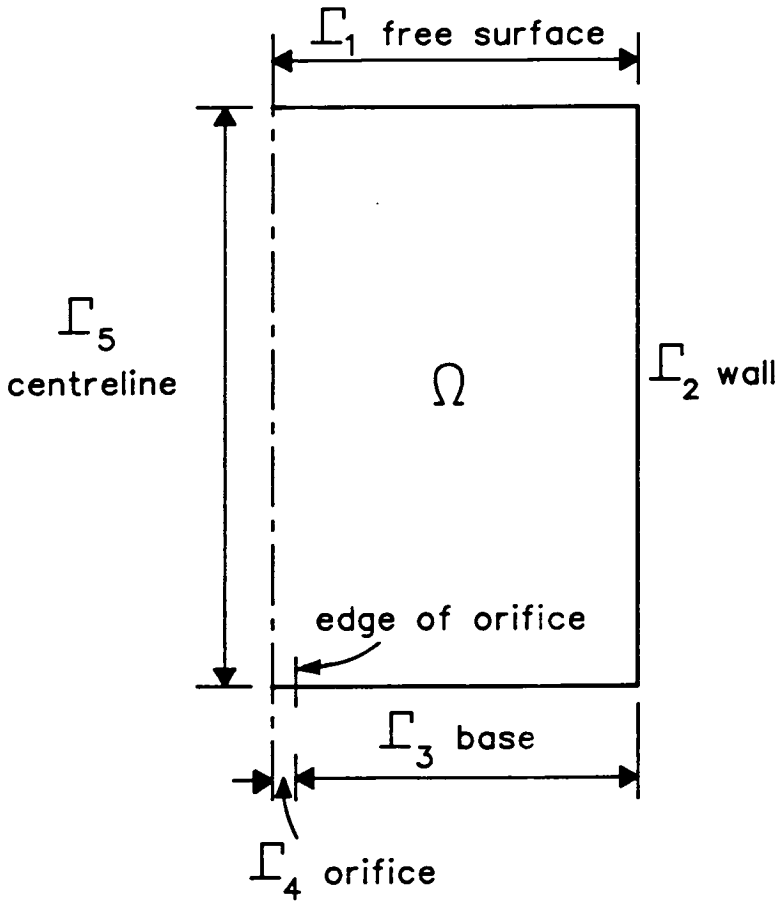

Fig. 3.3 The domain boundary segments

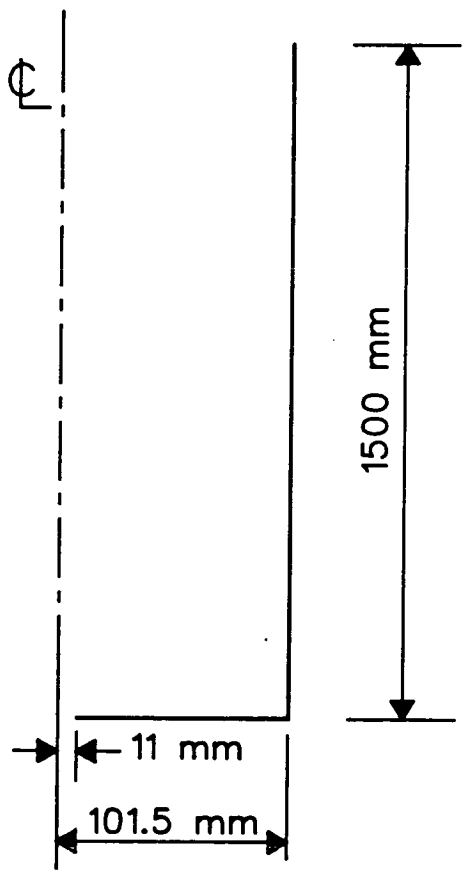

Fig. 3.4 Silo used to verify the current theory (symmetric section)

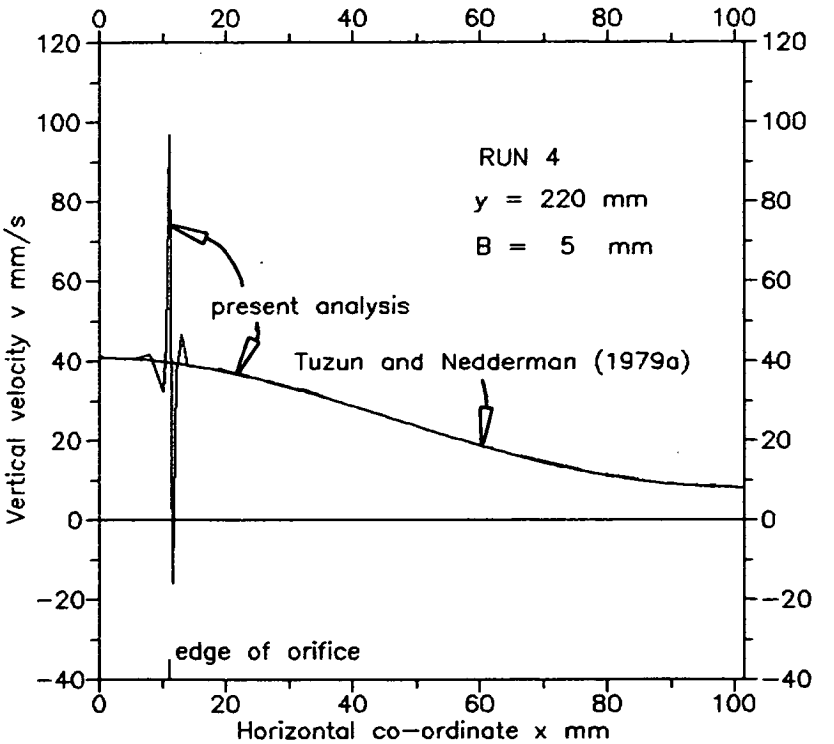

Fig. 3.5 Comparison between analyses with constant exit velocity profiles

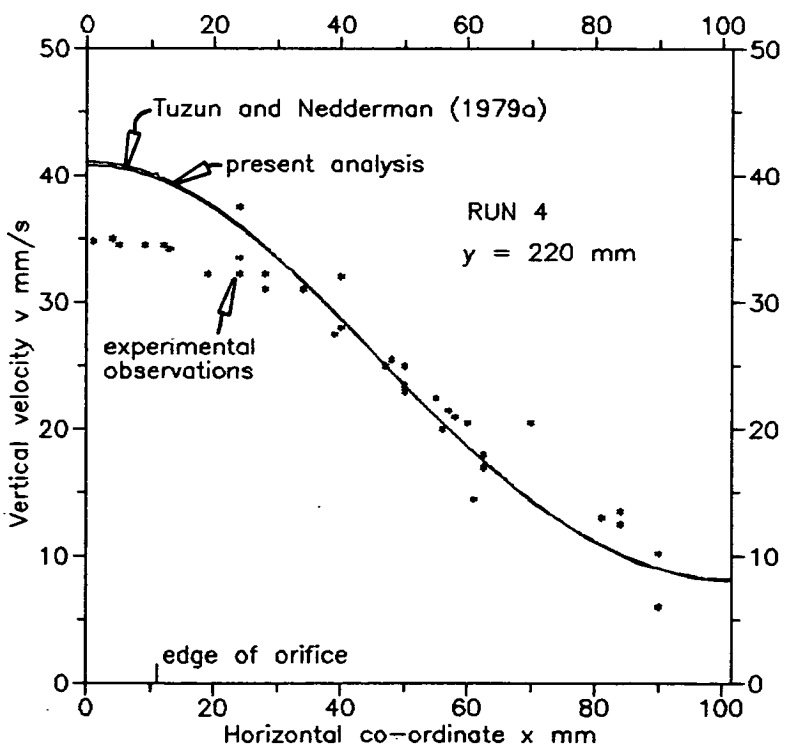

Fig. 3.6 Comparison between analyses with cubically-varying exit velocity profiles

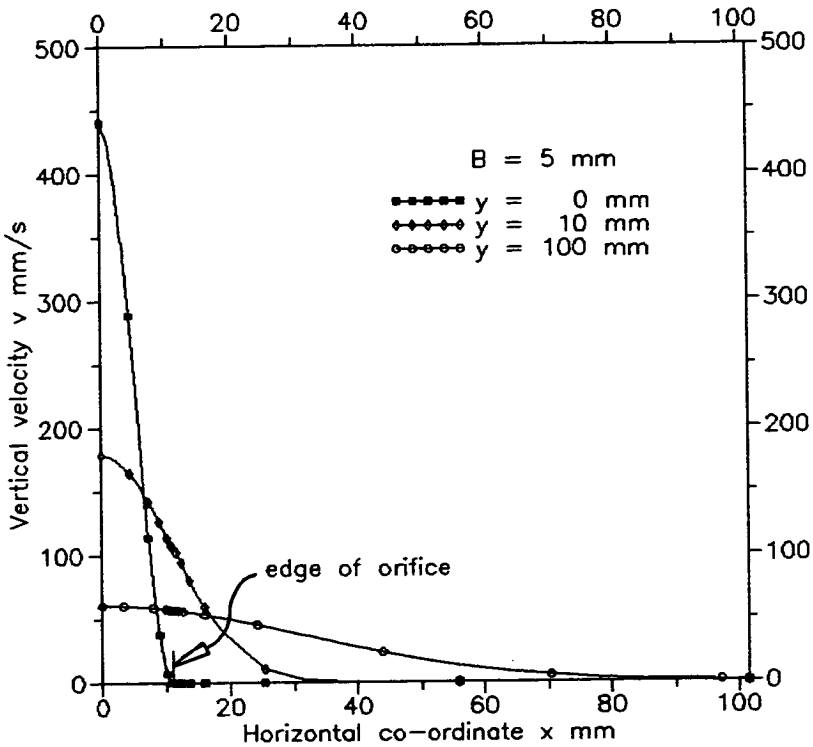

Fig. 3.7 Horizontal profiles of vertical velocity

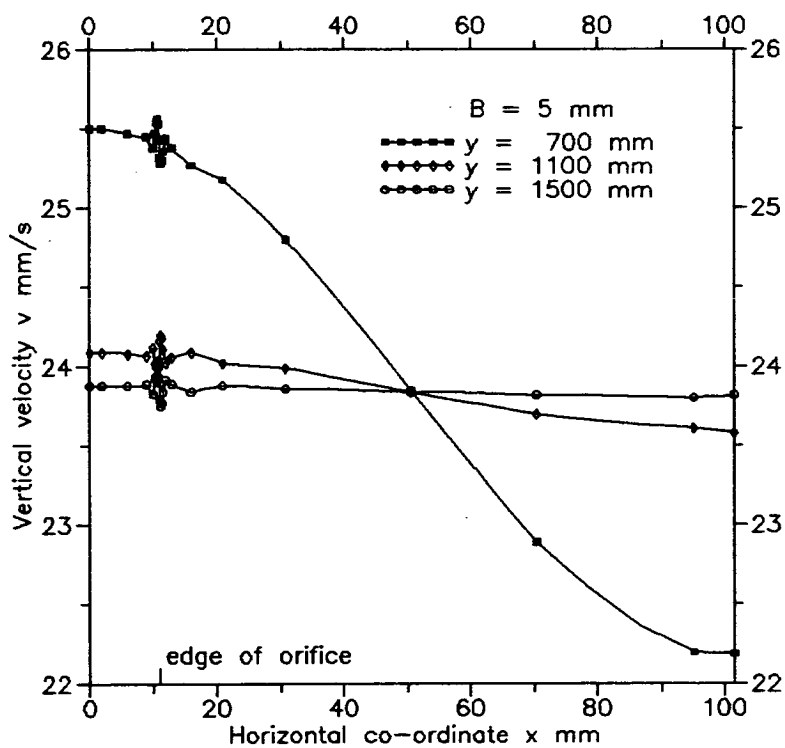

Fig. 3.8 Horizontal profiles of vertical velocity

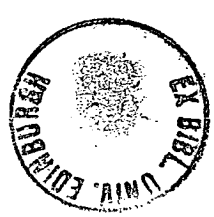

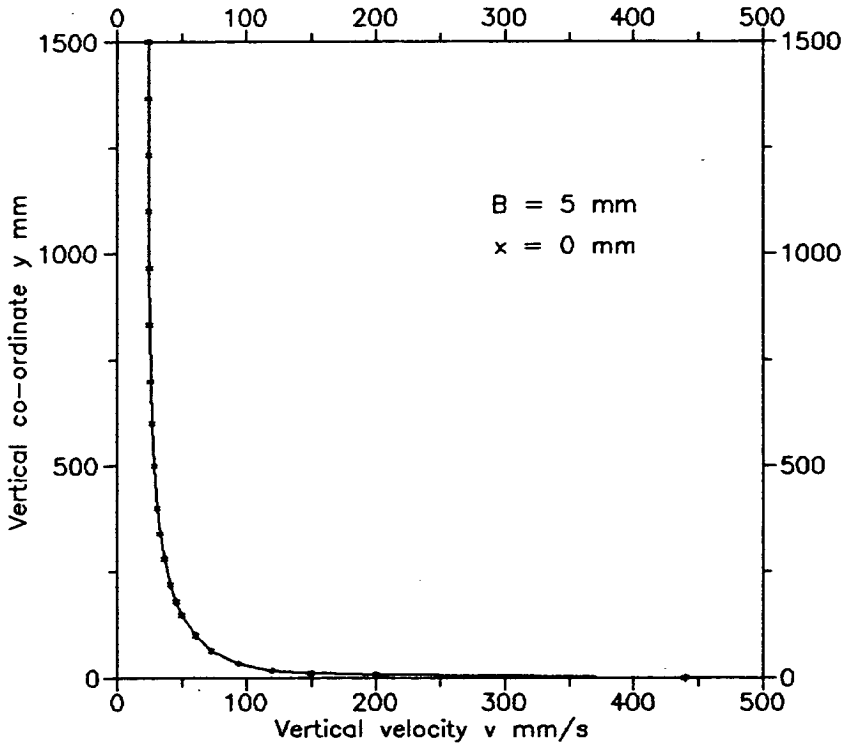

Fig. 3.9 Vertical velocity profile down the centreline

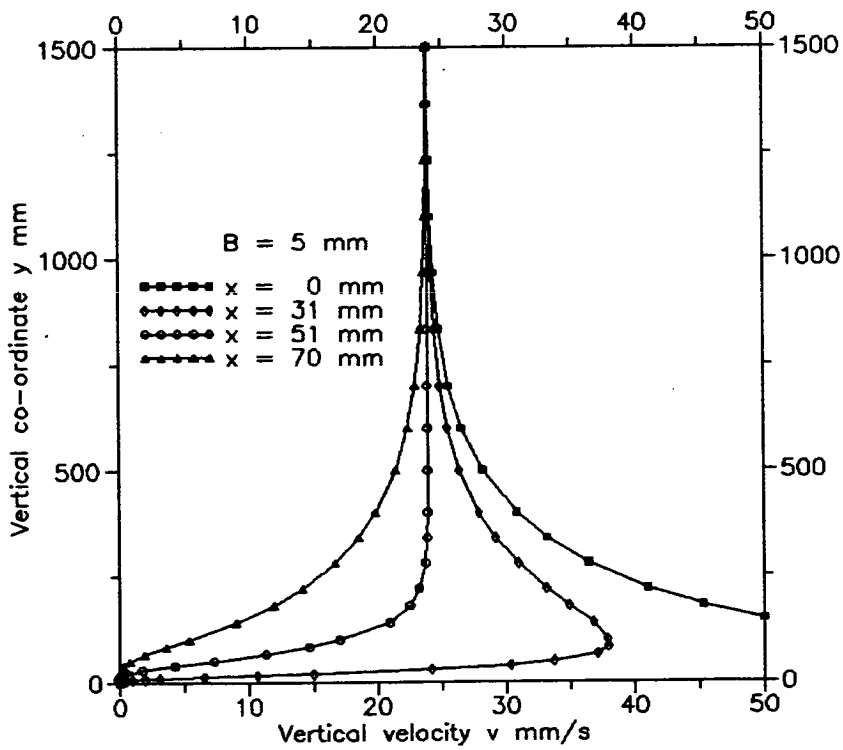

Fig. 3.10 Vertical profiles of vertical velocity

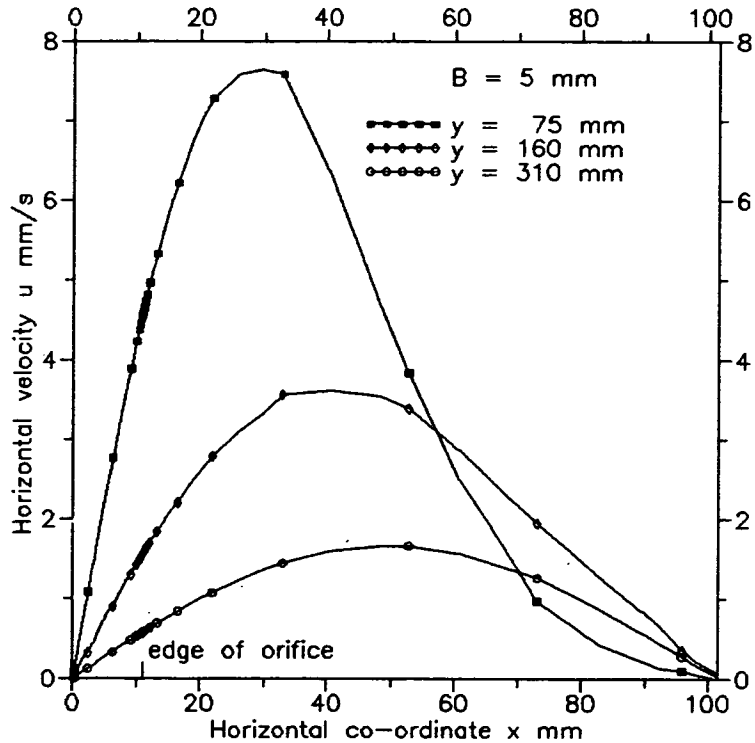

Fig. 3.11 Horizontal profiles of horizontal velocity

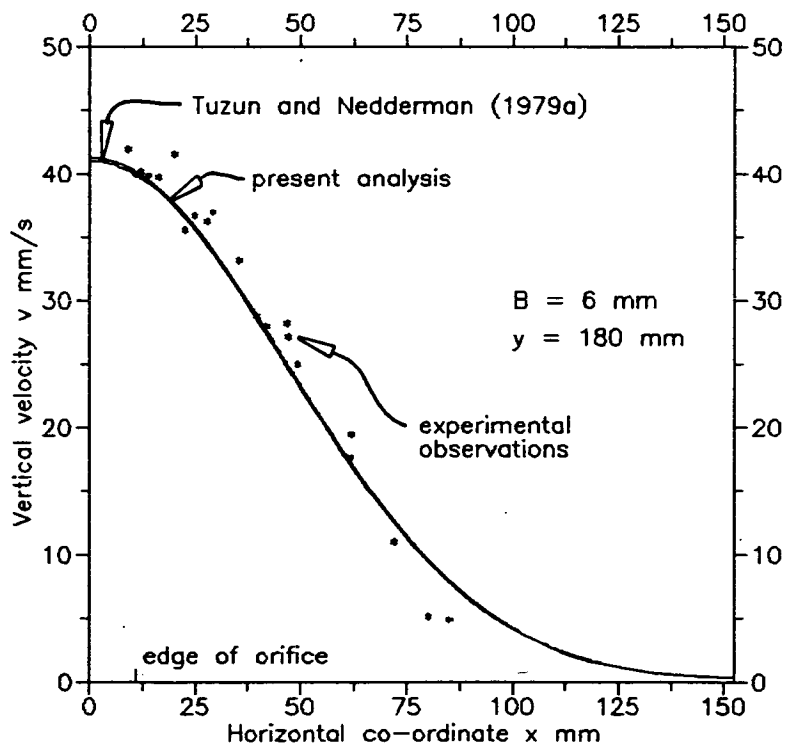

Fig. 3.12 Comparison between analyses

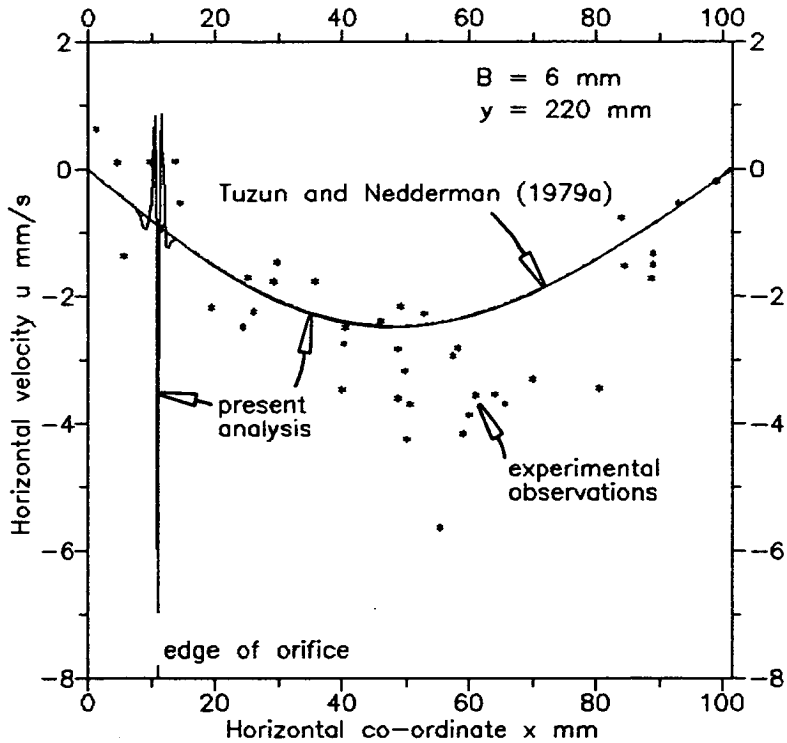

Fig. 3.13 Comparison between analyses

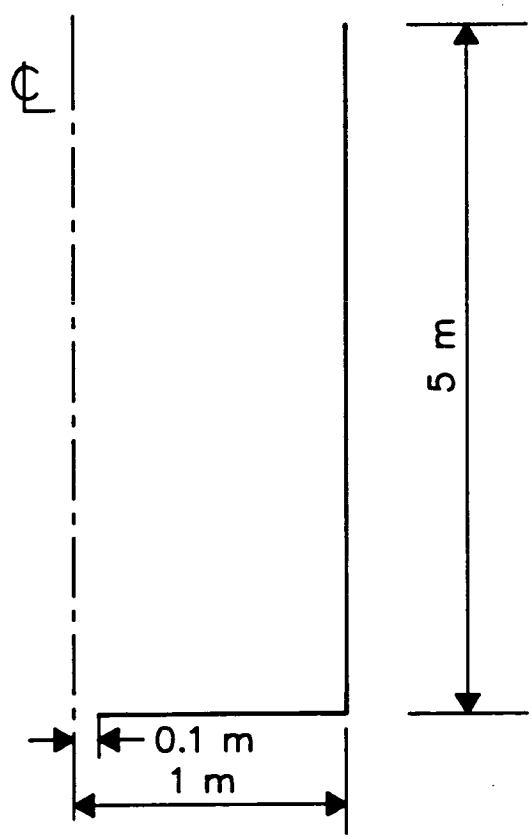

Fig. 3.14 Silo used in the parametric study

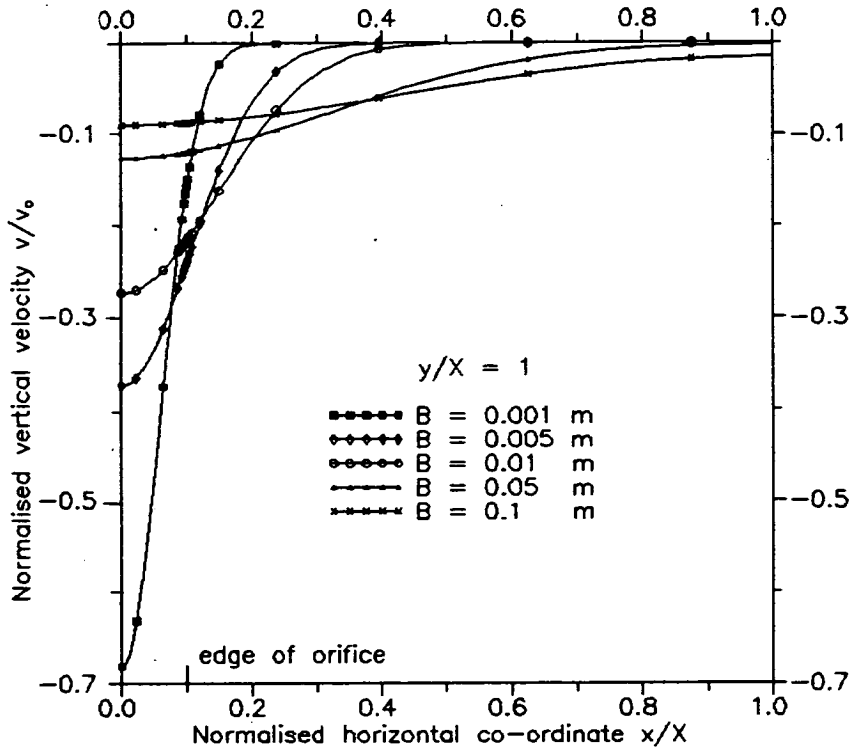

Fig. 3.15 Horizontal profiles of vertical velocity

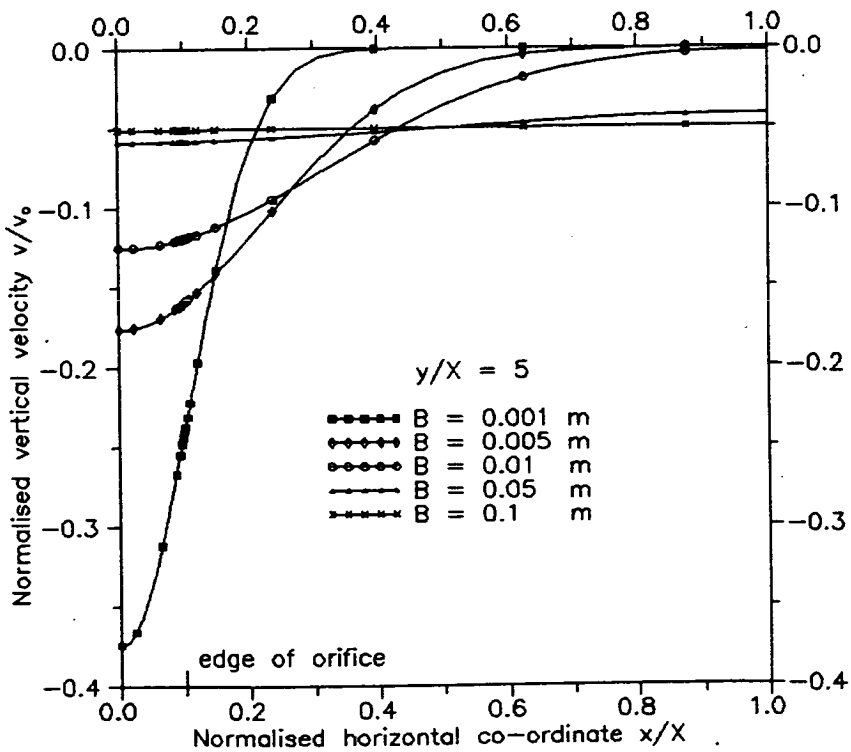

Fig. 3.16 Horizontal profiles of vertical velocity

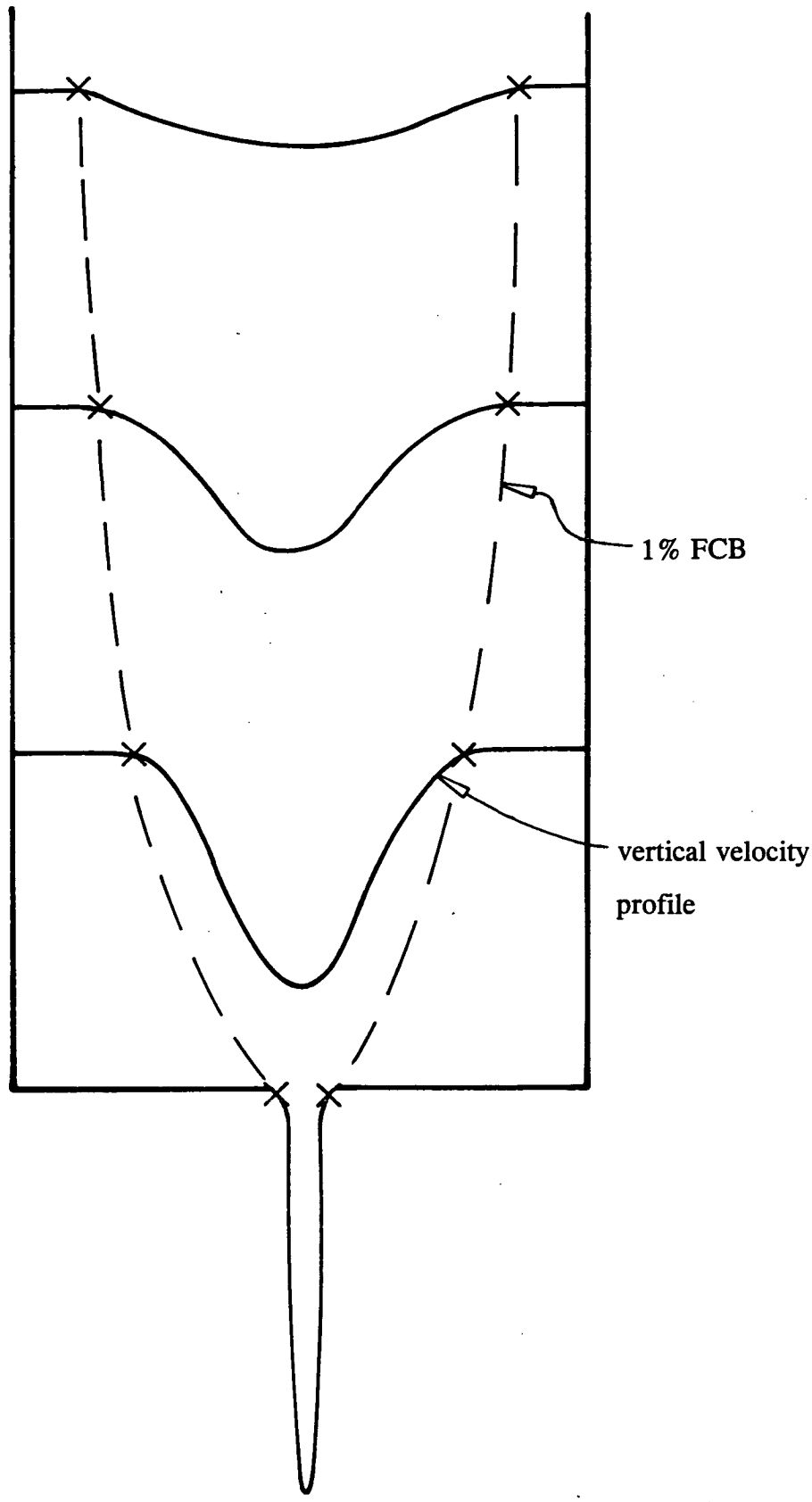

Fig. 3.17 Schematic representation of the flow channel boundary (FCB) definition

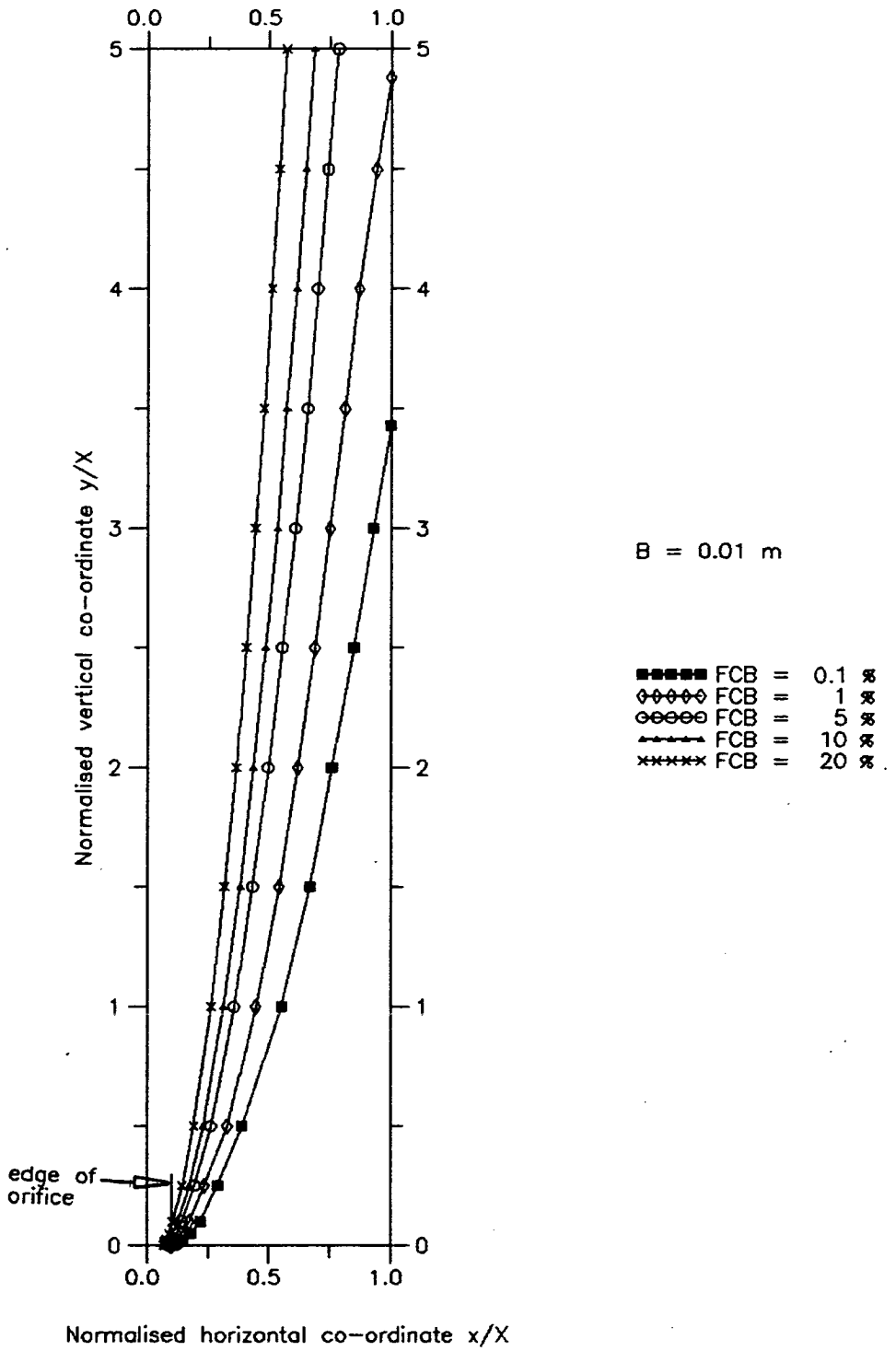

Fig. 3.18 Variation of the flow channel boundary (FCB) with the chosen criterion

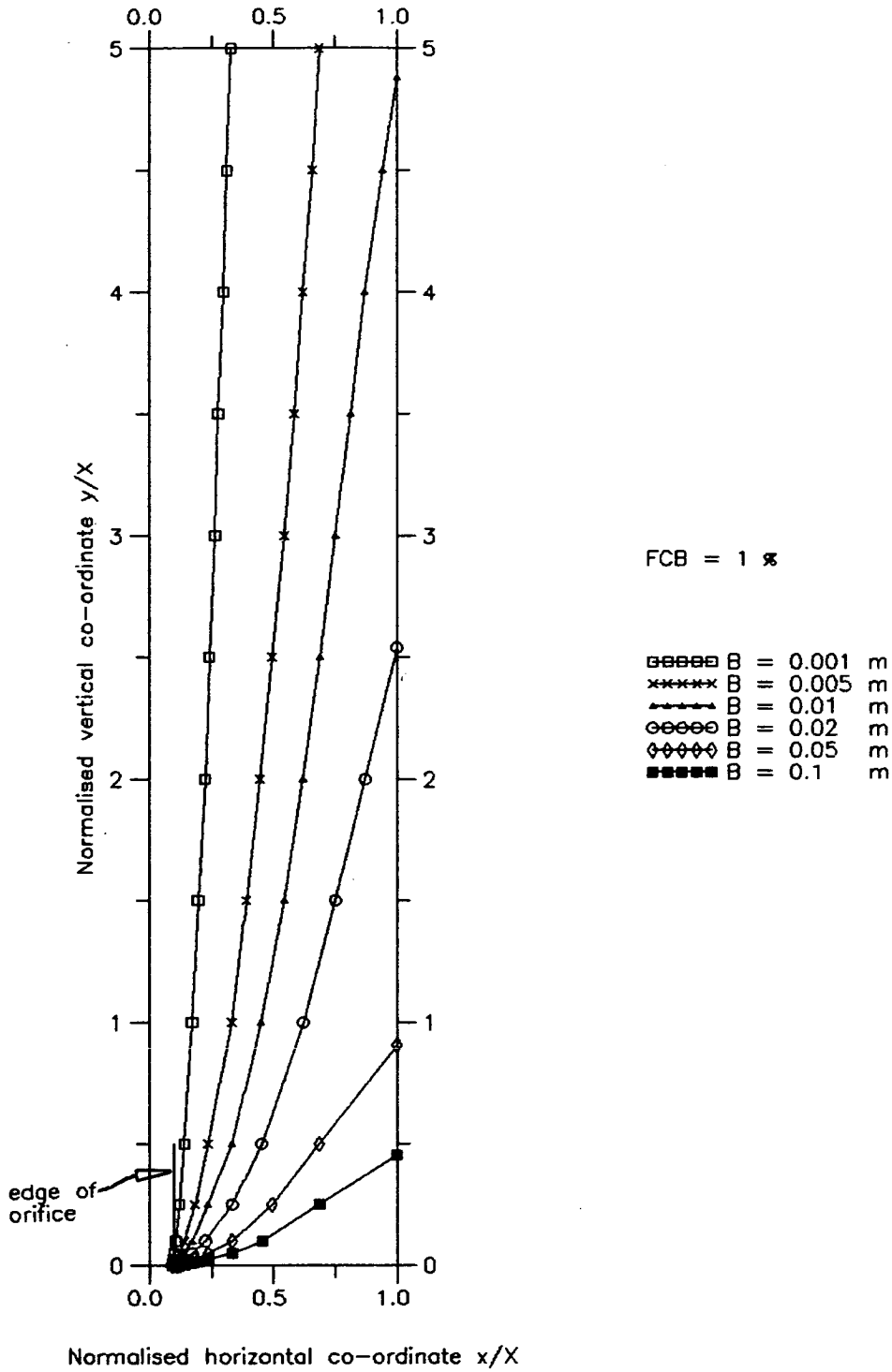

Fig. 3.19 Variation of the flow channel boundary (FCB) with the kinematic parameter

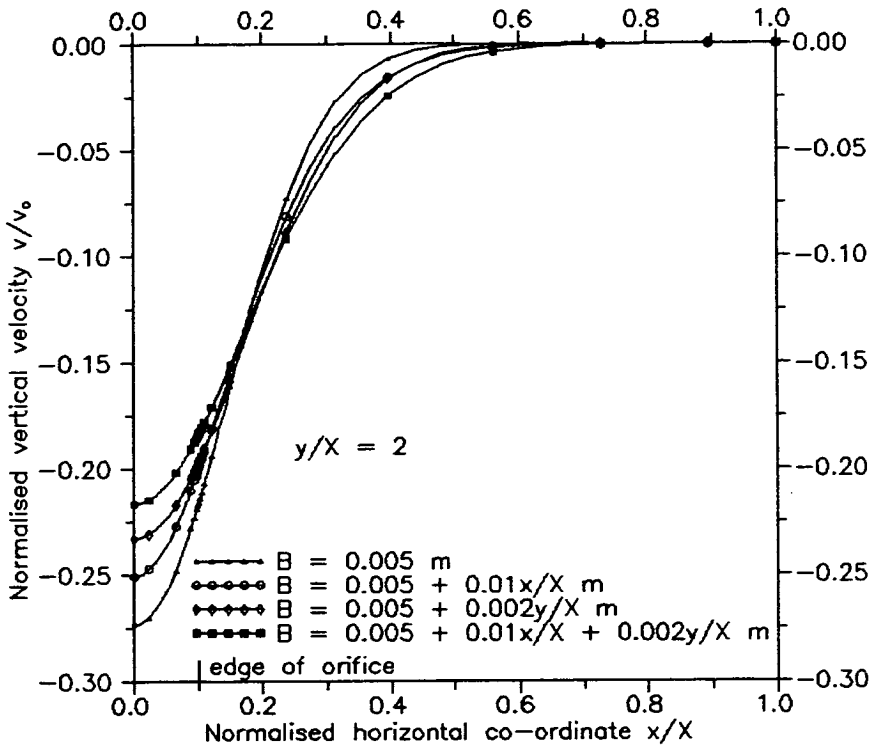

Fig. 3.20 Horizontal profiles of vertical velocity

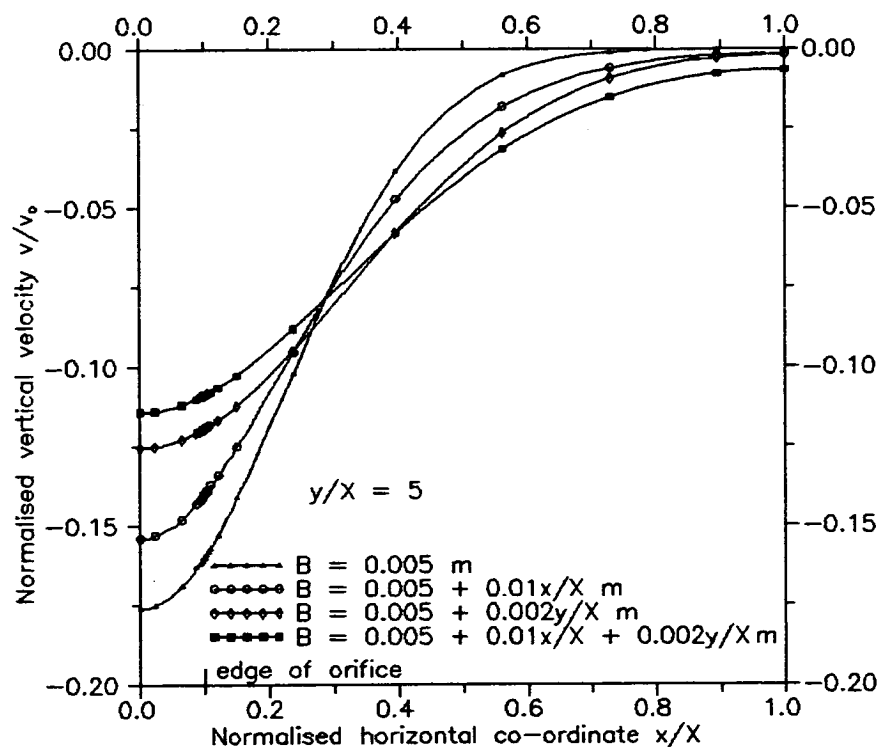

Fig. 3.21 Horizontal profiles of vertical velocity

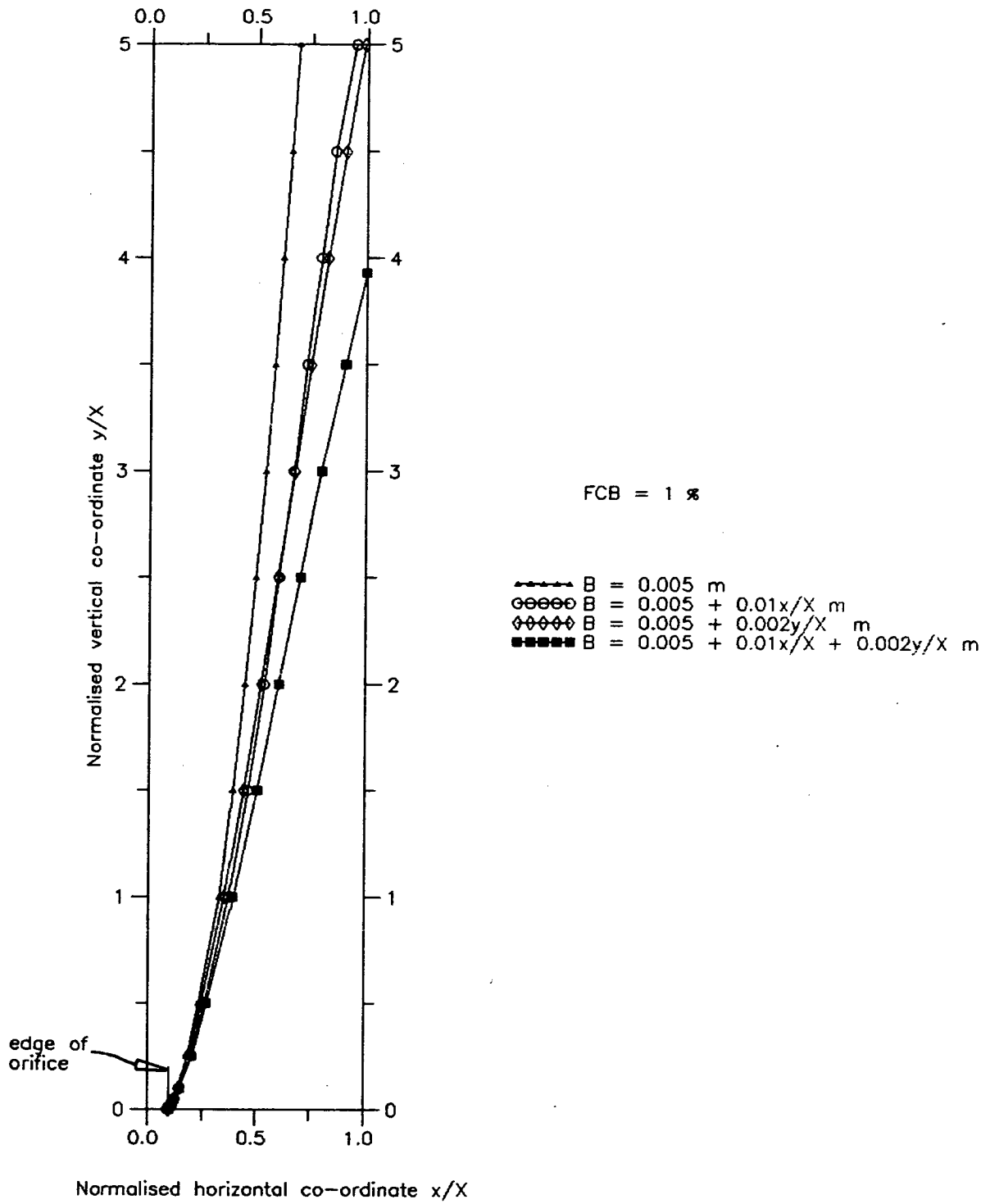

Fig. 3.22 Flow channel boundaries (FCBs) for different kinematic parameters

CHAPTER 4

A FINITE ELEMENT KINEMATIC ANALYSIS OF AXISYMMETRIC GRANULAR SOLIDS FLOW

4.1 Introduction

The starting point for the numerical formulation of the last chapter was Tuzun and Nedderman's (1979a) kinematic equation coupled with the continuity criterion. This coupling produced the governing partial differential equation for kinematic granular solids flow pertaining to planar geometries. In this chapter, an axisymmetric form of the governing partial differential equation is developed and solved using the finite element method. The inherent flexibility of this method again allows the silo geometry to be varied and realistic boundary conditions to be prescribed. Spatial variations in the kinematic parameter can also be accommodated.

4.2 Theoretical formulation

4.2.1 Introduction

This theory applies to a granular solids container with axisymmetric geometry, a central filling chute and discharge outlet and an axisymmetric flow regime. Thus, although the regime is three-dimensional, it is assumed that there are no variations in the circumferential direction.

4.2.2 Development of theory and computational procedure

As was discussed in Chapter 3, the fundamental assumption of Tuzun and Nedderman (1979a) linearly relates the horizontal velocity u to the horizontal gradient of the vertical velocity v:

$$u = -B\frac{\partial v}{\partial x} \tag{4.1}$$

in which B is termed the kinematic constant. Their theory and the corresponding statistical mechanics theory of Litwiniszyn (1963) both strictly only apply to planar silo geometries, in which a single section through a long container with a slot outlet is under investigation. Mullins' (1972) statistical theory, although applicable to axisymmetric geometries, dealt only with the theoretical cases of a finite orifice in the floor of a semi-infinite bed or a point orifice in the bottom of a pipe. In the present work, an assumption corresponding to Eq. 4.1 that is applicable in axisymmetric geometries is put forward. It is postulated that the horizontal velocity should again be made a linear function of the horizontal gradient of the vertical velocity:

$$u = -B(r,z)\frac{\partial v}{\partial r} \tag{4.2}$$

where B(r,z) is termed the kinematic parameter and can vary spatially in any desired manner. The above assumption was reinforced by showing that the velocity fields obtained in the following two cases were identical:

(a) an axisymmetric silo with an annular plan with a large radius compared to its width; and

(b) a planar silo of the same cross-sectional dimensions and with the same value of B.

The condition for continuity of incompressible solid in an axisymmetric geometry is given by

$$\frac{\partial u}{\partial r} + \frac{u}{r} + \frac{\partial v}{\partial z} = 0 \tag{4.3}$$

Substituting Eq. 4.2 into Eq. 4.3 leads to

$$L(v) = \frac{\partial}{\partial r}\left(-B(r,z)\frac{\partial v}{\partial r} \right) - \frac{B(r,z)}{r}\frac{\partial v}{\partial r} + \frac{\partial v}{\partial z} = 0 \tag{4.4}$$

or written more succinctly

$$L(v) = -\frac{1}{r}\frac{\partial}{\partial r}\left(-B(r,z)\, r \frac{\partial v}{\partial r} \right) + \frac{\partial v}{\partial z} = 0 \tag{4.5}$$

The solution of this governing partial differential equation follows the method outlined by Baker and Pepper (1991), *i.e.* the method of weighted residuals. Thus, the Galerkin weak statement is written

$$WS = \iiint_{\Omega} \phi_i(r,z)\, L(v^N)\, d\Omega = 0 \tag{4.6}$$

The elemental volume $d\Omega$ in axisymmetry is given as $rdrd\theta dz$ and the approximate value of the vertical velocity, written as v^N, is

$$v^N = \sum_{i=1}^{N} a_i\, \phi_i(r,z) \tag{4.7}$$

Hence

$$WS = \iiint_{\Omega} \phi_i \left(- \frac{\partial}{\partial r} \left(B(r,z)\, r\, \frac{\partial v^N}{\partial r} \right) + r\, \frac{\partial v^N}{\partial z} \right) drd\theta dz = 0 \tag{4.8}$$

Applying Green's First Identity to the first term of the integrand:

$$WS = S_e \left| \iiint_{\Omega} \frac{\partial \phi_i}{\partial r}\, B(r,z)\, r\, \frac{\partial v^N}{\partial r}\, drd\theta dz - \iint_{\Gamma} \phi_i\, B(r,z)\, r\, \frac{\partial v^N}{\partial r}\, n_r\, d\Gamma + \iiint_{\Omega} \phi_i\, r\, \frac{\partial v^N}{\partial z}\, drd\theta dz \right| = 0 \tag{4.9}$$

When introducing a discretization the superscript ^{h} is used, so that WS becomes WS^h and v^N becomes v^h with

$$v^h(r,z) = \cup_e\, v_e(r,z) \tag{4.10}$$

and within the individual element

$$v_e(r,z) = \{N_k\}^T \{v\}_e \tag{4.11}$$

Adopting the Galerkin weighting function:

$$\phi_i(r,z) = \{N_k\} \tag{4.12}$$

and integrating around the circumference, the weak statement (Eq. 4.9) becomes

$$WS^h = S_e \Bigg(2\pi \iint_{\Omega_e} \frac{\partial\{N_k\}}{\partial r} B(r,z)\, r \frac{\partial\{N_k\}^T}{\partial r} \, dr dz \, \{v\}_e - \int_{\Gamma_e} \{N_k\} B(r,z)\, r \frac{\partial\{N_k\}^T}{\partial r} \underline{n}_r \, d\Gamma \, \{v\}_e + 2\pi \iint_{\Omega_e} \{N_k\}\, r \frac{\partial\{N_k\}^T}{\partial z} \, dr dz \, \{v\}_e \Bigg) \equiv 0 \tag{4.13}$$

if the following abbreviations are used

$$[K]_e = 2\pi \iint_{\Omega_e} \frac{\partial\{N_k\}}{\partial r} B(r,z)\, r \frac{\partial\{N_k\}^T}{\partial r} \, dr dz$$

$$[H]_e = 2\pi \iint_{\Omega_e} \{N_k\}\, r \frac{\partial\{N_k\}^T}{\partial z} \, dr dz$$

and

$$[P]_e = \int_{\Gamma_e} \{N_k\} B(r,z)\, r \frac{\partial\{N_k\}^T}{\partial r} \underline{n}_r \, d\Gamma \, \{v\}_e$$

the global matrix statement may then be expressed as

$$S_e([K + H - P]_e\{v\}_e) = \{0\} \tag{4.14}$$

The method of solution, *i.e.* assembly, right-hand-side vector formation and equation solution follows the procedure outlined in Chapter 3. Examples of the matrices $[K]_e$, $[H]_e$ and $[P]_e$ are given in Appendix 4.1.

4.2.3 Boundary conditions

The boundary conditions for the axisymmetric case are directly analogous to those of the planar case (Eqs 3.17 and 3.18a-3.18d). However, when an analogous cubic exit vertical velocity profile is adopted:

$$v_{exit} = 2v_o\left(\frac{r}{r_o}\right)^3 - 3v_o\left(\frac{r}{r_o}\right)^2 + v_o \qquad r \le r \le r_o \tag{4.15}$$

a slightly different relationship between the centreline exit velocity v_o and the total volumetric flow rate Q is found:

$$v_o = \frac{10Q}{3\pi r_o^2} \tag{4.16}$$

In this equation, r_o is the radius of the orifice and v_o the vertical velocity at $r = z = 0$ (see Fig. 4.1).

4.3 Parametric study

4.3.1 Introduction

A parametric study was next undertaken to investigate the range of flow channel predictions which this analysis can give as various parameters are changed. The geometry of the silo that was used in the parametric study is as shown in Fig. 4.1.

The dimensions are those of the laboratory model used in the experiments described in Chapter 6. The parametric study was undertaken in three parts to explore:

(a) the effect of the parameter B on the flow pattern with a homogeneous material (constant B throughout the silo).

(b) the interpretation of the flow pattern predictions in terms of a flow channel and stationary solid.

(c) the effect of material inhomogeneity on the flow pattern.

4.3.2 Vertical velocity distributions for different values of B

In this section, the kinematic constant took values of 1 mm, 5 mm and 20 mm. The vertical velocity profiles at z/R = 0.23 and z/R = 2.77 for different values of B are shown in Figs 4.2 and 4.3.

All the velocities have been normalised by dividing them by the modulus of the value of the vertical velocity at r = z = 0 (outlet centreline). This produces a maximum value in the entire domain of -1.

From Figs 4.2 and 4.3, it can be seen that the horizontal profiles of vertical velocity, at a particular height, are flatter when the value of B is higher. These flatter profiles have lower centreline velocities but higher velocities towards the wall. For a higher value of B, therefore, the channel of flowing solid is wider and has lower mean velocities associated with it. In a flat-bottomed silo then, a high value of B represents semi-mass flow whereas a low value represents pipe flow.

It can also be seen that, for a particular value of B, the profiles flatten out with height. As the height above the orifice is increased then, the channel of flowing solid widens.

4.3.3 Flow channel boundary (FCB) predictions

As in Chapter 3, the flow channel boundary is chosen as the position where the vertical velocity at a given height falls below a given proportion of the centreline velocity at that height.

4.3.3.1 Definition of the flow channel boundary

Taking the case with B = 2 mm, Fig. 4.4 shows contours of points at which the vertical velocity has fallen to a given proportion of the centreline velocity at the same height. These contours are deemed to provide a useful criterion from which the FCB may be drawn.

A wide range of conceivable FCB definitions is shown to indicate the insensitivity of the criterion to the adopted proportion: that is, to demonstrate that this continuum model does result in a FCB which is reasonably well defined. As in Chapter 3, the FCB was chosen somewhat arbitrarily to be defined by the criterion of the locus of points at which the vertical velocity is equal to 1% of the centreline vertical velocity at the same height. However, as can be seen from Fig. 4.4, the choice of this criterion does not make a great difference to the predicted channel geometry.

It can also be seen that the FCB found using a criterion of this kind is not a conical surface (which would be given by a linear relationship between r and z) but that it is curved. It may be fortuitous and only valid for special geometries, but a parabola again fits the data remarkably well. This suggests that the flowing solid may take up the shape of a paraboloid of revolution.

4.3.3.2 Variation of the flow channel boundary with B

The above criterion for the FCB was applied to calculations using the same geometry but several different values of the kinematic parameter B. As the value of the kinematic parameter B is increased, the flow channel becomes wider and more sharply curved near the outlet. The increased volume of flowing solid at a given height naturally has lower relative velocities associated with it. In Fig. 4.5, a whole range of different flow patterns are exhibited, from a fast-moving narrow central pipe (B = 0.5 mm) to a wide-spreading, and perhaps unrealistic, enlarged flow regime (B = 50 mm). These correspond well to the familiar definitions of pipe flow and semi-mass flow respectively. The point at which the FCB intersects the silo wall (the effective transition) is evidently strongly dependent on the kinematic parameter B, though it is only weakly dependent on the criterion used to define the FCB.

4.3.4 Variation of the kinematic parameter with height

Tuzun and Nedderman (1979) reported that the kinematic constant increased slightly with height in their experiments. In the present formulation, the kinematic parameter B(r,z) can be appointed to be any chosen function of r and z.

To investigate the effect of allowing B to vary in (r,z) space, the following four variations were examined:

(a) $B = 1$ mm
(b) $B = 1 + 3r/R$ mm
(c) $B = 1 + 0.65z/R$ mm
(d) $B = 1 + 3r/R + 0.65z/R$ mm

The variations were chosen to give the same range of B from the centreline to the wall in Case (b) and from the base to the surface in Case (c), with Case (d) being these two variations superimposed. All four patterns had the same value of B at the centre of the outlet.

Velocity profiles at $z/R = 0.92$ and $z/R = 4.62$ are presented in Figs 4.6 and 4.7 respectively and the 1% FCBs for the four cases are plotted in Fig. 4.8.

From Figs 4.6, 4.7 and 4.8, it can be seen that as B increases with r and/or z, the flow channel widens out producing flatter vertical velocity profiles that have lower centreline velocities but have higher velocities as the side wall is approached. It can also be seen that Cases (b) and (c) produce very similar widening effects on the FCB. If B is specified to vary with respect to both r and z, as in Case (d), the effects are compounded and the FCB becomes even wider.

4.4 Conclusions

A theory that describes the concentric discharge of cohesionless granular media from axisymmetric silos has been presented. The theory is founded on a simple proposed relationship between the horizontal velocity and the horizontal gradient of the vertical velocity. Combining this relationship with the continuity criterion, a

governing partial differential equation is developed. This equation is solved using Galerkin's technique of weighted residuals and a finite element formulation. Generalised geometries and a spatially-varying kinematic parameter are made possible with this approach. Flow channel boundary criteria have been proposed and the resulting flow channel geometries have been illustrated.

Appendix 4.1 Element matrices

$$[K]_e = \int_{\Omega_e} \int \begin{pmatrix} \frac{\partial N_1}{\partial r} B(r,z)\, r \frac{\partial N_1}{\partial r} & \frac{\partial N_1}{\partial r} B(r,z)\, r \frac{\partial N_2}{\partial r} & \cdots & \frac{\partial N_1}{\partial r} B(r,z)\, r \frac{\partial N_k}{\partial r} \\ \frac{\partial N_2}{\partial r} B(r,z)\, r \frac{\partial N_1}{\partial r} & \frac{\partial N_2}{\partial r} B(r,z)\, r \frac{\partial N_2}{\partial r} & \cdots & \frac{\partial N_2}{\partial r} B(r,z)\, r \frac{\partial N_k}{\partial r} \\ \vdots & \vdots & \cdots & \vdots \\ \frac{\partial N_k}{\partial r} B(r,z)\, r \frac{\partial N_1}{\partial r} & \frac{\partial N_k}{\partial r} B(r,z)\, r \frac{\partial N_2}{\partial r} & \cdots & \frac{\partial N_k}{\partial r} B(r,z)\, r \frac{\partial N_k}{\partial r} \end{pmatrix} d\Omega$$

$$[H]_e = \int_{\Omega_e} \int \begin{pmatrix} N_1\, r \frac{\partial N_1}{\partial z} & N_1\, r \frac{\partial N_2}{\partial z} & \cdots & N_1\, r \frac{\partial N_k}{\partial z} \\ N_2\, r \frac{\partial N_1}{\partial z} & N_2\, r \frac{\partial N_2}{\partial z} & \cdots & N_2\, r \frac{\partial N_k}{\partial z} \\ \vdots & \vdots & \cdots & \vdots \\ N_k\, r \frac{\partial N_1}{\partial z} & N_k\, r \frac{\partial N_2}{\partial z} & \cdots & N_k\, r \frac{\partial N_k}{\partial z} \end{pmatrix} d\Omega$$

$$[P]_e = \int_{\Gamma_e} n_r \begin{pmatrix} N_1 B(r,z)\, r \dfrac{\partial N_1}{\partial r} & N_1 B(r,z)\, r \dfrac{\partial N_2}{\partial r} & \cdots & N_1 B(r,z)\, r \dfrac{\partial N_k}{\partial r} \\ N_2 B(r,z)\, r \dfrac{\partial N_1}{\partial r} & N_2 B(r,z)\, r \dfrac{\partial N_2}{\partial r} & \cdots & N_2 B(r,z)\, r \dfrac{\partial N_k}{\partial r} \\ \vdots & \vdots & \ddots & \vdots \\ N_k B(r,z)\, r \dfrac{\partial N_1}{\partial r} & N_k B(r,z)\, r \dfrac{\partial N_2}{\partial r} & \cdots & N_k B(r,z)\, r \dfrac{\partial N_k}{\partial r} \end{pmatrix} d\Gamma$$

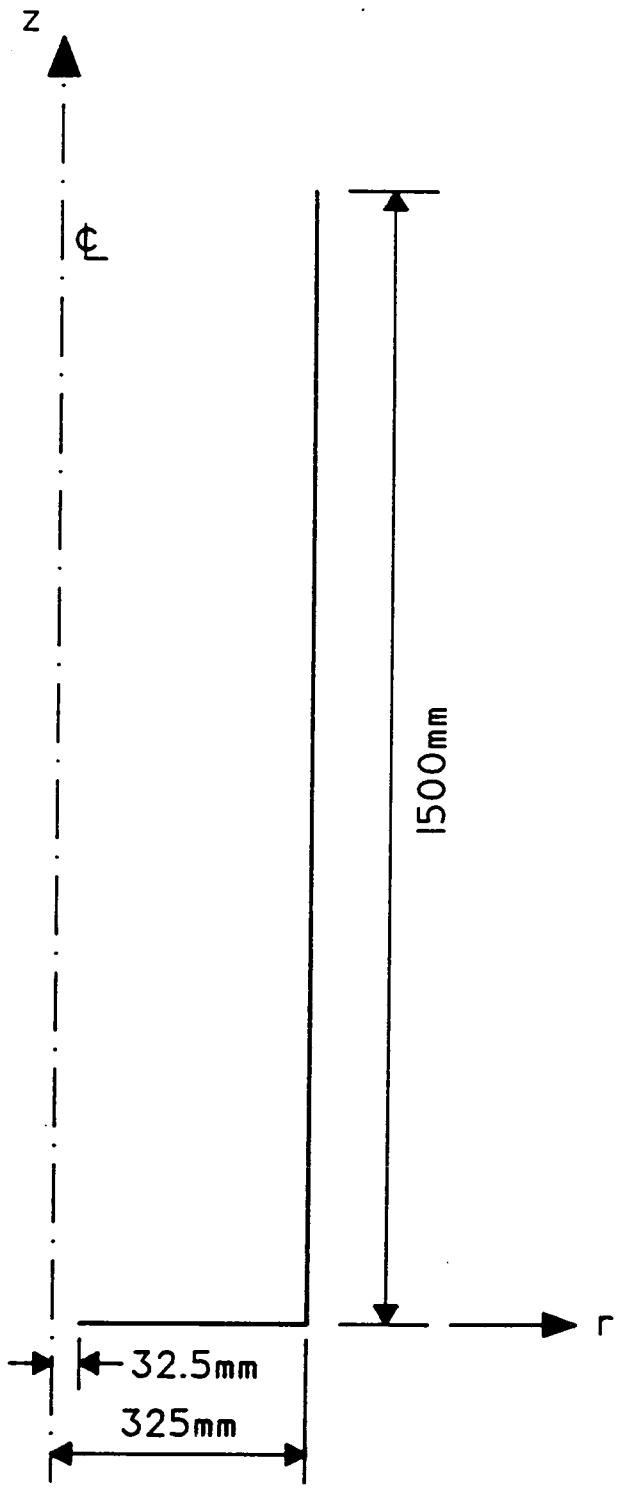

Fig. 4.1 Silo used in the parametric study

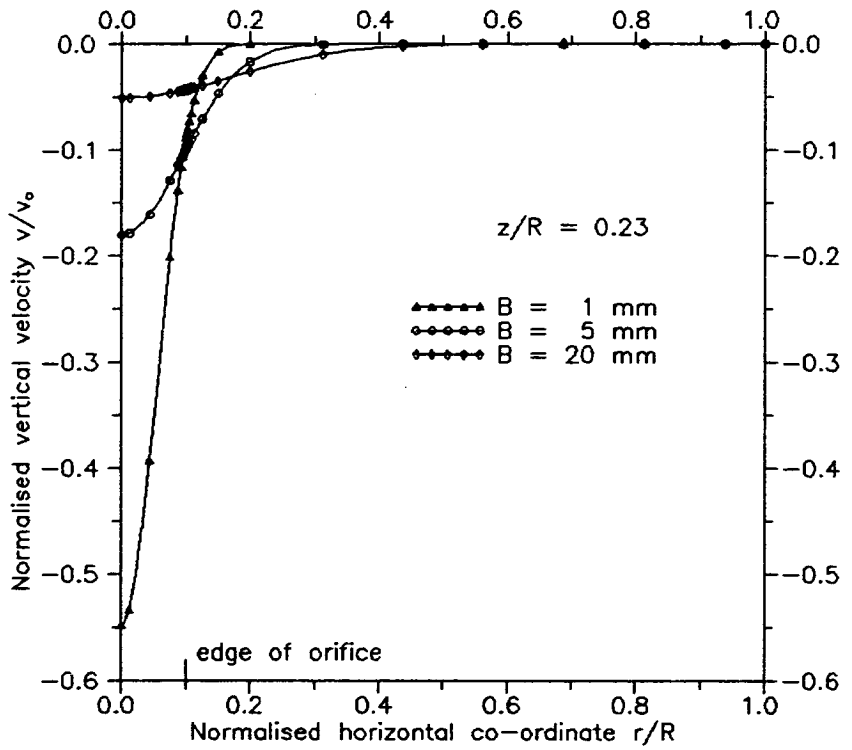

Fig. 4.2 Horizontal profiles of vertical velocity

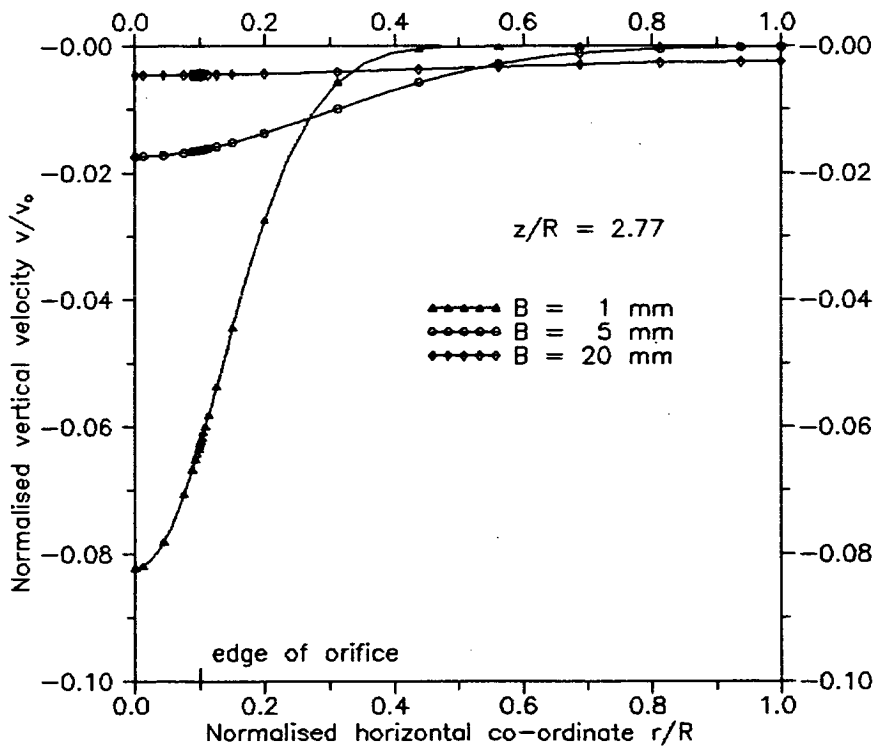

Fig. 4.3 Horizontal profiles of vertical velocity

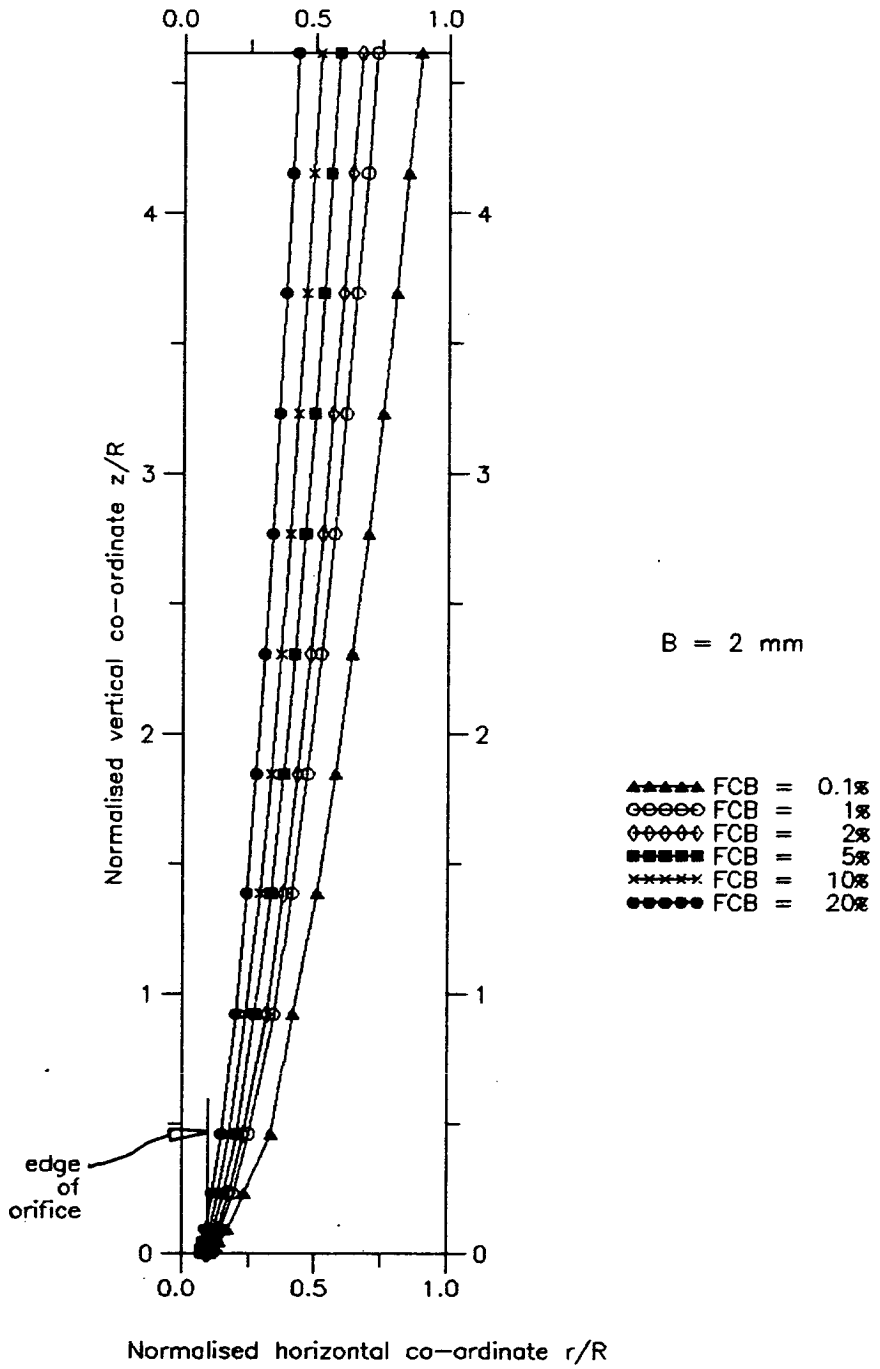

Fig. 4.4 Variation of the flow channel boundary (FCB) with the chosen criterion

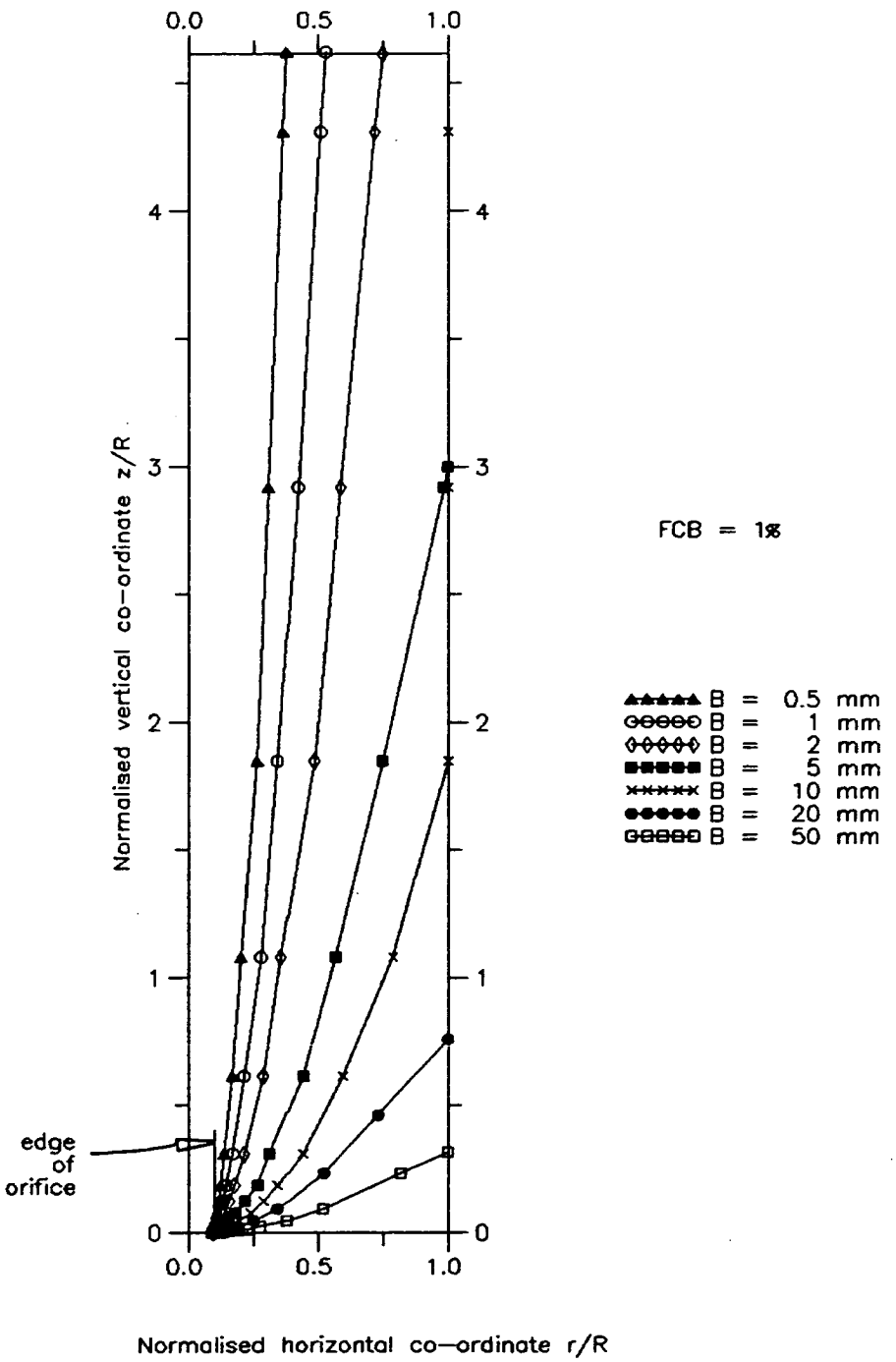

Fig. 4.5 Variation of the flow channel boundary (FCB) with the kinematic parameter

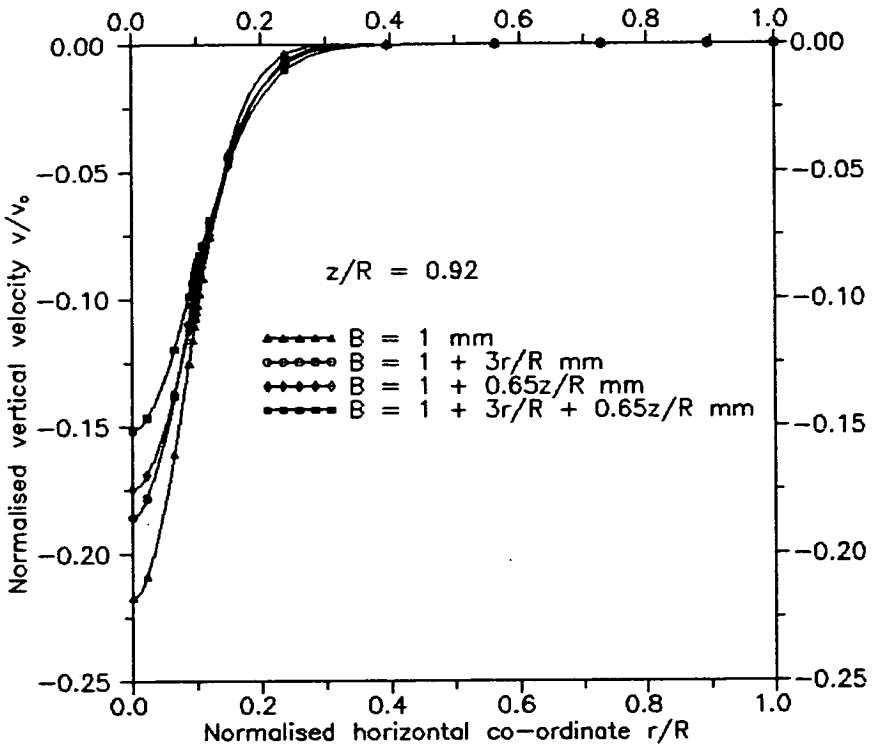

Fig. 4.6 Horizontal profiles of vertical velocity

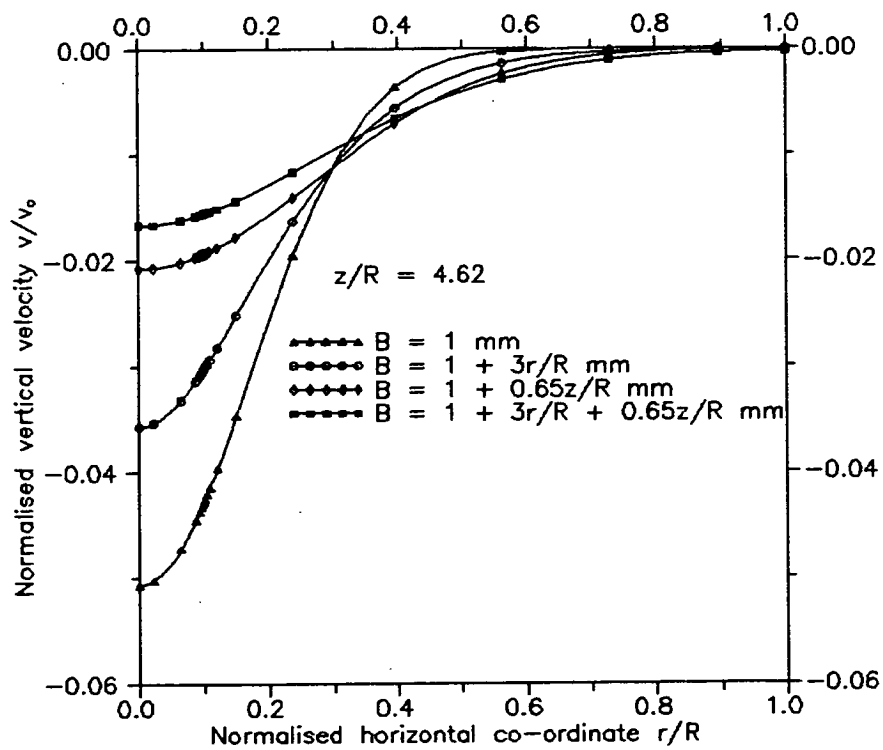

Fig. 4.7 Horizontal profiles of vertical velocity

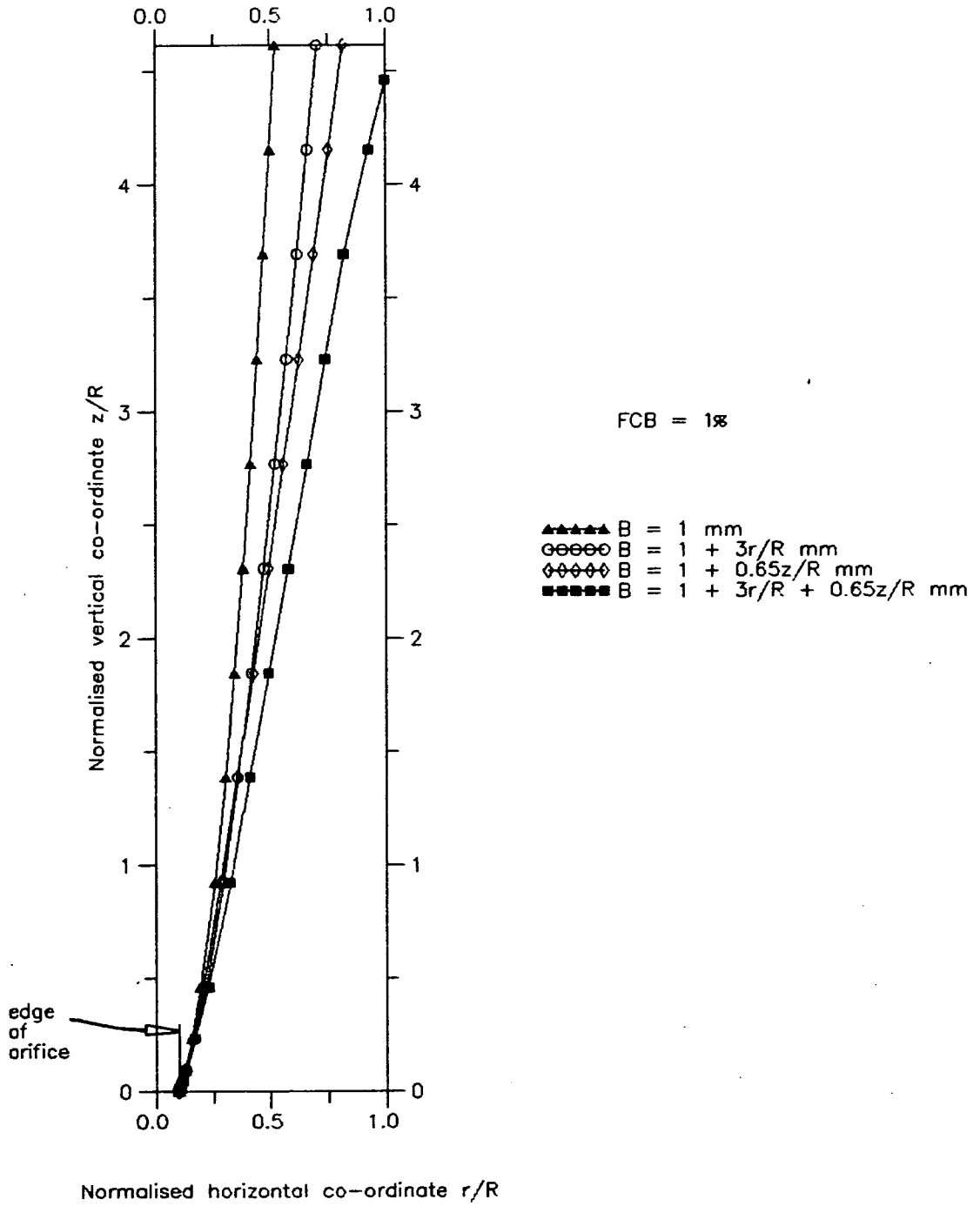

Fig. 4.8 Flow channel boundaries (FCBs) for different kinematic parameters

CHAPTER 5

PARAMETRIC STUDY

5.1 Introduction

In this chapter, a parametric study is undertaken to illustrate the range of application of the numerical finite element formulations developed in the previous two chapters. The study was undertaken in seven parts to explore the predictions of this theory for:

(1) the trajectories of individual particles.
(2) the effects on the flow channel boundary (FCB) of varying the silo dimensions.
(3) the variation of the kinematic parameter B to model density gradients.
(4) the displacement of the top surface during incipient discharge.
(5) the flow patterns produced by eccentric discharge.
(6) the flow patterns produced in a double-outlet silo.
(7) the analysis of flow through hoppers.

In all parts, cubic exit velocity profiles were used and the method of solution follows that outlined in Chapter 3. For all calculations on symmetrical silos, only the right-hand half the silo was analysed (exploiting symmetry) and the origin of axes was positioned at the bottom left-hand corner of the domain.

Unless otherwise stated, the theoretical FCBs are defined as the locus of points where the vertical velocity falls to 1% of that at the centreline at the same height. The centreline is defined as a line extending vertically upwards from the centre of the outlet. It will later be seen that this simple definition results in a FCB that is indistinguishable from a streamline.

5.2 Trajectories of individual particles

5.2.1 Introduction

In the first part of this parametric study, the trajectories of individual particles are traced as they descend and converge towards the orifice. Accurate predictions of particle trajectories are serviceable in residence time analyses where they can be used to determine steady-state velocity fields. The trajectory of a particle can be found from the present analysis because the steady-state horizontal and vertical velocity fields are known. The procedure is as follows. First, the vertical and horizontal velocities are calculated at a given starting co-ordinate. Next, an arbitrary time increment is taken and, assuming constant velocities, new co-ordinates are calculated for the position of the particle at the end of the time increment. The horizontal and vertical velocities are then determined at this new position. This process is continued until the particle reaches the orifice.

To ensure suitable accuracy, a large number of steps was used. It was found that 60 steps were generally adequate. Therefore, if the number of steps taken to reach the orifice was less than 60, the time increment was decreased and the tracking began anew. Conversely, if the time increment became too low, the number of steps taken to reach the orifice would become unacceptably high. An upper limit on the number of steps was therefore set. This was chosen as 100 steps. If the particle still had not reached the orifice after 100 steps, the time increment was increased and the tracking began again from the starting co-ordinates. Thus, time increments that resulted in the number of steps lying between 60 and 100 were used in all calculations. This time increment, multiplied by the number of steps taken to reach the orifice, gave the residence time of the particle.

In this section, it was necessary to use an unrealistically high value of the kinematic parameter B (*i.e.* a value that was much greater than those that have been previously reported from the limited experiments from which B has been backfigured). Such high values of B are here employed in the analysis of squat silos, where, in order to present a comprehensive theoretical demonstration, it is desirable to explore cases where the FCB strikes the wall. Constant values of the kinematic parameter of B = 0.1 m, 0.2 m, 0.5 m and 1.0 m were used.

Particles were tracked in both planar and axisymmetric geometries. The silos used in this study all had a height of 10 m. In the planar section silo, the half-width was 10 m and in the axisymmetric silo the radius was 10 m. The silos are shown in Fig. 5.1. These dimensions were felt to be reasonably representative of large full scale silos. The low aspect ratio of 0.5 also ensured that any curvature in the particle trajectories would be clearly displayed.

For each value of B, the paths of five particles were tracked on their journeys through the silo. Starting positions on the top surface (y/X or z/R = 1, where in planar geometries X is the silo half-width and in axisymmetric geometries R is the silo radius) were chosen and the positions were equally spaced with respect to the horizontal co-ordinate (x/X or r/R = 0.1, 0.3, 0.5, 0.7 and 0.9). Information could be gained about the flow regime as each of these trajectories represents a streamline. Streamlines are a common concept used in fluid dynamics to describe the flow pattern. A streamline is defined as a line which is always tangential to the local velocity vector *i.e.* a line across which no flow takes place. For each particle, a residence time was also calculated as described above.

To complete this section, the particle trajectories and residence times calculated using the current finite element analysis are compared with those calculated using the analytical expressions of Mullins (1974).

5.2.2 Planar geometry

The trajectories and residence times for each group of five particles for each different value of B are shown in Figs 5.2-5.5. The theoretical 1% FCB is also shown for reference in each of these figures. In all four figures, the general pattern is that the particles follow a roughly parabolic path towards the orifice and the residence time increases with horizontal co-ordinate. In Fig. 5.2, the value of B is relatively low at 0.1 m and this produces a pipe flow pattern as can be seen from the narrow 1% FCB that does not intersect the wall. There are large surrounding regions of 'stationary' solid where the velocities approach zero. It was not possible to track particles through such slow-moving solid (even if a vast number of steps was used) as numerical errors disrupted the analysis. Any particle whose calculated residence time exceeded 1000 times that of the centreline top surface particle was therefore deemed to be 'stationary'. The trajectories of these particles were

ignored. In Fig. 5.2, those particles that had starting co-ordinates numbered 4 and 5 and in Fig. 5.3 the particle that had starting co-ordinate number 5 were rendered stationary by this definition.

It may be observed from Figs 5.2 and 5.3 that the curve that represents the 1% FCB lies between two adjacent particle trajectories. In Figs 5.4 and 5.5 the flow channel is so enlarged that the FCB lies to the right of all the particle trajectories. The relative position of the 1% FCB between the two adjacent particle trajectories, in Figs 5.2 and 5.3, does not change with height. Since the trajectories are streamlines, it is evident that the curve representing the 1% FCB is an approximate streamline. This was confirmed by tracing the trajectory of a particle that started from the position where the 1% FCB, in Figs 5.2 and 5.3, intersected the free surface. It was found that this trajectory was almost identical to the 1% FCB.

The fact that the present finite element method predicts a 1% FCB that is a streamline correlates well with the definition of a flow boundary as being the interface between flowing and stationary solid. It may be recalled that in Chapter 3 the FCB was arbitrarily defined as the locus of points where the vertical velocity falls to 1% of the vertical velocity at the centreline at that level. The founding equations of the kinematic theory are parabolic in nature and consequently cannot predict a sharp velocity discontinuity. If the locus of a discontinuity could be found, where the particle velocity falls to identically zero, this locus would also be a streamline, since no flow could take place across it. This discontinuity would also mark the strictly-defined FCB. Even though the prediction of velocity discontinuities is not possible with the present kinematic theory and even though the FCB definition is made somewhat arbitrarily, the resulting boundary is indeed found to be a streamline. This supports the simple definition used in this thesis for the position of the FCB. The advantage of this 1% FCB is that it is a simple criterion which can be quickly applied without the need to calculate streamlines. It is therefore a useful empirical shortcut.

The different values of the kinematic parameter B used in this study represent different stored granular solids. By superimposing the Figs 5.2-5.5 upon one another, the trajectories of particles could be compared. An example of this is given in Fig. 5.6, which shows a blown-up section of the particle path with starting co-ordinate ($x/X = 0.3$, $y/X = 1$) for each of the four different values of B. It can be seen that the particles follow a slightly wider trajectory when the value of B is

higher *i.e.* the trajectories that correspond to the higher values of B lie below those that correspond to lower values of B. This widening is more obvious for particle paths that start at larger values of horizontal co-ordinate *i.e.* particle paths that are wider anyway. The starting co-ordinate of (x/X = 0.3, y/X = 1) was chosen as this had the largest horizontal starting co-ordinate from which all particles discharged, none being deemed stationary. It will be recalled that with a higher value of B the flow channel is wider. Thus the widening of particle paths at higher values of B, especially for those close to the FCB, is to be expected.

The kinematic parameter B has a prominent effect on the residence time. In Fig. 5.7, the residence times are shown for particles starting from different horizontal positions at three different heights. The value of B is 0.5 m. It can be seen that the residence time of a particle starting on the centreline increases with height. Near to the wall, the opposite is true: a particle positioned close to the free surface discharges before a particle that was positioned lower down.

In Fig. 5.8, the residence times of a group of five particles distributed across the free surface with a given value of B is shown. It may be recalled that for low values of B, the flow pattern exhibited is pipe flow with high vertical velocities in the region of the centreline. As the value of B is increased, the flow pattern tends towards semi-mass flow and the vertical velocity profiles become more uniform. It is noticed from Fig. 5.8 that the profiles of residence time against initial horizontal co-ordinate are steeper for the case where the value of B is lower and flatter for the case where the value of B is higher. For the particle closest to the centreline, the residence time is smallest for the case with the lowest value of B and this time increases as the value of B increases. Further away from the centreline, say at x/X = 0.5, the opposite holds true. Thus, the residence time plots of Fig. 5.8 represent the different possible flow patterns in a discharging silo.

5.2.3 Axisymmetric geometry

As mentioned in the introduction to this section, the axisymmetric silo used in this analysis had the same radius R as the half-width of the planar silo X, and the two silos had the same height. Values of B of 0.1 m, 0.2 m, 0.5 m and 1 m were again used. It was found that the 1% FCBs calculated in axisymmetric geometries were

very nearly identical to those calculated for planar geometries, despite the differences in the governing differential equations (Eqs 3.3 and 4.5).

In Fig. 5.9, the trajectories of particles in planar and axisymmetric geometries are compared. Near to the silo axis, the paths of particles in axisymmetric geometries are closer to the centreline (*i.e.* less curved) than those in planar geometries. Near to the wall, the reverse is true *i.e.* the paths of particles in axisymmetric geometries lie further from the centreline and have a higher curvature than those in planar geometries. For a particle that starts in the middle of the top surface, the paths in both geometries are very similar.

The plot of residence time against initial horizontal co-ordinate for axisymmetric geometries is directly analogous to the equivalent plot for planar geometries (Fig. 5.8). For this reason, a plot is omitted here.

In axisymmetric geometries, the slight widening of the particle paths at higher values of B is similar to those found in planar geometries and so is not discussed further.

5.2.4 Comparison with analytical results

Mullins (1974) presented analytical expressions for a particle's residence time and the path it follows as it travels down through a semi-infinite bed towards a point orifice. He included expressions for both planar and axisymmetric geometries. The expressions that he derived for the planar case can be shown to reduce to the similarity solution of Tuzun and Nedderman (1979a) (see Appendix 5.1). This demonstrates that the analytical solution to the governing partial differential equation for kinematic granular solids flow in planar geometries (Eq. 2.5) can be written in terms of horizontal and vertical velocity fields (as was done by Tuzun and Nedderman, 1979a) or in terms of particle paths and residence times (as was done by Mullins, 1974). The two analytical solutions are effectively identical. It is the purpose of this section to compare these analytically-predicted residence times and particle paths with those obtained from the current finite element analysis which makes fewer assumptions, and has finite boundaries.

The comparisons were made for many different geometries and values of B, but the overall pattern was found to be very similar. For this reason, only one geometry and one value of B will be discussed here. In Fig. 5.10, the paths of five particles travelling through a silo with planar geometry are again shown for a solid with a constant kinematic parameter of B = 1 m. Superimposed on top of these paths are the analytically-calculated paths obtained using Mullins' (1974) equations. In Fig. 5.11, the residence times predicted using the current finite element formulation and from Mullins' analytical equation are plotted against the horizontal co-ordinate of the starting position.

It can be seen that for particles close to the centreline the numerical and analytical treatments both produce almost identical particle trajectories and residence times. As the distance from the centreline is increased, however, the two techniques begin to differ in their predictions. This is because Mullins ignores the effect of the wall.

For particles starting closer to the wall, Mullins predicts paths that lie closer to the centreline than those predicted by the present finite element method. The residence times for these particles as calculated from the expression of Mullins are also slightly less than those calculated from the present finite element method. This is to be expected since the paths of particles starting close to the wall, as predicted by Mullins, are shorter. It may also be noticed that the point orifice assumption made by Mullins leads all his particle paths to meet at the origin. His paths are slightly more curved as they approach the point orifice. Tuzun and Nedderman (1979a) only claim their similarity solution to be valid in the convergent flow zone where the influence of the walls is assumed to be slight. They propose a product solution for the rest of the flow field. It is perhaps because of this, that, close to the wall, the anomalies between the analytical and numerical methods exist.

5.3 The effect on the 1% FCB as the silo dimensions are varied

5.3.1 Introduction

In this section, the predicted effect of changing the silo dimensions on the 1% FCB is investigated. These predictions are vital in interpreting scale effects *i.e.* if one wishes to relate the behaviour of model-scale silos to full-scale silos. The dimensions investigated were the width and height of the silo and the orifice size.

The kinematic parameter B, as defined in Eq. 3.1, has the dimensions of length. A first key question is the relationship between this length and some other length or lengths in the system. Knowing this relationship would allow the value of B to be calculated from basic material tests and the silo geometry without having to resort to elaborate, time-consuming and often expensive flow experiments.

Tuzun and Nedderman (1979a) experimentally established the independence of the kinematic constant B of geometric parameters such as silo width and orifice size. In 1982, the same authors reported the experimental variation of the FCB (determined from long-time exposure photographs) with the silo dimensions. They found that, except close to the wall, the FCB is independent of the silo dimensions. The validity of the definition of the FCB used in this thesis, as put forward in Chapter 3, can be tested against these findings.

Takahashi and Yanai's (1974) equations (Eqs 2.1 and 2.2) predict FCBs that are geometrically similar as the overall silo dimensions are varied. This is in direct contrast to the boundaries predicted by Tuzun and Nedderman (1982) which are thought to be governed by only the particle diameter, and thus provides another comparison for the current FCB definition.

Graham *et al* (1987) suggested that the flow fields in different axisymmetric silos are identical provided that the term BH/R^2 (where H is the silo height) is kept constant. This proposal is tested in terms of the 1% FCB definition.

5.3.2 Effect on the 1% FCB as the height and width of the silo are varied

Keeping the absolute value of the orifice width at 0.1 m, the width and height of a planar silo were varied to gauge the effect on the FCB. The predicted FCBs for a range of different silos are shown, together with the silo dimensions, in Fig. 5.12. As can be seen, these boundaries are barely distinguishable from each other. The same phenomenon is found in axisymmetric silos. This implies that the walls have a negligible influence on the predicted position of the FCB. It can be concluded, therefore, that in a homogeneous bed of granular solid discharging through an orifice of a given size, the present kinematic formulation predicts that there is one characteristic FCB that forms within the solid. The FCB extends until it hits the

wall or reaches the top surface. In other words, the horizontal dimension and the height of the silo do not effect the FCB. This is in keeping with the experimental findings of Tuzun and Nedderman (1979a and 1982) but is in contrast to the theoretical predictions of Takahashi and Yanai (1974).

5.3.3 Effect on the 1% FCB as the orifice size is varied

The different silos that were used to investigate the effect of the orifice size on the FCB are shown in Fig. 5.13. The analyses were carried out on both planar and axisymmetric silos. The different orifice sizes adopted were x_o/X or r_o/R = 0.05, 0.3 and 0.5 (where, in planar geometries, x_o is the orifice width; in axisymmetric geometries, r_o is the orifice radius). In all the analyses, the value of B was kept constant at 0.005 m. The 1% FCBs for all these silos are presented in Fig. 5.14. It can be seen that, even with different orifice sizes, the FCBs tend to approach one another as the height above the base of the silo is progressively increased. Thus, the present finite element method predicts that the channel near the orifice is governed by the orifice dimension, whereas the channel distant from it is governed only by the kinematic parameter.

As mentioned in Section 5.2.3, the 1% FCBs formed in planar silos and those formed in axisymmetric silos are very similar. To highlight the minor differences, the horizontal scale in Fig. 5.14 was expanded. The resulting graph is shown in Fig. 5.15. As can be seen, the FCBs predicted in the axisymmetric silos are slightly narrower than those formed in the planar silos. The differences are so small, however, that they can be neglected.

5.3.4 Effect on the 1% FCB as the silo is scaled

The silo that was used in this section is shown in Fig. 5.16. This silo was scaled up by factors of 2 and 20 and the effect on the FCB was investigated. This scaling affected all the linear dimensions of the silo: the width, the height and the orifice size. The analyses were carried out on axisymmetric silos. A kinematic parameter of B = 0.005 m was chosen and the FCBs were plotted on normalised axes. Following Graham *et al* (1987), the value of B was adjusted for different absolute

silo sizes in such a way as to keep the term BH/R^2 constant and the FCBs were again plotted.

All the FCBs can be seen in Fig. 5.17. It can be seen that the FCB does not follow the same path for the same value of B as the silo is scaled up. This is only because the axes are being normalised by lengths that are characteristic of the silo used. However, if the term BH/R^2 is held constant by adjusting the value of B, it is seen that the FCBs become identical. Graham *et al* (1987) reported that if the term BH/R^2 is held constant, the "flow patterns" will be identical. It has been shown in this section that the FCBs predicted by the present finite element analysis are also indistinguishable on a normalised plot if the term BH/R^2 is held constant.

5.4 The variation of B to model inhomogeneous density distributions

5.4.1 Introduction

Silos are commonly filled either concentrically or eccentrically (Fig. 5.18). An example of concentric filling is the flow of the incoming solid through a centrally-placed chute positioned above the centre of the (concentric) orifice. Eccentric filling occurs when the point of impact of the granular solid in the silo is not always directly above the (concentric) orifice. Examples of eccentric filling may be down an inclined chute or off the end of a conveyor belt (Fig. 5.18). A third filling technique is distributed filling, in which the granular solid is evenly distributed over the entire cross-section during the filling process (in the manner of rainfall).

Munch-Andersen and Nielsen (1990) reported that the filling technique effects the bulk unit weight of the stored solid. They found that distributed filling produces a higher mean density than stream filling (concentric or eccentric) for barley, wheat and rape seed. A silo filled concentrically will produce higher densities at the point of impact and lower densities in the surrounding regions. The tumbling of the grains into these peripheral regions is thought to lead to looser packing arrangements, lowering the density in the process.

Eccentric filling can produce higher horizontal pressures against the wall that faces the chute or belt (Munch-Andersen and Nielsen, 1990). The anisotropic behaviour of grains in the bulk, that is often the result of an eccentric filling technique, may

also give rise to an unsymmetrical flow pattern, even in a silo system that possesses geometrical symmetry. It is the object of this section of the parametric study to model the density differentials prevalent in concentrically- and eccentrically-filled silos, by spatially varying the kinematic parameter, B.

From the previous two chapters, it may be recalled that a low value of B led to pipe flow, whereas a larger value of B led to semi-mass flow. In regions of high bulk density, the grains will be packed tightly with a high degree of interlocking. It is difficult for them to dilate and flow freely. Rigid-block movement will therefore be more probable. This closely corresponds to pipe flow since this flow regime harbours a flow channel which has almost vertical, parallel walls and the channel converges little.

In regions of lower bulk density, the grains are more loosely packed and the free flow of individual grains relative to one other will be facilitated since little dilation is required. The fully-dilated, convergent flow pattern characterised by semi-mass flow will therefore be more probable at lower initial filling densities.

From the above argument, it was decided to model regions where a high initial density was expected (*i.e.* close to the point of impact) with a low value of B. Conversely, in the peripheral regions, where low initial densities were expected, a higher value of B was prescribed.

The silos used for the analyses of concentric and eccentric filling methods are shown in Fig. 5.19. Because the concentric filling technique is symmetrical about the centreline, only the right-hand half of the silo is analysed. Two control analyses were carried out for each filling method. These were chosen to display the reference cases of pipe flow and semi-mass flow clearly. They had constant values of B throughout the silo and took values of 0.005 m to illustrate pipe flow and 0.05 m for semi-mass flow. The constant value of B of 0.005 m was used to represent an isotropic high-density fill, whereas the constant value of 0.05 m was used for an isotropic low-density fill. In each of the two filling methods modelled below, three spatial variations of B were used to model assumed density gradients. These were compared with the two control analyses. The kinematic parameter was not varied with height as it was thought that the variation with horizontal co-ordinate would be more significant in practice.

The eccentric filling of an axisymmetric silo could lead to density gradients right across the diameter which would render the analysis three-dimensional and thus outwith the scope of this thesis. The analysis of the concentric filling of an axisymmetric silo produced results that closely correlated with those of the planar case. For these reasons, the analyses described are only those for planar silos.

5.4.2 Vertical concentric filling

When a silo is filled concentrically, the point of impact is always above the orifice. It is to be expected, then, that the density will be higher in the central core than around the periphery. To model this density variation, the kinematic parameter was set to increase from 0.005 m on the centreline to 0.05 m at the silo wall. The kinematic parameter B was chosen to vary with horizontal co-ordinate in three different patterns: two were discontinuous and one was a linear variation. These are shown, together with the two reference cases (B = 0.005 m and B = 0.05 m) in Fig. 5.20. Each case is designated by a letter for identification purposes.

The 1% FCBs for these five cases are presented in Fig. 5.21. Horizontal profiles of vertical velocity at heights above the orifice of y/X = 0.5, 2, 3 and 5 are presented in Figs 5.22-5.25 respectively.

It can be seen that for Cases (d) and (e) there is a discontinuity of slope in the profile of vertical velocity against horizontal co-ordinate. This discontinuity occurs at the position where the discontinuity in B exists *i.e.* at x/X = 0.25 for Case (e) and at x/X = 0.5 for Case (d). At these ordinates the value of B changes by a factor of 10. This discontinuity does not correspond to a discontinuity in the horizontal velocity, as can be seen from Fig. 5.26. This figure shows horizontal profiles of horizontal velocity at a height above the silo base of y/X = 2. Apart from very localised fluctuations, all these profiles vary smoothly. There are three such fluctuations. One occurs in Case (b) at an ordinate that corresponds to the edge of the orifice. The other two fluctuations occur at ordinates that correspond to the position where B changes abruptly. The gradients immediately before and after each fluctuation are equal. On this evidence, it can be said that there are no discontinuities at the positions where the value of B changes abruptly. It can be concluded from this that at x/X = 0.25 for Case (e) and at x/X = 0.5 for Case (d), the gradient in the profiles of vertical velocity against horizontal co-ordinate in

Cases (d) and (e) must change by a factor of 10. So although there is an abrupt change in the gradient of the vertical velocity profile, the horizontal velocity profile remains smooth because of the changing nature of B.

Returning to Fig. 5.21, it can be seen that there is a discontinuity in the slope of the FCB for Cases (d) and (e) at the ordinate where B changes abruptly. The profiles of vertical velocity against horizontal co-ordinate and the FCBs for Cases (a), (b) and (c) are all smooth.

An interesting observation can be made by careful inspection of Fig. 5.21. In Cases (d) and (e), the FCB comes closer to the axis than in Case (a), although the value of B never drops below 0.005 m. This can be seen as the ordinate, where the discontinuity in B occurs in Cases (d) and (e), is approached. Case (a) has a constant value of B of 0.005 m so a simple interpretation would have been that the FCB at lower ordinates would have been identical for Cases (a), (d) and (e). However, the changed FCB in Cases (d) and (e) shows that the flow pattern at lower levels or smaller ordinates is still influenced by the value of B (or the initial packing density) at higher levels or higher ordinates. This is discussed in greater detail below, with a careful comparison of Cases (a) and (d).

At the top of the silo (y/X = 5), the FCB for Case (a) is much narrower than that for Case (d) (Fig. 5.21). The vertical velocity profiles for these cases have the same centreline values at this height (Fig. 5.25). The same reference velocity is therefore being used to define the 1% FCB. These two velocity profiles gradually diverge at increasing ordinates, the velocities for Case (d) becoming lower than those for Case (a). The profiles then cross over, as they must to satisfy the global continuity condition. The vertical velocity at the 1% FCB criterion is less than that at which the profiles cross. Therefore, the FCB for Case (a) lies inside that of Case (d).

It is seen that lower down the silo, at y/X = 3, the FCB for Case (d) lies inside that of Case (a). The 1% criterion for Cases (a) and (d) gives almost identical FCBs, because of very similar centreline velocities. The 1% criterion is greater than the value of vertical velocity where these two profiles cross and so when calculating the distance of the FCBs from the centreline, the profile of Case (d) is reached first.

In Cases (d) and (e), the FCBs closely follow Case (a) (B = 0.005 m) until the abrupt jump in B is reached (at x/X = 0.25 for Case (e) and x/X = 0.5 for Case (d)). At these horizontal co-ordinates, B jumps to the higher value of 0.05 m and the flow channels immediately start to widen. Even if B takes the lower value of 0.005 m for only a quarter of the silo's width and the higher value of 0.05 m for the remaining three quarters (Case e) the FCB is drastically different from that formed with B = 0.05 m for the whole width (Case b). Thus a small zone of high density solid down the centre of the silo is predicted by the present analysis to influence the entire flow pattern very markedly. It may be noticed that for Case (e), the FCB impinges the wall at a height y/X = 2.75 whereas in Case (b) the corresponding point is at y/X = 0.9. This would suggest that the switch pressure, that is thought to occur at the effective transition, is highly sensitive to density gradients and may occur at a completely different position depending on how the silo had been filled.

The above discussion suggests that calculations which use a variable B, somehow correlated to the density, and possibly varying with time would be very revealing. However, the development of such a model is beyond the scope of this thesis.

5.4.3 Eccentric filling

Eccentric filling from an inclined chute or conveyor belt is likely to produce higher densities against the wall that faces the chute or belt. To model these density gradients, three variations of the kinematic parameter were again examined: two discontinuous functions of B with horizontal co-ordinate and one linear variation. These are shown, along with the two reference cases (B = 0.005 m and B = 0.05 m), in Fig. 5.27. In this figure, Case (c) models a linear density gradient across the silo's width, Case (d) models a silo in which the left half is occupied with high-density solid and the right half with low-density solid and Case (e) models a silo in which the high-density solid only occupies the left-hand quarter, the remaining volume being occupied with low-density solid. Case (c) may represent the situation that exists when a silo is filled eccentrically with free-flowing solid that cannot support any density discontinuities. Cases (d) and (e) may approximate the density gradients in silos that are filled eccentrically with very frictional solids. During filling, the stream of this free-falling, frictional solid is modelled to be as wide as half the silo's whole width in Case (d) and only a quarter of the width in Case (e).

Reference cases with constant values of B = 0.005 m (Case a) and B = 0.05 m (Case b) were again analysed and used for comparison.

The 1% FCBs for Cases (a), (b) and (d) are shown in Fig. 5.28, for Cases (a), (b) and (e) in Fig. 5.29 and for Cases (a), (b) and (c) in Fig. 5.30. The horizontal profiles of vertical velocity at heights y/X = 0.25, 1.0 and 5.0 are shown in Figs 5.31-5.33 respectively. It is seen that the maximum value of vertical velocity does not always occur at the centreline. For this reason, the 1% FCBs, in eccentrically-filled silos, were defined as the locus of points where the vertical velocity fell to 1% of the maximum value occurring at that level.

Considering the cases where B increased from left to right (Cases c, d and e) collectively, several trends can be seen. The position of the maximum vertical velocity has shifted off the centreline and to the left for all three cases (see, for example, Fig. 5.33). This feature becomes more prominent in those profiles that are further from the base of the silo. This skewing of the vertical velocity profiles causes the flow channel to become unsymmetrical. In all three cases, the FCB intersects the right wall at a lower position than it does the left wall (if, indeed, it intersects the left wall at all).

In Case (d), the FCB approximates the FCBs for Case (a) in the left half of the silo and Case (b) in the right half, as might be expected, but is not exactly the same as them (Fig. 5.28). To investigate this phenomenon, the profiles of vertical velocity are examined (Figs 5.31-5.33). In the central region the vertical velocity associated with Case (d) lies between those of Cases (a) and (b). The profile of vertical velocity for Case (d) approaches that of Case (a) as one moves to the left of the centreline and approaches that of Case (b) as one moves to the right. Although the centreline velocity of Case (d) is quite different from that of Case (a), the position where the centreline velocity of Case (d) falls to 1% of its value and the position where the centreline velocity of Case (a) falls to 1% of its value are very nearly coincident. A similar explanation can be put forward for the right half of the silo using Cases (b) and (d). This explains why the FCB for Case (d) approximates that of Case (a) in the left half of the silo and that of Case (b) in the right half.

In line with the findings of the previous section, it can be seen that in Case (d) a discontinuity in the gradient $\partial v/\partial x$ occurs on the centreline, x/X = 1; that is, at the position where the discontinuity in B exists (Figs 5.31-5.33). A similar

discontinuity exists in Case (e) at x/X = 0.5 which corresponds to the position of the discontinuity in B for this case.

It is also seen, from Fig. 5.29, that as one moves from the centreline to the left, the FCB for Case (e) follows the FCB for Case (b) up until the horizontal position where B switches to the lower value of 0.005 m, *i.e.* at x/X = 0.5. After this point has been passed, the FCB and velocity profiles for Case (e) become more-or-less parallel to those for Case (a), which had a constant value of B = 0.005 m throughout.

Considering the right half of the silo, Cases (b) and (e) both have a value of B of 0.05 m. The velocity profiles for these cases are barely distinguishable at a height of y/X = 1. At the top of the silo (Fig. 5.33), these velocity profiles have separated a little but do not cross in the right-hand half of the silo and are of similar shape. It is for these reasons that the FCBs for Cases (b) and (e) are very nearly identical in the right half of the silo.

Case (c) has a linear variation of B across the silo's width, so no discontinuities in the velocity profiles (Figs 5.31-5.33) or the FCB (Fig. 5.30) occur. It may be noticed that although the FCB for Case (c) is quite close to that of Case (b) in the right half of the silo, it is far from that of Case (a) in the left half. This difference is reflected in Figs 5.32 and 5.33. In these figures, the profiles of vertical velocity for Case (c) more closely approach those of Case (b) in the right half of the silo than they do Case (a) in the left half.

These analyses show that the density gradients that may occur in an eccentrically-filled but symetrically-discharged silo may lead to a FCB that intersects the wall on the opposite side to the eccentricity at an unusually-low position. This could lead to overpressures occurring in this location. In terms of silo design then, the current finite element analysis suggests that care must be taken if it is at all likely that the filling method may be eccentric.

5.5 The displacement of the top surface during incipient discharge

5.5.1 Introduction

A feature of the finite element method is the ease with which complex boundary conditions can be introduced. This capability was exploited in modelling the displacement of the top surface during the first stages of discharge. As mentioned in Chapter 3, the elements used in all the analyses were general quadrilaterals, known as cubic isoparametric serendipity elements (Zienkiewicz, 1971). These allow the dependent variable, in this case the vertical velocity, to vary cubically within the element. They also allow the element boundaries to vary in any general cubic fashion.

To model the initial stages of discharge, an arbitrary time increment, chosen from experience, was used to step the co-ordinates of all nodes forward in time. The vertical co-ordinate of a node at the new time station was calculated as the vertical co-ordinate at the previous time station plus the vertical velocity at the previous time station multiplied by the time increment. An analogous algorithm was used to redefine the horizontal co-ordinates of all nodes. This method is expressed mathematically below.

$$x_n^{t+1} = x_n^t + u_n^t \Delta t \tag{5.1}$$

$$y_n^{t+1} = y_n^t + v_n^t \Delta t \tag{5.2}$$

The superscript t represents a particular time station. The co-ordinates of the n^{th} node are (x_n,y_n) and Δt is the time increment.

As the solid above the orifice flowed through it, the boundary condition in the region of the orifice had to be altered. It was decided to prescribe the vertical velocity of any node that fell below the base level of the silo. The value of this vertical velocity was calculated from Eq. 3.19. This equation calculates the prescribed vertical velocity as a cubic function of the horizontal co-ordinate only. The advantage of prescribing the velocities of all nodes which had passed through the orifice is that the orifice velocity profile is maintained despite the loss of much material.

The time-marching solution was not concerned with modelling the entire discharge process and was only stepped forward for a limited time. It is well-known that the highest pressures in a silo often occur at the onset of discharge and it seems reasonable that this is the most interesting period to examine. At larger time steps, the geometry of some elements became so distorted that for the solution to proceed, these elements would have to be removed from the domain. The modelling of the complete discharge was therefore judged to be a complex procedure that would lead to results of limited value and was therefore deemed beyond the scope of this thesis.

5.5.2 Examples studied

Three different initial top surface profiles were analysed (Fig. 5.34). One top surface profile was initially horizontal and was analysed in both planar and axisymmetric geometries. The other two initial top surface profiles were sloped and were analysed only in a silo of planar geometry. One of these formed an upward-pointing wedge (representing a silo that had be newly filled), and the other formed a wedge-shaped crater (representing a silo that had already undergone partial discharge). An angle of repose of 30° has been assumed. Two different values of the kinematic parameter B were used, 0.1 m and 0.2 m.

5.5.3 Results and Discussion

In Figs 5.35 and 5.36, the displacement of an originally-horizontal top surface is shown for the two different values of B in a silo of planar geometry. The 1% FCBs are included for reference. The time increment is 0.25 seconds and four steps are taken forward in time. Figs 5.37 and 5.38 represent the analogous modelling for a silo with axisymmetric geometry. The vertical scales in Figs 5.35 and 5.36 are the same and those in Figs 5.37 and 5.38 are the same to allow easier comparisons to be made. It can be seen from all four figures that the top surface displaces from the horizontal into a approximately cubic-shaped crater. This becomes progressively deeper and wider as further time steps are taken. It can be seen that, in both geometries, when B is 0.2 m the flow channel is wider and the crater is broader and shallower than that formed when B is 0.1 m. It can also be noticed from these four figures that the depth of the crater in planar geometry, at any particular time instant, is deeper than that in axisymmetric geometry at the same time instant. In

axisymmetric geometries, the shape of the flow channel is roughly a paraboloid of revolution whereas the shape in planar geometries is a prism of roughly parabolic cross-section. When the same exit velocity distributions are used for both geometries, these differently-shaped flow channels cause the velocities to be smaller at any particular point in axisymmetric geometries. The displacement craters associated with axisymmetric geometries are therefore less pronounced than those associated with planar geometries at the same time instant.

In Figs 5.39 and 5.40 the top surface displacements for the other two silos (*i.e.* those which had originally-sloping top surfaces) are shown. It was considered necessary to show the results of these analyses only in one geometry and only for one value of B since other combinations could be interpolated from what has been reported in the preceding paragraphs. The geometry chosen was planar, as mentioned above, and the value of B was 0.1 m. It was decided that the vertical scale should not be expanded relative to the horizontal scale, as was done in the previous four figures, so the true angle of repose could be represented. Although this results in the displacement profiles being rather close together, it was considered important to maintain the correct angle of the original top surface. In this way, one could gain a qualitative feel for the predicted shape of the top surface as it displaces.

It can be seen from Figs 5.39 and 5.40 that the top surface displaces as a combination of the original linear profile plus an approximately cubic-shaped displacement. As the solution proceeds through time, the displacement profile again becomes lower and also widens out laterally. It can be seen that the absolute displacements in Fig. 5.40 are greater than those in Fig. 5.39. In Fig. 5.40, the original top surface slopes down from the wall to the centreline. In Fig. 5.39, the original top surface slopes, from the same position on the wall, upwards to the centreline. The top surface in Fig. 5.40 is therefore closer to the orifice than in Fig. 5.39. The velocities along the top surface are therefore greater in Fig. 5.40 than they are in Fig. 5.39. Therefore, the displacement that occurs in Fig. 5.40 in any set time interval will be greater than that occurring in Fig. 5.39.

In this section, it has been found that the changing profile of the top surface has little influence on the velocity field and flow channel. It was therefore considered unnecessary to pursue this work further.

5.6 Flow patterns produced by eccentric discharge

5.6.1 Introduction

It is frequently necessary to discharge a silo through an eccentrically-positioned outlet. The task which the silo is required to meet may demand that the granular solid be discharged from the edge of the silo. This is one example of how eccentricity can be introduced into the storage/recovery system. Eccentric discharge is also manifest if more than one outlet is utilised, for example to release the solid from the stagnant zones in a flat-bottomed silo. The complex asymmetric pressure distribution that is produced on the silo walls during eccentric discharge is little-understood and is often the cause of catastrophic failures. If the flow patterns that occur in an eccentrically-discharging silo were more fully understood, the pressure distribution could be more accurately predicted. This would lead to a safer and more economical design of eccentrically-discharging silos. This section of the parametric study aims to provide some quantitative and qualitative information about the velocity fields and the FCB during the eccentric discharge of granular solid from flat-bottomed silos.

Three silos were analysed. These are shown in Fig. 5.41 and the prescribed exit velocity distributions are shown in Fig. 5.42. Figure 5.41a shows a silo with a concentrically-positioned outlet. The theoretical predictions from this silo were used for reference purposes. The other two silos (Figs 5.41b and 5.41c) had outlets that were eccentrically positioned. The eccentricity e was defined as the ratio of the distance between the centreline of the silo and the middle of the outlet to the half-width X of the silo. The eccentricities that were analysed were $e = 0.45$ and $e = 0.9$.

For the silo which had an outlet with an eccentricity of 0.9, two different exit velocity distributions were analysed. These are also shown in Fig. 5.42. One of these exit velocity distributions is the same 'full' cubic velocity distribution that was used for the other two silos. This, however, prescribes the vertical velocity at the left-hand edge of the orifice, which is adjacent to the left-hand wall, as zero. Since this is unrealistic, an additional exit velocity was prescribed for this silo. This took the form of a 'half' cubic which prescribed the vertical velocity to be a maximum adjacent to the left-hand wall and zero at the right-hand edge of the orifice. The

two exit velocity distributions, although of different shape, had the same maximum value of vertical velocity and produced the same flow rate. The effects on the flow field of using these two different exit velocity distributions were compared. The value of the kinematic parameter used was B = 0.1 m.

In an eccentrically-discharging silo, the FCB cannot realistically be defined in terms of the centreline velocity as was done for concentrically-discharging silos. The FCB in eccentric discharge is therefore defined as the locus of points where the vertical velocity falls to 1% of the maximum vertical velocity which occurs at that particular level. This is the same definition that was used to define the FCB in silos which were filled eccentrically. The FCBs produced in eccentrically-discharging silos were examined.

Since any eccentricity renders the system three-dimensional, this section of the parametric study only concerns itself with silos of planar geometry.

5.6.2 Discussion

The 1% FCBs for the three silos that were analysed are shown together in Fig. 5.43. For the case where the eccentricity was 0.9, two different exit velocity distributions were used as detailed above. It can be seen from Fig. 5.43 that the FCBs produced by these different exit velocity distributions are nearly identical. This is to be expected from the form of the governing partial differential equation (Eq. 3.3), and further supports Tuzun and Nedderman's (1979) suggestion that the flow pattern at distances far from the orifice is only negligibly affected by the shape of the exit velocity distribution. It is clear that this proposition is as valid in eccentric discharge as in concentric discharge.

In Fig. 5.44, the FCBs associated with the two eccentrically-discharging silos (e = 0.45 and 0.9) are transposed and sited over the concentric orifice to enable closer comparison. The FCB formed in the silo with a concentric orifice is also included. It can be seen that the FCBs do not all exactly overlay one another. When e = 0.45, the FCB follows that of the concentrically-discharging silo quite closely. However, when the orifice is fully eccentric (e = 0.9), it is seen that the FCB clearly lies inside that produced when the eccentricity is 0.45. This suggests that the flow channel is narrower when the orifice is placed adjacent to the wall than

when it is placed concentrically. Thus, the present analysis suggests that narrow pipe flows are more likely to occur in very eccentric discharge than in concentric discharge.

In Figs 5.45-5.47, horizontal profiles of vertical velocity at respective heights above the orifice of y/X = 2, 5 and 10 are shown. The maximum vertical velocity associated with the e = 0.9 silo is seen to be greater than those associated with the other two silos. It was noted above that the width of the flow channel is narrower when the orifice is positioned adjacent to a wall. The mean vertical velocity within the 1% FCB for this silo must therefore be higher, so as to produce the same flow rate.

The reason why the FCBs for the high eccentricity are almost identical for the two different exit velocity distributions can be obtained from Figs 5.45-5.47. Although the exit velocity distributions are quite different, the horizontal profiles of vertical velocity quickly tend towards one another as the height at which these profiles are taken increases. By the time the top of the silo is reached, the profiles overlap each other almost completely. Therefore, the FCBs will be very nearly identical.

The most interesting phenomenon in the present set of predictions (Figs 5.45-5.47) concerns the silo which has its outlet positioned at an eccentricity of 0.45. The profiles of vertical velocity associated with this silo are not symmetrical about the vertical line that extends upwards from the centre of the orifice *i.e.* the line x/X = 0.55. At y/X = 2, the vertical velocity profile for this silo is very similar in shape to that of the silo with the concentric outlet. Indeed, if the profile for the concentrically-discharging silo were moved to the left, superimposing the two profiles, the match would be good everywhere except close to the left-hand wall. As this wall is approached, the profile associated with the eccentrically-discharging silo levels off. This is required to comply to the u = 0 boundary condition at x/X = 0. Higher up the silo at y/X = 5, this levelling off extends further into the silo. This renders the vertical velocity profile associated with the eccentrically-discharging silo a very different shape from that for the concentrically-discharging silo. The horizontal profile of vertical velocity for the eccentrically-discharging silo is now certainly not symmetrical about the vertical line through the centre of the orifice. This process of symmetry loss continues up the silo. Indeed, at the top of the silo, the maximum value of vertical velocity occurs at the left-hand wall. This implies that, for this silo, the pit of the crater that is formed in the free surface

would lie adjacent to the left-hand wall and not above the orifice centre. This is a phenomenon that is well-known in practice and so demonstrates the qualitatively realistic character of the predictions made by the current finite element analysis.

5.7 Flow patterns produced in a silo with two outlets

5.7.1 Introduction

Silos commonly have more than one outlet orifice through which the stored granular solid discharges. For example, in a chemical processing plant, a certain stored granular solid may be needed for use in two different processes at the same time. Rather than have two separate silos, it is often more efficient to have two orifices in the one silo. Another example of a silo with more than one outlet might be the discharging of a large grain silo. To facilitate this in the quickest way, two or more outlets discharging into waiting trucks or conveyors may be required. The complex flow regime that is produced from the interactions of the flow channels that lead down to each orifice is far from understood. Adding to the complexity of this flow situation, the outlets are seldom opened and closed simultaneously. The flow pattern associated with one outlet may be fully-developed when a second outlet is opened. The effect that this has on the velocity fields in the bulk solid and on the pressures on the silo walls is not understood. Although the current finite element formulation deals only with steady-state analyses, the extension to time-dependent analyses is a possible step. This would facilitate a time-dependent analysis of the effect of intermittent opening and closing of one outlet in double-outlet silos. Even though such an analysis is outside the bounds of this thesis, the kinematic modelling of flow from a silo with any number of outlets is, for the first time, possible.

In this parametric study, silos with two outlets were analysed. It was thought unnecessary to analyse silos in which the number of outlets exceeded two. The quantitative and qualitative knowledge gained from the analysis of a silo with two outlets was considered to be sufficient. This knowledge can be used to gain some feel for the flow patterns that would be produced in a silo with any number of outlets. The analysis of double-outlet silos also demonstrates the capability of the current finite element formulation.

Since an axisymmetric silo with a circular eccentric outlet would constitute a three-dimensional arrangement, this section of the parametric study is restricted to the analysis of planar silos.

Two double-outlet silos were analysed and are shown in Fig. 5.48. One was symmetrical about the centreline and had orifice centres that were one-quarter and three-quarters of the silo's width from the left-hand wall. The other was asymmetrical about the centreline and had one orifice adjacent to the left-hand wall and one that was three-quarters of the silo's width from this wall. All the orifices had widths that were one tenth the silo's width. The prescribed exit velocity distributions are shown on Fig. 5.49. The volumetric flow rate from each orifice was the same. The kinematic parameter took constant values of 0.02 m, 0.05 m, 0.1 m and 0.2 m. Velocity profiles and FCBs were predicted and are discussed below. As in the previous section on eccentric discharge, the FCB was again defined as the locus of points where the vertical velocity falls to 1% of the maximum vertical velocity which occurs at that particular level. The effect of closing one orifice on the FCB was also investigated.

5.7.2 Discussion

5.7.2.1 Silo with symmetrical outlets

The 1% FCBs, each one for a different value of B, are shown in Fig. 5.50. As can be seen, the FCBs are symmetrical about the centreline of the silo. An 'island' of stagnant solid forms between the two orifices. The height of this island increases as the value of B decreases. Some selected horizontal profiles of vertical velocity are shown in Fig. 5.51. The profiles in this figure are taken at two different heights for two different values of B. It can be seen that as the height is increased, the velocity profiles become flatter but retain their general shape. As the value of B is increased, the same change is seen. So, at any particular height, higher values of B correspond to a wider flow channel which has lower vertical velocities associated with it. In addition, profiles near the top of the silo relate to a wider flow channel of slower-moving solid, whereas the profiles low down in the silo correspond to a narrower channel of faster-moving solid.

In Fig. 5.52, two horizontal profiles of horizontal velocity are shown. These were taken at the top of the silo and illustrate the horizontal velocities associated with the widest part of the flow channel. For B = 0.05 m, there is a narrow region in the centre of the silo where the horizontal velocity is zero. No such region is evident for the case where B = 0.20 m. It can be seen from Fig. 5.50 that for the case where B = 0.20 m, the internal FCBs meet at about a quarter of the silo's height above the base. For the case where B = 0.05 m, these FCBs meet at about two-thirds of the silo's height. Because the two flow channels for the case where B = 0.20 m meet much lower, by the time the top of the silo is reached, the channels have well and truly grown together. For this reason, the horizontal velocities at the top of the silo for the case where B = 0.20 m are always non-zero except on the axis of symmetry or at the walls. In contrast, when B = 0.05 m, the flow channels are narrower and there exists a broad region in the centre of the silo where the horizontal velocities are zero.

In Fig. 5.53, the effect of closing one outlet on the FCB is examined. The FCBs that are produced from two outlets are compared with that from only the right-hand outlet. When the left-hand outlet is closed, it is seen that the FCB from the right-hand outlet follows the same path as if both outlets were open. Only a very slight difference is noticed near the centreline and this is due to the interpolation used to find the position where two internal FCBs meet. When the left-hand outlet is closed, the left-hand section of the right-hand FCB does not terminate at the centreline but continues on and intersects the free surface.

5.7.2.2 Silo with asymmetrical outlets

The 1% FCBs for this double-outlet silo are shown in Fig. 5.54. As can be seen, the general pattern is the same as that for the silo with symmetrically-positioned outlets. The flow channel becomes wider as the value of B is increased and, for the larger values of B, an island of stagnant solid forms between the two outlets. Since the left-hand outlet is adjacent to the left wall, solid is always flowing rapidly down this wall. Because of this, the left wall forms the left-hand section of the FCBs that are associated with the left-hand orifice.

It was discovered that the FCBs are different in shape from those formed in the silo with two symmetrically-positioned outlets. Consider the width of the flow channel

at the top of the silo for the case where B = 0.02 m. In the silo with asymmetrical outlets, this width is 0.76 of the silo's half-width (Fig. 5.54). In the silo with symmetrical outlets, this width has increased to 0.82 of the silo's half-width (Fig. 5.50). To investigate this effect some typical velocity profiles (Fig. 5.55) are examined. Horizontal profiles of vertical velocity at heights of y/X = 0.1 and y/X = 2 are shown for the case where B = 0.05 m. The value of the maximum prescribed vertical velocity was the same for each orifice, as can be recalled from Fig. 5.49. As one moves away from the silo base, however, the vertical velocity of granular solid adjacent to the left wall is clearly greater than that above the centre of the right-hand orifice, at x/X = 1.5. The criterion that is used to define the FCB was 1% of the maximum value of vertical velocity, irrespective of where this occurs. Because the vertical velocity adjacent to the left wall is higher than above the centre of the right-hand orifice, the criterion will be higher in the silo with asymmetrically-positioned orifices, than in the silo with symmetrically-positioned orifices, as in the previous analysis. The theoretically-calculated flow channel will therefore be narrower when an orifice is positioned adjacent to a wall.

This influence also prevails when the effect of closing the left-hand orifice is examined. In Fig. 5.56, the FCB for the case where the left-hand orifice is closed is compared to that for the case where both orifices are open. The value of the kinematic parameter was taken as 0.05 m as this serves as a suitable example. When the left-hand orifice is closed, the maximum vertical velocity occurs above the centre of the right-hand orifice. This velocity is lower than the velocity that would occur adjacent to the left wall, were both orifices open. The 1% criterion is therefore lower and so the flow channel is wider. The velocity profiles do not alter when an orifice is closed.

5.8 The analysis of flow through hoppers

5.8.1 Introduction

A hopper is required for the mass-flow of stored granular solids. Mass-flow was described in Chapter 1 as the flow mode in which every particle of solid is in motion. Mass flow is vital for many installations where regions of stagnant solid are not acceptable. For example, the flow pattern should always be mass-flow where the granular solid is organic and degradeable. Mass flow silos also have a

more controllable and predictable discharge flow rate and so are widely used in preference to funnel flow or flat-bottomed silos with difficult materials or where guaranteed reliable flow is required: for example, in the chemical process industry.

Hoppers commonly take the form of a cone for axisymmetric silos and a wedge for planar silos.

5.8.2 The analysis of flow through hoppers using the theory of Tuzun and Nedderman (1979a)

Nedderman (1990, *via* Cleaver, 1991) used a stream function analysis to demonstrate that the kinematic model of Tuzun and Nedderman (1979a) cannot accommodate radial flow. This analysis, first performed whilst the present study of hoppers was in progress, is reproduced below. It may be recalled from Chapter 2 that in Tuzun and Nedderman's (1979a) model, the ratio of the horizontal velocity u to the horizontal gradient of the vertical velocity $\partial v/\partial x$ was taken to be a constant and was termed the kinematic constant.

The stream function is a fluid-mechanical concept used to describe the flow pattern. Along a streamline, the stream function is constant and is given a numerical value. This value represents the flow rate per unit depth between the streamline and some reference streamline. Radial flow is the flow condition expected in a mass-flow hopper. It is characterised by flow along radii towards the virtual apex of the hopper situated below the orifice *i.e.* radial streamlines (see Fig. 5.57). For radial flow, the stream functions are described by $\Psi = ax/y$, where a is a constant.

In general, the stream function Ψ may be defined as follows (Douglas *et al*, 1986):

$$u = \frac{\partial \Psi}{\partial y} \tag{5.3}$$

$$v = -\frac{\partial \Psi}{\partial x} \tag{5.4}$$

The kinematic equation of Tuzun and Nedderman (1979a) is

$$u = -B\frac{\partial v}{\partial x} \tag{5.5}$$

Substituting Eqs 5.3 and 5.4 into Eq. 5.5 leads to

$$\frac{\partial \Psi}{\partial y} = B\frac{\partial^2 \Psi}{\partial x^2} \tag{5.6}$$

Nedderman (1990, *via* Cleaver, 1991) defined a function $\beta = x/y$. Therefore

$$\frac{\partial \Psi}{\partial y} = \frac{\partial \Psi}{\partial \beta}\frac{\partial \beta}{\partial y} = -\frac{x}{y^2}\frac{d\Psi}{d\beta} \tag{5.7}$$

$$\frac{\partial^2 \Psi}{\partial x^2} = \frac{d^2\Psi}{d\beta^2}\left(\frac{\partial \beta}{\partial x}\right)^2 = \frac{1}{y^2}\frac{d^2\Psi}{d\beta^2} \tag{5.8}$$

Substituting Eqs 5.7 and 5.8 into Eq. 5.6 gives

$$-x\frac{d\Psi}{d\beta} = B\frac{\partial^2 \Psi}{\partial \beta^2} \tag{5.9}$$

This shows that Ψ is not a function of β alone but must also vary with x. Therefore, it was concluded (Nedderman, 1990, *via* Cleaver, 1991) that radial flow, which requires all streamlines to be radial towards the apex and thus dependent only on β, is not accommodated by the kinematic theory of Tuzun and Nedderman (1979a).

Graham *et al* (1987) also employed the kinematic theory with a constant kinematic parameter. For their wall boundary condition, they considered flow down an inclined surface. Since this constitutes radial flow, it is concluded that some of their boundary conditions must not be satisfied.

5.8.3 The analysis of flow through hoppers using the present theory

In the present work, the ratio of the horizontal velocity u to the horizontal gradient of the vertical velocity $\partial v/\partial x$ was allowed to vary spatially in any desired manner

and was termed the kinematic parameter B in Chapter 3. It may be noticed that if B is set, for example, to equal bx (where b is a constant) in Eq. 5.9, Ψ becomes a function of β only and radial flow can therefore be accommodated.

The boundary condition along the hopper wall is now considered. The velocity components at the hopper wall are shown in Fig. 5.58. The resultant velocity must be parallel to the wall *i.e.*

$$u = v \tan\alpha \tag{5.10}$$

where α is the included hopper half-angle. The kinematic equation used in the planar formulation in this thesis (Eq. 3.1) is :

$$u = -B(x,y) \frac{\partial v}{\partial x} \tag{5.11}$$

Combining Eqs 5.10 and 5.11 and rearranging gives

$$\frac{\partial v}{\partial x} + \frac{\tan\alpha}{B(x,y)} v = 0 \tag{5.12}$$

Equation 5.12 is the boundary condition applicable to the hopper wall. Since Eq. 5.12 includes the dependent variable v and its first derivative $\partial v/\partial x$, the boundary condition is termed mixed (Zienkiewicz, 1971). A similar boundary condition was derived for axisymmetric geometries. The development of the present finite element method to accommodate mixed boundary conditions, although desirable, was judged to be outside the scope of this thesis.

5.9 Closing remarks

In this chapter, the kinematic finite element formulations developed in Chapters 3 and 4 have been rigorously applied to a wide range of silo geometries and flow situations. The formulations are seen to behave well and produce realistic predictions of velocity fields and FCBs in all cases. Several extensions to situations not susceptible to analysis by existing analytical methods have been shown. This chapter serves to demonstrate that these formulations can be a powerful tool for the

numerical analysis of discharging silos, though further verification of their predictions against experimental findings is certainly required.

Appendix 5.1 Equivalence of Mullins' (1974) and Tuzun and Nedderman's (1979a) equations

The aim of this appendix is to demonstrate the equivalence of the analytical solutions of Mullins (1974) and Tuzun and Nedderman (1979a) to the governing partial differential equation for kinematic granular solids flow in planar geometries (Eq. 2.5). The trajectory equations of Mullins (1974) are reproduced below using the notation of this thesis.

$$y = y_i\left(1 - \frac{t}{T(x_i,y_i)}\right)^{2/3} \tag{A5.1}$$

$$x = x_i\left(\frac{y}{y_i}\right)^{1/2} \tag{A5.2}$$

$$T(x_i,y_i) = \frac{4(\pi B)^{1/2}}{3Q}\, e^{\frac{x_i^2}{4By_i}}\, y_i^{3/2} \tag{A5.3}$$

In these equations, (x_i,y_i) are the starting co-ordinates, (x,y) are the co-ordinates of the particle at time t, T is the residence time and Q is the volumetric flow rate. The vertical velocity is obtained by differentiating Eq. A5.1 with respect to t:

$$v = \frac{dy}{dt} = -\frac{2y_i}{3T}\left(1 - \frac{t}{T}\right)^{-1/3} \tag{A5.4}$$

and using Eq. A5.1 to substitute y for t:

$$v = -\frac{2y_i}{3T}\left(\frac{y}{y_i}\right)^{-1/2} \tag{A5.5}$$

and now using Eq. A5.2 to substitute x for y:

$$v = -\frac{2y_i}{3T}\left(\frac{x_i}{x}\right) \tag{A5.6}$$

Substituting Eq. A5.3 into A5.6 leads to

$$v = -\frac{Q}{(4\pi By_i)^{1/2}}\, e^{\frac{x_i^2}{4By_i}} \tag{A5.7}$$

Apart from the negative sign, which is due only to differing sign conventions, Eq. A5.7 is identical to Tuzun and Nedderman's similarity solution (1979a).

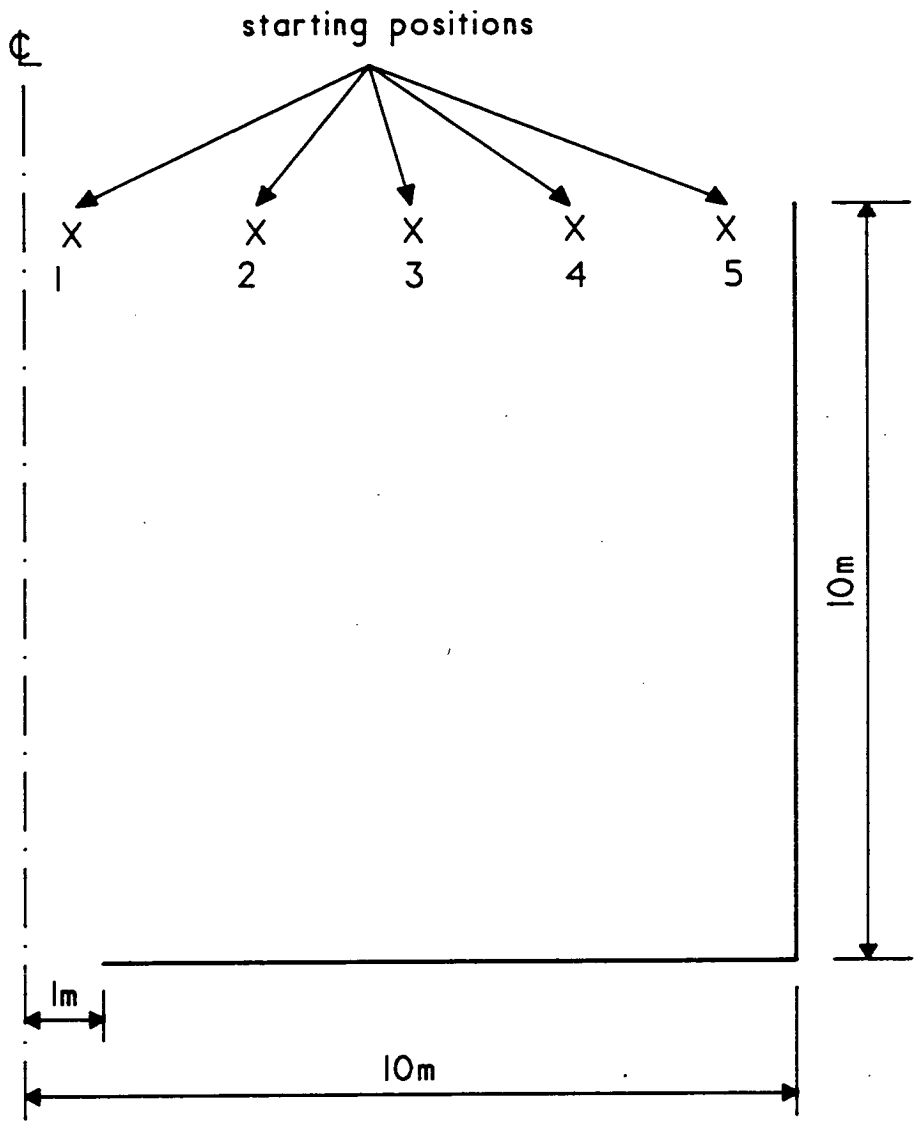

Fig. 5.1 Silo used for tracing trajectories

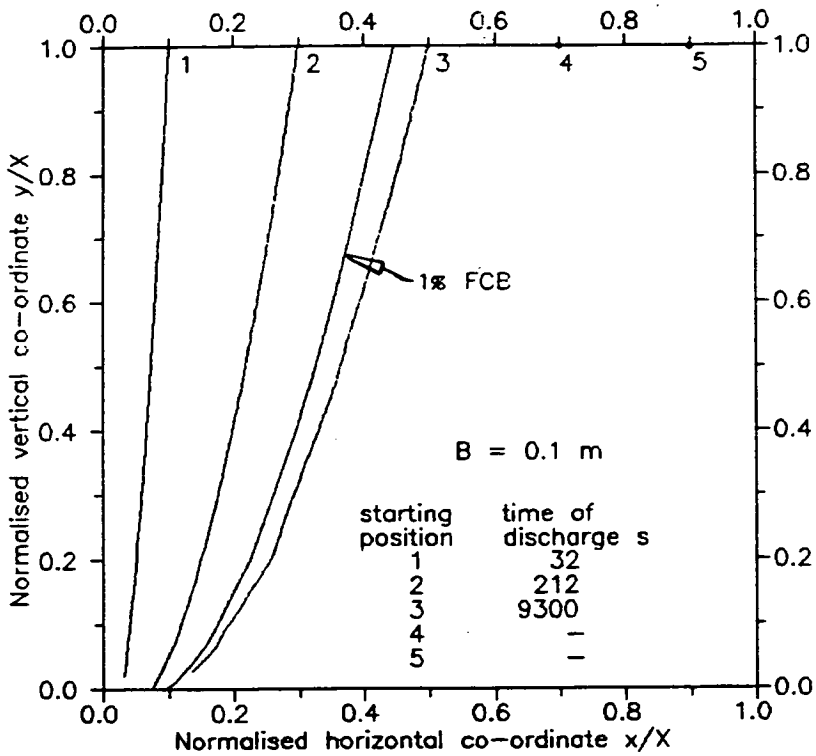

Fig. 5.2 Particle trajectories in planar geometries

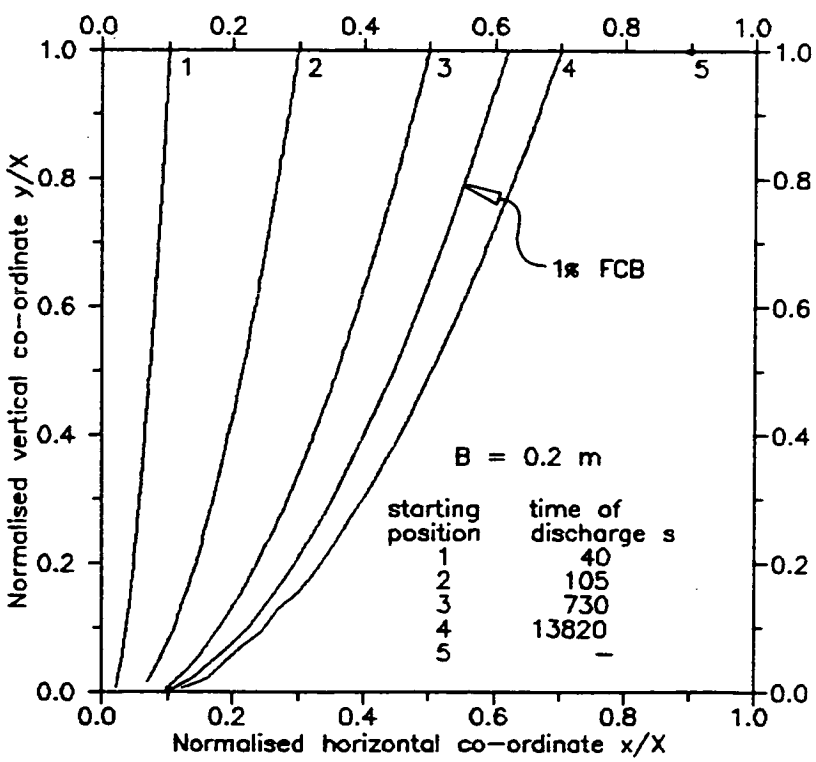

Fig. 5.3 Particle trajectories in planar geometries

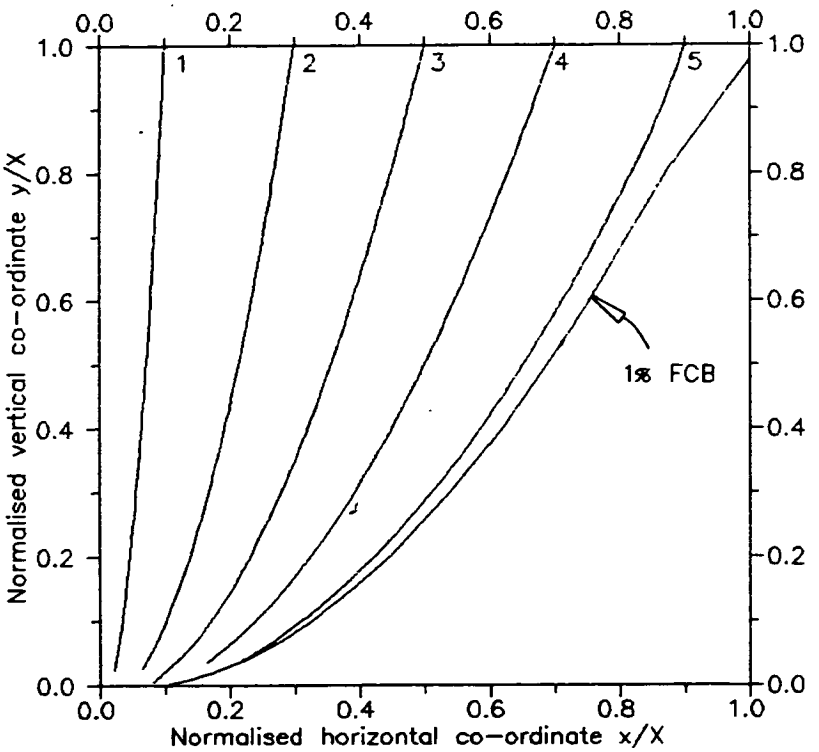

B = 0.5 m

starting position	time of discharge s
1	58
2	86
3	190
4	625
5	3360

Fig. 5.4 Particle trajectories in planar geometries

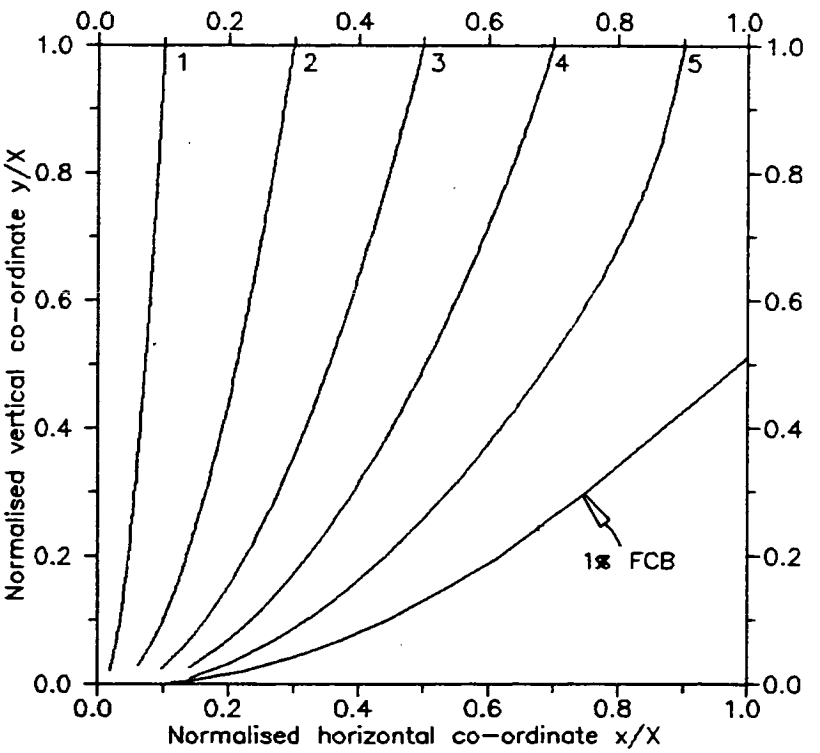

B = 1.0 m

starting position	time of discharge s
1	78
2	96
3	143
4	265
5	704

Fig. 5.5 Particle trajectories in planar geometries

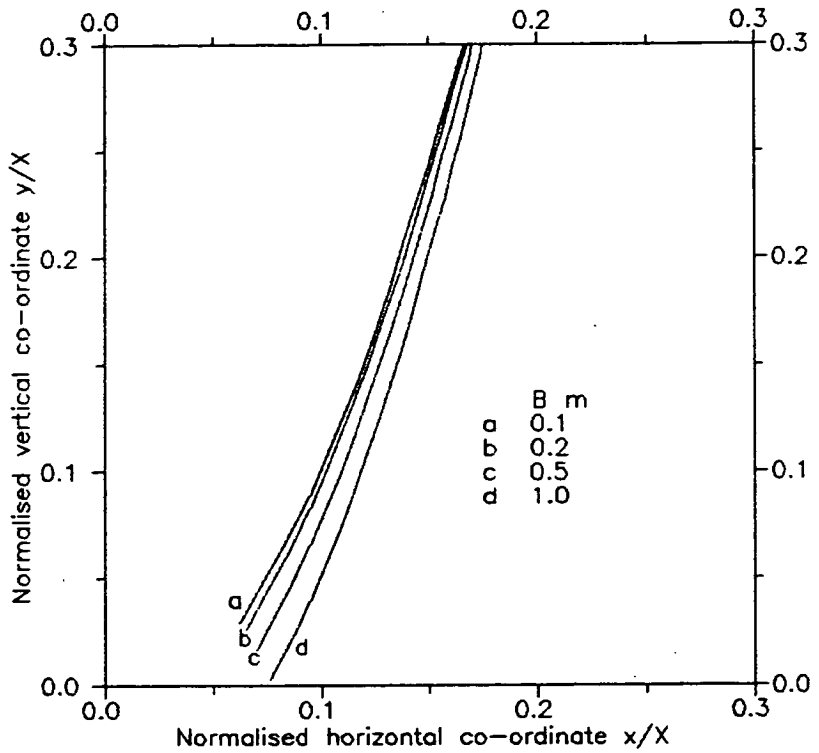

Fig. 5.6 Comparing particle trajectories in planar geometries

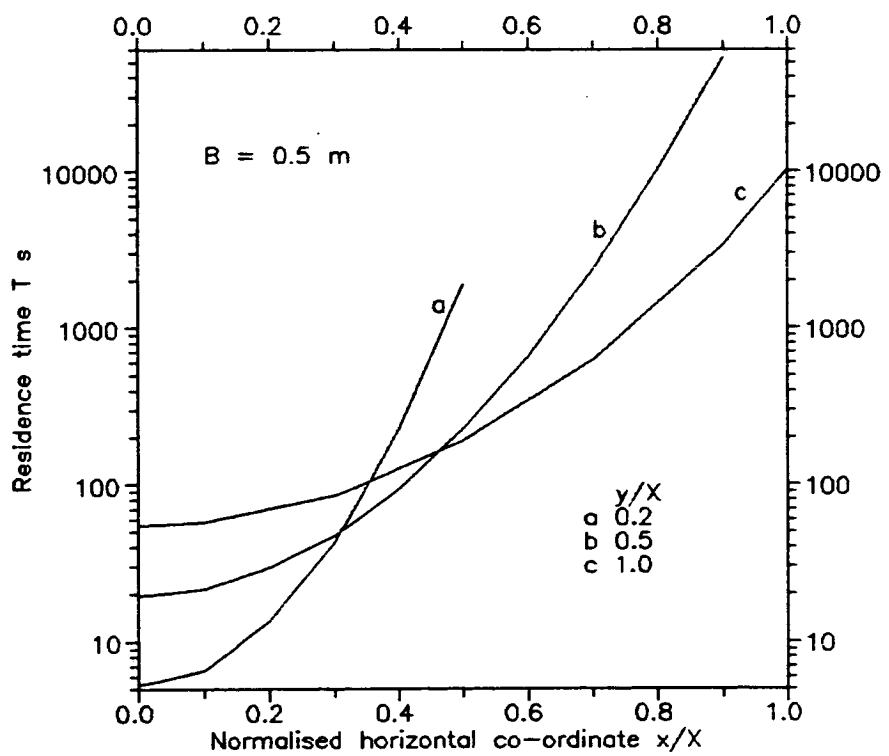

Fig. 5.7 Effect of initial position on residence time

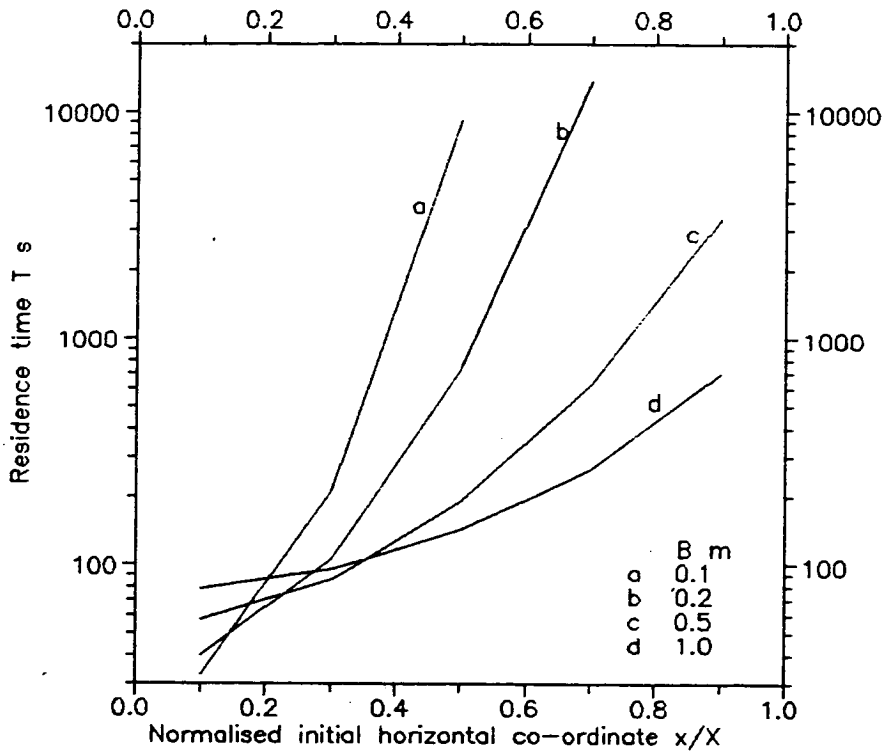

Fig. 5.8 Effect of kinematic parameter on residence time

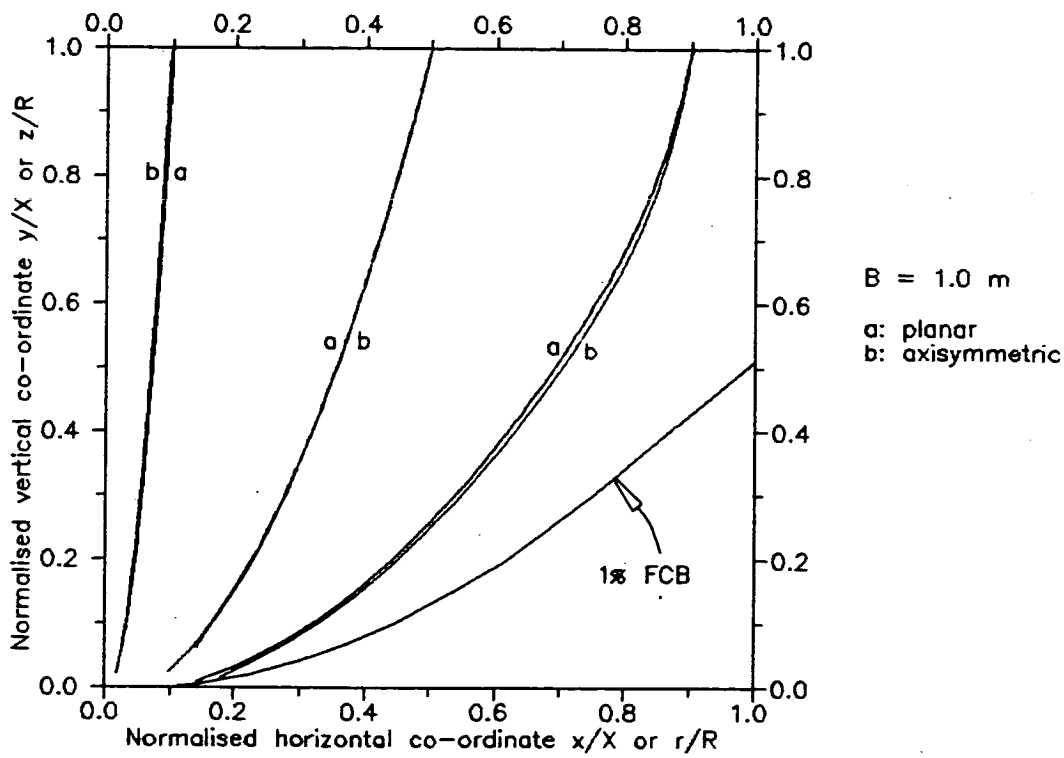

Fig. 5.9 Comparing trajectories in planar and axisymmetric geometries

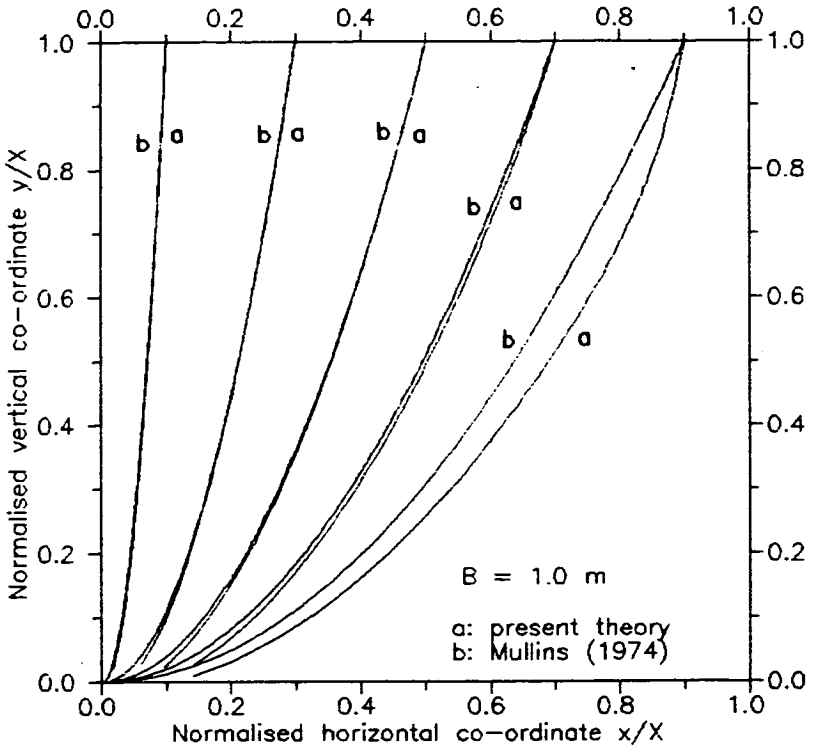

Fig. 5.10 Comparing trajectories of present theory with those of Mullins (1974)

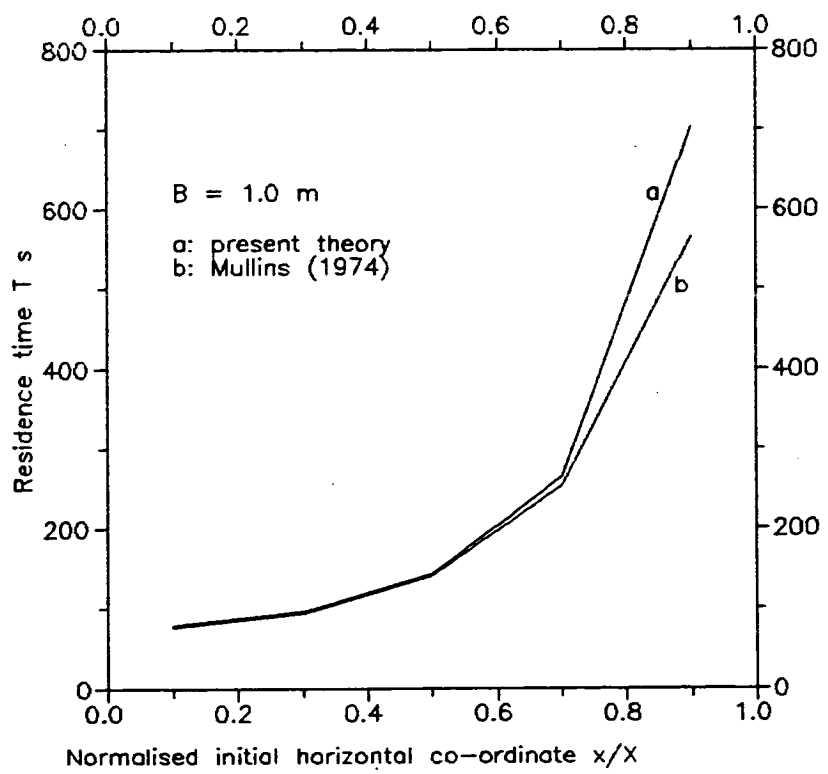

Fig. 5.11 Comparing residence times of present theory with those of Mullins (1974)

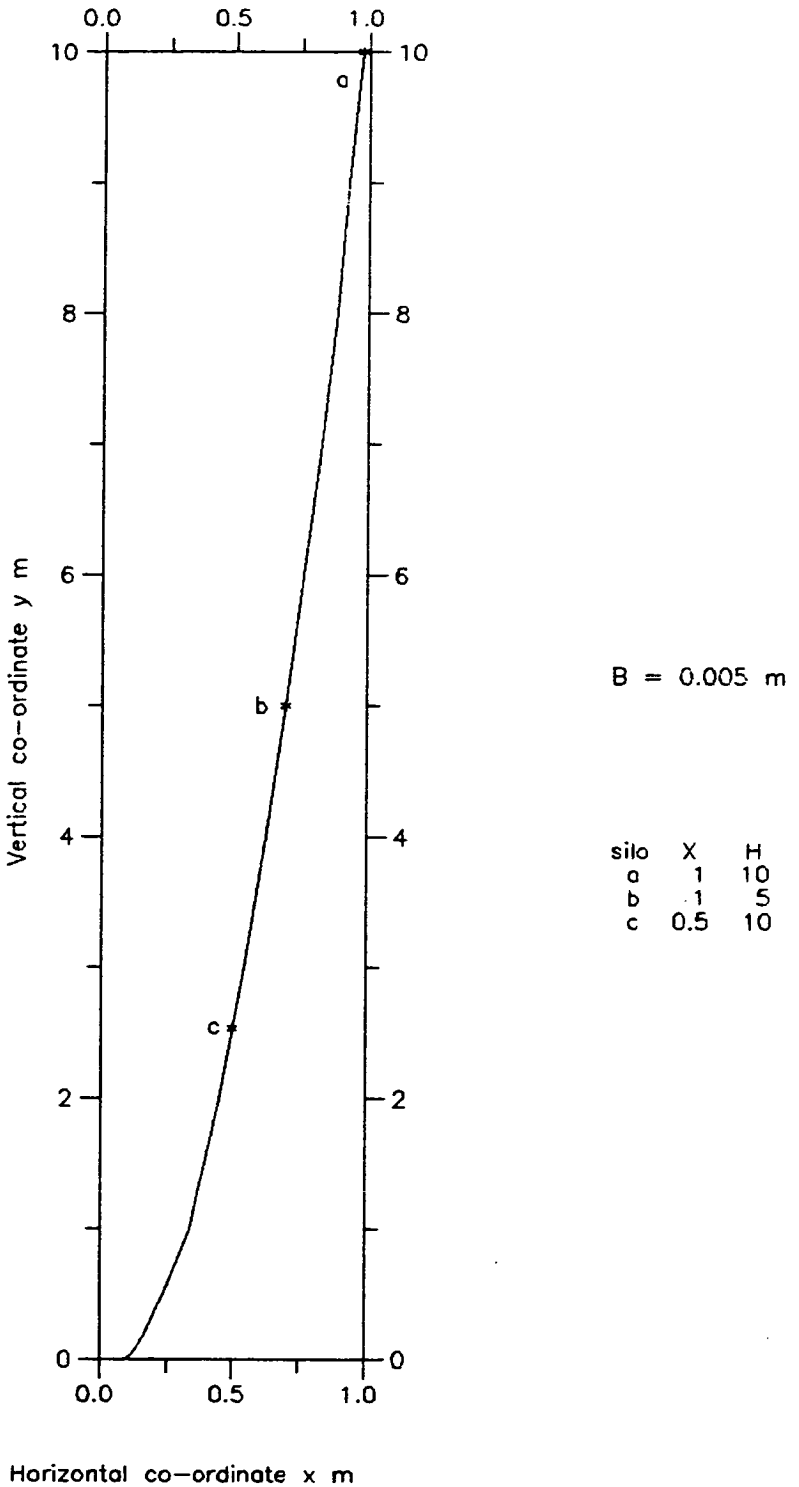

Fig. 5.12 Effect on the 1% FCB as the height and width of the silo are varied

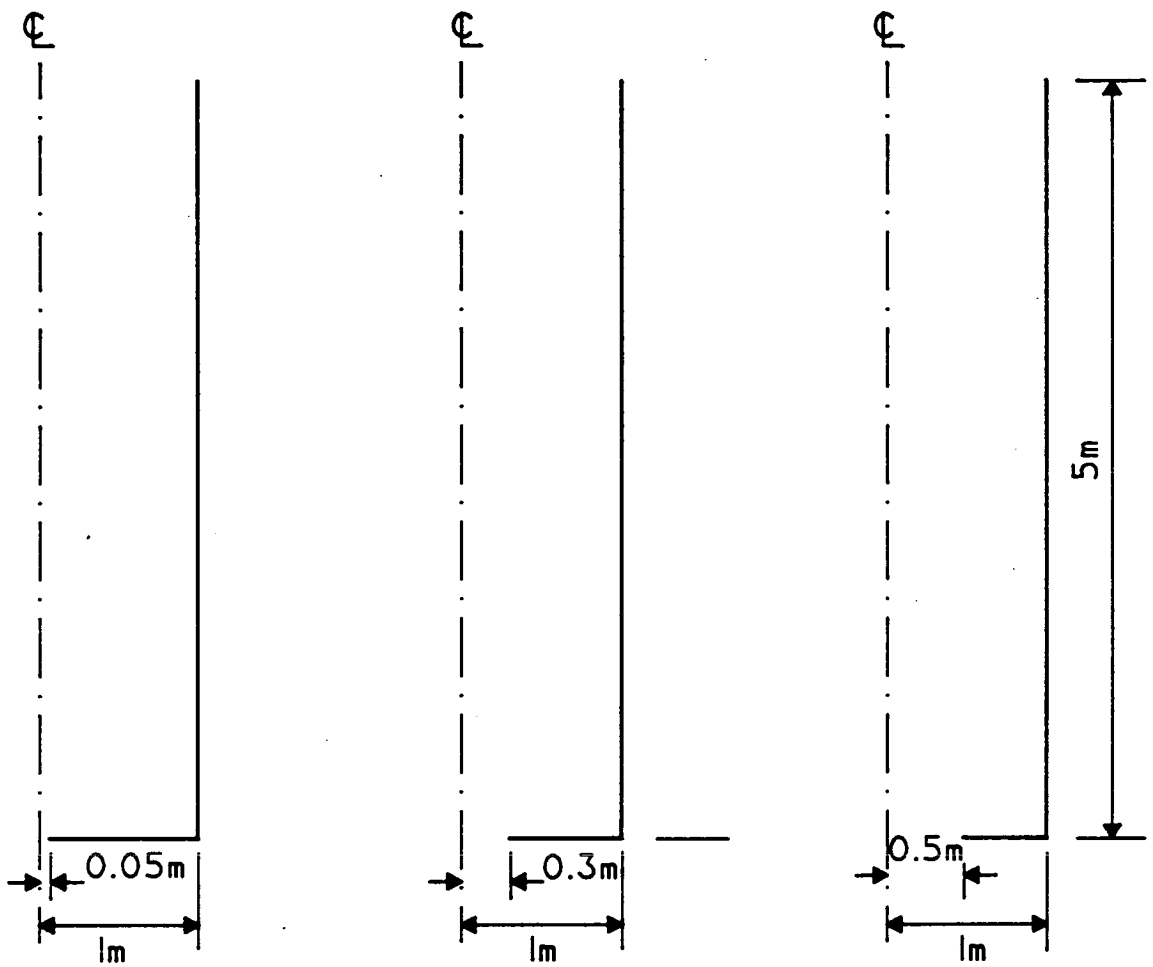

Fig. 5.13 Silos used to investigate changing orifice size

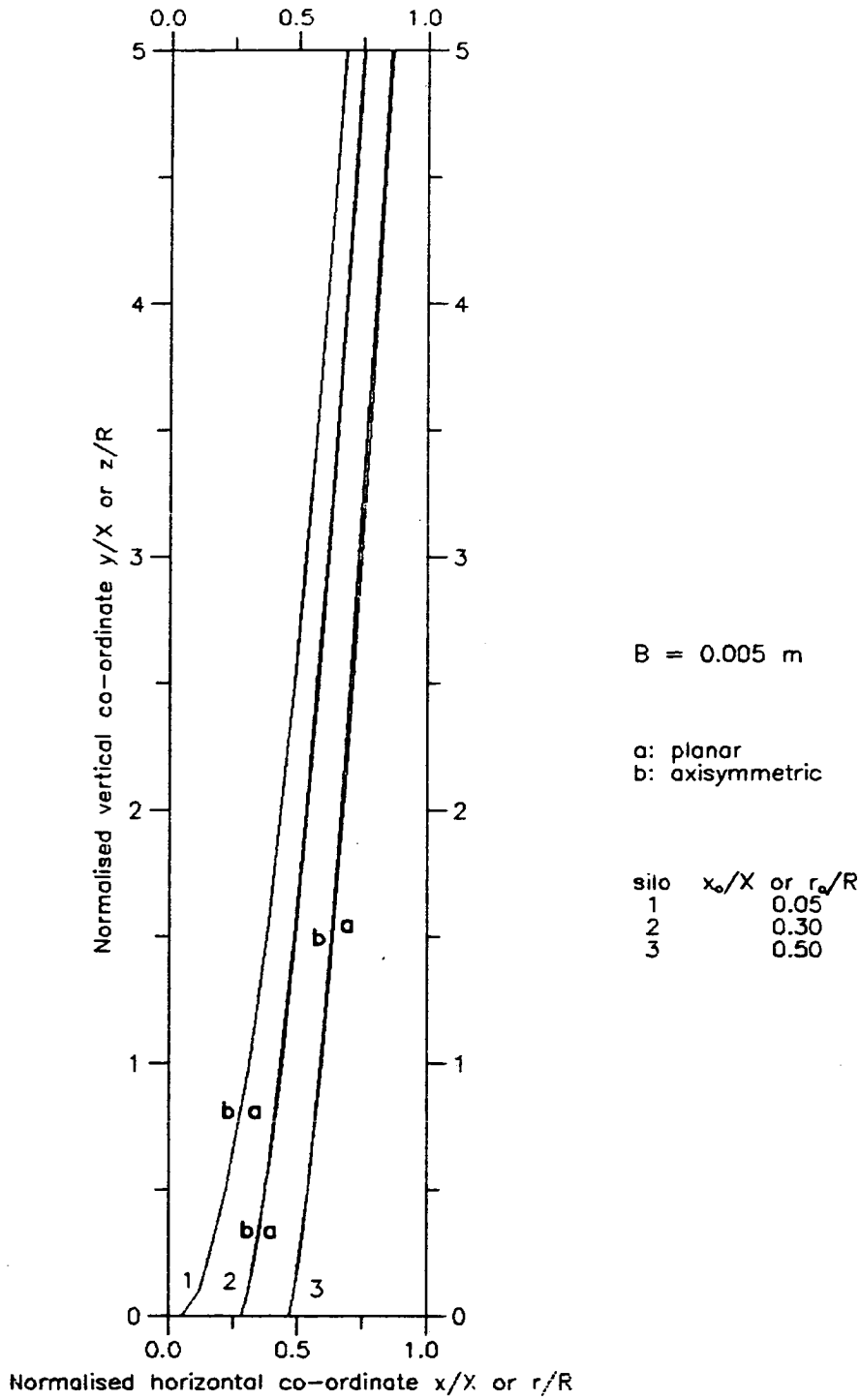

Fig. 5.14 1% FCBs for different orifice sizes

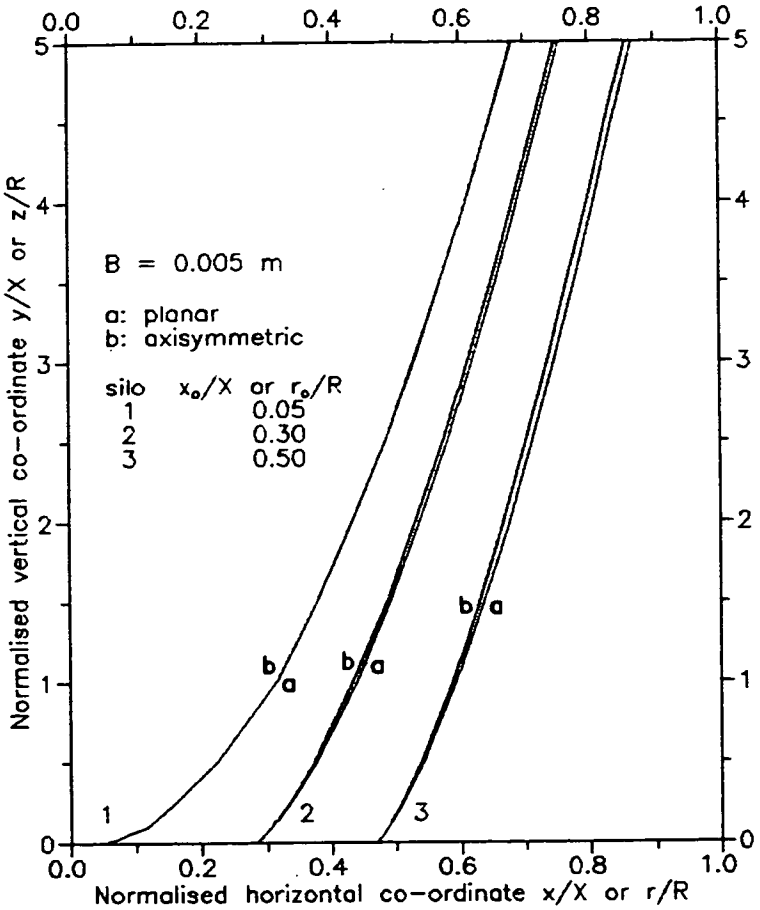

Fig. 5.15 1% FCBs for different orifice sizes (enlarged section)

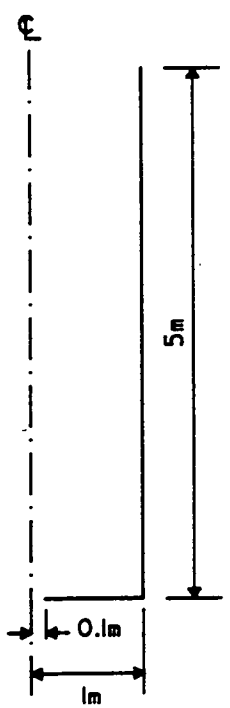

Fig. 5.16 Silo used for scaling

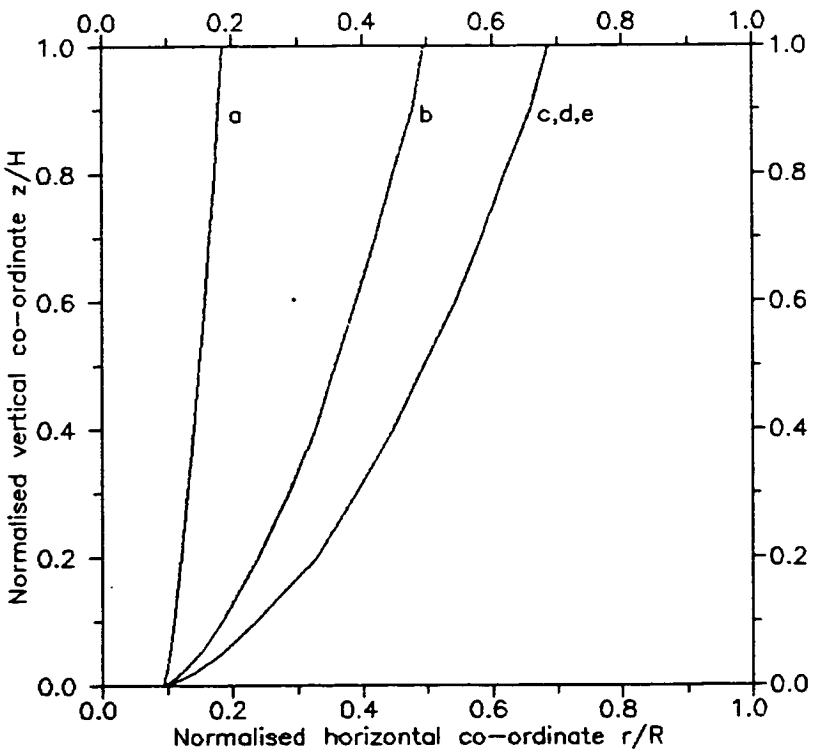

silo	R	H	B	BH/R^2
a:	20	100	0.005	0.00125
b:	2	10	0.005	0.01250
c:	1	5	0.005	0.02500
d:	2	10	0.010	0.02500
e:	20	100	0.100	0.02500

Fig. 5.17 1% FCBs for scaled silos

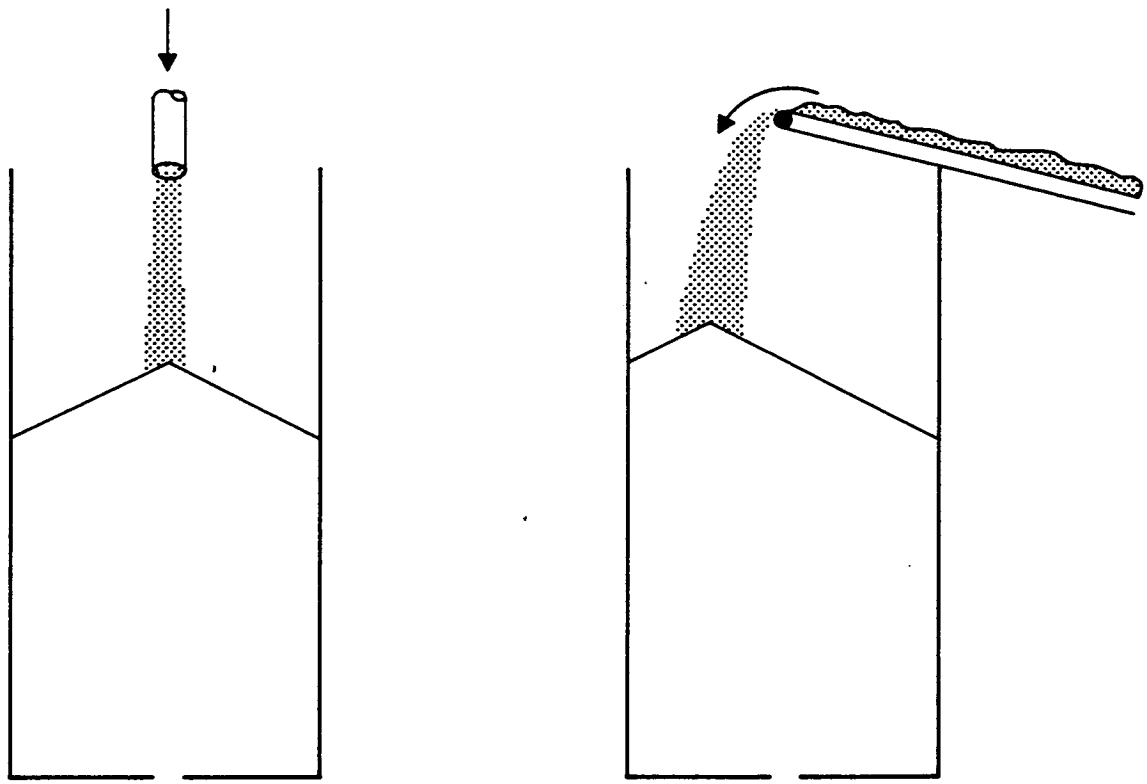

(a) concentric filling

(b) eccentric filling

Fig. 5.18 Filling techniques modelled

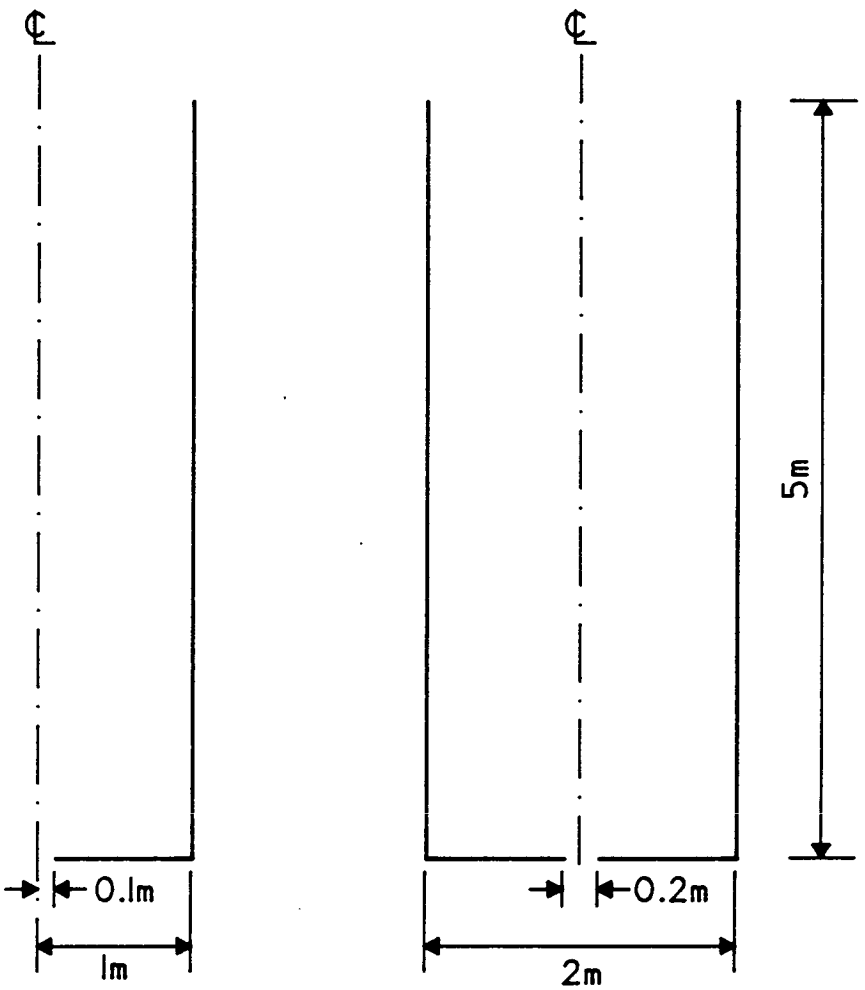

(a) concentric filling (b) eccentric filling

Fig. 5.19 Silos used to model filling techniques

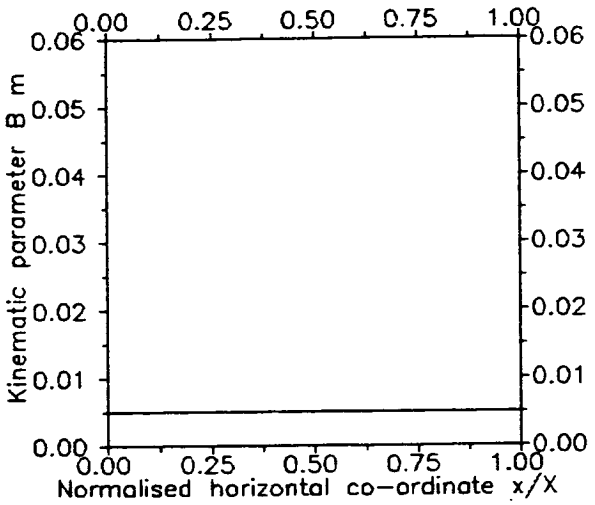

Case (a)

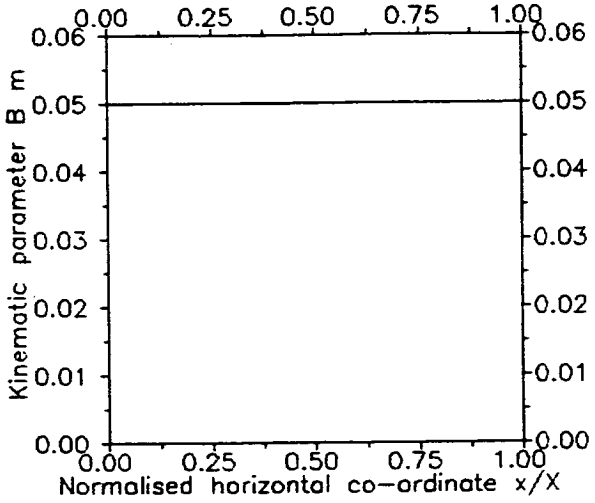

Case (b)

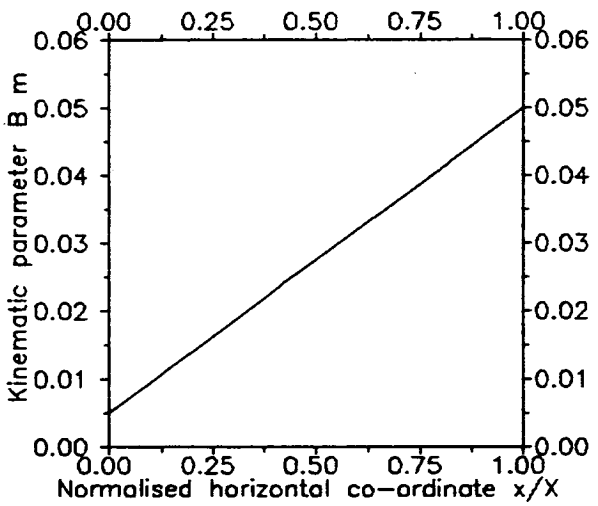

Case (c)

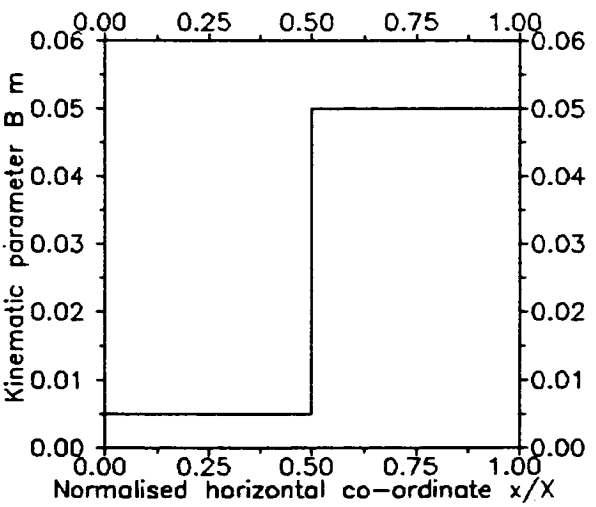

Case (d)

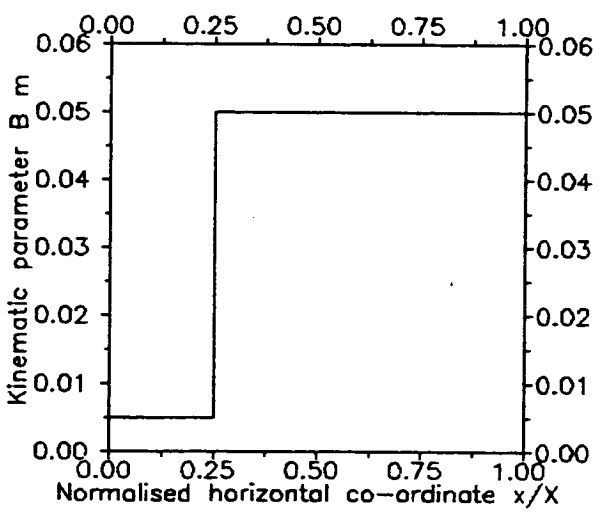

Case (e)

Fig. 5.20 Kinematic parameters used

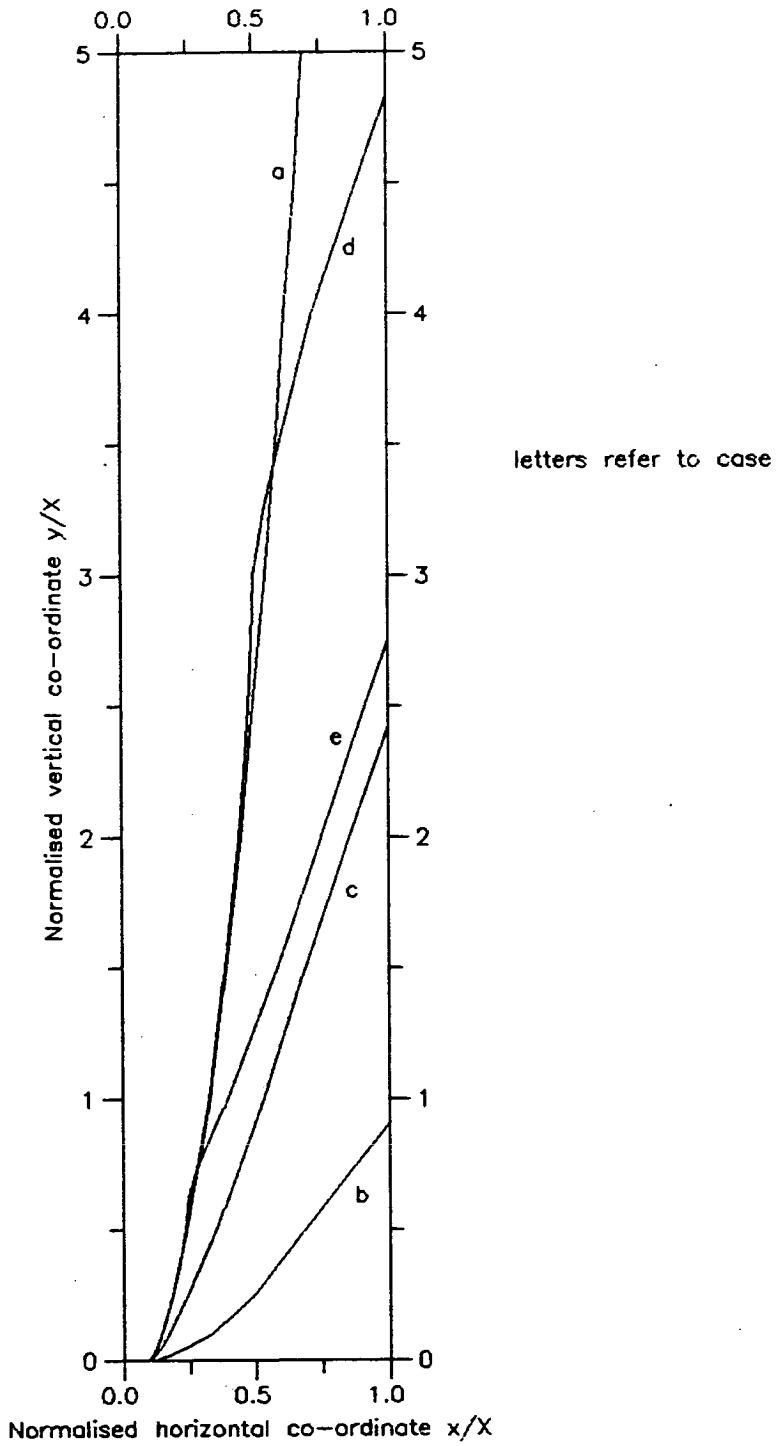

Fig. 5.21 1% FCBs for different kinematic parameters

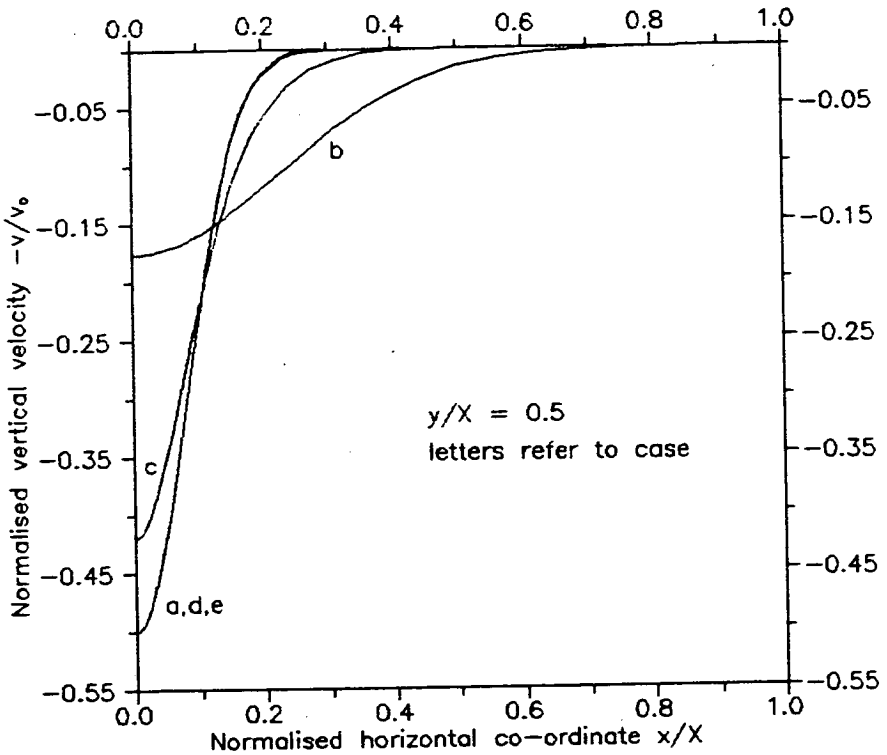

Fig. 5.22 Horizontal profiles of vertical velocity

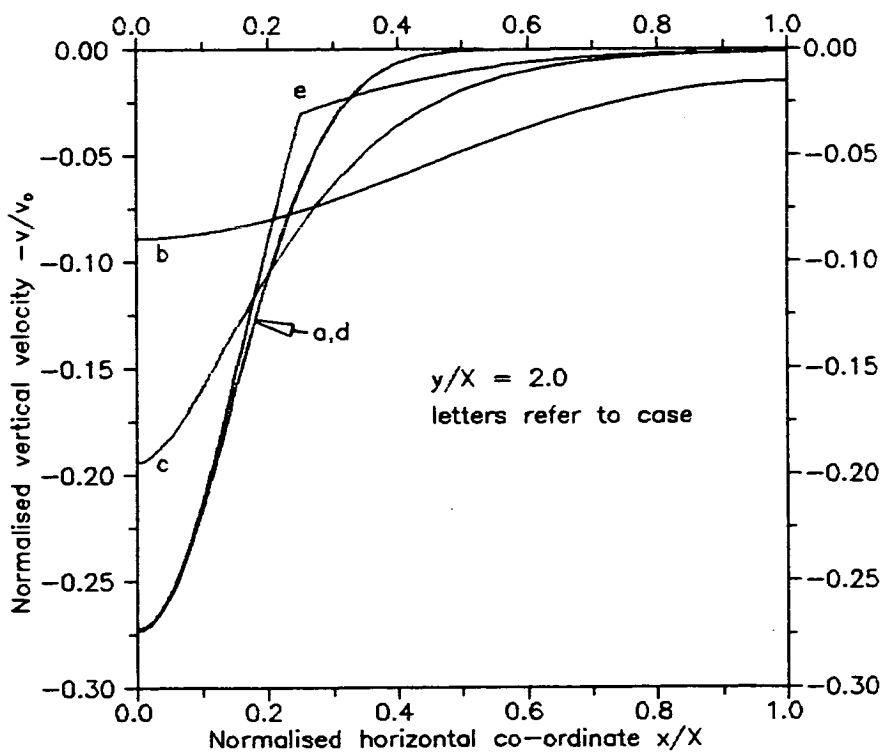

Fig. 5.23 Horizontal profiles of vertical velocity

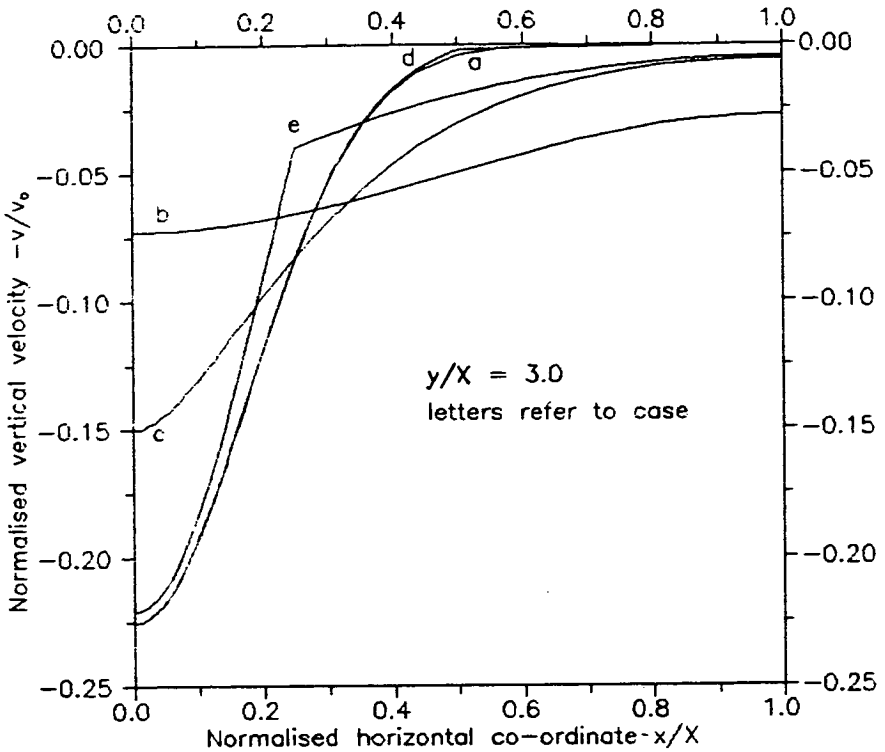

Fig. 5.24 Horizontal profiles of vertical velocity

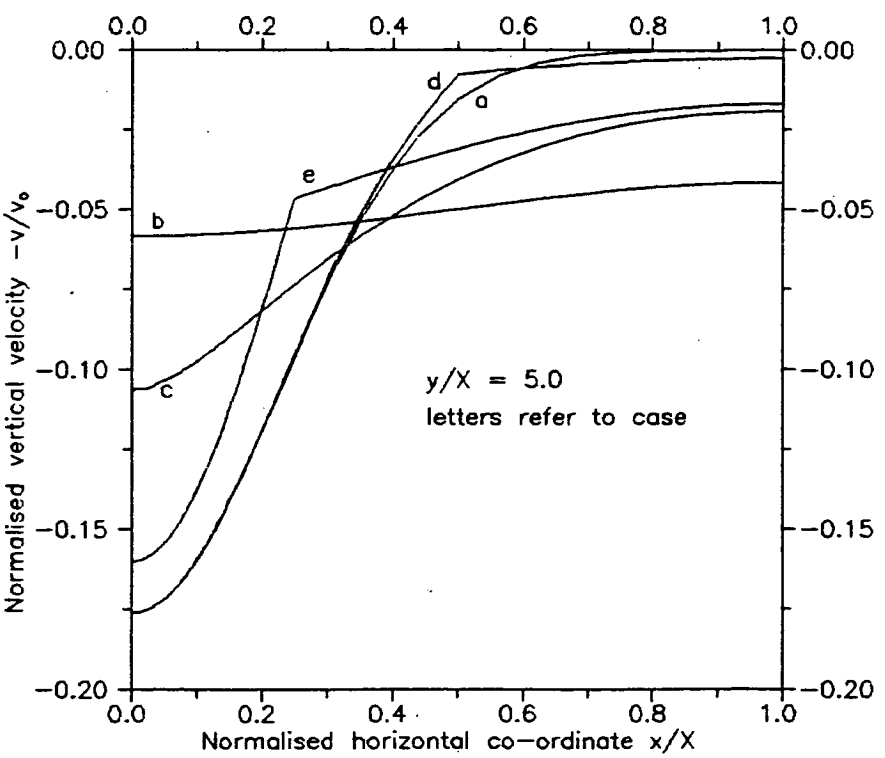

Fig. 5.25 Horizontal profiles of vertical velocity

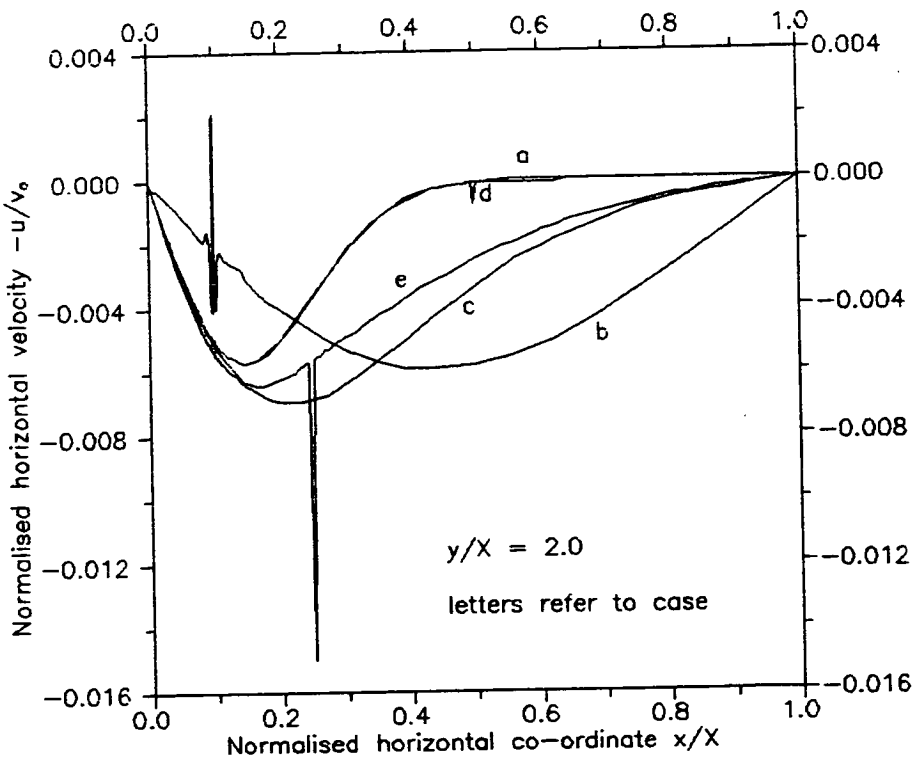

Fig. 5.26 Horizontal profiles of horizontal velocity

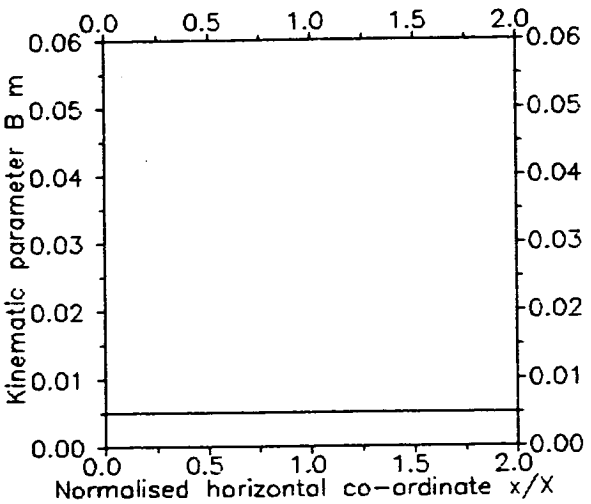

Case (a)

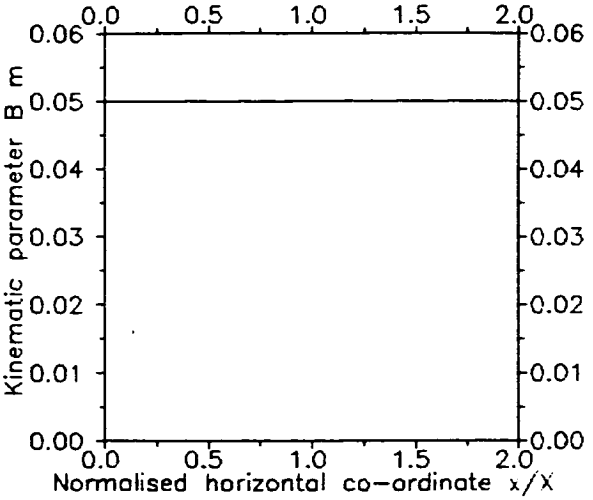

Case (b)

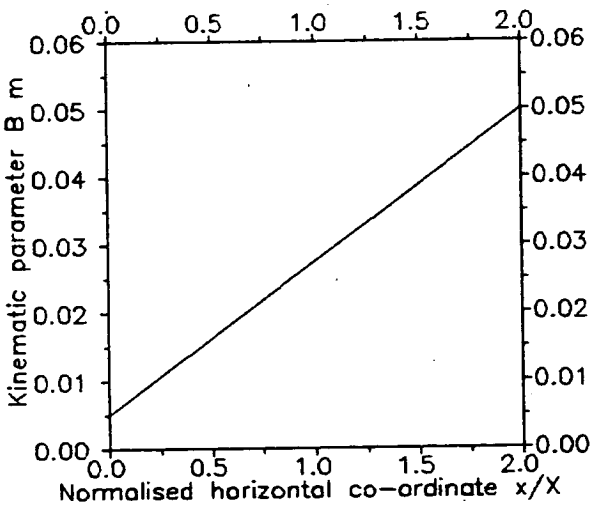

Case (c)

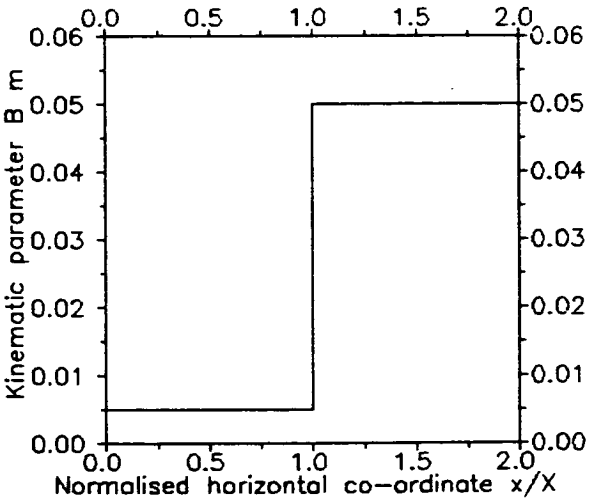

Case (d)

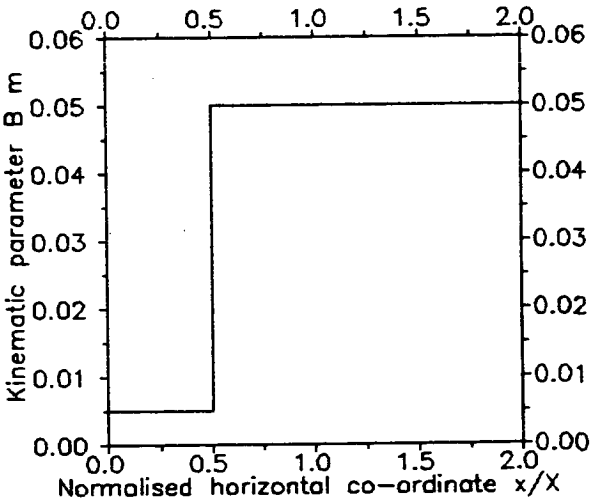

Case (e)

Fig. 5.27 Different kinematic parameters used

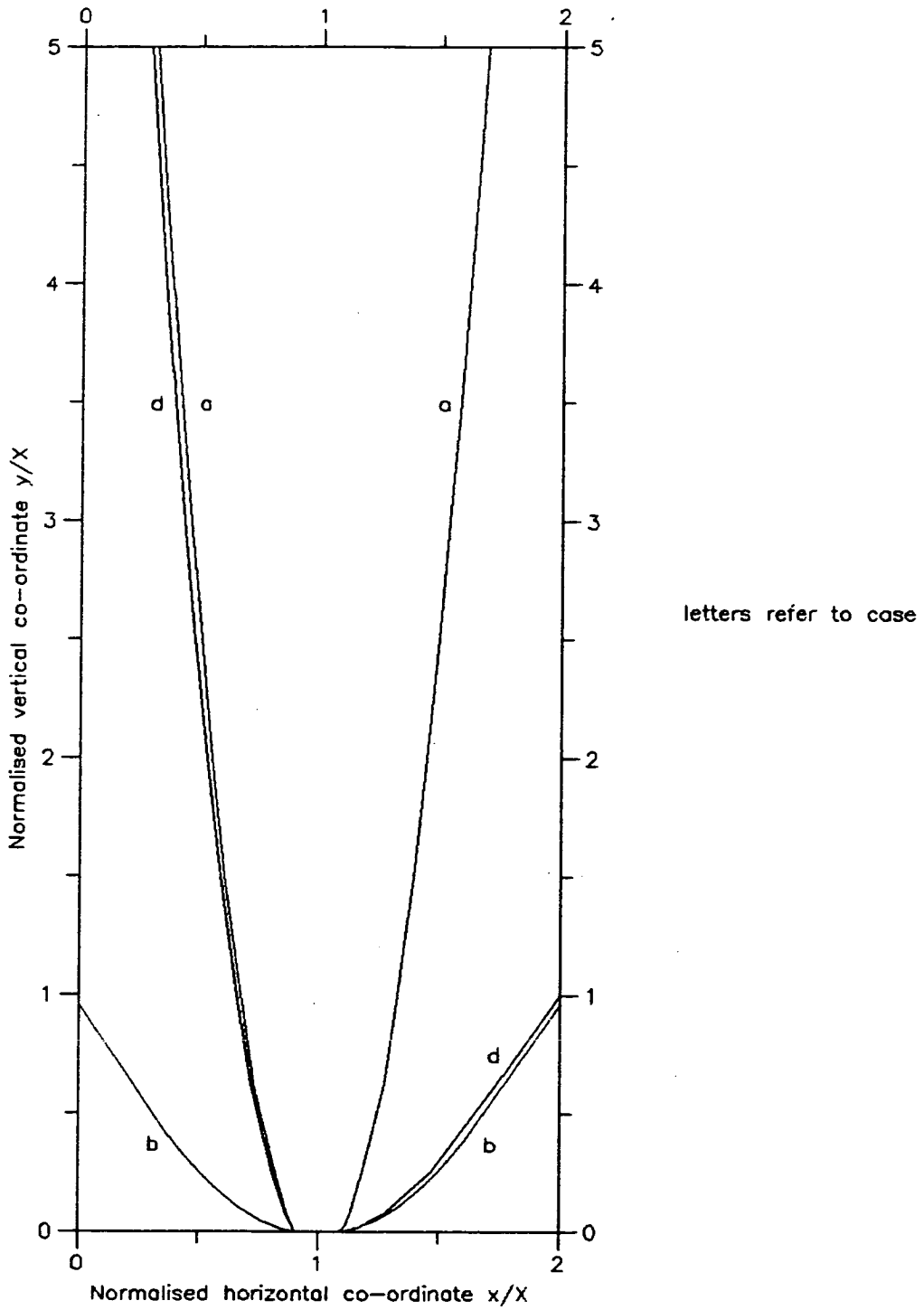

Fig. 5.28 1% FCBs for Cases (a), (b) and (d)

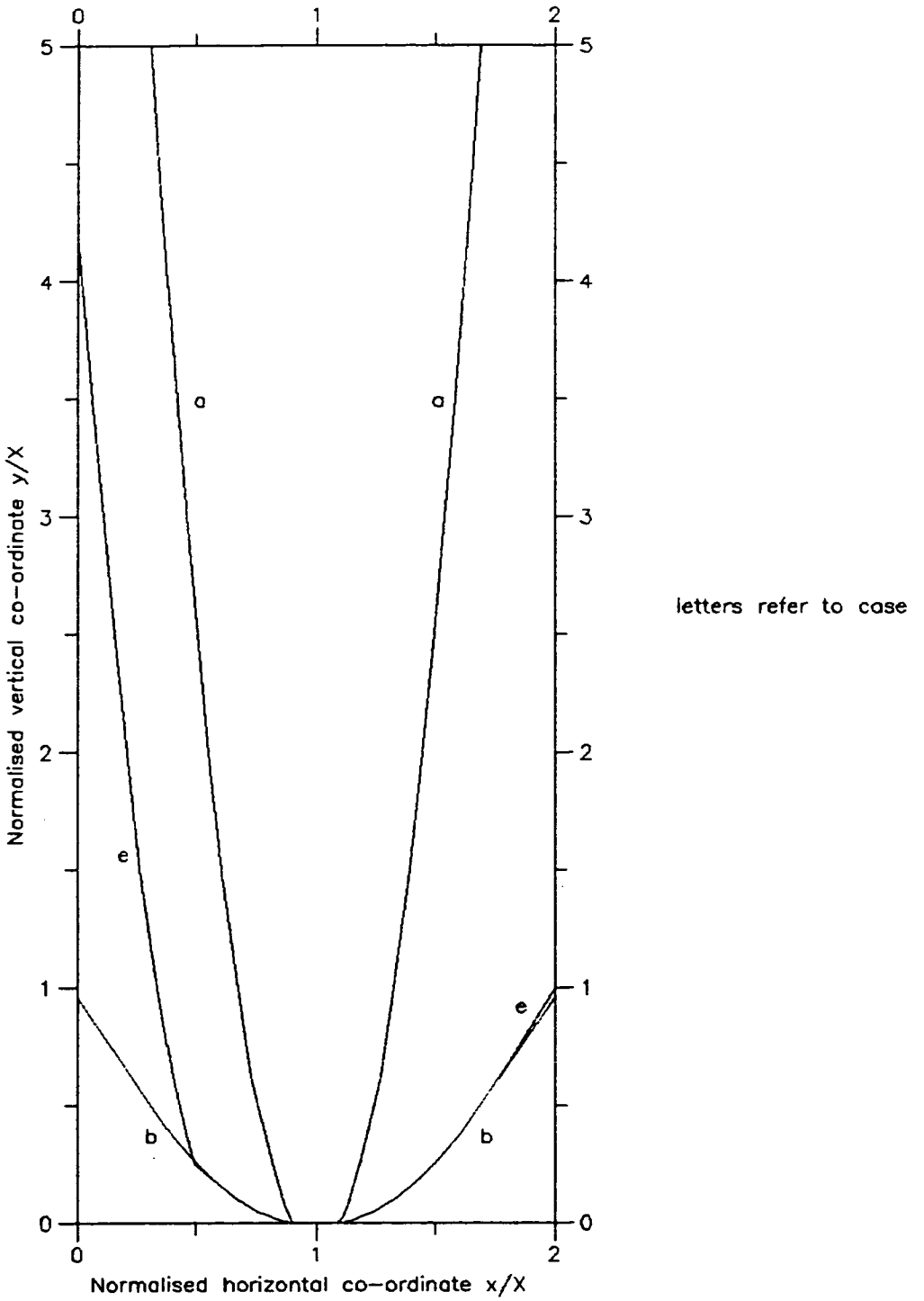

Fig. 5.29 1% FCBs for Cases (a), (b) and (e)

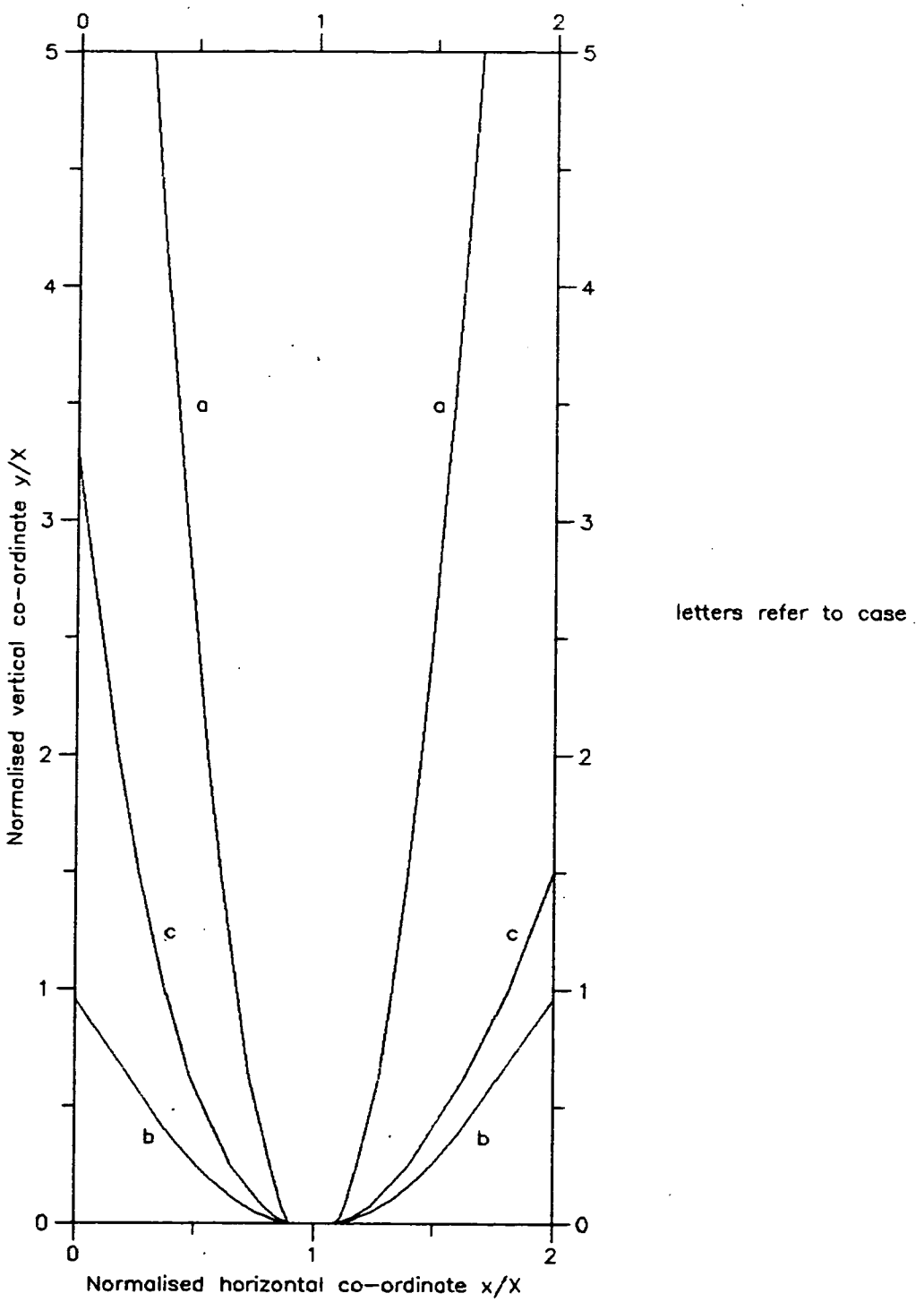

Fig. 5.30 1% FCBs for Cases (a), (b) and (c)

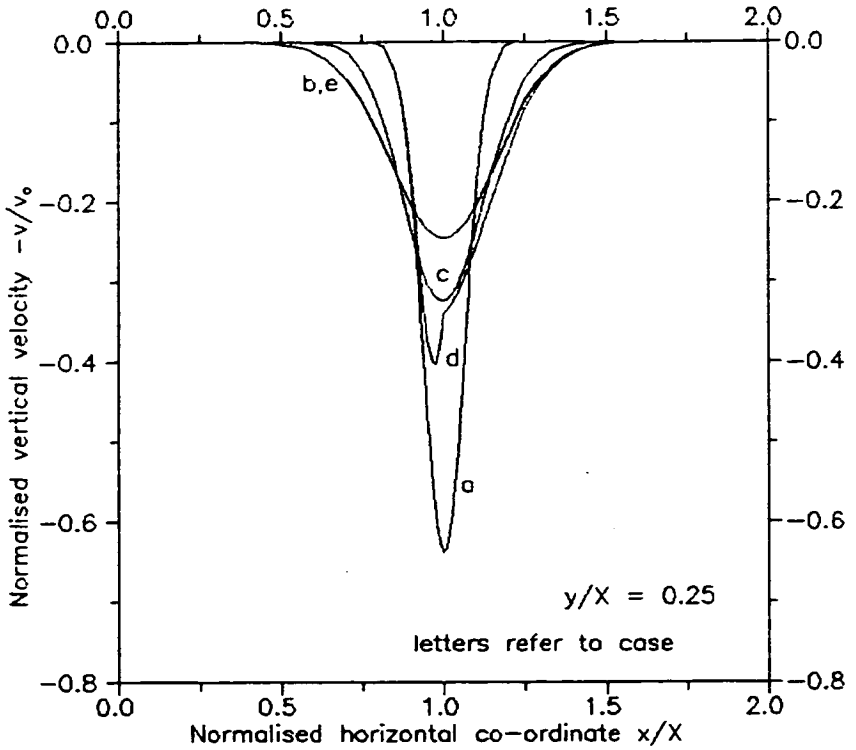

Fig. 5.31 Horizontal profiles of vertical velocity

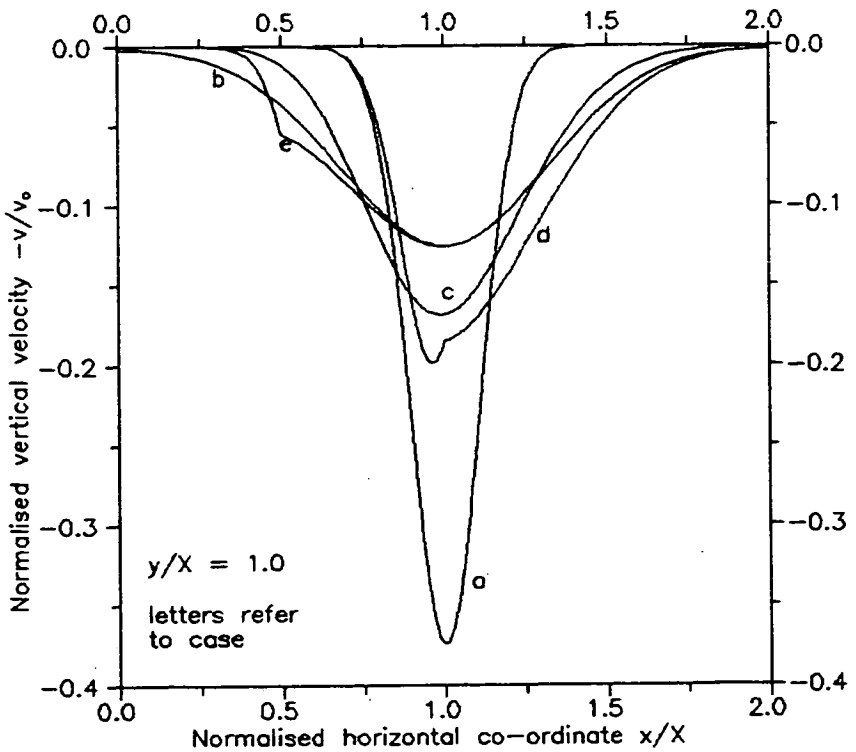

Fig. 5.32 Horizontal profiles of vertical velocity

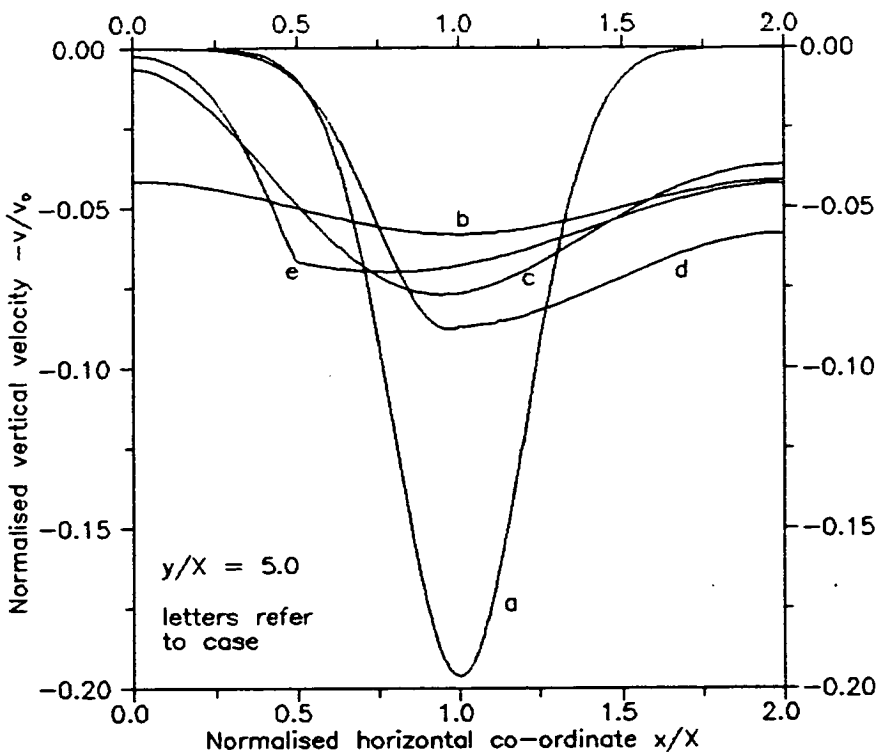

Fig. 5.33 Horizontal profiles of vertical velocity

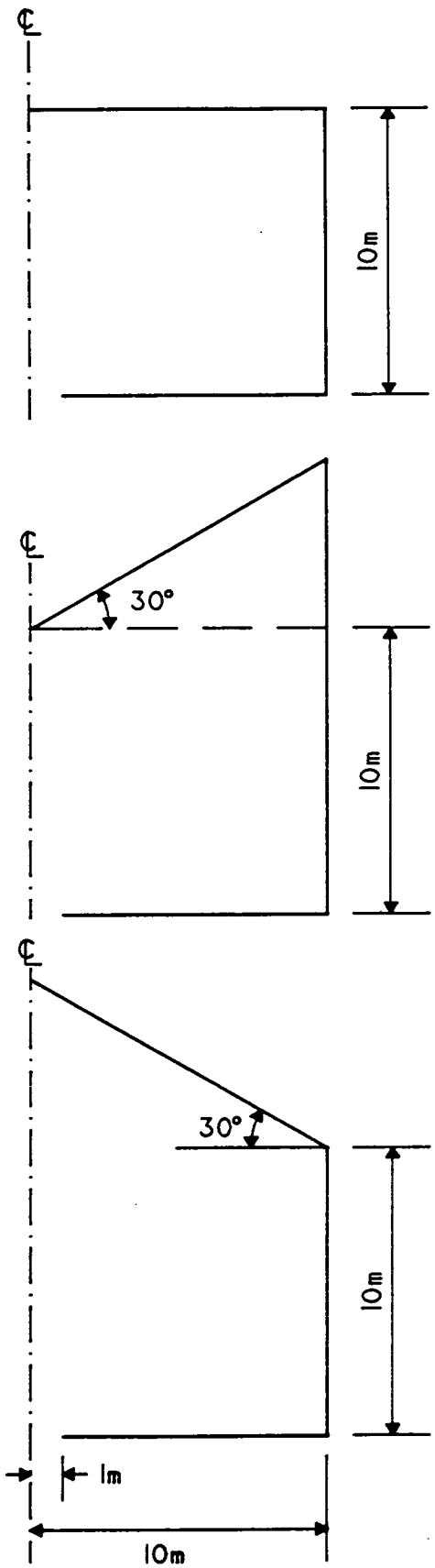

Fig. 5.34 Silos used to model top surface displacement

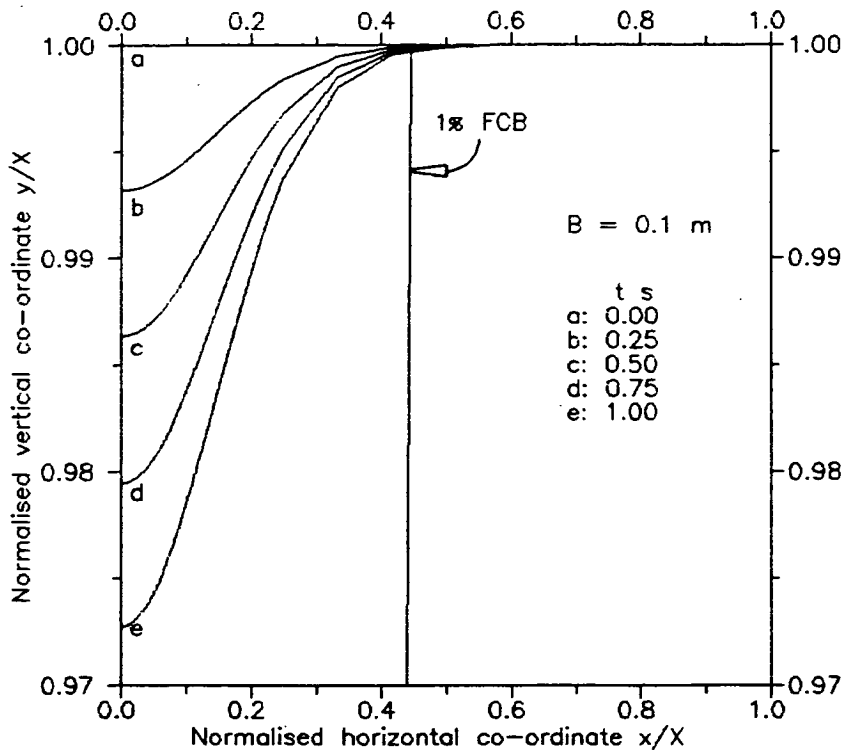

Fig. 5.35 Displacement of top surface in planar geometry

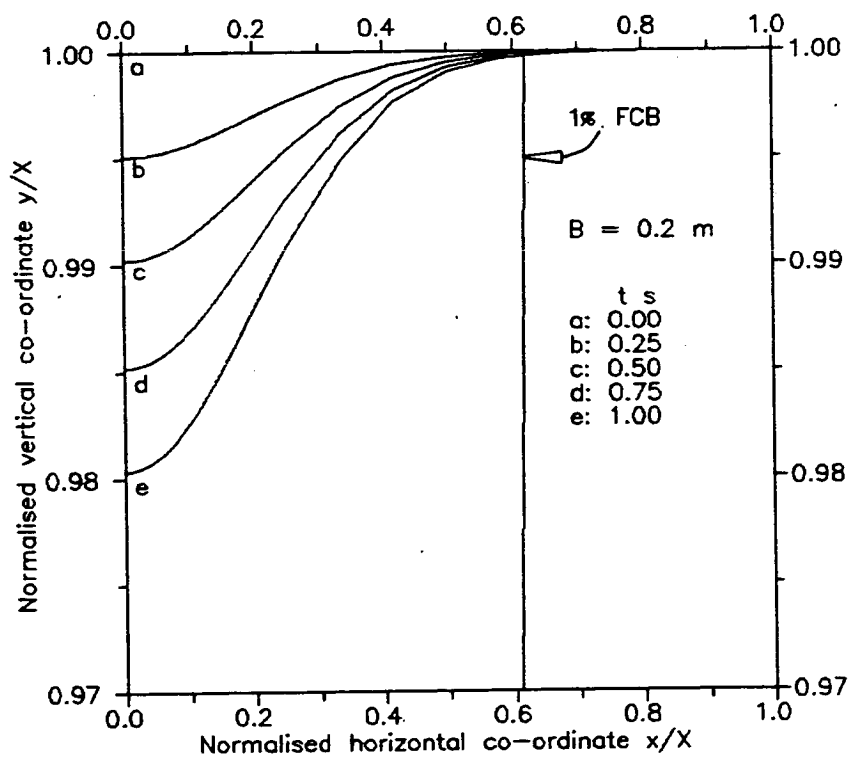

Fig. 5.36 Displacement of top surface in planar geometry

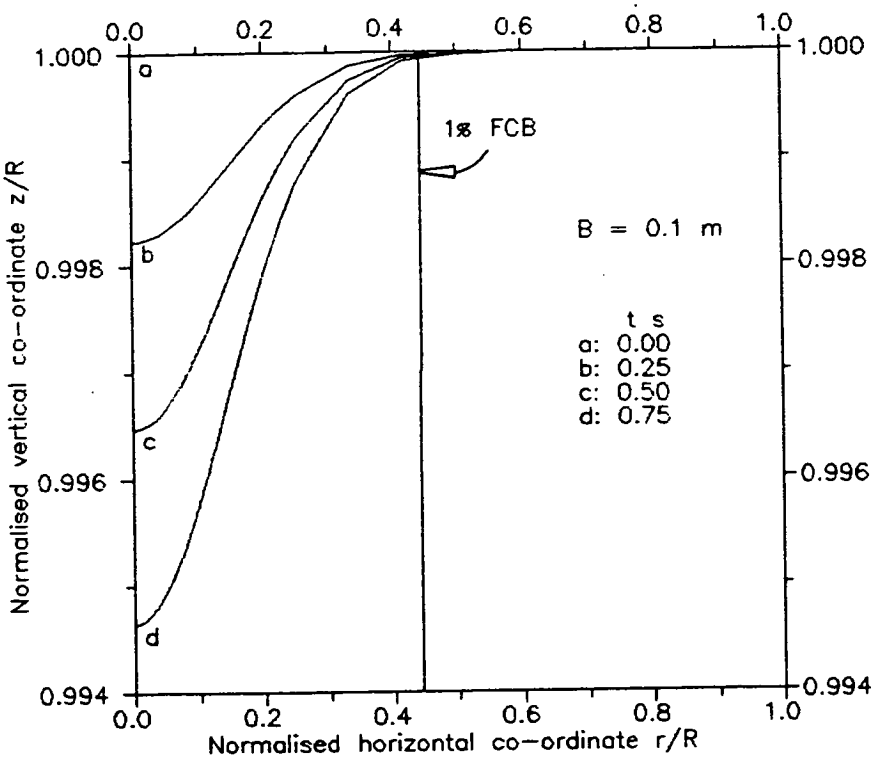

Fig. 5.37 Displacement of top surface in axisymmetric geometry

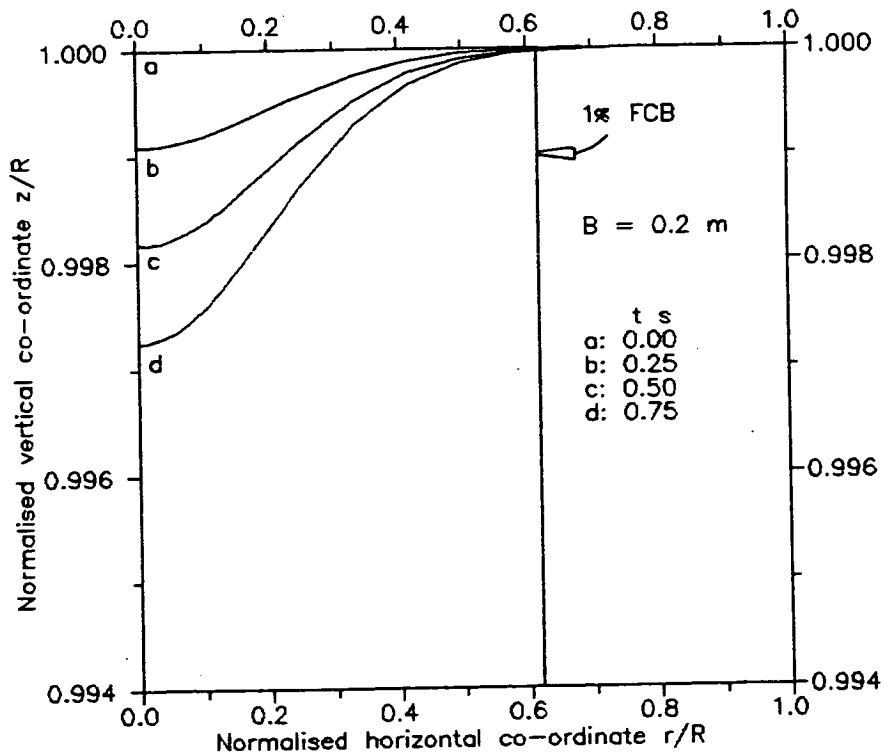

Fig. 5.38 Displacement of top surface in axisymmetric geometry

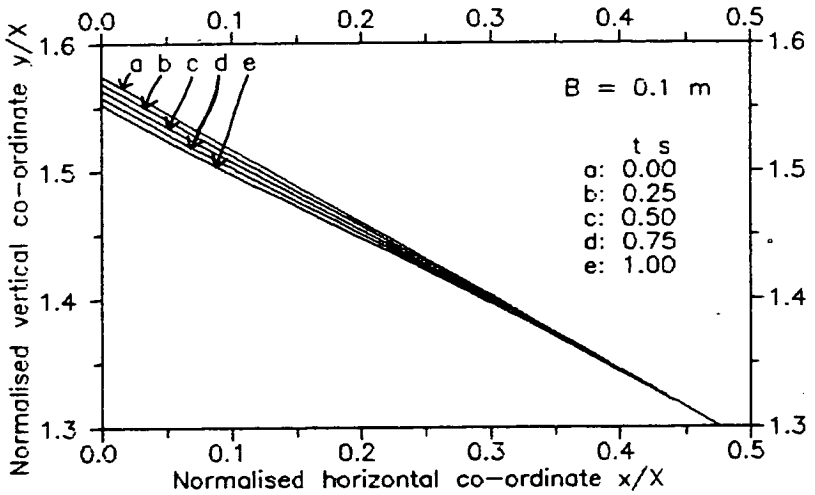

Fig. 5.39 Displacement of top surface in planar geometry

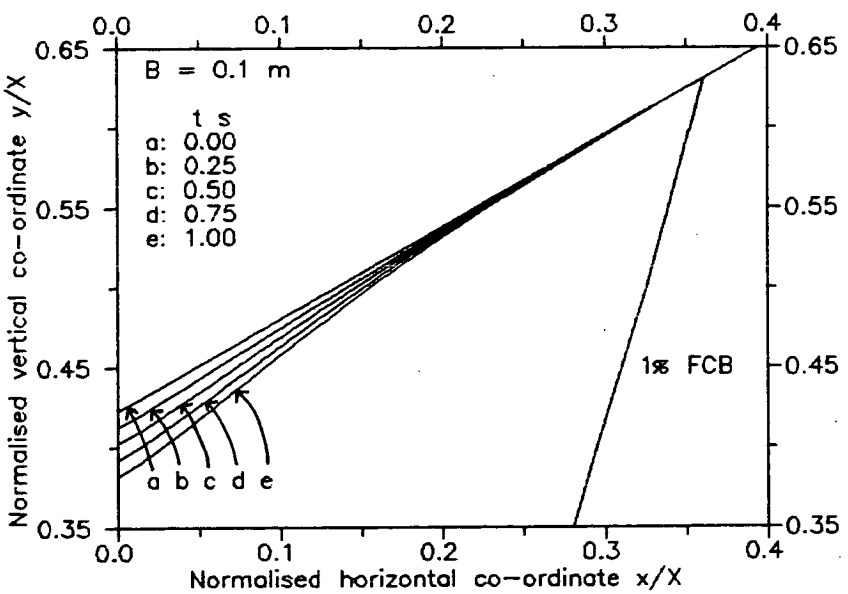

Fig. 5.40 Displacement of top surface in planar geometry

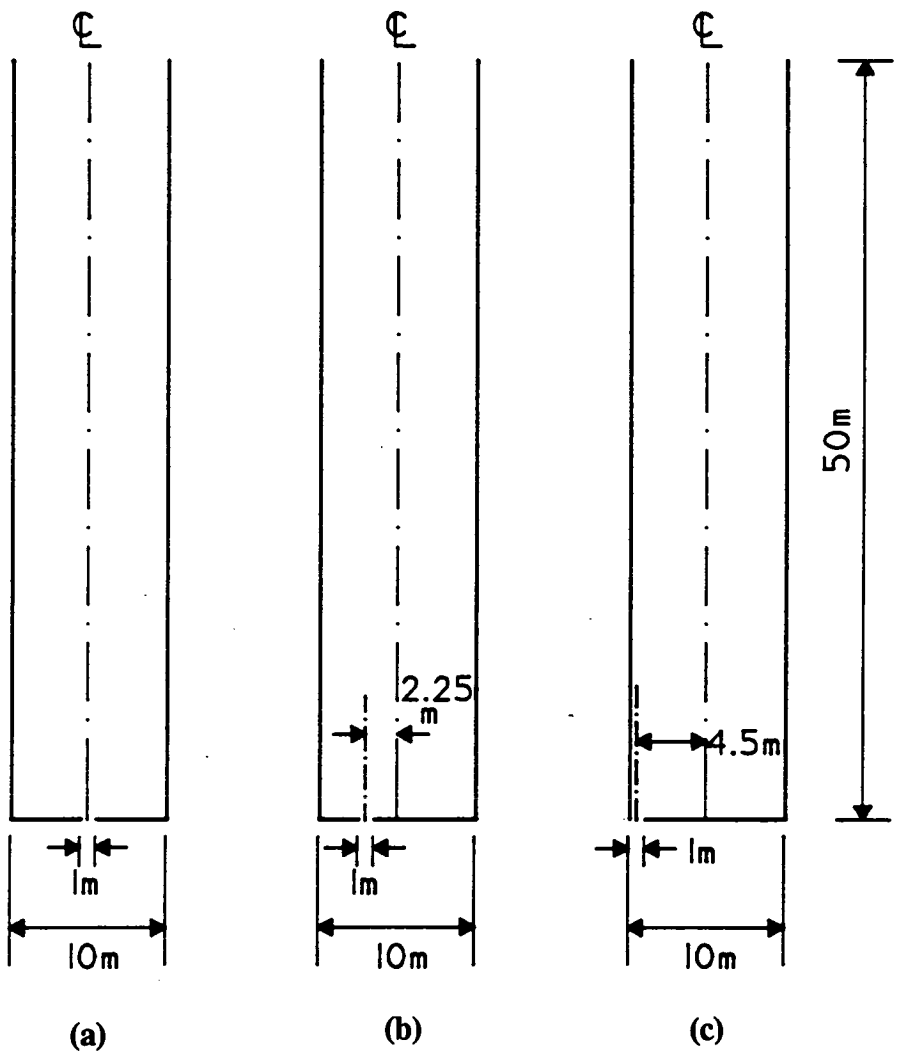

Fig. 5.41 Silos used to model eccentric discharge

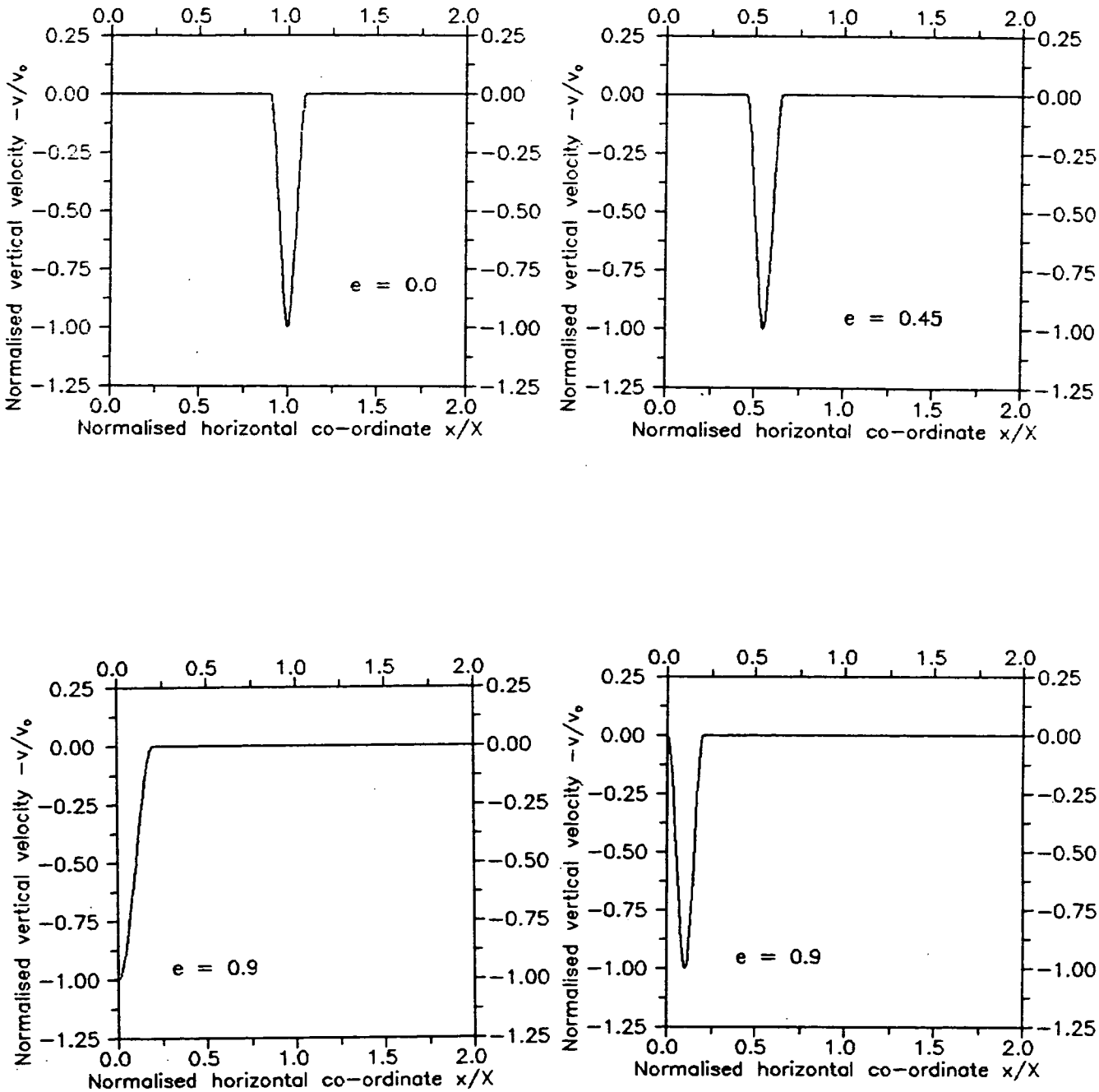

Fig. 5.42 Prescribed exit velocity distributions

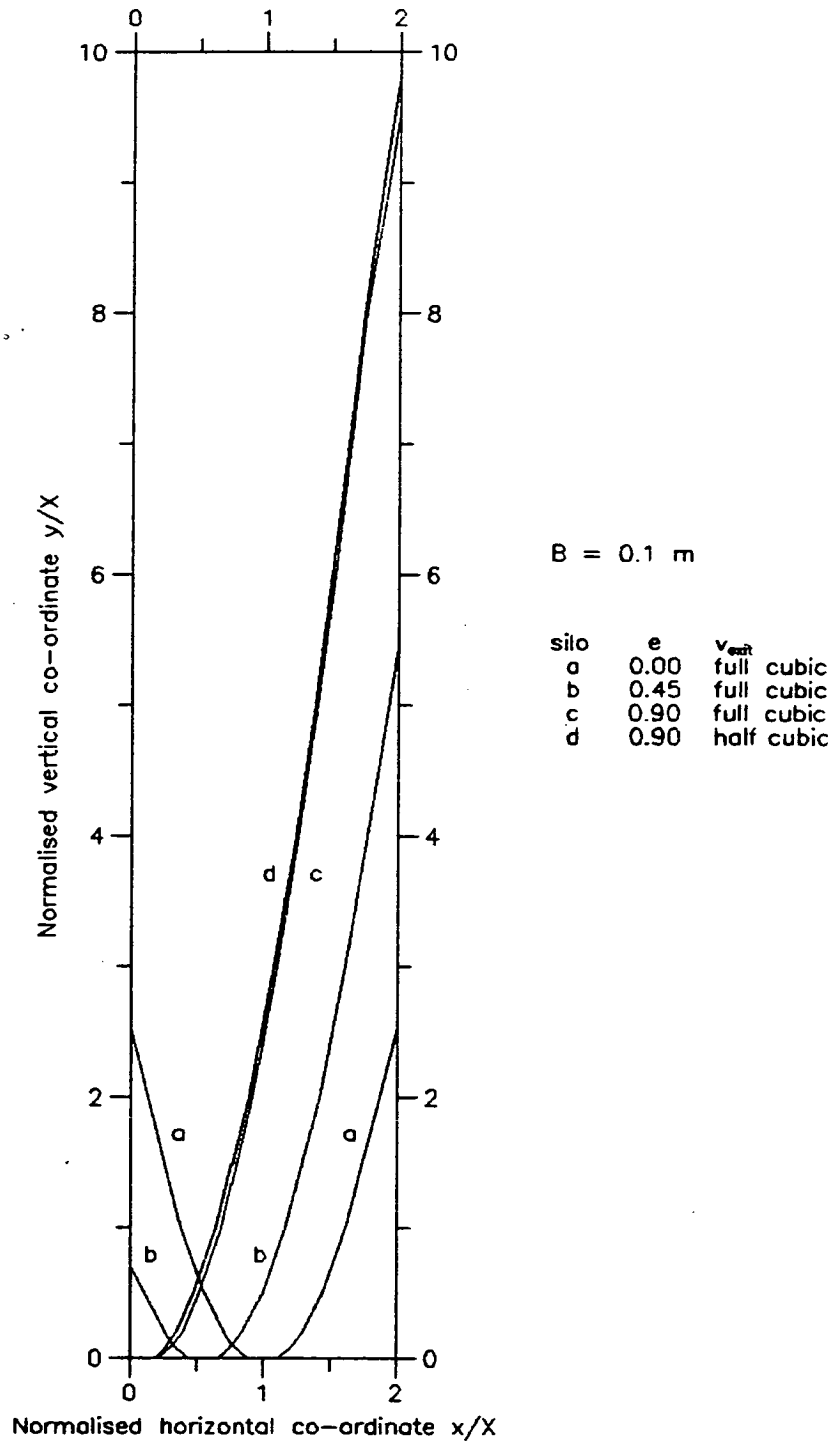

Fig. 5.43 1% FCBs for eccentrically-discharging silos

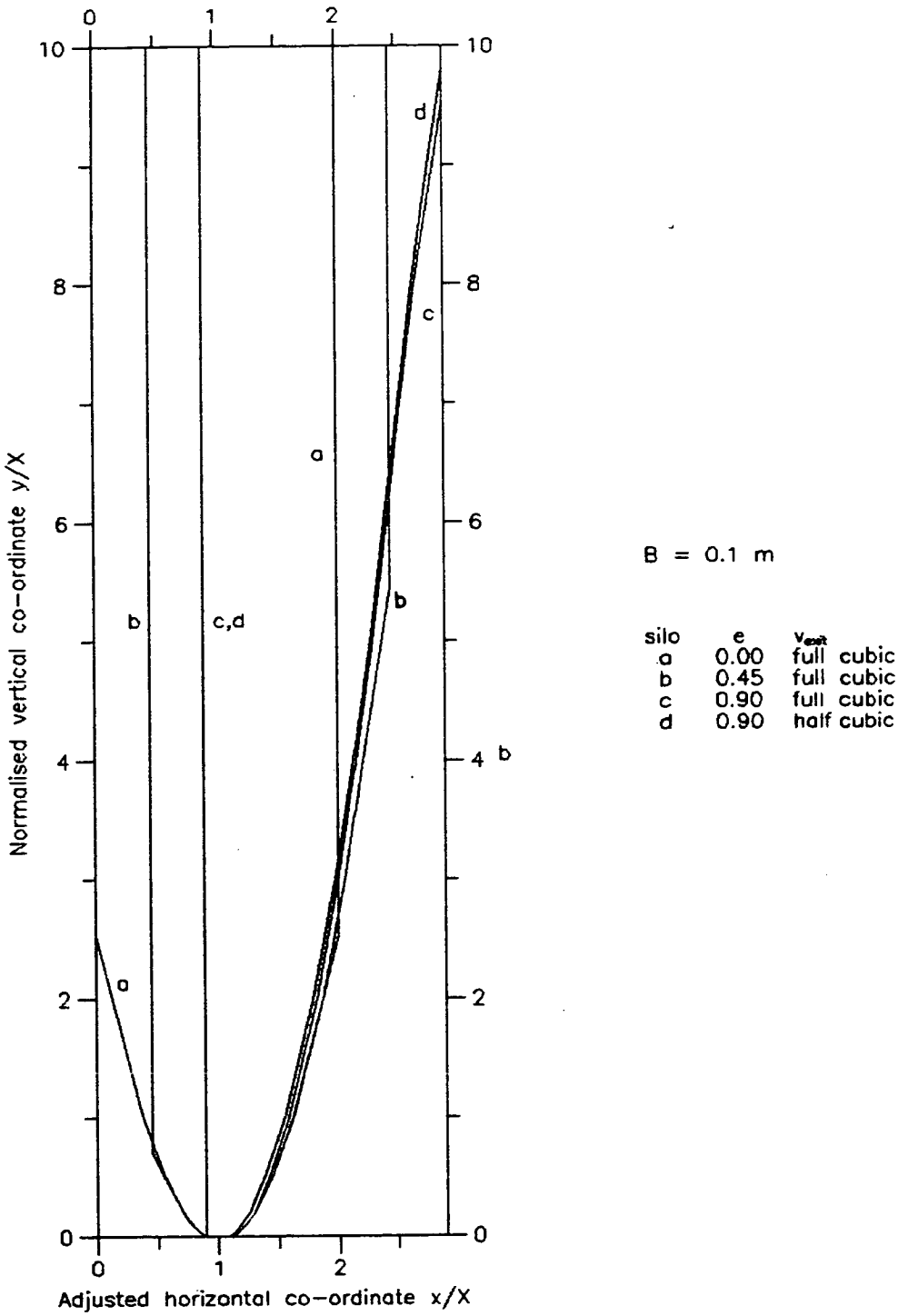

Fig. 5.44 Transposed 1% FCBs for eccentrically-discharging silos

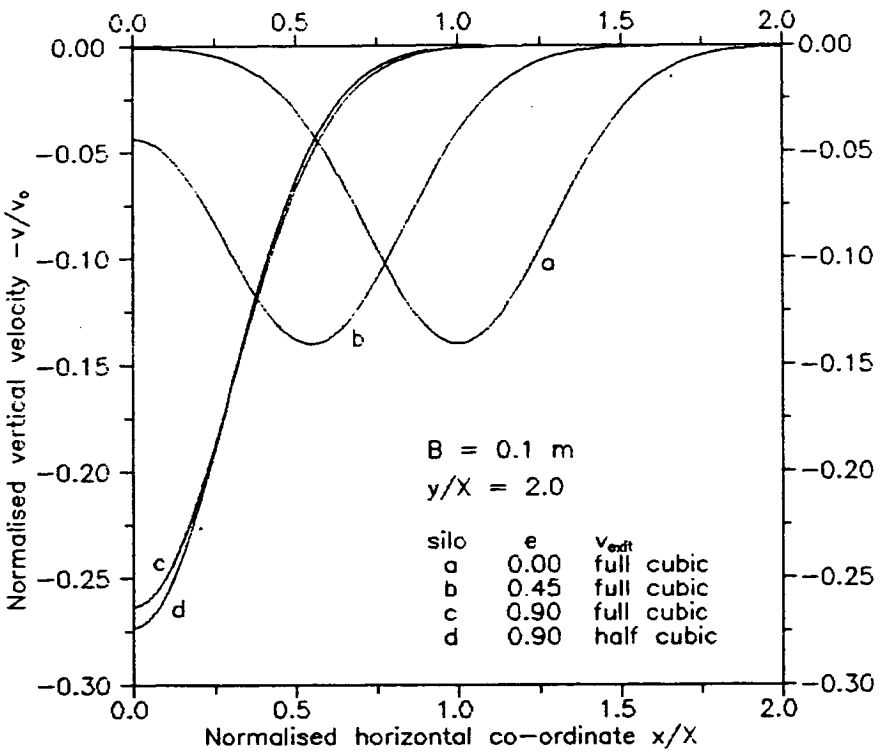

Fig. 5.45 Horizontal profiles of vertical velocity

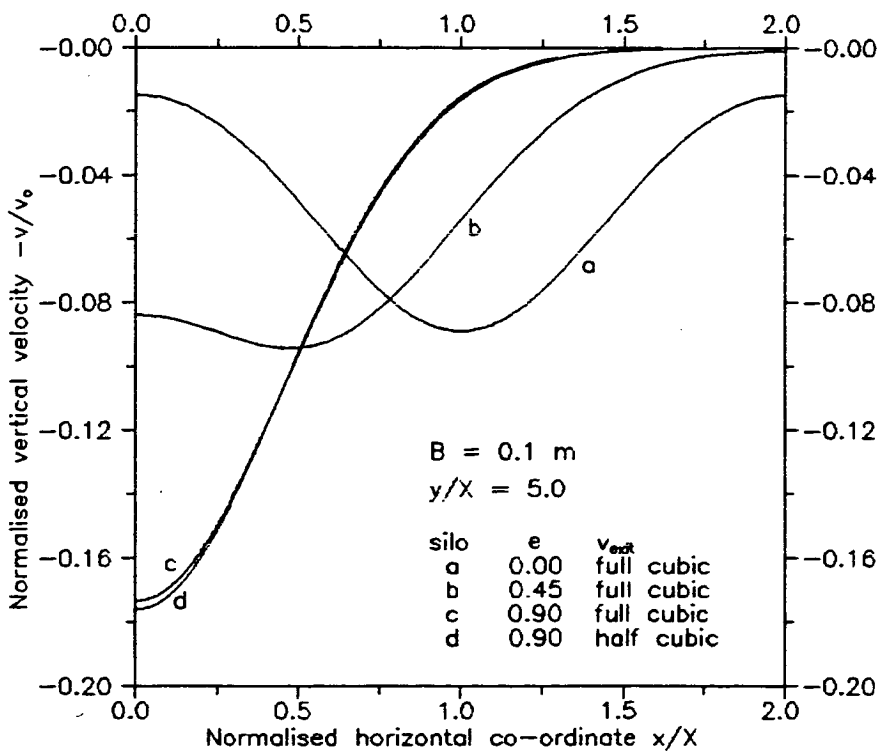

Fig. 5.46 Horizontal profiles of vertical velocity

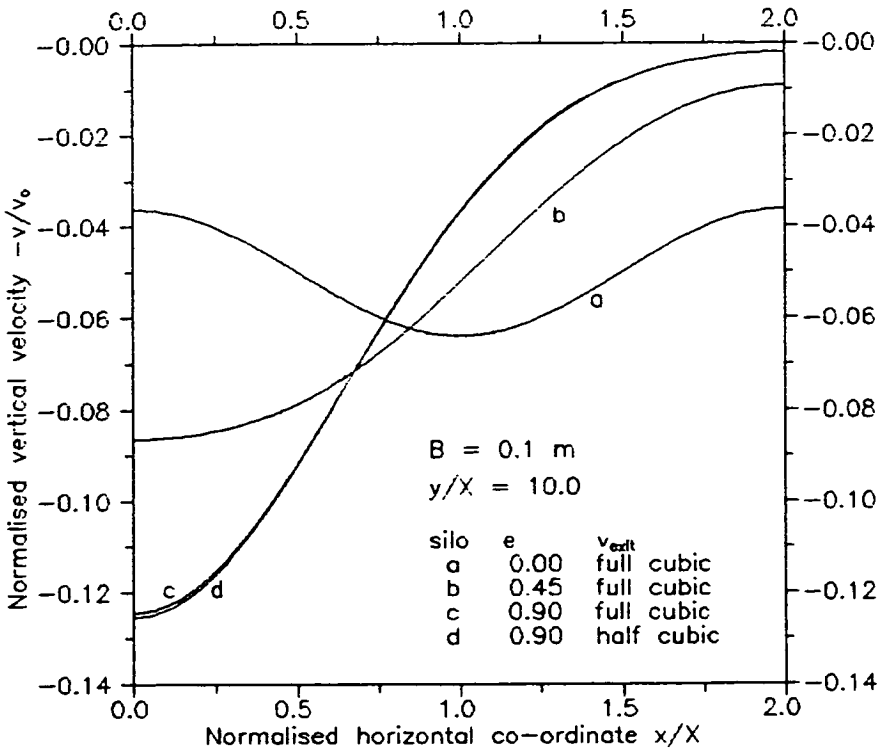

Fig. 5.47 Horizontal profiles of vertical velocity

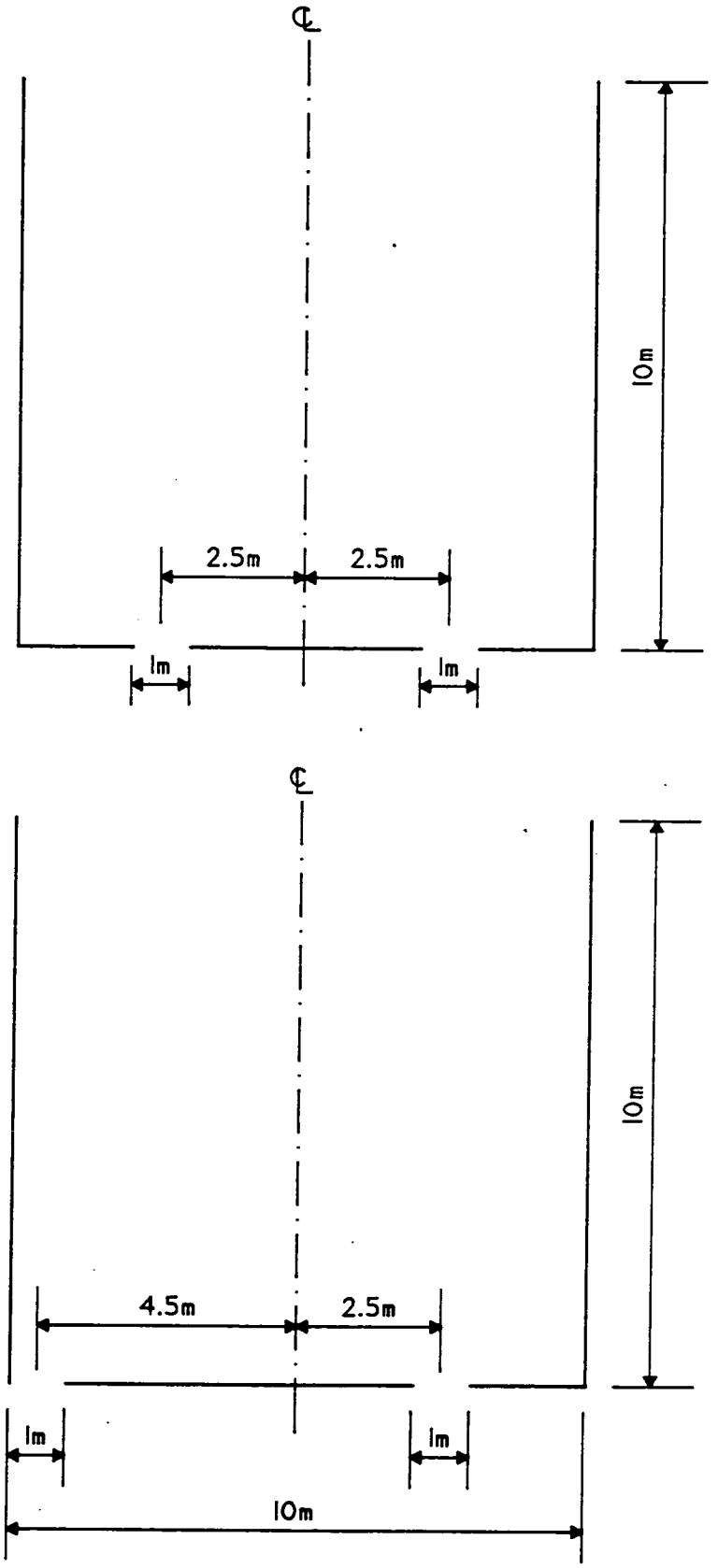

Fig. 5.48 Silos with two outlets

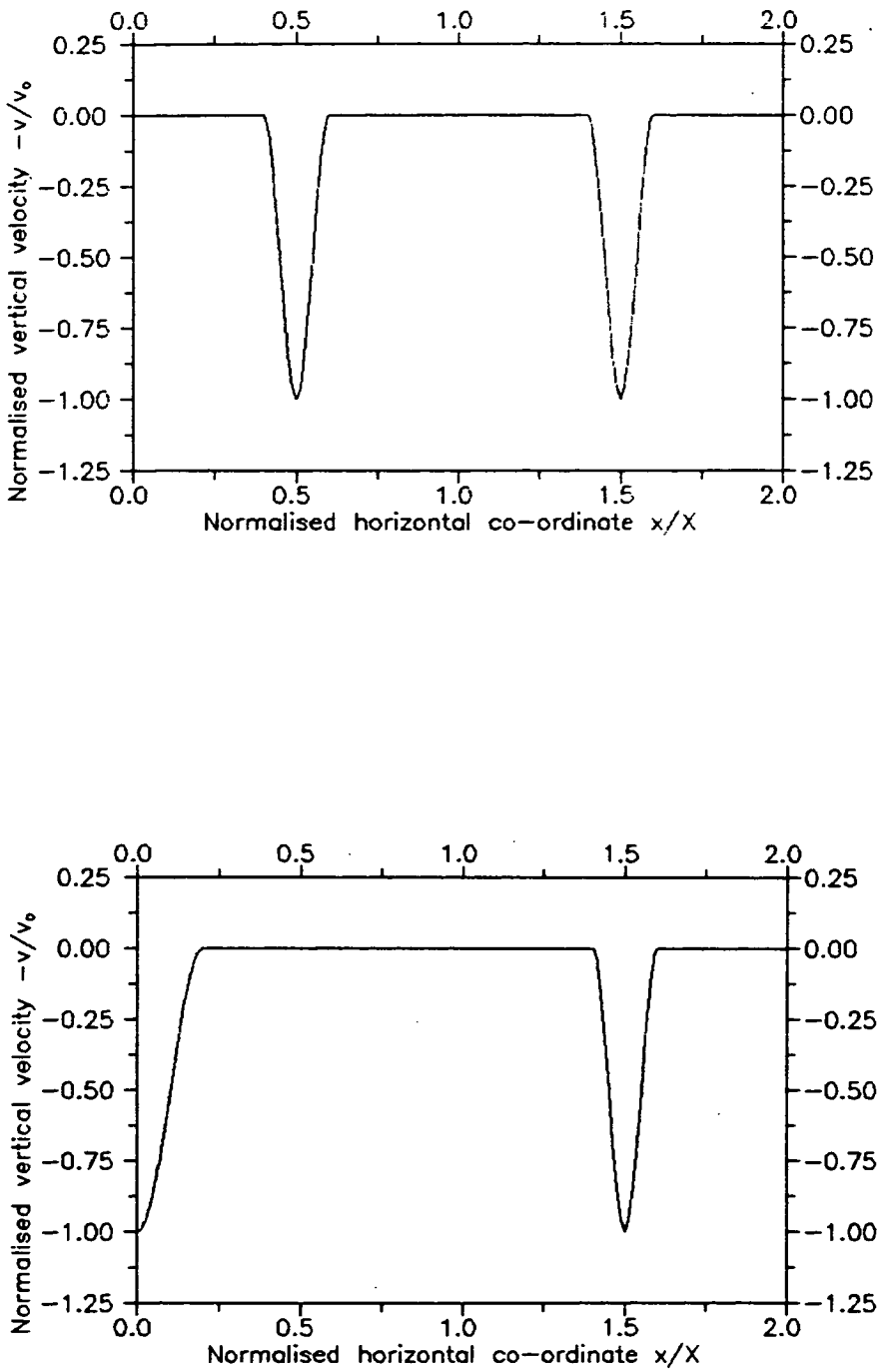

Fig. 5.49 Prescribed exit velocity distributions

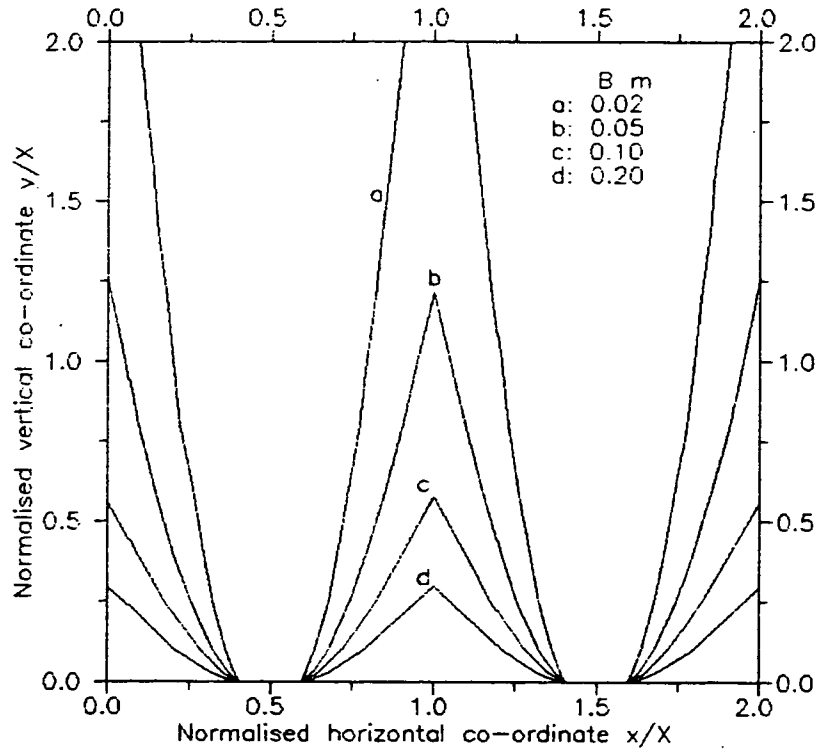

Fig. 5.50 1% FCBs for symmetrical double-outlet silo

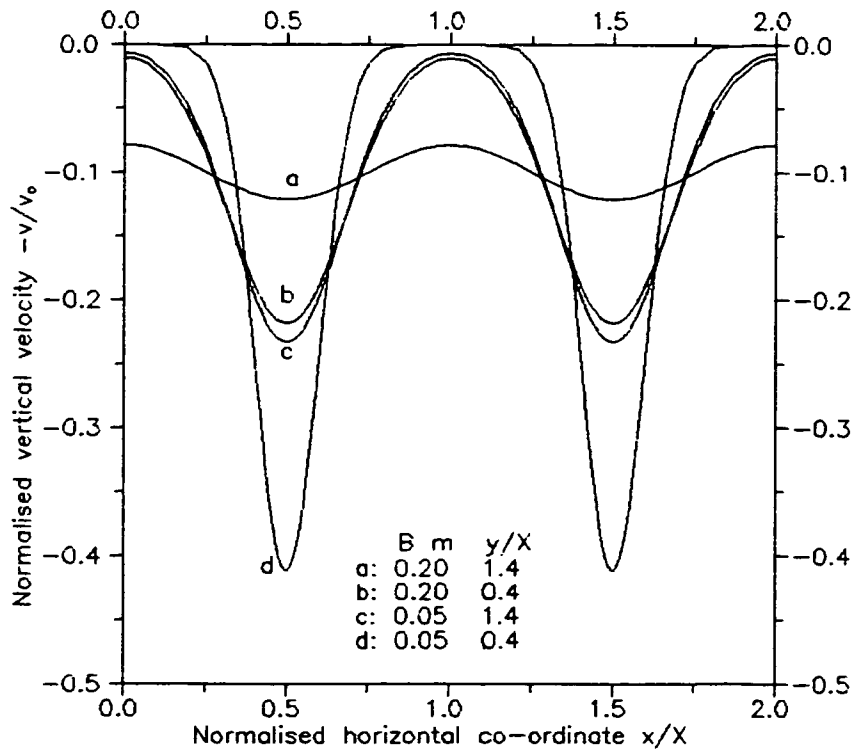

Fig. 5.51 Horizontal profiles of vertical velocity

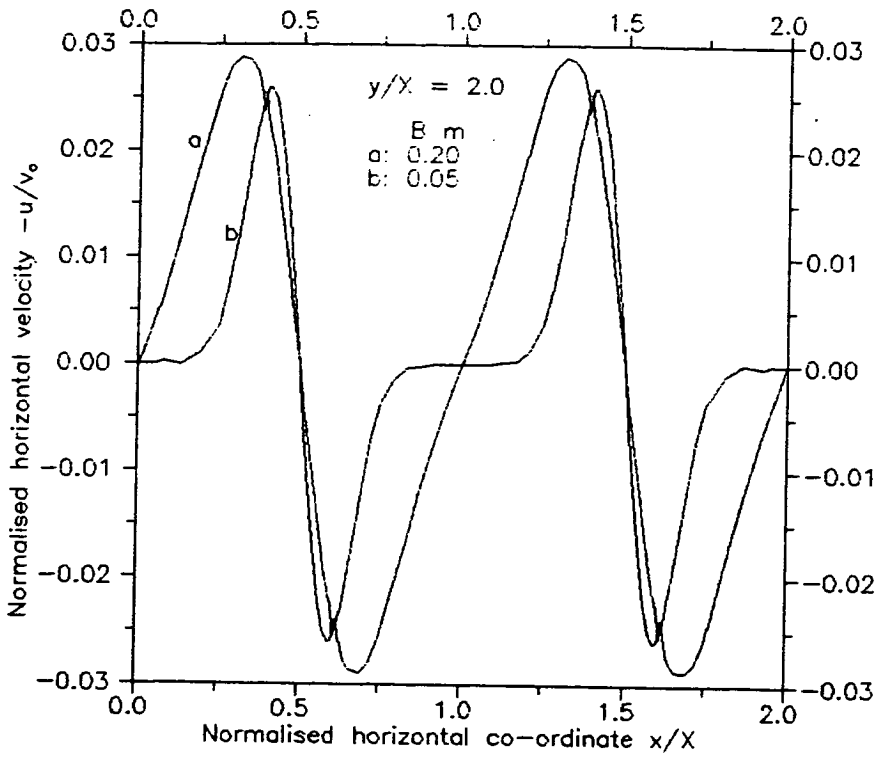

Fig. 5.52 Horizontal profiles of horizontal velocity

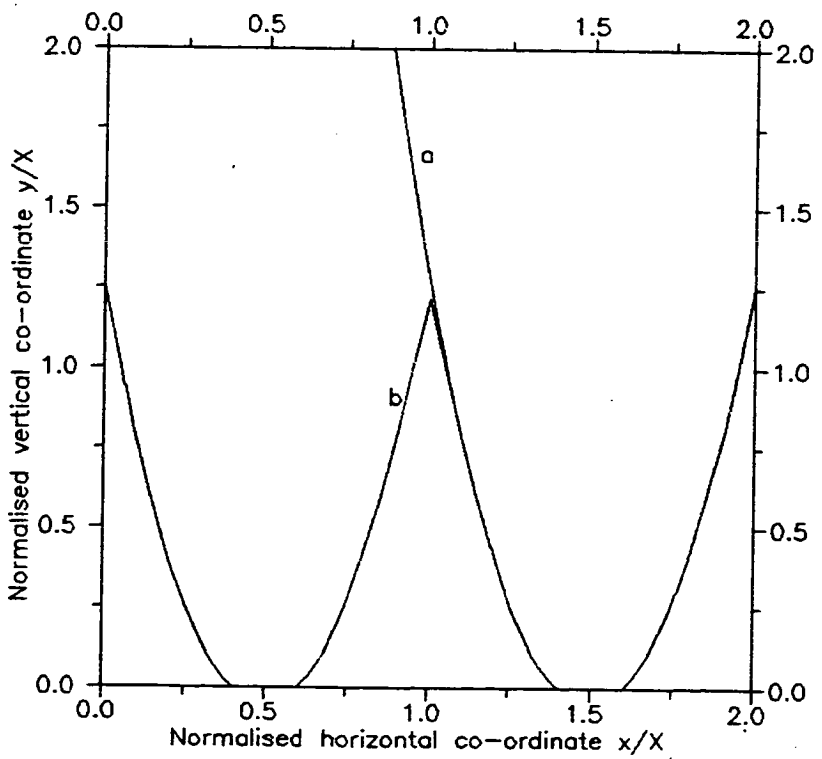

Fig. 5.53 1% FCB with one outlet closed

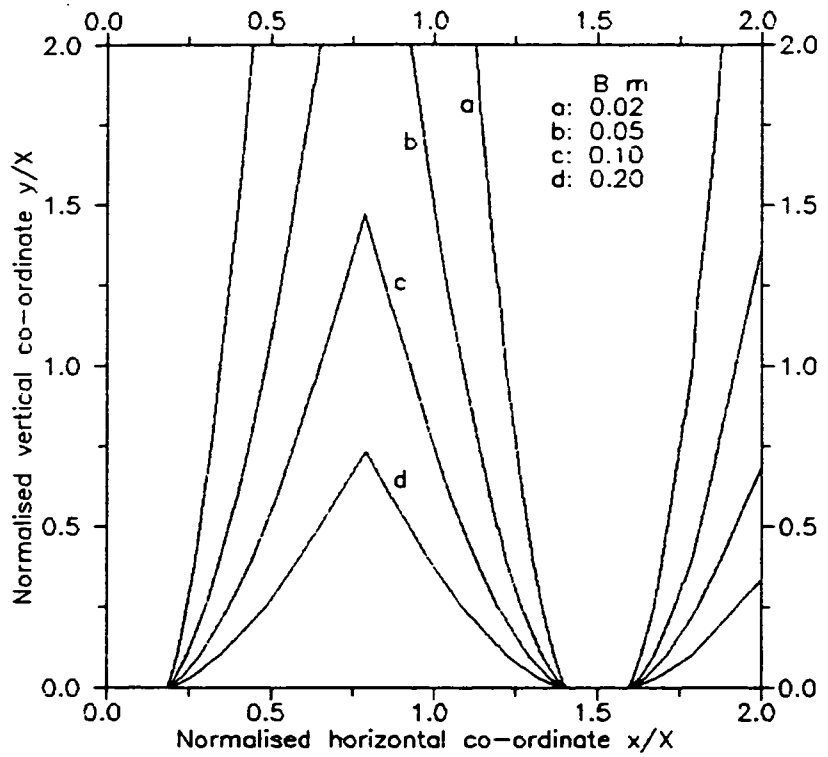

Fig. 5.54 1% FCBs for unsymmetrical double-outlet silo

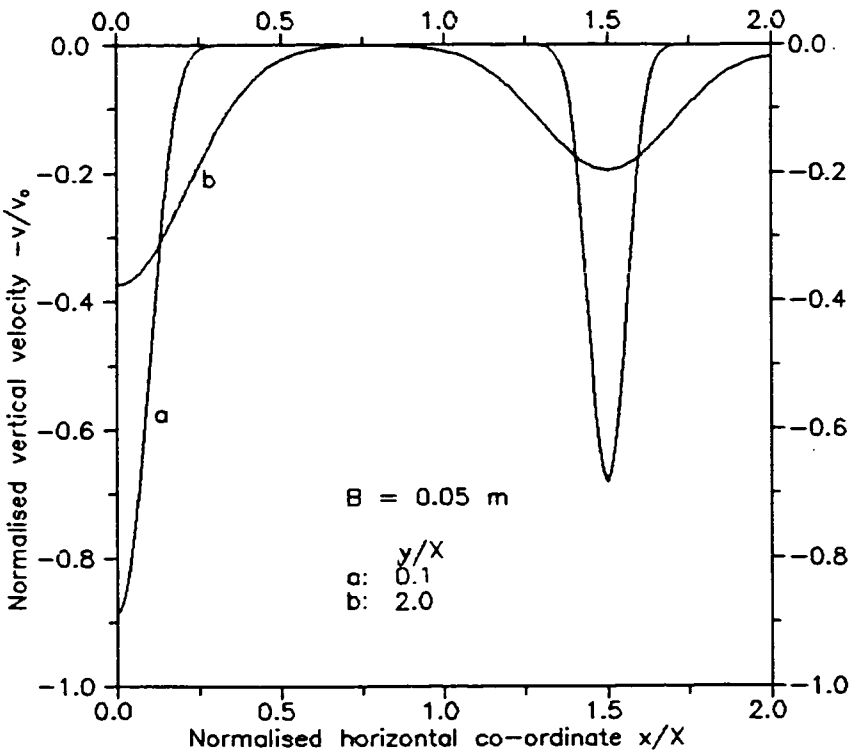

Fig. 5.55 Horizontal profiles of vertical velocity

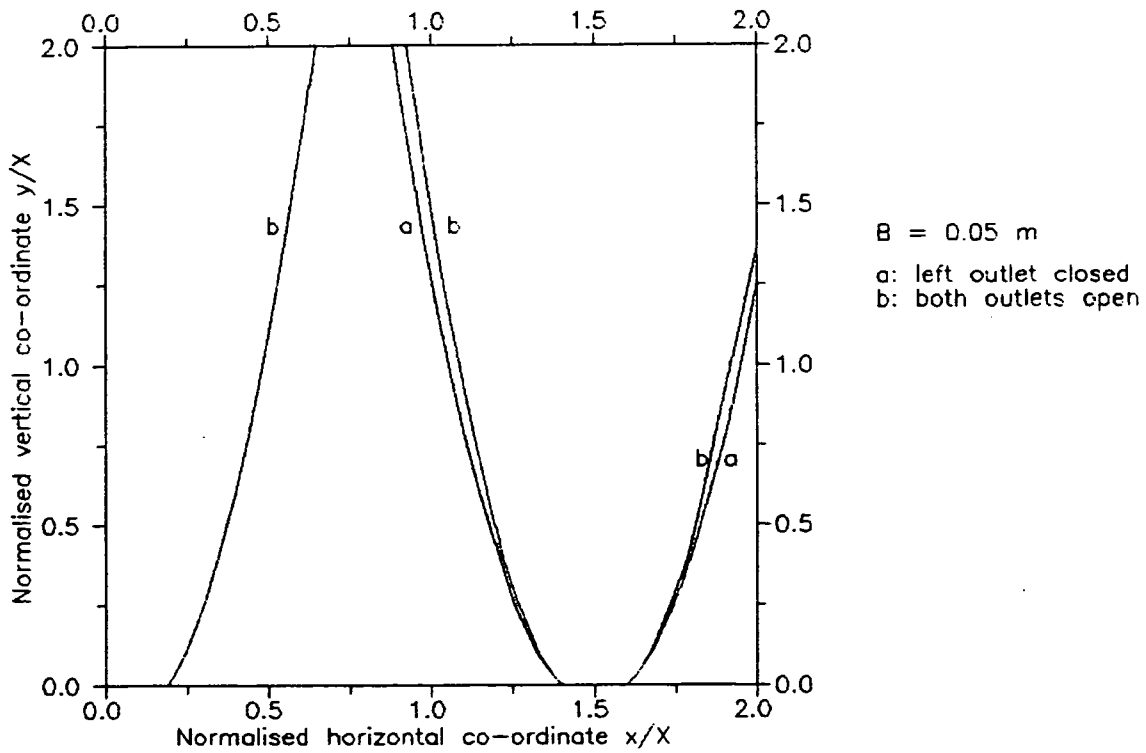

Fig. 5.56 1% FCB with one outlet closed

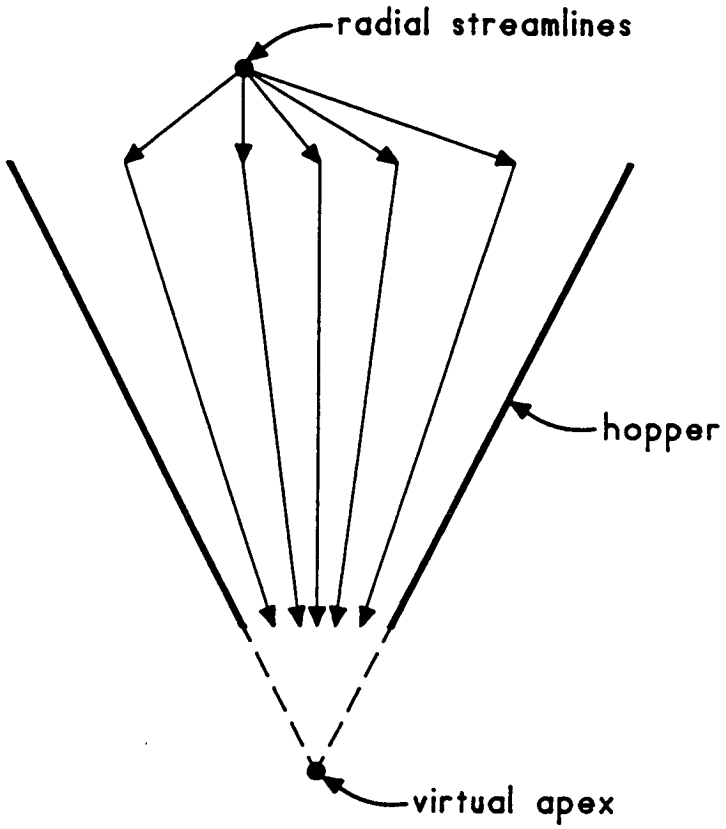

Fig. 5.57 Radial flow definition

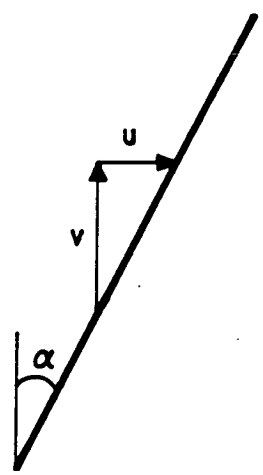

Fig. 5.58 Velocity components at hopper wall

CHAPTER 6

EXPERIMENTS IN FLAT-BOTTOMED HALF-CYLINDRICAL SILOS

6.1 Introduction

The experiments described in this chapter were carried out in a half-cylindrical silo which had a transparent front wall clamped across its diameter. The aim of the experiments was to determine the position of the flow channel boundary (FCB), to make estimates of the kinematic parameter B and to gain a comprehensive understanding of the discharge process.

The transparent front wall allowed the experimenter to observe at first hand the shape of the FCB, to trace particle trajectories and to make visual observations which could subsequently be used to find a value for the kinematic parameter B. Although the front wall slightly retarded the flow, the retardation could be estimated and taken account of in the calculations. The front wall was assumed to have a negligible effect on the general shape of the flow pattern. Similar studies of flow in planar silos (*e.g.* Johanson, 1964; Brown and Richards, 1965; Gardner, 1966 and Bransby *et al*, 1973) are affected more by the silo boundaries.

In this chapter, the apparatus is described and results of some experiments are presented and discussed.

Two distinct methods were employed in the experimental work: visual observation through the front wall and the measurement of residence times. Residence time analyses have been successfully employed in the past by a number of researchers (*e.g.* Smallwood and Thorpe, 1980; Murfitt, 1980; Graham *et al*, 1987; Nedderman, 1988 and Cleaver, 1991). The merits of this experimental technique over other possible techniques (*e.g.* wax fixing or X-ray radiography) were discussed in Chapter 2.

The visual observations were recorded on the front wall using a water-soluble pen. To measure the residence times, ceramic tracer particles were seeded into the solid at known positions. The resulting data were used to determine the position of the FCB and to estimate the kinematic parameter B. Four methods for the determination of the FCB and five methods for the estimation of B are described. Of these nine procedures, seven are implemented in this chapter. The remaining two are implemented in the following chapter where the correlation between the numerical kinematic model of Chapter 4 and the experiments described here is investigated.

6.2 Experimental apparatus

6.2.1 Introduction

The apparatus is shown diagrammatically in Fig. 6.1 and a photograph is shown in Fig. 6.2. The apparatus consists of a half-cylindrical model silo with a transparent front wall, a collector tank, a reservoir tank, and a semi-circular seeding tray that was used to position the tracer particles. A square supporting structure was built to accurately position the silo and the two tanks relative to each other. Two different granular solids were tested: a sand and a grade of polypropylene pellets.

6.2.2 Details of the supporting structure

A square supporting structure of side length 1.25 m and height 4.19 m was constructed to accommodate the experimental apparatus. At a level of 1.34 m above the laboratory floor, a square wooden base board was inserted. This was positioned horizontally and checked using a spirit level. This base board acted as the silo base as well as supporting the silo walls. The base board was supported on two horizontal scaffolding tubes.

6.2.3 Details of the silo

The silo had a height of 1.5 m and a diameter of 0.65 m. These dimensions produced an aspect ratio a little over 2. The silo provided a large area in which to

observe the flow mechanics and the evolution of the FCB without the hindrance of either narrow restricting walls (as would be the case in a slender silo) or large regions of stationary material (as would occur in squat silos). The silo was made of mild steel of thickness 1.5 mm. The semi-circular wall was fabricated from a sheet of dimensions 1.12 m by 1.5 m. The height of the silo was chosen as the maximum length that could be put through a set of available rollers and the width was chosen to give a suitable aspect ratio.

The volume of the silo was 0.25 m^3 which is adequate to avoid scale effects yet to keep the silo down to model proportions. The mild steel was susceptible to corrosion and so the inside of the silo was thoroughly smoothed with emery paper before the tests and at frequent intervals during the tests. The wall friction angle is discussed in Section 6.2.6.

The sheet of mild steel was rolled into a semi-circular shape. The straight edges were then folded back 50 mm to create flanges onto which the glass front wall could later be clamped. Thin rubber strips of width 50 mm were glued onto these flanges to cushion the glass. For stability, wooden templates of thickness 20 mm were cut, positioned and firmly glued on the outside of the silo at the base, the midway point and the top. Wooden runners ran vertically between the templates to increase the overall rigidity of the silo. The templates ensured that an accurate semi-circular shape was achieved by the rolling process and that this shape was maintained throughout the flow experiments.

The discharge orifice was then constructed. A square hole of side length 165 mm was cut into the base board as shown in Fig. 6.3. Into this hole, a wooden insert of the same thickness as the base board was placed. This contained a semi-circular hole through which the bulk could discharge. An orifice diameter of 65 mm was chosen to give a ratio of orifice diameter to silo diameter of 0.10.

The semi-circular silo was lowered onto the base board and symmetrically positioned about the semi-circular orifice (Fig. 6.3). In this way, the front wall, when attached, lay flush against the flat side of the semi-circular orifice (taking into account the thickness of the rubber strips on the flanges) and the curved silo wall lay equidistant from the centreline of the front wall. Thus, a semi-circular silo with a semi-circular orifice was constructed. This resembled a full circular silo, with a circular concentric orifice, that had been bisected longitudinally. Once the position

of the silo on the base board had been established, the silo was securely bolted down through the bottom wooden template to the base board.

A pneumatic shutter valve was fitted onto the underside of the base board below the orifice. This was used to start and stop the flow and was chosen over a manual slide door for its speed of flow interception and ease of use.

6.2.4 Details of the front wall

The front wall was assembled from a sheet of 0.66 m wide by 1.8 m high by 10 mm thick glass and a sheet of 6 mm thick perspex of the same width and height with a co-ordinate grid sandwiched between them. The 100 mm by 100 mm grid was marked on the glass using 1.5 mm wide black tape. The grid was labelled and acted as a radial r and axial z co-ordinate system. The origin was chosen in the middle of the bottom edge of the glass sheet, at the centre of the orifice. The axial co-ordinate was taken as being positive when measured upwards away from the orifice. Using this co-ordinate system, the base of the silo is described by the plane $z = 0$ and the curved silo walls are described by $r = 325$ mm. The assembled front wall was lifted onto the base board, correctly positioned and clamped onto the flanges of the silo. The glass sheet was used for the solids contact surface because it had a lower wall friction and a higher resistance to scratching from the flowing granular solid. The vertical centreline of the grid was positioned exactly midway between the insides of the flanges. The verticality of the grid and silo walls was checked using a plumb bob and any anomalies were rectified by adjusting the feet of the supporting structure.

6.2.5 The solids recycle system

Underneath the base board, a large square collector tank was housed to receive the discharging bulk solid. Above the silo, a rectangular reservoir tank was situated to store the solid before filling the silo. The distance between the base of the reservoir tank and the base of the silo (the maximum height through which solid fell) was 1.9 m. After a discharge from the silo, the full collector tank was lifted above the reservoir tank and the solids were returned to the reservoir tank.

The technique by which the silo was filled is now discussed. Sugden (1980) and Munch-Andersen and Nielsen (1990) have reported that the flow pattern is dependent upon the filling technique and the density. The primary objective of this thesis was to develop methods for determining the position of the FCB. For this reason, the effect on the flow pattern of different filling techniques was not investigated. Only one filling technique was used throughout the experiments. The distributed filling technique was chosen. This technique produced a level surface, for easy positioning of the tracers, and a uniform bulk density.

To facilitate this filling technique, the solids were rained down from the reservoir tank into the silo through a large number of holes. The holes were large enough to prevent arching of the bulk solid in the reservoir tank. They were symmetrically positioned in the base of the reservoir tank and took up the large-scale pattern of a semi-circle (see Fig. 6.4). It was found that 59 25-mm-diameter holes were required. The semi-circle of holes was just smaller than the cross-section of the silo and was positioned directly above the silo. A sliding shutter was fitted over the holes to allow the discharge from the reservoir tank into the silo to be controlled.

The sliding shutter consisted of a 1.5 mm thick metal sheet that moved between the base of the reservoir tank and a 20 mm thick wooden board screwed onto the base. The 25-mm-diameter holes were at 50 mm spacings and were drilled through the whole assembly so that by sliding the metal sheet relative to the two pieces of wood, the holes could be brought into or out of alignment. In this way, the discharge from the reservoir tank could be fully initiated or fully shut off. When the shutter was opened, the solid rained down and filled the silo's cross section uniformly.

6.2.6 The bulk solids used

Two different solids were used in the experiments: sand and low density polypropylene pellets. The sand was classed as being uniformly graded, coarse, and rounded with an effective grain size of 630 μm. A particle size distribution is shown in Fig. 6.5. The polypropylene pellets were cylindrical in shape, with a diameter of 5 mm and a length that varied between 0.5 mm and 4 mm. Samples of each solid are shown in Fig. 6.6. Control tests were carried out to determine the frictional parameters of the solids. The internal friction angle ϕ_i, the angle of

friction between the solid and the steel wall ϕ_{ws} and the angle of friction between the solid and the glass front wall ϕ_{wg} were determined using a shear box apparatus. The results are presented in Table 6.1. The moisture content and cohesion of both solids were negligible.

6.2.7 The tracer particles and the tracer seeding tray

The residence time of a particle in a bed of granular solids in a silo is defined as the time it takes to move through the silo from its initial (known) position to the orifice. By measuring the residence times of tracer particles (tracers), with known initial positions, valuable information on the flow pattern can be gained. Nedderman (1988) reported that tracers move with very nearly the same velocity as the surrounding bulk, even if the tracers are very large compared with the particle diameter. He also reported that tracer residence times would be more accurate if the tracers had a density that was close to the density of the bulk solid. Based on these criteria, ceramic tracers of 14 mm diameter were chosen for use in the experiments. The tracers were white, and were individually labelled. The tracers were chosen at a larger diameter than the bulk solid particles to permit easy separation at the outlet. It was assumed that the measured residence time of a tracer represents the residence time of adjacent granular solid particles.

The tracers were carefully placed onto the level surface of the solid at known positions, using the seeding tray shown in Fig. 6.7. The tray was designed to explore the symmetry of the flow and the effect of the front wall. The procedure was as follows. Firstly, tracers were placed into the tray. Once the silo had been partly filled, the loaded tray was slowly lowered onto the surface of the solid. By activating a catch on the tray, the tracers were released and deposited onto the surface of the solid (see Fig. 6.8). The filling process was continued until the surface rose by approximately 100 mm. Another layer of tracers was then deposited. In this way, tracers were placed in known positions throughout the bulk solid.

Each tracer was uniquely identified by a colour code and a number. Each horizontal layer consisted of tracers of one colour numbered from 1 to 26 (see Figs 6.7 and 6.9). A maximum of ten such layers were seeded into the silo as it was

filled. A sieve was positioned below the orifice to catch the tracers as they emerged and the residence time of each tracer was measured.

The design of the seeding tray is now described. The tray was constructed from two semi-circular pieces of wood, each 8 mm thick (see Figs 6.7 and 6.9). The diameter of each piece of wood was 645 mm, just less than the internal diameter of the silo. A total of 26 holes of diameter 16 mm were drilled through the two pieces of wood. The size of these holes was just larger than the diameter of the tracers. The holes were positioned along a line 25 mm from the straight edge of the semi-circle and along three radii at 45°, 90° and 135° relative to the front wall. These radii, measured from the centre of the straight edge, were 65 mm, 123 mm, 182 mm, 241 mm and 301 mm. (Figs 6.7 and 6.9). The resulting pattern of tracers consisted of 5 half-rings of 5 tracers each (labelled C1 to C5) and one tracer close to the centreline of the silo (Tracer 26, labelled C0).

The two semi-circular plates of wood were joined together and spring-loaded in such a way that they could slide relative to one another. The spring allowed the plates to be 'cocked' relative to one another in a position where the holes in the top plate only partially overlapped those in the bottom plate. In this position, the tracers were loaded into the top plate where they sat supported on the bottom plate. The plates were held in this cocked position by a steel pin onto which a length of string was attached. By tugging this string, the pin was dislodged and the plates slid relative to one another. Thus, the holes in the top and bottom plates were brought into alignment and the tracers fell out of the seeding tray.

6.3 Experimental programme

6.3.1 Introduction

The experiments described in this section fall into four categories. These categories are:

(1) preliminary residence time experiments;
(2) the determination of the flow channel boundary (FCB);
(3) the tracing of particle trajectories; and
(4) the estimation of the kinematic parameter B.

A discontinuous discharge technique was used for the residence time experiments. Continuous discharge was used for all other experiments. Each experiment was repeated twice to ensure that the results obtained were quite repeatable. Before each experiment is described, some general points are discussed which are relevant to the flow behaviour of both tested solids.

Flow regimes

A fully-discharged silo, with only small zones of stationary solid lying at the angle of repose around the orifice, was filled up. On initiating the discharge, the density above the orifice was seen to decrease, as the packing arrangement loosened to allow flow to begin (see Fig. 6.10a). This region of lower density spread rapidly up the silo in a column to the free surface (Fig. 6.10b,c). The residence times of tracers lying closest to the centreline, being in this column, were therefore relatively low. The FCB then spread out laterally (Fig. 6.10d,e) and temporarily stabilised (Fig. 6.10f). The flow regime that endured from the initiation of discharge to the formation of the quasi-stable FCB is defined here as *principal flow*. The FCB is defined as the *principal* FCB. Johanson (1964), Deutsch and Clyde (1967) and Arteaga and Tuzun (1990) reported that during this stage of the discharge conditions closely approximate steady-state. In the latter stages of discharge, the FCB widened out further as shown in Fig. 6.10g. After discharge was completed, the solid lay around the orifice at the angle of repose (Fig. 6.10h).

If half of the silo's contents were allowed to discharge, and the silo was then refilled, it was found that the flow channel immediately took up a dilated pattern. This is understood to be because the solid in the lower section of the silo had already undergone dilation. This flow regime is described here as the *post-refilling flow regime* and is observed when a partially-emptied silo is refilled. The FCB that occurred during this regime was stable and is termed the *post-refilling* FCB. The post-refilling FCB was also briefly encountered after principal flow when the silo was in its last stages of discharge. Both the principal and post-refilling flow regimes were investigated and results from the two flow regimes are compared.

In the post-refilling flow regime, the volume of solid that was allowed to discharge before refilling occurred did, of course, affect the subsequent flow pattern. If only a small volume was discharged (or, in fact, if the silo was fully discharged), the subsequent flow regime was best defined as principal flow. If, however, half of the silo's contents were discharged before refilling, the subsequent flow immediately

became highly-dilated and the FCB was relatively wide. For the purpose of this thesis, the post-refilling flow regime was set up as follows. Discharge was allowed to proceed until the outer edge of the free surface fell to a height of 800 mm (or 1.28D, where D is the silo diameter) above the silo floor. The discharge was then halted and the silo was refilled. The flow regime that manifested in such a silo is here termed a post-refilling flow.

By allowing the edge of the free surface to drop to 800 mm above the silo floor, a large part of the solid remaining in the silo became dilated and mobile. On refilling the silo and re-initiating the flow, the FCB immediately took up what appeared to be the widest FCB possible in a full silo.

Although Tuzun and Nedderman (1979b) suggested that the kinematic parameter B is a material parameter, it will be seen that different values of B were found for the two different flow regimes for the same solid. This is because the solid behaved quite differently in the two regimes. The behaviour of the solid in the principal flow regime is characterised by one value of B, whereas the behaviour in the post-refilling flow regime is characterised by another. This is a reasonable consequence of the different density distribution at the start of discharge for the two regimes.

In the latter stages of any silo discharge, the FCB spread into the zones of stationary solid, eroding them back until they finally lay at the angle of repose (Fig. 6.10g,h). The position of the FCB in these stages is usually less important in silo design since, with only a small amount of solid remaining in the silo, the wall pressures are relatively small. Conversely, in the post-refilling flow regime the position of the FCB is thought to be of great significance for reasons outlined in Chapter 2. This FCB, being perhaps the widest possible in a full silo, is likely to intersect the silo wall, except in very squat silos. If such an intersection does occur, an effective transition will be formed and surges in the lateral wall pressure may be expected to develop there. Since it is possible for a post-refilling flow pattern to manifest in a completely full silo, the overpressures may be at their highest. The above definition of the post-refilling flow regime is therefore expected to be the condition of most interest to the silo designer.

Tracer positioning

Although principal flow is a time-dependent phenomenon that spans from the instant the orifice is opened until the development of a quasi-stable FCB and a quasi-

steady-state velocity field, an assumption has to be made before the residence times of tracers in a principal flow field can be interpreted. The tracers closest to the centreline discharged before the quasi-stable FCB for principal flow was set up. The residence times of these tracers therefore correspond to the initial stages of principal flow where the flow channel is relatively narrow (Fig. 6.10a, b, c and d). These tracers can, however be used to give estimates of values of the kinematic parameter B during this stage (Sections 6.3.5.3, 6.3.5.5 and 6.3.5.6).

The method of placing tracers during post-refilling flow is now described. The silo was allowed to discharge until the edge of the free surface fell to 800 mm above the silo floor. A post-refilling flow regime was thus set up. The free surface formed a crater. Because of the small degree of friction against the front wall, the centre (or lowest point) of this crater was not quite in contact with the front wall, but was found to be 25 mm behind the inner surface of the front wall. A single tracer was dropped into the centre of the crater and its level (height above the silo floor), taking into account the small degree of impacting, was noted. Flow was then recommenced and the stop-watch was simultaneously started. After the centre of the crater had fallen by approximately 75 mm, the flow and the stop-watch were stopped. Another tracer was dropped into the centre of the crater. This process was continued until the centre of the crater became very close to the orifice. Throughout this period, the sieve was held in place to catch the tracers as they discharged and when they did, their residence times were noted. In this way, the residence times of tracers close to the centreline in the bottom section of the silo during post-refilling flow were obtained.

To obtain the residence times from the top section of the silo during post-refilling flow, discharge of a full silo was allowed to proceed until the edge of the free surface again fell to 800 mm above the silo floor. The silo was then topped up, positioning tracers 25 mm from the centreline at frequent intervals. The heights above the silo floor of these tracers were noted. Once the silo was completely refilled, discharge was re-begun and simultaneously the stop-watch was started. To allow the first tracer to approach the vicinity of the orifice, a short time was allowed to pass before the start-stop discharge technique was brought into use. The discharge was then halted at 5 second intervals and the sieve was checked for tracers. The residence times of tracers close to the centreline in the top section of the silo during post-refilling flow were thus obtained.

Discharge technique

Since the process of retrieving the tracers involved the repeated halting and restarting of the flow, its effect was investigated. It was found that if the silo was allowed to discharge without stopping the flow, the total time of discharge differed by a maximum of 5% from the equivalent time obtained when a start-stop discharge technique was used. The event which should be used to define precisely the end of a discharge (*i.e.* when the stop-watch should be stopped) was not obvious. As the discharge approached its completion and the static angle of repose was reached (Fig. 6.10h), the flow from the silo became intermittent. The reason for this was that particles trickled slowly down the static solid shunting other particles, that were stationary, into motion. These particles in turn may have shunted others into motion, being halted themselves in the process, or they may have continued all the way to the orifice. The sporadic nature of flow at the very end of a discharge made the measurement of the total time of discharge a slightly subjective matter. Taking this into account, the 5% difference in the total time of discharge mentioned above is acceptable and it was deduced that stopping and starting the flow had a negligible effect on the total discharge time. It was also visually observed that, during the start-stop discharge technique, the FCB did not alter its position upon re-initiation of the flow. These observations indicate that stopping and starting the flow had a negligible effect on the flow pattern. This is in keeping with the observations of Tuzun *et al* (1982).

6.3.2 Preliminary residence time experiments

6.3.2.1 Description of experiments

As the silo was filled, the filling process was halted at frequent intervals to seed a layer of tracers by the method described in Section 6.2.7. A total of 10 such layers were included in the solid during filling.

The discharge was stopped approximately every 2 seconds and the sieve was checked for tracers. If any tracers were found, their number and colour code were recorded, together with the total time it had taken for them to discharge *i.e.* their residence time. The length of the time interval when the orifice door was open and

flow was allowed to take place was increased from 2 seconds to approximately 5 seconds in the final stages of discharge. The reason for this was that tracers had been placed at a higher concentration in the centre of the silo than around the periphery (see Fig. 6.8), so the number of tracers discharged per unit time was higher at the start of discharge and became lower towards the end. Using these different time intervals, it was possible to regulate the number of tracers discharged during each interval, thus maintaining high accuracy and efficiency.

6.3.2.2 Results and discussion

Data sheets, used to record the laboratory results for experiments using sand and polypropylene pellets, are shown in Appendices 6.1 and 6.2 respectively. Each column displays the residence times of a layer of tracers. The height of a particular layer is given at the column heading. The numbers given under these column headings relate to the tracer positions (Fig. 6.9).

Some general observations can be made from the raw data presented in these data sheets. It may be recalled that the tracers at each level were arranged in 6 rings C0 to C5 (see Fig. 6.9). From the data sheet, the development of the flow channel through time can be followed. At any particular level, the order of tracer rings discharged starts at the centre, C0, and works its way outwards towards C5, as the spreading flow channel erodes away the stagnant zones.

A uniform pattern, discernible from the data sheets, is the axisymmetric nature of the flow. It can be seen that, in most cases, the residence times of tracers belonging to the same ring are all closely grouped. This implies that the evolution of the FCB during principal flow was symmetrical about the vertical centreline of the front wall *i.e.* the flow was axisymmetric.

The residence times of tracers in some rings are, however, not closely grouped. The significance of these rings is now discussed. As the FCB widened and began to stabilise, its rate of expansion decreased. The FCB was not precisely axisymmetric, so tracers of the same ring did not discharge simultaneously. Differences in the residence times of tracers from the same ring were increased as the FCB approached its quasi-stable position. Therefore, when the residence times of tracers belonging to the same ring were not closely grouped, these tracers must have lain

on or close to the quasi-stable FCB for principal flow. This observation is exploited in Section 6.3.3.3 to determine the position of the quasi-stable FCB of principal flow.

Another trend observed from the raw data relates to the retarding effect of the front wall. If rings of tracers which were supposed not to lie on the quasi-stable FCB are considered, it can be seen that the tracers closest to the front wall from rings C1 to C5 (those numbered 1, 5, 6, 10, 11, 15, 16, 20, 21 and 25) took slightly longer (typically 5%) to discharge than the other tracers on the same ring. Tracers of the same ring still have closely-grouped residence times however. This shows that the glass inner surface of the front wall had a small retarding effect on the flow. The residence times of the tracers numbered above were therefore ignored in subsequent FCB analyses but are used here to estimate the degree of retardation.

6.3.2.3 Correction of residence times due to front wall retardation

The calculated retarding effect of the front wall was used to correct the residence times of Tracer 26. This tracer is unique since it was positioned alone 25 mm from the centreline (*i.e.* at r/R = 0.08), on ring C0. The corrected residence times of these tracers represented the residence times of tracers at r/R = 0.08 in a full circular silo, which would closely approximate the behaviour on the axis.

Rings C1 to C5, that were supposed not to lie on the FCB, are considered. The two tracers close to the front wall have slightly longer residence times than the other three tracers in the ring. A ratio f is defined here as the ratio of the mean of the residence times for the two tracers close to the front wall to the mean of the residence times of the other three tracers in the ring. This ratio was calculated for all rings. Where the effect of the front wall is not great and when the rings are not close to the FCB, f is found to be close to unity. Close to the FCB, f becomes large for the following reasons. A plan view of the FCB is shown in Fig. 6.11. The shape of the flow channel is not a perfect semi-circle because of the retardation of the front wall. If a ring of tracers lies on or close to the FCB, the three tracers farthest from the wall will lie in the flow channel whereas the two tracers close to the front wall will lie outside the flow channel (Fig. 6.11). Therefore, for this ring, the three tracers farthest from the wall will discharge from the silo much sooner than the other two tracers. The value of f will therefore be much higher than 1.

The position of the FCB can therefore be estimated from an examination of rings where the value of f is very high. Such a method was not used in this thesis because more accurate methods were developed and utilised (see Section 6.3.3). Rings which had a large value of f were therefore excluded from the estimation of the retarding effect of the front wall. From an examination of how f varies over all other rings, an estimation can be made of the adjustment which is required for the residence times of Tracer 26. Once adjusted, the residence times of Tracer 26 can be used in subsequent analyses to represent the behaviour close to the axis of a full circular silo.

The relationship between the ratio f and the radial co-ordinate r/R at three different heights for sand and polypropylene pellets is shown in Figs 6.12 and 6.13 respectively. These plots have been interpolated to r/R = 0. At r/R = 0.08, the retarding factor can be read. It can be seen that the intercept is very close to 1.04 for sand and 1.05 for polypropylene pellets. The residence times for Tracer 26 were therefore decreased by 3.8% (= 1 - 1/1.04) for sand and by 4.8% (= 1 - 1/1.05) for polypropylene pellets.

6.3.2.4 Correction of residence times due to initial transient

After flow initiation, the tracers remained stationary until the spreading FCB reached their position. For those tracers numbered 26, this transient period was very short, and can be ignored. However for tracers positioned close to the side wall, the transient period was quite considerable, especially at lower heights. Therefore, the residence times of these tracers do not represent the time the tracers were in motion. By correcting these residence times, the actual time the tracer was in motion can be calculated. The variation of the kinematic parameter B with radial co-ordinate can then be estimated by fitting the kinematic formulation of Chapter 4 to these experimental results. This correlation is carried out in Chapter 7. Uncorrected residence times can, however, be used to estimate the position of the quasi-stable FCB during principal flow (see Sections 6.3.3.3 and 6.3.3.4).

By tracing the evolution of the FCB on the front wall, it was possible to estimate the time interval between the opening of the orifice and when any particular tracer began to move. The slight inward curvature of the FCB at the front wall (Fig. 6.11) was ignored. The method by which the evolution of the FCB was determined

is as follows. A number of thin horizontal layers of coloured solid were placed adjacent to the front wall during filling. A start-stop discharge technique was used. At each flow hiatus, the time since flow initiation was noted and the extent of displacement of the coloured layers was traced on the front wall.

Figure 6.14 shows the FCB evolution for polypropylene pellets. It can be seen that the pattern of flow channel development closely follows that described in Section 6.3.1 and shown schematically in Fig. 6.10.

Since the positions of the tracers were known, the time before a tracer started to move could be determined. This time was subtracted from the measured residence time. In this way, a corrected residence time was obtained that represented the time from the start of tracer movement until the tracer discharged. The relationship between these corrected residence times and the radial co-ordinate for polypropylene pellets is shown in Fig. 6.15 at four different heights. It can be seen that the residence time increases with radial co-ordinate, more markedly at higher levels.

In Chapter 7, Fig. 6.15 is used to estimate the variation of B with radial co-ordinate, by fitting with the numerical formulation of Chapter 4. It will be seen in Chapter 7 that problems arose when this fitting was attempted (see Section 7.3.3). For this reason, the FCB evolution was not traced for sand.

6.3.3 · Experimental determination of the flow channel boundary (FCB)

6.3.3.1 General

As discussed in Chapter 1, the prediction of the FCB in flowing granular solids is important because it is widely believed that high overpressures occur where this boundary intersects the silo wall.

Four methods for determining the position of the quasi-stable FCB of principal flow are described in this section. These methods determine this FCB from:
(a) visual observation though the front wall;
(b) discontinuities in residence time data;

(c) isochrone maps; and
(d) interpretation as a radial velocity field.

Methods (a) and (d) were also used to determine the position of the stable FCB for post-refilling flow. Each of these methods is examined in turn. Comparisons between the resulting FCBs are then presented.

In this thesis, the FCB is not presented as a time-dependent phenomenon because it was observed that this boundary appeared to become stable for a large proportion of the discharge for each of the two flow regimes.

6.3.3.2 Determination of the FCB from visual observation through the front wall

In this method, the FCB was traced on the front wall using a water-soluble pen. This method represents the most accurate way of determining the FCB that would occur in a full circular silo. The method cannot, however, be used in full circular silos. The FCBs obtained using this method are therefore used to compare the accuracy of the other methods (b to d listed above) of predicting the FCB. Methods (b) to (d) can be used in full circular silos where internal visual observations are impossible. The comparison is carried out in Section 6.3.3.6.

The quasi-stable FCB of principal flow (*i.e.* the principal FCB) and the stable FCB of post-refilling flow were traced on the front wall for both solids. The position of the principal FCB was traced at the stage when the evolving FCB appeared to have stabilised (Fig. 6.10f). Since the FCB during principal flow did not totally stabilise, its position remains somewhat uncertain. However, the tracing of an approximate FCB during principal flow is important as it can be used by the silo designer carrying out stress calculations. The principal FCB can also be used to find an approximate value for the kinematic parameter B corresponding to this flow regime.

Although the FCB for post-refilling flow has been described as a stable phenomenon, this boundary was not a clearly-defined locus either, especially in experiments using polypropylene pellets. In the region of the FCB, it was observed that the motion of some particles was intermittent and other particles moved

incredibly slowly. The determination of the position of the FCB during post-refilling flow, as traced through the front wall, was therefore slightly subjective.

The principal and post-refilling FCBs for sand and polypropylene pellets are shown in Figs 6.16 and 6.17 respectively. It can be seen that both FCBs for polypropylene pellets are wider than those for sand and that the principal FCB is wider than the post-refilling FCB for both solids. All FCBs are approximately parabolic in shape when viewed through the front wall. The curvature of all the FCBs decreases away from the orifice and the principal FCBs become almost vertical in the upper section of the silo. The post-refilling FCB for polypropylene pellets was the only one to make contact with the silo walls (Fig. 6.17).

6.3.3.3 Determination of the FCB from discontinuities in residence time data

The residence times of tracers at five different heights are plotted against the normalised radial co-ordinate in Figs 6.18 and 6.19 for sand and polypropylene pellets respectively. The residence times were not corrected for the effect of the initial transient, so that any discontinuities in the residence times could be highlighted. With the exception of Tracer 26 (see Fig. 6.9), the tracers that lay adjacent to the front wall were ignored. Therefore, there were three tracers at a given (r_i,z_i) co-ordinate and the mean residence time was calculated. The residence times of Tracer 26 were corrected for the front wall retardation (see Section 6.3.2.3).

The curves of residence times for tracers at low z_i co-ordinates have steep gradients in the middle part of the curve (Figs 6.18 and 6.19). The curves associated with higher layers (large z_i) are much flatter. This illustrates the changing width of the flow channel with height and is discussed below.

Low down in the silo, the flow channel was narrow and the velocities were high. Tracers that lay within the flowing channel therefore have very short residence times. Conversely, outside the channel (at the same height) the tracers were not discharged until the silo was in its very last stages of discharge, so the residence times of these tracers are very large. The curve of residence time against radial co-ordinate (*e.g.* Fig. 6.18) thus shows a marked contrast between the early and late discharged tracers. High up in the silo, it did not take long for the free surface to

erode down to the level of the tracers. These tracers then rolled into the flow channel (sloughing of the surface). This flow pattern is shown in Fig. 6.10e. Thus, tracers originally positioned high in the silo have residence times that are closely grouped. For this reason, the curves of residence time against normalised radial co-ordinate for high layers of tracers are much flatter (*e.g.* Fig. 6.18, z/R = 4.3).

Comparing Figs 6.18 and 6.19, it can be quickly ascertained that the flow channel was wider when the silo was filled with polypropylene pellets than when it was filled with sand. By way of explanation, the residence times of the tracers closest to the centreline (at r/R = 0.08) are considered. The volumetric flow rate was measured as 840,000 mm^3/s for sand and 685,000 mm^3/s for polypropylene pellets, these values being stable within 3%. If the flow patterns for the two solids had been identical, the velocities in the sand would have been 1.23 (= 840/685) times larger than those in the polypropylene pellets. This would cause the residence times for tracers in the sand to be 0.815 times of those in the polypropylene pellets. As it is, the residence times of tracers in sand at a particular height are considerably less than this expectation. This can only mean that the relative velocities on the silo axis in the sand are higher than those in the polypropylene pellets. Continuity considerations dictate that the flow channel in the sand must have been narrower than that in the polypropylene pellets. This matches the visual observations described in Section 6.3.3.2 above.

Plots of the cumulative number of tracers discharged through the orifice per layer against residence time T are now considered. If the velocity distribution varied gradually everywhere, having no high gradients with respect to radial co-ordinate r/R, such plots would also vary gradually (see Fig. 6.20) because the tracers were positioned uniformly with respect to r/R (Fig. 6.9). Experimental plots of the cumulative number of tracers discharged per layer against residence time for sand and polypropylene pellets are shown in Figs 6.21 and 6.22 respectively. These plots do not vary smoothly, but typically have a discontinuity in the residence time T. This discontinuity arises because some tracers lay inside the flow channel and therefore had relatively short residence times, whilst other tracers lay outside the flow channel and had much longer residence times, not discharging until the free surface eroded down to their position. The position of the discontinuity can be used to estimate a locus for the principal FCB.

Figures 6.21 and 6.22 were used to determine inner- and outer-bound estimates of the position of the principal FCB. All the tracers that lay closest to the front wall were excluded. The remaining tracers formed five rings of three tracers each. Referring to Fig. 6.9, these tracers were numbered 2, 3, 4, 7, 8, 9, 12, 13, 14, 17, 18, 19, 22, 23 and 24. It was expected that the tracers would discharge in groups of three. If there was a discontinuity between the mean residence time of any two groups of three at a particular level, then it was deduced that the principal FCB lay between the radii of the two rings that contained these two groups. These two radii provide the inner and outer limits of the FCB at that particular height. In Figs 6.21 and 6.22, discontinuities between the residence times of groups of three tracers on adjacent rings are represented by a level part of the curve. Quite clearly-defined level sections are apparent in all curves apart from those that are associated with the highest two layers of tracers. At these heights, the flow channel takes only a short time to erode down to the layer of tracers (Fig. 6.10e). These tracers then roll onto the centreline and therefore discharge as a group of fifteen with little variation in residence times. At the other eight heights, the discontinuity permits the inner and outer limits of the principal FCB to be established. These limits are plotted in Fig. 6.23 for sand and Fig. 6.24 for polypropylene pellets. In these figures, it has been assumed that the FCB passes through the edge of the orifice, and this point provides a limiting position for the FCB.

6.3.3.4 Determination of the FCB from isochrone maps

As described in Section 6.3.3.3, a single mean residence time can be associated with the radial and vertical co-ordinates of the ring. As before, the residence times of tracers adjacent to the front wall, except Tracer 26, were excluded. The corrected residence times of Tracer 26 were used (see Section 6.2.3.2). A grid of points was produced, each one having a single residence time associated with it. Using this grid, contours of equal time (isochrones) were plotted. The resulting isochrone map concisely summarises all the residence time data in one figure. Isochrone maps for sand and polypropylene pellets over the range of tracer positions are shown in Figs 6.25 and 6.26 respectively.

The isochrone maps represent the evolution through time of the FCB for the stage described above as principal flow. At the initiation of discharge, the granular solid above the orifice comes into motion and a FCB forms. This takes the form of a

front that spreads upwards and outwards from the orifice as more and more solid comes into motion (Fig. 6.10a-c). From the information presented in Fig. 6.25, it can be inferred that, on flow initiation, a narrow column of flowing sand rapidly forms above the orifice, and stretches up to the free surface. The column of flowing solid then swells laterally at all levels to form the principal FCB. This pattern of flow channel development matches the visual observations and is characteristic of cohesionless, relatively rough granular solids like sand.

For the polypropylene pellets (Fig. 6.26), the region of flow was initially wider than that in sand. The flow front took longer to reach the free surface. This more expanded pattern is characteristic of smoother granular solids. Both solids follow the general pattern hypothesised by Lenczner (1963) and Arteaga and Tuzun (1990).

The positions where the isochrones are closest together gives a good guide to the position of the quasi-stable FCB during the principal flow regime. An isochrone was chosen from this region to represent the principal FCB as assessed from interpretation of residence time data as isochrones. The choice of which isochrone was chosen was not critical, because the isochrones are so close together in this region, especially in the bottom half of the silo. After studying the isochrone maps, the 100 second isochrone was used here to define the principal FCB for sand (Fig. 6.25) and the 120 second isochrone to define the principal FCB for polypropylene pellets (Fig. 6.26). These both represent isochrones for approximately 35% of the total discharge time for each solid.

6.3.3.5 Determination of the FCB from a radial velocity field interpretation

General

Another technique for estimating the position of the FCB from observed data can be devised, based on the assumption that the flow just above the orifice is a radial velocity field (*e.g.* Brown and Richards, 1965 and Drescher, 1991). Using only data for the residence times of tracers close to the the silo axis, the expansion of the flow channel above the orifice can be estimated. Using this assumption, the FCB is taken to be a linear locus in r,z co-ordinates. The residence times of these tracers were again corrected to take into account the retarding effect of the front wall (see Section 6.3.2.3). The behaviour close to the silo axis is assumed to represent closely the behaviour on the axis. The geometry and co-ordinate system used for

this theory are defined in Fig. 6.27. From this figure, the angle that the channel of flowing solid makes with the vertical is defined as

$$\theta_1 = \tan^{-1}\left(\frac{r_o}{r^*_1}\right) \tag{6.1}$$

A radial velocity field assumes that particles travel on radial streamlines towards a single point (point P in Fig. 6.27) and that there is no velocity normal to these radial lines. On the centreline of the silo, the velocity v is vertically downwards and can be written as

$$v = \frac{A}{r^{*2}} = -\frac{dr^*}{dt} \tag{6.2}$$

where A is a constant and r* is measured vertically upwards from the centre of the hypothesised radial velocity field as shown in Fig. 6.27. Thus, if a particle moves along the centreline from a position r* down to the orifice, r^*_1, in a time T:

$$\int_0^T A\,dt = -\int_{r^*}^{r^*_1} r^{*2}\,dr^* \tag{6.3}$$

Evaluating this integral and substituting $r^* = z_i + r^*_1$ (where z_i is the initial vertical co-ordinate of a tracer) gives

$$3AT = z_i^3 + 3z_i^2 r^*_1 + 3z_i r^{*2}_1 \tag{6.4}$$

From the experiments described above, relationships between T and z_i were found for tracers positioned close to the centreline (Fig. 6.28). During post-refilling flow, the residence times of tracers closest to the centreline were obtained first from the bottom section of the silo and then from the top section (see Section 6.3.1). Thus two separate curves can be drawn as shown in Fig. 6.28. One curve joins the points in the top section of the silo and the other curve joins those in the bottom section. In the post-refilling flow regimes of both solids, these two curves can be seen to run together (Fig. 6.28). This suggests that the method for measuring the residence times of tracers in post-refilling flow produces results from the top and bottom sections of the silo that are compatible. In this analysis and in subsequent

analyses, therefore, both sets of data on the residence time for the post-refilling flow regime are treated as components of a single data set.

In the radial velocity field analysis, the tracers positioned closest to the centreline were assumed to move vertically downwards. In Eq. 6.4, both A and r^*_1 are unknowns. Consequently, Eq. 6.4 cannot be solved directly for r^*_1, and an iterative solution is required. The following technique was used here, based on two alternative cases: $z_i < r^*_1$ and $z_i > r^*_1$.

If $z_i < r^*_1$, then

$$z_i^3 < 3z_i^2 r^*_1 < 3z_i r^{*2}_1$$

Dividing Eq. 6.4 by $3r^*_1 z_i$ and re-arranging:

$$z_i + \frac{z_i^2}{3r^*_1} = \frac{A}{r^*_1}\frac{T}{z_i} - r^*_1 \qquad (6.5)$$

It is initially assumed that $r^*_1 >> z_i$, so that the term $z_i^2/3r^*_1$ can be ignored, and z_i is plotted against T/z_i. The resulting plot is expected to have a slope of A/r^*_1 and a negative intercept of $-r^*_1$. This intercept gives a first approximation to the value of r^*_1. To obtain a better approximation, $z_i + z_i^2/3r^*_1$ is plotted against T/z_i and a new intercept, and thus a better approximation for r^*_1, is found. The process is repeated until convergence, or divergence, is evident. If the solution converges, a value for r^*_1 has been found and the angle the flowing solid makes with the vertical can be found.

Conversely, if $r^*_1 < z_i$, the inequality relationships can be reversed:

$$z_i^3 > 3z_i^2 r^*_1 > 3z_i r^{*2}_1$$

Dividing Eq. 6.4 by z_i^2 and re-arranging:

$$z_i + \frac{3r^{*2}_1}{z_i} = 3A\frac{T}{z_i^2} - 3r^*_1 \qquad (6.6)$$

If the term $3r^{*2}_1/z_i$ is initially ignored (r^*_1 is initially assumed to be zero), z_i can be plotted against T/z_i^2, yielding first approximations for A and r^*_1. Using the value

of r^*_1 obtained from the intercept, $z_i + 3r^*_1{}^2/z_i$ can be plotted against T/z_i^2, leading to a better approximation of r^*_1. Again, this process is continued until convergence or divergence is evident. If the iteration converges, the angle that the flowing solid makes with the vertical can be estimated from Eq. 6.1.

Both iteration procedures were continued until the value of r^*_1 converged to the extent that the value of θ_1 calculated from Eq. 6.1 was accurate to within 1°.

Results and Discussion

An example of the first iteration type is shown in Fig. 6.29. This figure is for sand during the principal flow regime. The plot can be accurately represented by two linear best-fit lines. In such a situation, the upper and lower sections are treated separately. The lower section is considered in Fig. 6.30. From the intercept, a first estimate of r^*_1 was found to be 2.285 m. The vertical co-ordinates were then adjusted as described above and a new value of r^*_1 was found. This process was continued until convergence to the above-mentioned accuracy was achieved. The final plot for this iteration is shown in Fig. 6.31. The value of r^*_1 converged to 2.461 m. Equation 6.1 was then used with $r_o = 0.0325$ m and this gave $\theta_1 = 0.76°$.

The upper section of Fig. 6.29 was then considered. This did not converge. The reason for this was that the residence times of the tracers close to the silo axis in the top section of the silo relate to a period when the flow channel was expanding rapidly. Thus, even a quasi-stable FCB cannot be predicted. It is also possible that r^*_1 and z_i are of similar magnitude in the top section of the silo for this flow condition and so the assumption of initially ignoring a term in either Eq. 6.5 or Eq. 6.6 should not be made.

The plot of z_i against T/z_i for polypropylene pellets during the principal flow regime is shown in Fig. 6.32. This was again treated as two linear sections: $0 < z_i < 0.27$ m and 0.27 m $< z_i < 1.21$ m. The final stage of the iteration for the lower section is shown in Fig. 6.33. From the value of the intercept, r^*_1 was found to be 0.374 m. Equation 6.1 then gave θ_1 to be 5.0°. The upper section was again found to be unstable to this analysis for the reasons discussed above.

In the post-refilling flow regime, the value of r^*_1 was expected to be smaller since the flow channel was wider and so the second iteration method was adopted. Plots of z_i against T/z_i^2 for sand and polypropylene pellets are shown in Figs 6.34 and 6.35 respectively. The points in these plots are accurately approximated by one linear best-fit line. From the intercepts, the initial vertical co-ordinates were adjusted as described above. The plots representing the final iteration stage are shown in Figs 6.36 and 6.37 for sand and polypropylene pellets respectively. The calculated values of θ_1 from Eq. 6.1 were 23.1° for sand and 26.3° for polypropylene pellets.

The flow channel angles that result from interpretation as a radial velocity field are presented in Table 6.2 and the FCBs for sand and polypropylene pellets are shown together in Fig. 6.38.

6.3.3.6 Comparison between the experimentally-determined FCBs

Four methods of determining the FCB from empirical data and visual observation have been detailed above. It can be recalled that these methods were:

(a) from visual observation though the front wall;
(b) from discontinuities in the residence time data;
(c) from isochrone maps; and
(d) from interpretation as a radial velocity field.

All the methods were used to determine the position of the quasi-stable FCB for principal flow. In addition, Methods (a) and (d) were also used to find the position of the FCB that forms in post-refilling flow.

The FCB obtained using Method (a) is the closest possible to the FCB that would occur in a full circular silo of the same dimensions. Method (a) cannot, however, be used for a full circular silo whereas the other three methods can be used. The FCBs using Methods (b) to (d) are here compared with the FCB using Method (a) to assess which of Methods (b) to (d) would be the most accurate to use when determining the FCB in a full circular silo.

The FCBs for principal flow determined from all four methods are shown for sand and polypropylene pellets in Figs 6.39 and 6.40 respectively. Figure 6.39 is

considered first and the FCBs from Methods (b) to (d) are compared to the FCB using Method (a). It can be seen that the FCB using Method (c) most closely matches the FCB using Method (a). Method (c) predicts a FCB that is slightly less curved (*i.e.* closer to the centreline) than Method (a) in the bottom half of the silo. The maximum discrepancy is, however, only 14 mm. In the upper half of the silo the match is very good. The match between the FCB using Method (a) and the FCB using Method (b) is also good. Method (b) involves using discontinuities in the residence time data to predict inner and outer bounds for the position of the FCB. It can be seen from Fig. 6.39 that the FCB as traced through the front wall (*i.e.* using Method a) lies between these inner and outer bounds for the whole of the height that the FCB was traced on the front wall apart from a short section between $0.6 < z/R < 1.2$. The FCB using Method (a) is wider than that using Method (b) over this height, the difference being a maximum of 21 mm. The FCB using Method (d) is quite different from the FCB using Method (a). Method (d) predicts a FCB that rises as an almost vertical column from the edge of the orifice. The reason for this is now discussed. Method (d) used only those tracers positioned close to the silo axis. These were discharged very soon after the orifice was opened. The predicted FCB therefore relates to the earliest stages of discharge (see Fig. 6.10a-c) well before the principal FCB has been attained.

The principal FCBs for polypropylene pellets (Fig. 6.40) are now considered. The FCB using Method (a) is again very similar to the FCB using Method (c) although the match is not as close as it is for sand (Fig. 6.39). The FCB using Method (c) is slightly wider than that using Method (a) below $z/R = 1.1$ and is slightly narrower than that using Method (a) above this height. It is seen that the FCB using Method (a) lies within the inner and outer limits of the FCB using Method (b) for the entire height the FCB was traced on the front wall. The FCB using Method (d) is again much narrower than the FCBs using Methods (a) to (c) for the same reasons as discussed above.

Comparing Figs 6.39 and 6.40, the principal FCBs predicted using all methods are wider in polypropylene pellets than in sand. Method (d) predicts that the FCB that forms immediately after the orifice has been opened takes the form of a vertical column for sand (Fig. 6.39) and a steep cone for polypropylene pellets (Fig. 6.40). Both Methods (b) and (c) could be used to predict accurately the position of the FCB in a full circular silo. If more tracers were used in each layer and more layers were placed in the silo, the predictive accuracy would increase. The experiments

carried out in this thesis used 26 tracers per layer and 10 layers. The maximum horizontal difference between the principal FCB using Method (a) and the FCBs using Methods (b) and (c) is 24.5 mm. This represents only 7% of the silo radius.

The post-refilling FCBs are now discussed. Two methods were used to predict the position of these boundaries: direct visual observation (Method a) and interpretation of the residence time data as a radial velocity field (Method d). The FCBs using these two methods are shown in Fig. 6.41 for sand and Fig. 6.42 for polypropylene pellets. In both sand and polypropylene pellets, the post-refilling FCB using Method (a) is quite curved in the lower section of the silo. Since the FCB using Method (d) can only predict a linear boundary, too accurate a match is not to be expected. The linear FCB using Method (d) does, however, provide a good overall estimate of the position of the FCB during post-refilling flow.

6.3.4 Trajectories

6.3.4.1 General

The trajectories of individual particles were traced through the transparent front wall as they travelled towards the orifice. By simulating the experiment numerically using the theory of Chapter 4, theoretical particle paths were calculated, as described in Chapter 5. These trajectories give information on the flow mechanics of the granular solid. The experimental and theoretical particle paths were qualitatively compared to assess how well the kinematic model can predict experimentally-observed particle trajectories. The comparison is carried out in Chapter 7.

The trajectories of particles were only traced during the experiments for post-refilling flow when the FCB had become stable and an expanded flow channel had been set up. In this flow regime, the curvature of the trajectories reached a maximum and so clearer comparisons could be made. For each solid, the trajectories of four particles were traced on the front wall using a water-soluble pen. It was found that the traced trajectories were very similar for both solids and only those obtained from experiments with polypropylene pellets are presented and discussed.

6.3.4.2 Results and discussion

The trajectories of four particles are shown in Fig. 6.43. The two trajectories closest to the centreline descended vertically for about two thirds of their journey. They then followed inclined approximately linear paths to the orifice, characteristic of a radial velocity field. The trajectories of the other two particles, closer to the side wall, descended almost vertically for a short distance and then turned quite abruptly to travel along roughly straight–line paths that traversed the silo at about 40° to the vertical. The particles continued on this course until they approached the centreline. Here the paths became almost vertical again and remained so for the rest of their journey. The inclined paths described here are for a flow pattern in which material sloughs off the top surface into a funnel flow. The inclined path occurs when the free surface reaches the position of the particle in question. Thus, although the flow pattern may be regarded as constant, the particle trajectories are more complex. After its movement towards the axis, the particle entered the flowing channel where the velocities were relatively high, and then discharged rapidly. This also explains why the residence times are closely grouped for tracers in horizontal layers near the top surface. The flow mechanism is shown in Fig. 6.10e.

The two trajectories closest to the centreline represent the motion of particles in a steady-state velocity field and are theoretically simulated in Chapter 7.

6.3.5 Experimental determination of the kinematic parameter B

6.3.5.1 General

Five experimental methods for the determination of the kinematic parameter B are described in this section. These methods were used to determine a value of B from:

(a) kinematic fitting of the flow channel boundary (FCB) as traced through the front wall;
(b) kinematic fitting of the residence times;
(c) measurements of velocity through the front wall;
(d) comparing results with the theory of Mullins (1974); and
(e) comparing results with the theory of Graham *et al* (1987).

Methods (a) and (b) use the kinematic model, developed in Chapter 4, to find a value for B that accurately fits the experimental data. These two methods, although described here, are implemented in Chapter 7 where comparisons between experimental results and theoretical predictions are made. A comparison between the values of B obtained from all five methods is also presented in Chapter 7. Method (c) was used to estimate a value for B directly from measured velocities. The last two methods (d and e) compare the experimental data with analytical solutions, again to find a value of B that provides an accurate fit.

In Methods (b) and (d), the residence times of tracers closest to the centreline were used. It was easy to position these tracers during post-refilling flow, since the free surface formed a crater. As mentioned in Section 6.3.1, these tracers discharged before the attainment of the principal FCB. For this reason, the values of B relating to these tracers are expected to be slightly lower than values of B relating to the stage when the principal FCB has been set up.

6.3.5.2 Determination of B from the FCB as traced through the front wall

In this method, the FCB was traced on the front wall as described in Section 6.3.3.2. The FCB was then compared with numerical predictions from the kinematic model of Chapter 4. The value of B in this model was spatially varied in such a way that a good fit with the experimental results was obtained. Tuzun and Nedderman (1979a) reported that the kinematic 'constant', which they measured experimentally, increased slightly with height. For this reason, variations that set the kinematic parameter B to increase with height z were used in the kinematic model. This method of assessing a value of B was used during principal and post-refilling flow for both solids.

The small retarding effect of the front wall reduces the absolute velocities which are observed to values slightly below those that would prevail in a vertical plane through the axis of a circular silo. For the purpose of this thesis, the FCB was defined in Chapter 3 as the locus of points where the vertical velocity falls to 1% of that at the centreline at the same height. To take some account of the retardation effect, it was assumed that the glass reduced the local velocity by a factor which is invariant with radius r and axial height z (*i.e.* that the velocity of any particle adjacent to the front wall is a constant factor of the velocity that would occur at the

same point on the vertical plane of symmetry in a circular silo). Therefore, if the FCB is traced in experiments at 1% of the centreline velocity, the FCB obtained on the front wall of a half-cylindrical silo is identical to that which would have been obtained in a circular silo.

By altering the value of the kinematic parameter B in the numerical model, a variety of FCBs are predicted. By choosing a good physical fit to the observed FCB, a value of B which closely represented the experimentally-observed FCB was found. Comparisons of the experimental and theoretical FCBs are presented in Chapter 7.

6.3.5.3 Determination of B from measured residence times

A value for the kinematic parameter B can be estimated from measurements of the tracer residence times. The corrected residence times of those tracers closest to the centreline, due to the front wall retardation (see Section 6.3.2.3), were used to estimate the variation of B with height. This method of estimating B was used during both the principal and post-refilling flow regimes. In addition, the corrected residence times of the other tracers, due to the initial transient (see Section 6.3.2.4), were used to estimate the variation of B with radial co-ordinate. This method was used only in the principal flow regime, since it was not possible to position tracers at varying distances from the centreline during the post-refilling flow regime. Estimates of B are based upon a comparison of the experimental residence times with numerically-predicted residence times.

Plots of the starting height of a tracer above the orifice z_i against the residence time T during the principal and post-refilling flow regimes of sand and polypropylene pellets are shown in Fig. 6.28. Plots of the residence time T against the radial co-ordinate r/R at different heights for polypropylene pellets are shown in Fig. 6.15. In Chapter 7, these experimental plots are matched with the theoretical predictions from the kinematic model developed in Chapter 4. Linear variations of B with z_i/R and B with r/R are used in the kinematic model. In this way, a value of B is obtained which best fits the data.

6.3.5.4 Determination of B from measurements of velocity

The kinematic model is based on Eq. 3.1 which relates the horizontal velocity u to the horizontal gradient of the vertical velocity $\partial v/\partial x$. If, at a particular point, u and $\partial v/\partial x$ are known, then an estimate of B can be found at the point from

$$B = -\frac{u}{\partial v/\partial x} \tag{6.7}$$

It has been mentioned above that the front wall has a retarding effect on the flowing granular solid moving behind it. The velocity of the flow as observed through the front wall is therefore slightly less than the velocity that would occur on a vertical central plane in a circular silo but the differences are clearly small. However, since the calculation of B is based on the ratio of a velocity and a velocity gradient the frictional effect of the front wall on this assessment is small and a reasonably accurate value for B can be calculated.

The paths of two particles were traced on the front wall with a water-soluble pen. The time each particle took to travel its path was noted. The paths were chosen to be side by side and the total vertical displacement used in this assessment was kept to 100 mm, for reasons discussed below. Paths were not taken near the centreline since the value of $\partial v/\partial x$ was small here, which could result in large errors when B was calculated. The tracing of particle paths in the very slow-moving regions of solid was also avoided since the motion of these particles was often intermittent.

An example of a pair of paths is shown in Fig. 6.44. The paths are seen to be slightly curved. By restricting the vertical displacement to 100 mm, the curvature could not, however, become large. The paths were therefore assumed to be straight over this small distance. The error involved in making this assumption is discussed below. A vertical displacement less than 100 mm was not chosen because the particles would complete their paths very quickly and stopwatch errors would become prominent.

The value of the mean vertical velocity was calculated as the vertical distance travelled (100 mm) divided by the time taken for the particle to complete its path. The mean horizontal velocity was similarly calculated by dividing the distance the particle travelled in the horizontal direction by the time taken to complete the path. These two mean velocities were calculated for each path of the pair. The mean

velocities were taken to represent the value at the centre of the straight line joining the path's starting and finishing co-ordinates (Points A and B in Fig. 6.44). Because all velocities were assumed to be means, the curvature of the path had no effect on the velocity calculations. The only effect the curvature of the paths had was on the position where the mean velocities were assumed to occur. The maximum error involved in determining this position was estimated at only 10 mm, so the straight-line assumption was quite acceptable. The difference between the two mean vertical velocities divided by the horizontal distance between the points A and B gave an estimate of $\partial v/\partial x$. Since $\partial v/\partial x$ varies throughout the silo, the estimate was taken to represent the value of $\partial v/\partial x$ at Point C (Fig. 6.44). The horizontal velocity at C was estimated as the mean of the horizontal velocities at A and B. These two estimates were used in Eq. 6.7 to estimate the local value of B. An example of this calculation is shown in Appendix 6.3.

This method of determining B can only be used reliably in broad funnel flows, because it requires estimates of $\partial v/\partial x$ and the horizontal velocity u to be able to be made over a wide zone. In the principal flow regime, the trajectories of particles were almost vertical, so estimates of u were susceptible to large errors (*i.e.* the velocities are insensitive to the value of B, so this data is not useful in evaluating B). The values of B calculated at several points in the post-refilling flow regimes for polypropylene pellets and sand are presented in Tables 6.3 and 6.4 respectively. The mean value of B and the coefficient of variation are 18 mm and 68% for the data relating to polypropylene pellets. For sand, these values are 12.5 mm and 55%. The huge spread of calculated values of B in these tables (reflected by the relatively high coefficients of variation) shows immediately that a single value cannot really be adopted for the whole silo.

A linear regression to the data for polypropylene pellets (Table 6.3) yielded the following relationship: $B = -1.6 + 0.05r + 0.04z$ mm. For the data relating to the post-refilling flow regime of sand (Table 6.4), the equivalent relationship was $B = -24.5 + 0.25r + 0.04z$ mm. As can be seen, the kinematic parameter B, as measured using this technique, increases with both height and radial co-ordinate for both solids. The variations are quite systematic. It may be noticed that both regression fits predict a negative value of B at the centre of the orifice $r = z = 0$. This is counter-intuitive in terms of the kinematic model (Eq. 3.1) and may be because the grains have started to free fall in the region just above the orifice so the kinematic theory is no longer valid here. Negative values of B are predicted in

regions close to the orifice and for some height above it. The range may be acceptable for the polypropylene pellets, but the zone calculated for the sand is much too large to be reasonable. This may be due to the limited number of observations made for sand. It seems therefore that a non-linear regression with a constraint to positive values may be required. However, the data is insufficient to support such an analysis here and the linear variations are adopted as a first approximation. However, it is clear that direct observations of the value of B indicate strong spatial variations, presumably as a result of packing density variations.

6.3.5.5 Determination of B after Mullins (1974)

Mullins (1974) developed an expression for the residence time of a particle discharging from a flat-bottomed bed of granular solid. The expression involves the particle's starting co-ordinates and the kinematic constant B of the solid. Expressions for both planar and axisymmetric geometries are given. His steady-state analytical theory assumes that the granular solid forms a semi-infinite bed and discharges through a point orifice. The expression for axisymmetric geometries is

$$T = \frac{2\pi B}{Q} \, e^{\frac{r_i^2}{4Bz_i}} \, z_i^2 \qquad (6.8)$$

In this equation, T is the residence time, B is the kinematic constant, (r_i,z_i) are the co-ordinates of the particle before discharge and Q is the volumetric flow rate.

When tracers are placed on the silo axis, $r_i = 0$ and Mullins' relationship reduces to

$$T = \frac{2\pi B}{Q} \, z_i^2 \qquad (6.9)$$

Thus, it is to be expected that the residence time for these tracers will vary as z_i^2, and linearly with B. Equation 6.9 is therefore used here to estimate a mean value for B for the complete silo, assuming a homogeneous particulate solid.

Although the theory of Mullins assumes steady-state conditions, Eq. 6.8 can be applied to both the principal and post-refilling flow regimes. The FCB and velocity

fields change with time during principal flow, so strictly-speaking the steady-state theory of Mullins should not be applied to this flow regime. (Principal flow is defined as the flow regime that begins with the initial opening of the orifice and ends with the formation of a quasi-stable FCB). For the purposes of interpreting the behaviour, it is assumed here that the residence time data obtained during principal flow is that for the time interval from the initial opening of the orifice until the tracer that was positioned closest to the centreline in the highest layer exits the orifice. If it is assumed that the flow conditions approximate those of steady-state during this time interval, Eq. 6.8 can be used to estimate a mean value for B for the whole silo during the initial stages of principal flow.

Because a half-cylindrical silo is used, it is not possible to position tracers exactly on the centreline of the silo (*i.e.* at $r_i = 0$). As a consequence, the exponential term in Eq. 6.8 does not become unity and a numerical iteration procedure is required to determine a value for B. In the iteration procedure used here, the exponential term was initially ignored and T was plotted against z_i^2. A linear best-fit line was constructed and, from the gradient of this line, an estimate of B was calculated for the known volumetric flow rate. The exponential term was then approximately evaluated using this first estimate of B. The residence time was then plotted against this estimate of the exponential term multiplied by z_i^2. The gradient of the new best-fit line yielded a new estimate for B. This process of iteration was continued until the value of B converged to an accuracy of 1 mm. However, for all the experiments described here, it was found that the initial plot of T against z_i^2 provided the required accuracy. This is because the tracers were positioned at a radius of only 0.025 m and the exponential term is generally close to unity. This finding also strongly supports the assumption used elsewhere in this chapter, that data from the tracers closest to the silo centreline closely represent the behaviour on the centreline. Plots of T against z_i^2 for sand and polypropylene pellets in both the principal and post-refilling flow regimes are shown in Figs 6.45-6.48.

The data plotted in Figs 6.45 and 6.46 show that the approximation to a linear relationship between T and z_i^2 is very reasonable in the principal flow regime. The experimental data can be accurately matched using a single value of B. In the post-refilling flow regime (Figs 6.47 and 6.48), the data is matched more accurately by constructing two linear lines, corresponding to two different values of B. A higher value of B is found in the top section of the silo for both solids. The values of B obtained from all these linear best-fit lines are included in the figures and are also

shown collectively in Table 6.5. It is seen that the values of B are smaller for principal flow than for post-refilling flow for both solids. This is to be expected since the principal flow regime had a much narrower flow channel than the post-refilling flow regime. In post-refilling flow, the value of B is predicted to increase with height. The experiments for principal flow using sand yielded a lower value of B than those using polypropylene pellets. In the experiments on the post-refilling flow regime, the values of B for the top and bottom sections of the silo are very similar. The only significant difference is the height at which B changes. These results reflect the different flow conditions observed in the experiments. After discharge has been initiated, sand rapidly formed a very narrow column of flowing solid that stretched up from the orifice (B = 3.7 mm). The principal flow channel in polypropylene pellets was, however, slightly wider which is reflected in the higher value of B of 9.6 mm. However, the post-refilling flow regimes of both solids yield very similar values of B, suggesting very similar sizes of flow channels.

These values of B were substituted into Eq. 6.8 and analytical predictions of initial vertical co-ordinate z_i against residence time T were obtained. These are compared with the analogous experimental plots in Figs 6.49-6.52. In using Eq. 6.8, care was taken to avoid calculating residence times of tracers at very low initial heights, since the analytical solution of Mullins (1974) becomes singular at $z_i = 0$. It is seen from Figs 6.49 and 6.50 that a single value of B adequately describes the relationship between z_i and T for principal flow. For post-refilling flow (Figs 6.51 and 6.52), however, the relationship is characterised by one value of B in the lower section of the silo and another value in the upper section. A single value of B would not be sufficient. The data for the post-refilling flow regime for polypropylene pellets (Fig. 6.52) are quite accurately described by using two distinct values of B but the post-refilling flow regime for sand (Fig. 6.51) is less convincing. A linear variation of B with height would perhaps be better in this case. Such variations in the kinematic parameter cannot be accommodated using the theory of Mullins (1974) but can be taken account of with the numerical model of Chapter 4. The relationship between z_i and T is one of the correlations examined in Chapter 7.

It can therefore be concluded that the analytical solution of Mullins (1974) provides a reasonable approximation for the residence times of tracers on, or close to, the centreline during principal flow. In post-refilling flow, however, a single value of B for the whole silo was found to be inadequate.

6.3.5.6 Determination of B after Graham *et al* (1987)

Graham *et al* (1987) assumed that the granular solid concentrically discharged from an axisymmetric silo through a point orifice. This enabled them to exploit a standard series solution to find the vertical velocity distribution. They numerically integrated this velocity down the centreline and obtained a unique plot of dimensionless residence time against dimensionless initial height on the centreline. They found that the gradient of this plot tends to unity as the initial height increases and that the asymptote intercepts the vertical axis at $z_iB/R^2 = 0.14$. The value of this analytical intercept can be used to calculate a value for B from experimental plots of initial height against residence time. This method was used to estimate a mean value for B, assuming a homogeneous bulk solid, for both the principal and post-refilling flow regimes.

Figure 6.53 shows a plot of initial height z_i against residence time T for sand during principal flow. Figure 6.54 shows a similar plot for polypropylene pellets during principal flow, and Fig. 6.55 shows the plots for both solids during post-refilling flow. In all these figures, it can be seen that as z_i increases, the curves of z_i against T gradually become less steep. In the upper section of the silo, the gradient dz_i/dT approaches a constant value. For the post-refilling flow regime (Fig. 6.55), this gradient has reached its constant value for both solids and so a value of B can be reliably predicted. For the principal flow regime (Figs 6.53 and 6.54), however, this gradient has not yet stabilised, particularly for sand (Fig. 6.53). The values of B for principal flow are therefore only upper limits. The values of the intercept z_iB/R^2 are shown in the figures and the values of B deduced from these are presented in Table 6.6. It can be seen that the values of B for principal flow are so close to those for post-refilling flow that they probably do not provide an accurate measure of the magnitude of B. If the silo used in these experiments was much taller, the gradient dz_i/dT would have reached its constant value for principal flow.

Three of the five methods used to estimate B have been implemented above. The remaining two methods (Methods (a) and (b) listed in Section 6.3.5.1) are implemented in Chapter 7 where comparisons between all the methods used to estimate the kinematic parameter B are also made.

6.4 Conclusions

In this chapter, a detailed description the experimental apparatus has been given. Four methods have been described to determine the position of the FCB and the resulting estimated boundaries have been compared. A good match was found between direct visual observation of the principal FCB and two methods of deducing this boundary from residence time data. These two methods estimated the principal FCB from discontinuities in residence time data and from isochrone maps. These results strongly recommend these two methods for use in predicting the principal FCB in full circular silos. The method of interpreting the flow behaviour as a radial velocity field can be used to provide a good estimate of the post-refilling FCB in full circular silos.

Particle trajectories have been traced and these are compared with theoretically-predicted trajectories in the Chapter 7.

Five methods have been described for estimating the kinematic parameter B. Two of these methods rely on fitting the numerical kinematic model predictions to the experimental data. This is carried out in Chapter 7 where comparisons between the values of B yielded from all five methods are also made.

Appendix 6.1 Data sheet for sand

Time (secs)	z/R=0.34	0.68	0.99	1.32	1.69	2.15	2.77	3.38	4.03	4.31
0.7	26									
1.4		26								
2.2			26							
3	21-23			26						
3.8	24,25	21-24								
4.5		25	22,23		26					
5.3			21,24,25	23						
6.1				22,24,25						
7.2				21	23	26				
8.2					22,24,25					
9.2					21	23				
10.5						22,24				
11.5						21,25	26			
12.5										
13.8							23			
15.1							24			
16.2							22,25			
17.5							21	26		
18.8								23		
20.1								24		
21.1										
22.1								22,25		
22.9										
24.4								21	26	
25.8				18						
27.3										
28.5			18	17,19	17				23	26
29.7					18				22	22-24
30.7			17		19				24,25	21,25
31.7					20					
33						17			21	16-18
34.2						18				19,20
35.6										
37						19				
38			19							12,13,14
39.3										11,15
40.6				20			18,19			
42					16					
43.4						16,20	17			
44.7									18	7,8
46.4								18	17,19	6
47.9				16				19		
49.3		17,18						17		10
50.6							20		20	9
52.4			16							3
53.9									16	2
55.7							16		13	
57.4								20		
58.7										4
60										1
62										5
63.7									12,14	
66										
67.8		19							11,15	
69.4									8	
71.1								16	7	
73.4			20							
75.4										
77.5									4,9	
79.5									3	
81									10	
82.9										
85									1,5	
86.5									6	
90.6										
93.8									2	

Time (secs)	z/R=0.34	0.68	0.99	1.32	1.69	2.15	2.77	3.38	4.03	4.31
95.5						13				
99.6					13		12	12		
103							13			
107								13		
111		16				12		14		
113						14	14	8		
117								10		
119										
122								15		
124								4,6,9		
127					14			1,3,5,11		
130										
133					12					
137								2,7		
140										
142				13						
143							3			
146							6			
149							1			
153							5			
155							4,8,10			
158				12			2			
162							9,15			
166							7,11			
171										
175						3				
179						2				
181						8,10				
183						1,6				
185						4,5,9				
188						7,15				
172										
196										
198					6,15					
201					8,9,10					
204					2,3					
207					1,4,7,11	11				
211					5					
215										
218				11,15						
221				7,8,9,14						
225				6						
228				10						
232			11,13,14							
235			12							
240			15							
242			6,7,8							
245		20	9							
248			10							
251		11,12,14								
255		13,15								
257										
260										
263	16-20									
265		7,8,9								
269		6,10								
275										
278		1								
284		3								
292	13									
300		4								
309	11,14	5								
320	12	2								
322	15									

Appendix 6.2 Data sheet for polypropylene pellets

Time (secs)	z/R=0.15	0.35	0.62	0.83	1.11	1.54	1.97	2.49	3.23	3.71
0.8	26	26								
1.7		21,22,24	26							
2.7		23,25	23-25	26						
3.7	24,25		21,22	22-24						
4.7	23			21,25	26					
5.4					23,24					
6.5					21,22,25					
7.5										
8.5	21,22									
9.9						23-26				
11.1						21,22				
12.4										
13.7										
15.1			18	18	18		26			
16.3				17			26			
17.5				19	19		22-25			
18.6					17					
19.6							21			
21.2						19				
22.5			19		16	18				
23.9			17	16	20					
25						17	18			
26.1						20	19			
27.4			20	20						
28.6								23,26		
29.9							17,20	22,24,25		
31						16		21		
32.2										
33.3										
34.5										
35.7			16					18		
36.9										
38.3										
39.6								17,19		
40.7							16			
42.3										
43.7										
45.2										
46.6								20		
48								16		
49.4										
50.7										
52.2									26	
53.5									23,24	
54.8					13				22,25	
56									21	
57.3										
58.6									19	
60		19							18	
61.1						13				
62.2										
63.5					14	14			20	
64.8					12		13			
66.1									17	
67.5										23-26
68.8										18,19,21,22
70.2										
71.7							14			17,20
73.6										
75						12				13,14,16
76.3									16	15
77.8		17								12
79.5				13				13		
81.2							12			11
82.9										8
84.7										

Time (secs)	z/R=0.15	0.35	0.62	0.83	1.11	1.54	1.97	2.49	3.23	3.71
86.4										
88										9
89.5										7
91.4				12						
92.9								14		10
94.5								12	13	6
96										
97.4									14	
99.1										
101										3,5
103										4
104						15			12	
106										2
108										
110							15			1
112										
114		18								
116									15	
118										
120										
122										
124										
126										
128					11					
130								15		
132										
134						11			7	
136				14						
138					15				5	
141									3,10	
143										
145									4	
147								11	1,6	
150									2	
152			13				11			
154							8			
157										
159								8		
162										
166										
169										
173										
178						8				
181								1,5,6,10		
184								2-4,7		
186								9		
190										
198										
200							6,9,10			
204							3,4			
206							2			
209							1,5			
216										
219						6	7			
221						10				
224						2,3,4				
228		16				1,5				
232										
234										
238					7	7				
241					6,9,10					
245					3	9				
248				15	2,4					
252				8,11	1,5					
255				7,9	8					

Time (secs)	z/R=0.15	0.35	0.62	0.83	1.11	1.54	1.97	2.49	3.23	3.71
258			12,14	6,10						
262			15							
264			11	2,3,4,5						
268				1						
271		20	7,8,9							
274			6,10							
278		12								
281		13,15	2,3							
285		11,14	4							
290			5							
294										
298	19		1							

Appendix 6.3 Determination of the kinematic parameter from velocity measurements

An example is given of a calculation to determine B from measurements of velocity through the front wall. The notation is shown in Fig. 6.44 and an example set of readings are given below. Radial r and axial z co-ordinates are in millimetres and times t_1 and t_2 are in seconds.

r_1	z_1	r_2	z_2	r_3	z_3	r_4	z_4	t_1	t_2
135	500	110	400	185	500	145	400	15.4	34.0

The point A (see Fig. 6.44) is the midpoint of the assumed straight line path between the starting co-ordinates (r_1,z_1) and the finishing co-ordinates (r_2,z_2) of the path nearest the centreline. Point B is the analogous position on the other path. The vertical velocity at A, v_A, can be approximated as

$$v_A = \frac{z_2 - z_1}{t_1} \tag{A6.1}$$

and the horizontal velocity at A, u_A, can be approximated as

$$u_A = \frac{r_2 - r_1}{t_1} \tag{A6.2}$$

Analogous expressions can be written for the vertical and horizontal velocities at B, v_B and u_B. Evaluating such expressions, the following velocities are obtained: v_A = -6.49 mm/s, u_A = -1.62 mm/s, v_B = -2.94 mm/s and u_B = -1.18 mm/s. The horizontal gradient of vertical velocity at C can now be approximated as

$$\left.\frac{\Delta v}{\Delta r}\right|_C = \frac{v_B - v_A}{r_B - r_A} \tag{A6.3}$$

where

$$r_B - r_A = \left(\frac{r_3 + r_4}{2}\right) - \left(\frac{r_1 + r_2}{2}\right) \tag{A6.4}$$

Equations A6.3 and A6.4 yield the horizontal gradient of the vertical velocity at C to be 0.084 /s. The horizontal velocity at C can be approximately calculated as the average of the horizontal velocities at A and B *i.e.*

$$u_C = \frac{u_A + u_B}{2} \tag{A6.5}$$

Thus u_C = -1.40 mm/s. A value of B can now be found as

$$B = -\frac{u_C}{\left.\frac{\Delta v}{\Delta r}\right|_C} \tag{A6.6}$$

Hence B = 1.40/0.084 = 16.7 mm.

Table 6.1 Frictional properties of the tested solids

	sand	polypropylene pellets
ϕ_i	43°	25°
ϕ_{ws}	25°	17°
ϕ_{wg}	20°	14°

Table 6.2 Values of θ_1 from radial velocity field interpretation

	principal flow	post-refilling flow
sand	z/R < 1.4 0.76° z/R > 1.4 unstable	0 < z < H 21.3°
polypropylene pellets	z/R < 0.85 5.0° z/R > 0.85 unstable	0 < z < H 26.3°

Table 6.3 Experimental calculations of B from observation for polypropylene pellets

r_{mean} (mm)	z_{mean} (mm)	B (mm)
140	450	16.7
105	250	6.1
25	350	9.3
90	450	24.6
90	250	11.7
100	550	38.7

Table 6.4 Experimental calculations of B from observation for sand

r_{mean} (mm)	z_{mean} (mm)	B (mm)
80	380	12.1
80	550	19.6
60	350	5.8

Table 6.5 Values of B (mm) after Mullins (1974)

	principal flow	post-refilling flow
sand	3.7	$0 < z/R < 2.4$ 12.9 $2.4 < z/R < 4.2$ 20.1
polypropylene pellets	9.6	$0 < z/R < 1.8$ 13.0 $1.8 < z/R < 3.7$ 20.2

Table 6.6 Values of B (mm) after Graham *et al* (1987)

	principal flow	post-refilling flow
sand	≤ 19.8	21.7
polypropylene pellets	≤ 28.6	28.4

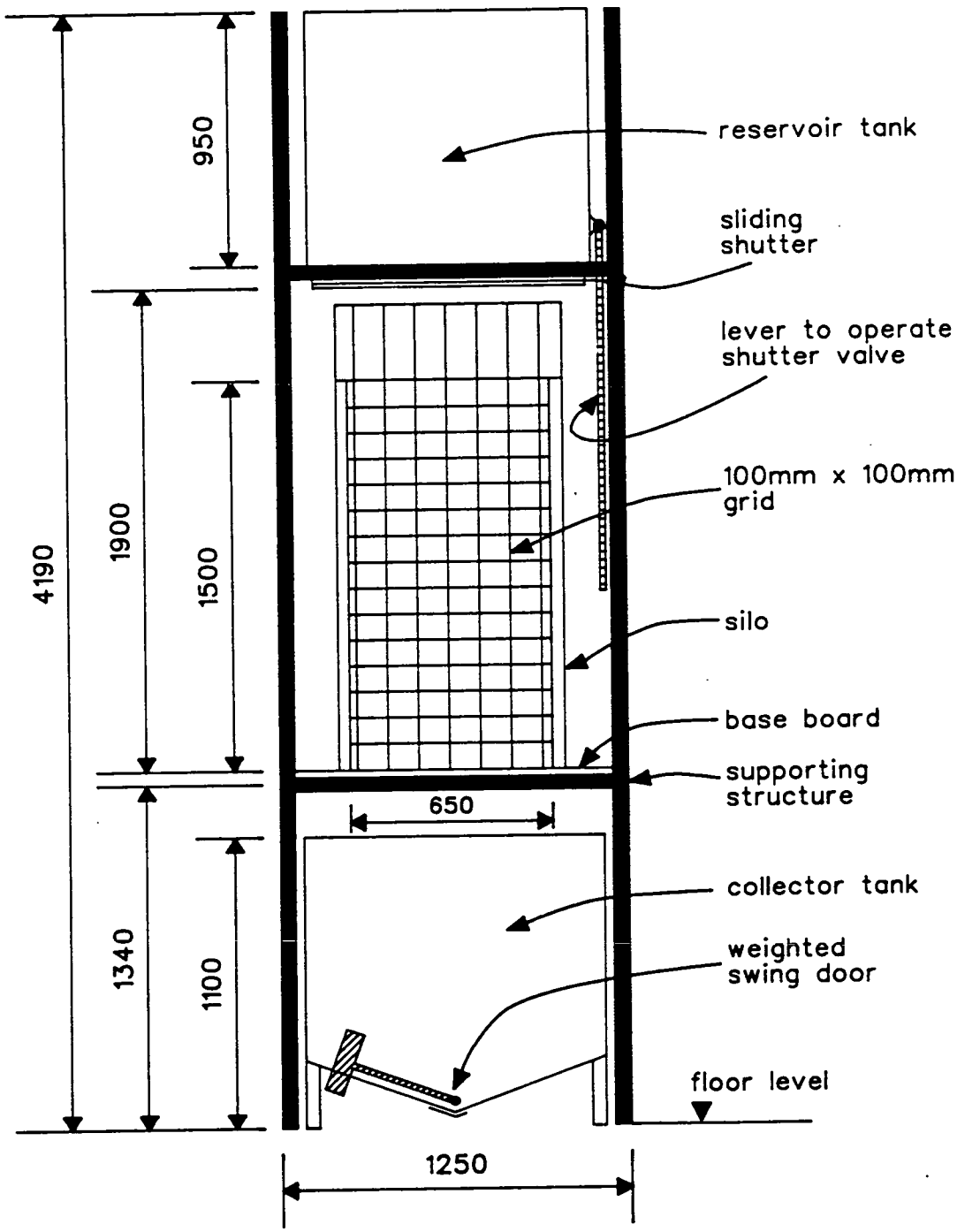

Fig. 6.1 Diagram of silo used in the experiments

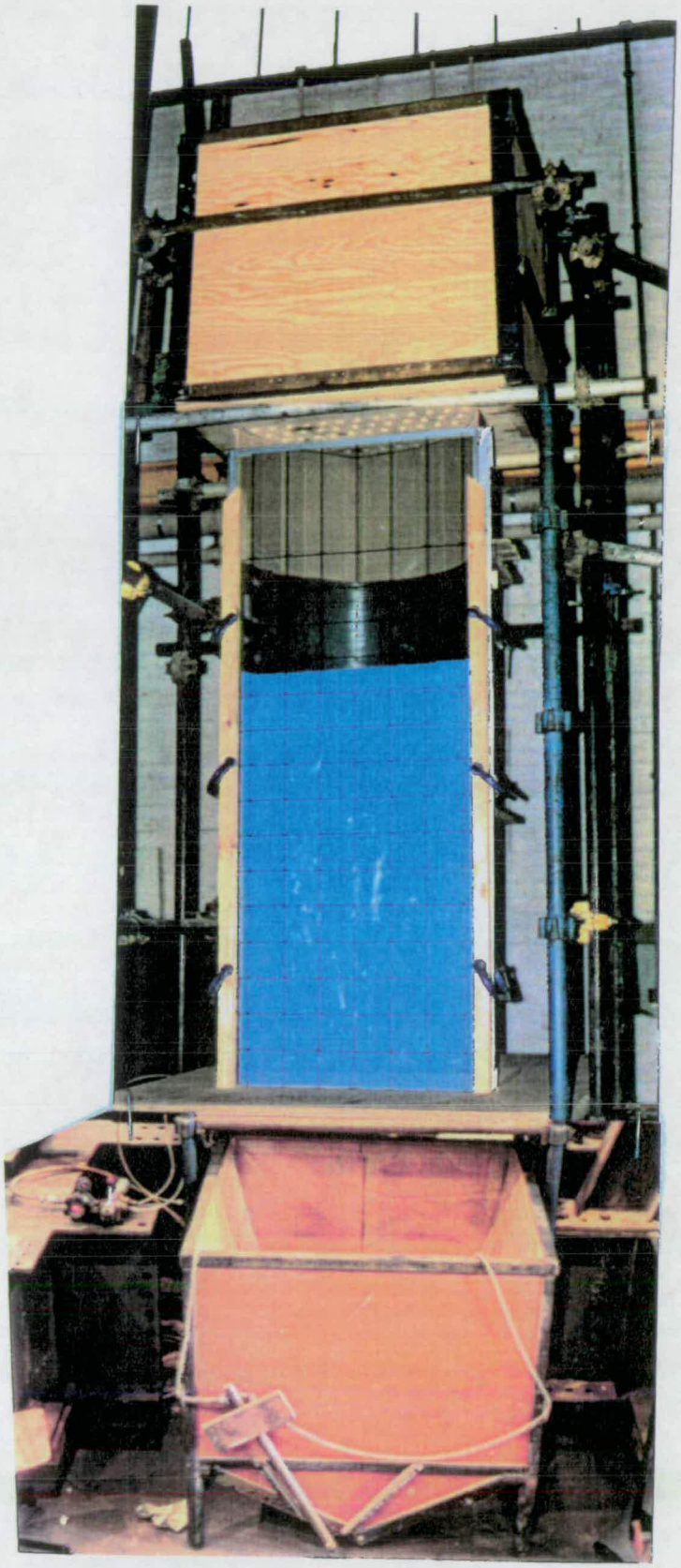

Fig. 6.2 Photograph of silo used in the experiments

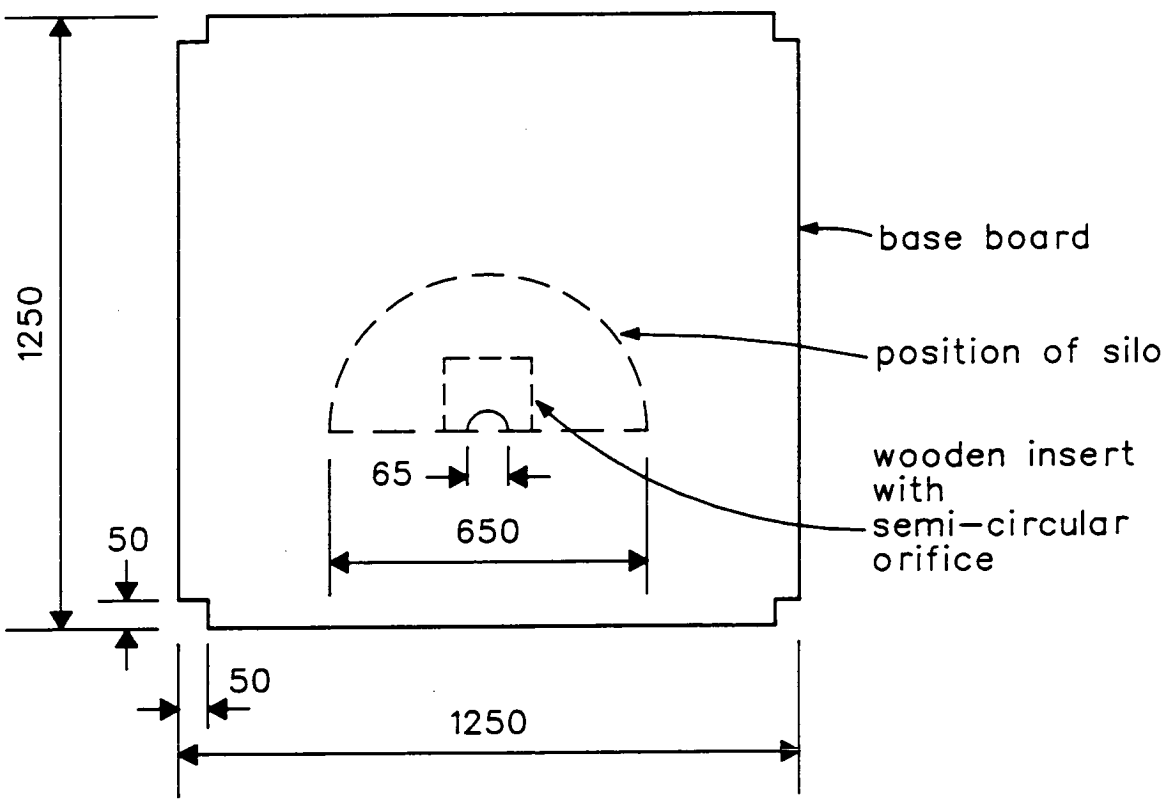

Fig. 6.3 Plan view of silo

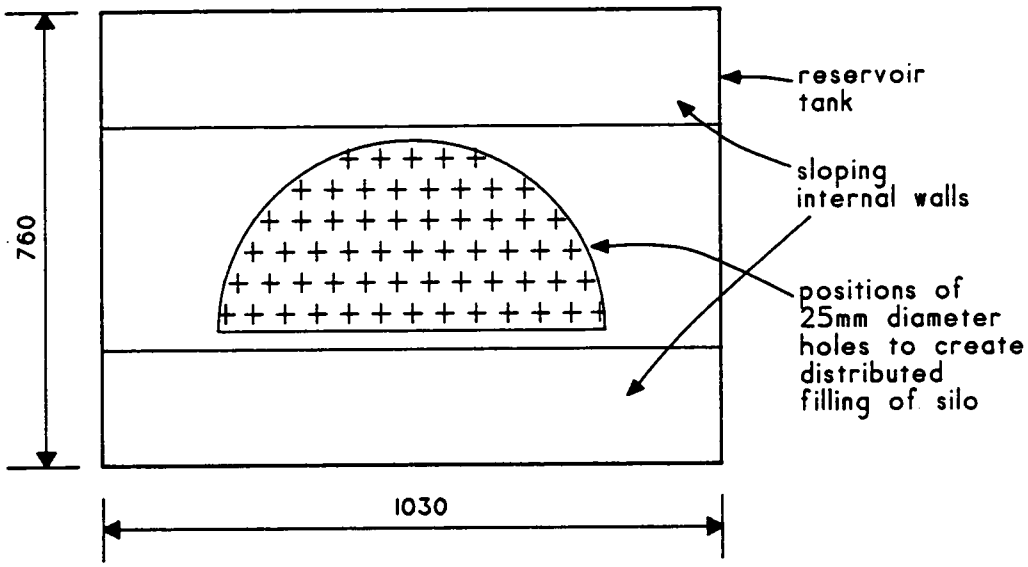

Fig. 6.4 Plan view of reservoir tank

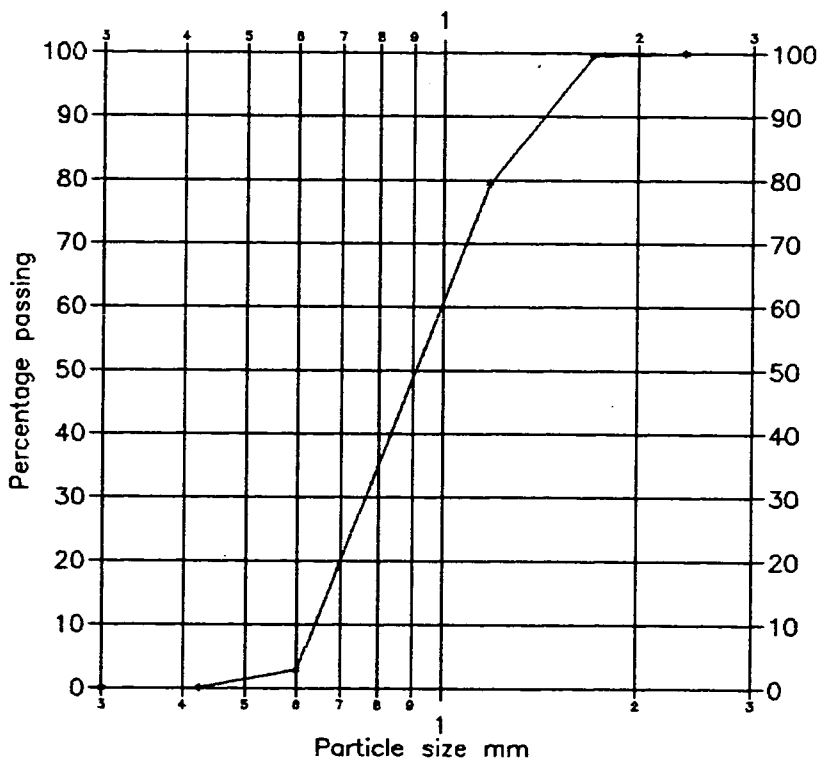

Fig. 6.5 Particle size distribution for sand used in experiments

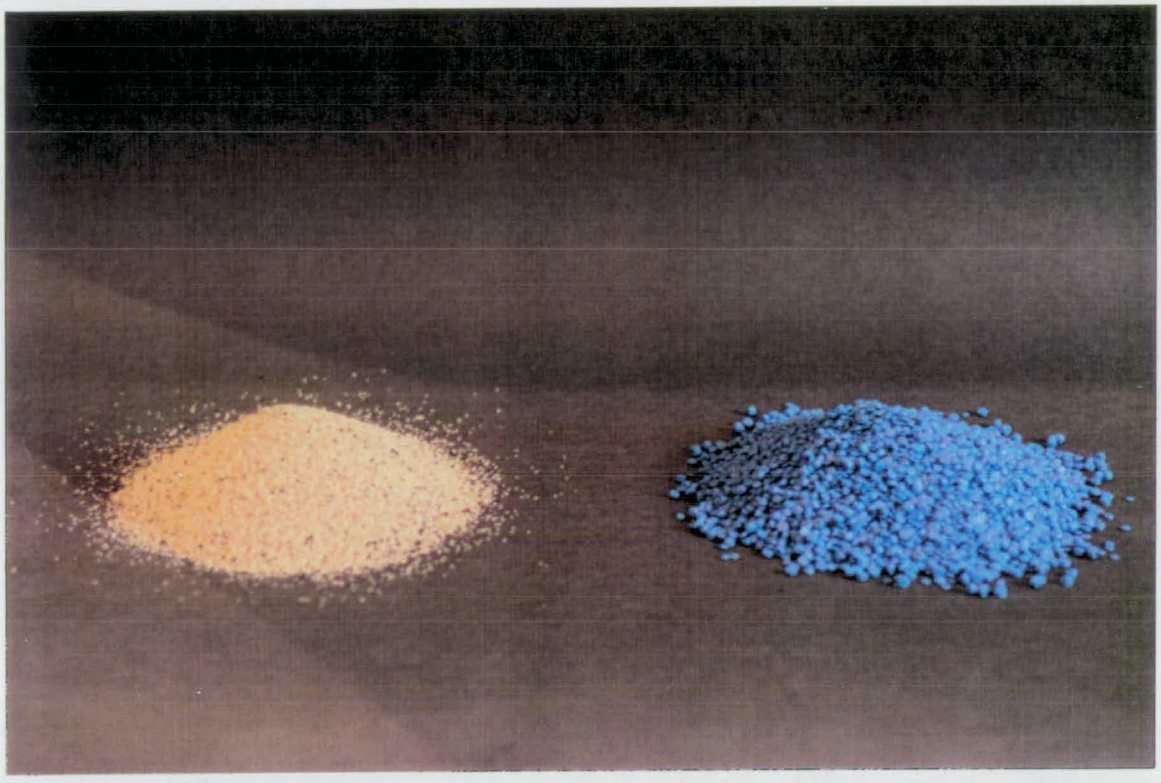

Fig. 6.6 Samples of tested solids

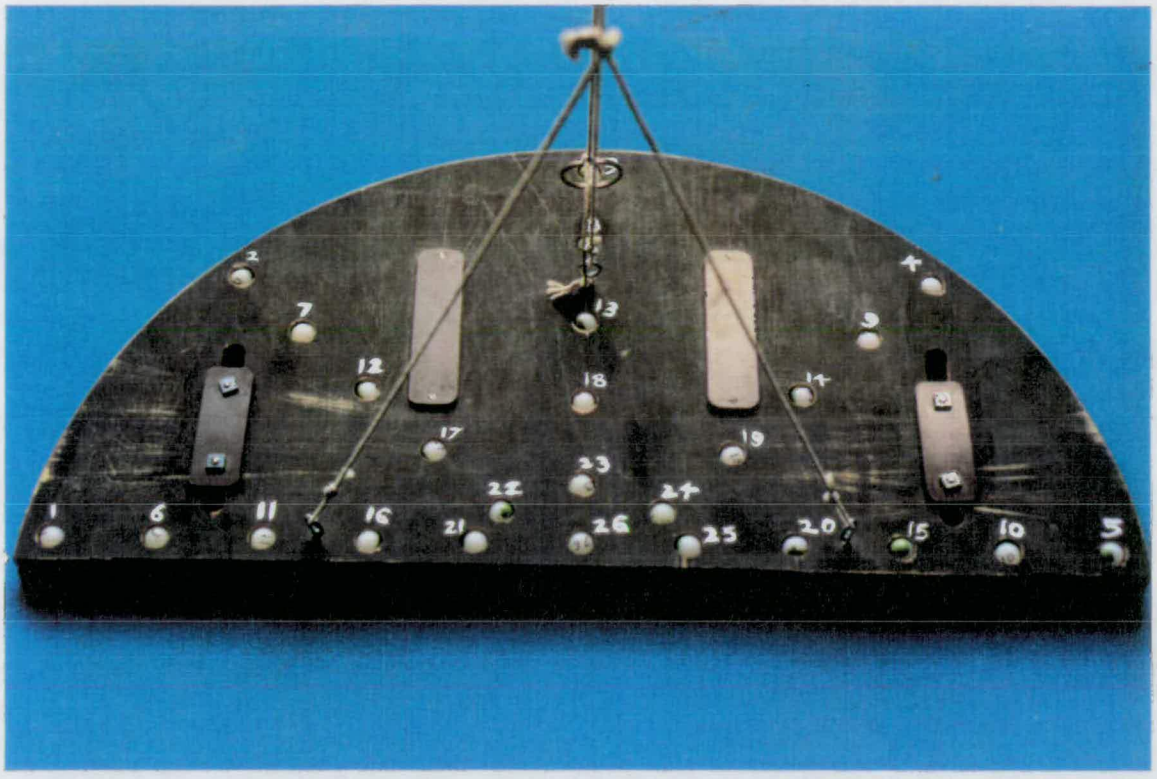

Fig. 6.7 The tracer seeding tray

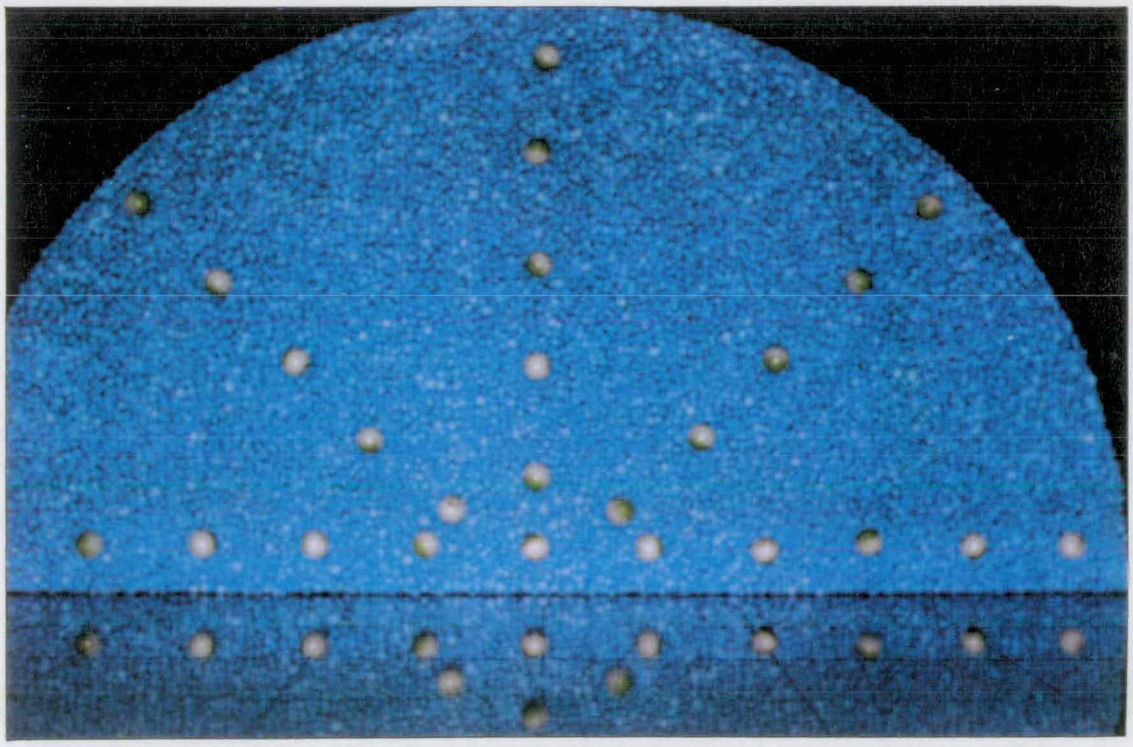

Fig. 6.8 Pattern of tracers on solids surface

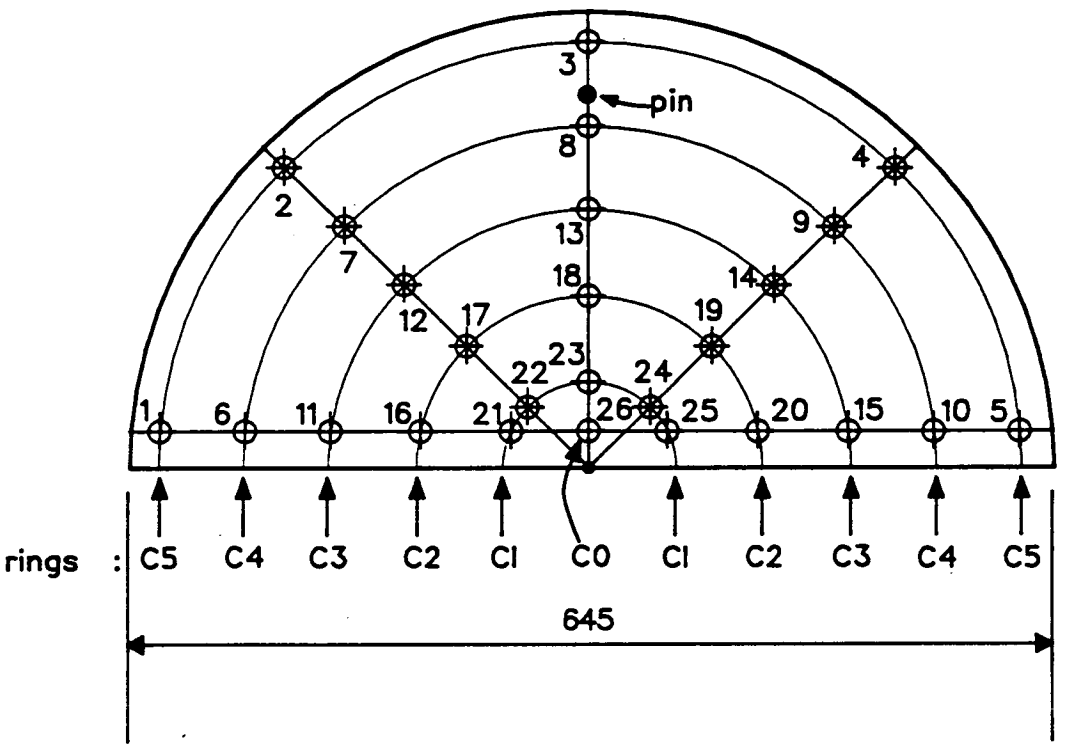

Fig. 6.9 Layout of tracer seeding tray

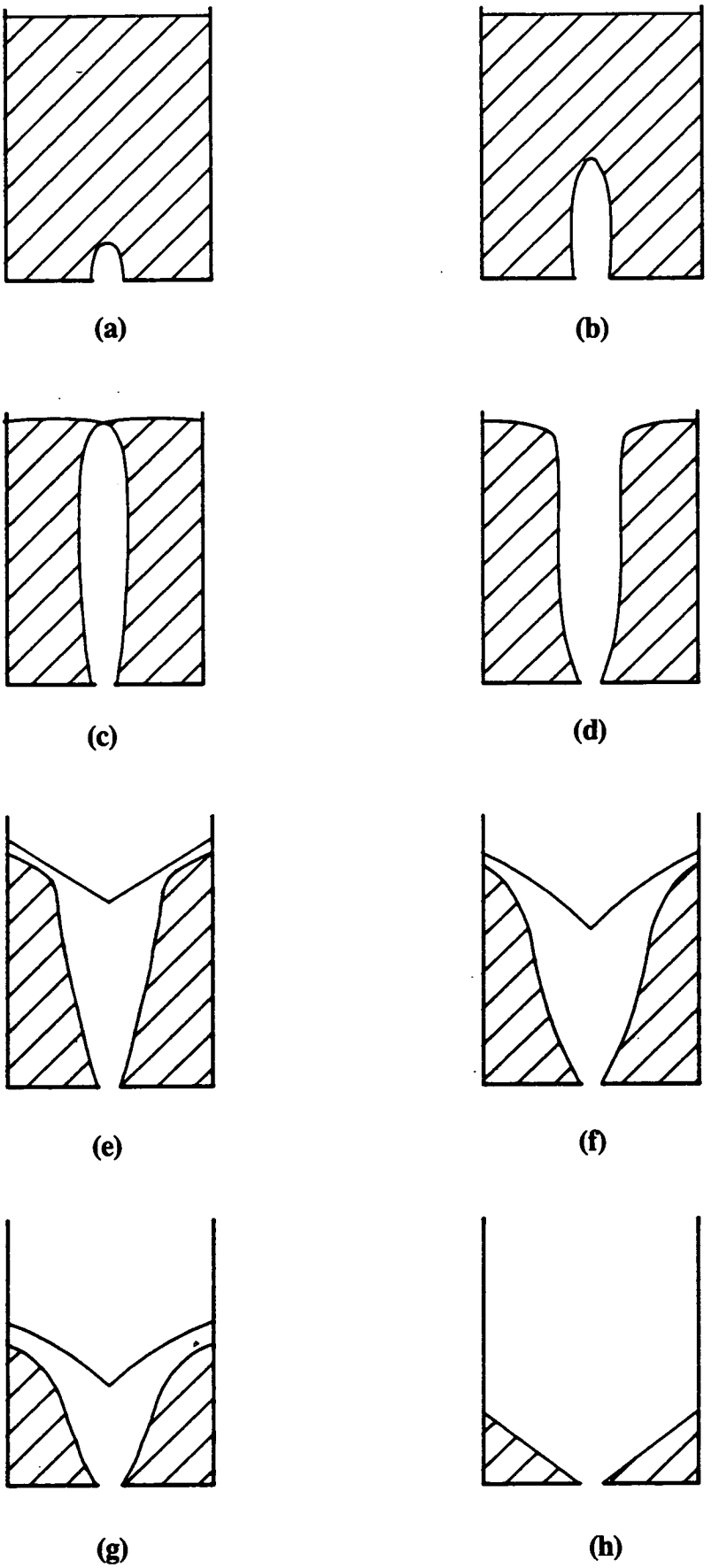

Fig. 6.10 Flow pattern stages (schematic)

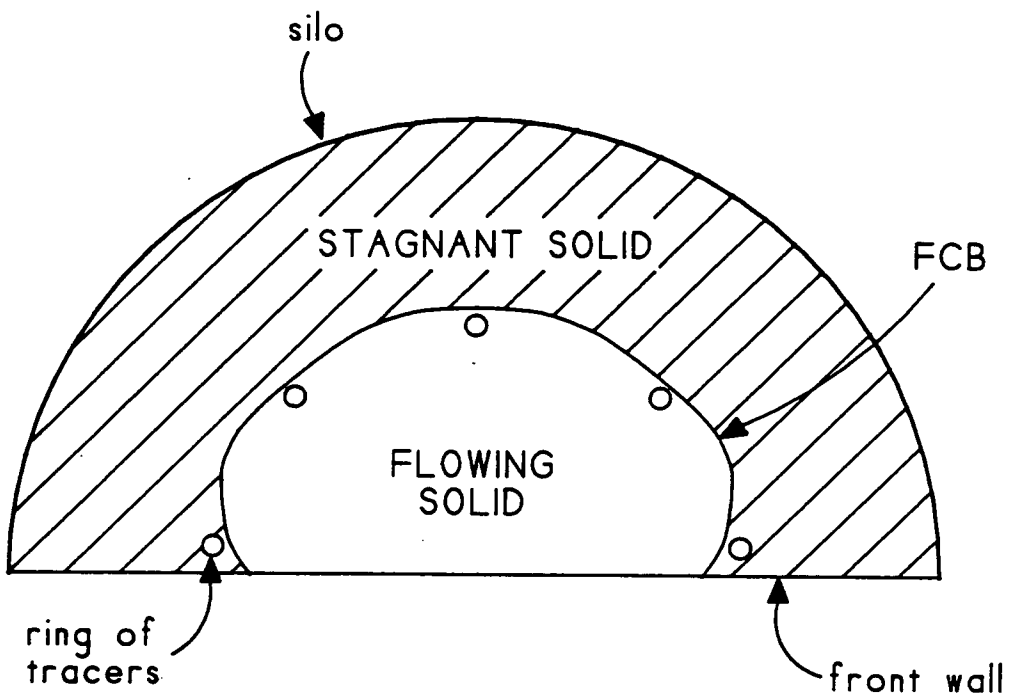

Fig. 6.11 Horizontal section through silo

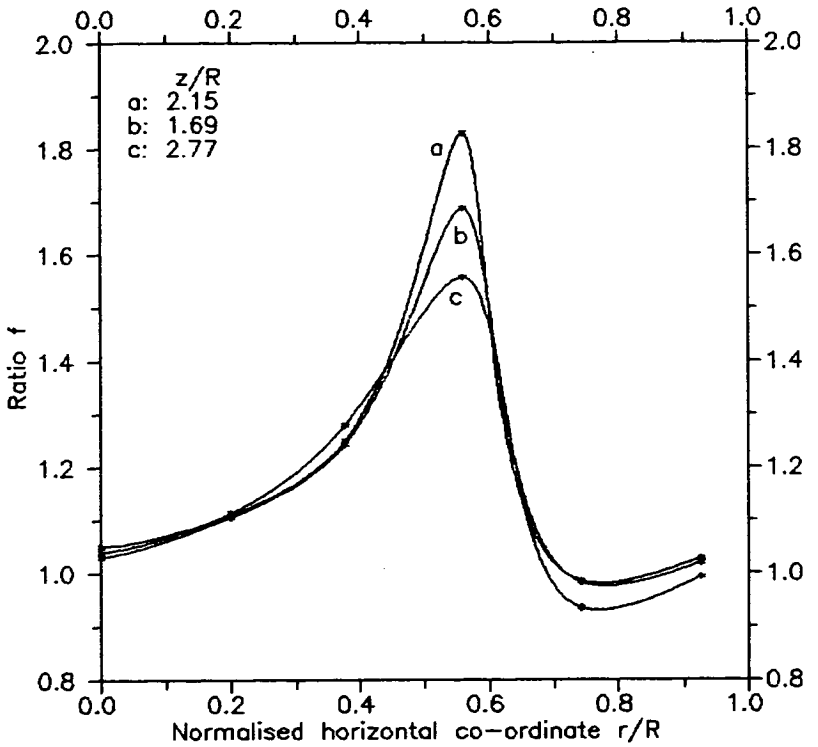

Fig. 6.12 Variation of f with radial co-ordinate for sand

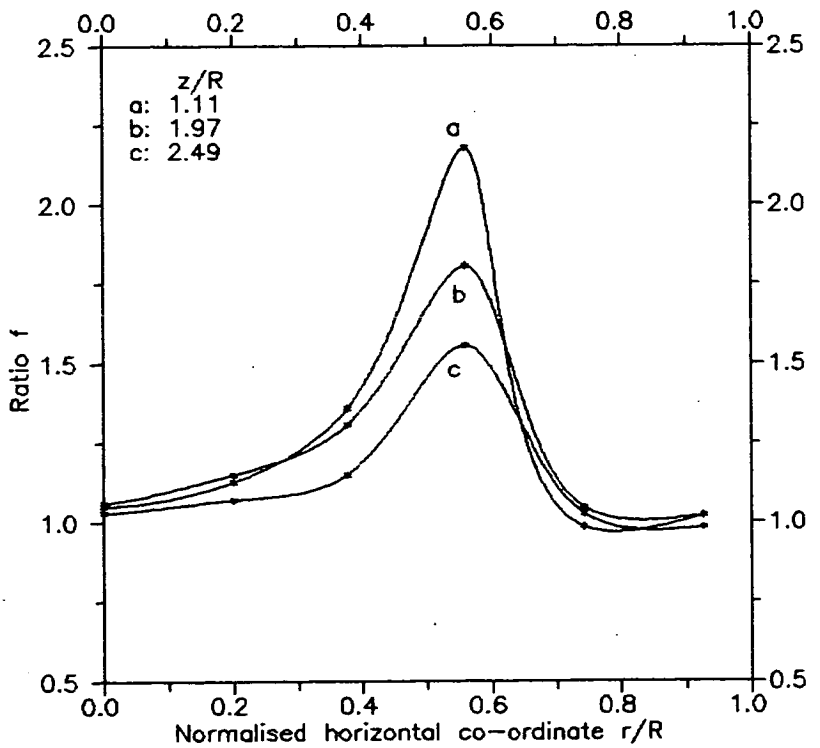

Fig. 6.13 Variation of f with radial co-ordinate for polypropylene pellets

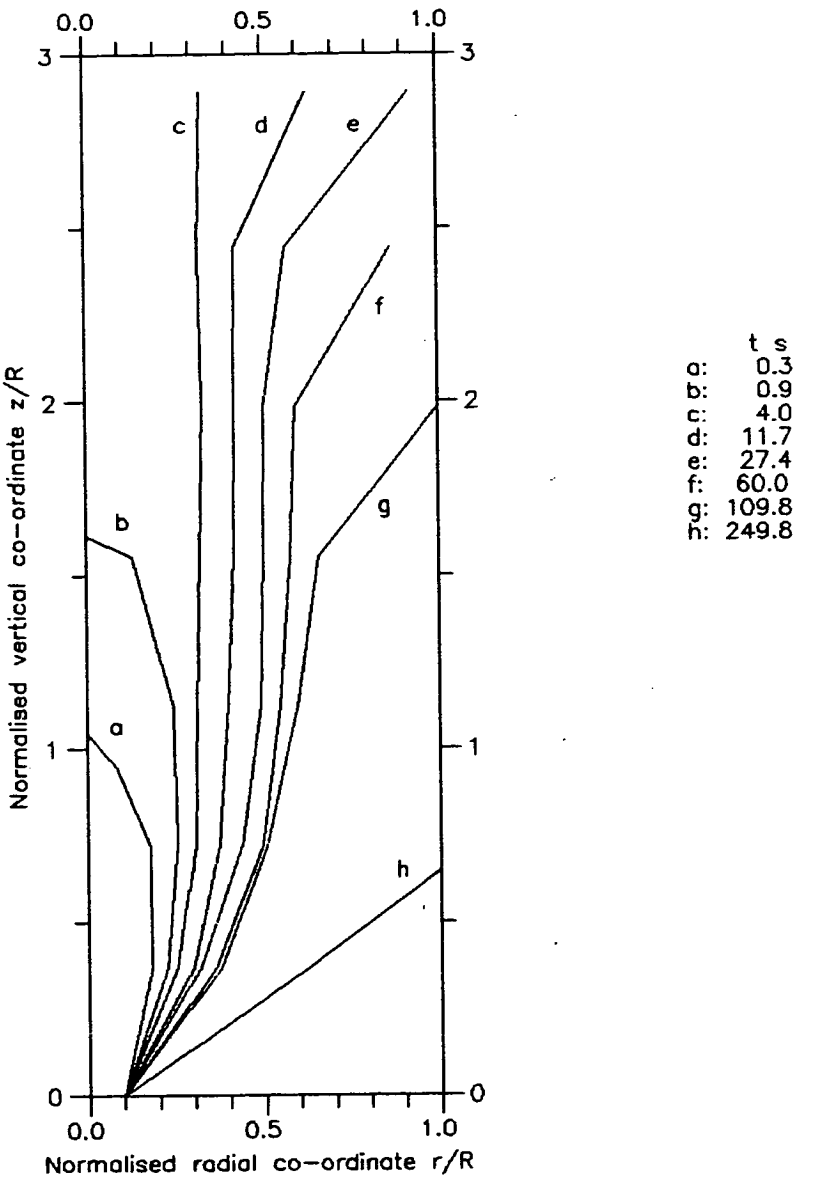

Fig. 6.14 Evolution of the FCB for polypropylene pellets

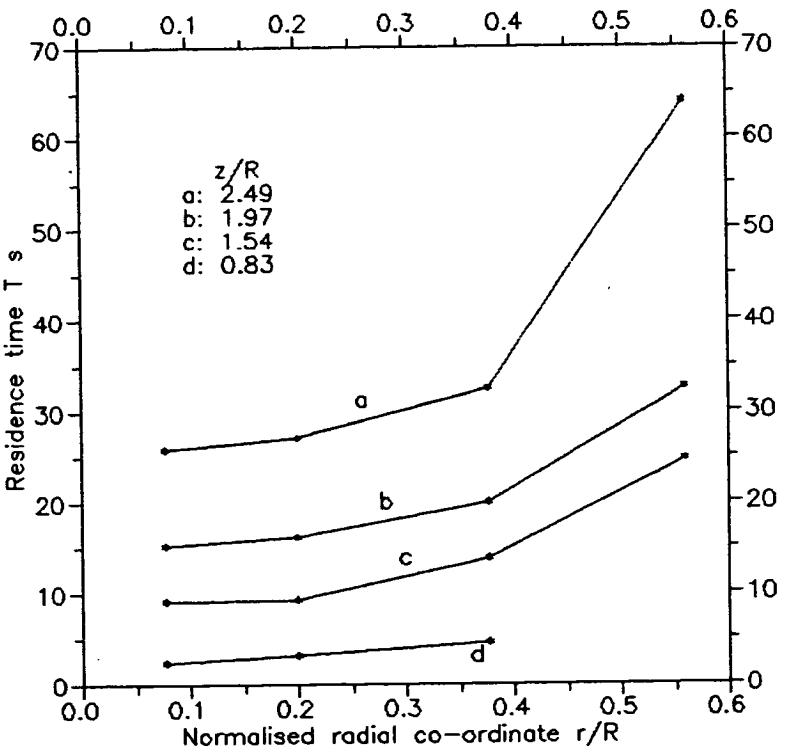

Fig. 6.15 Variation of corrected residence time with radial co-ordinate for polypropylene pellets during principal flow

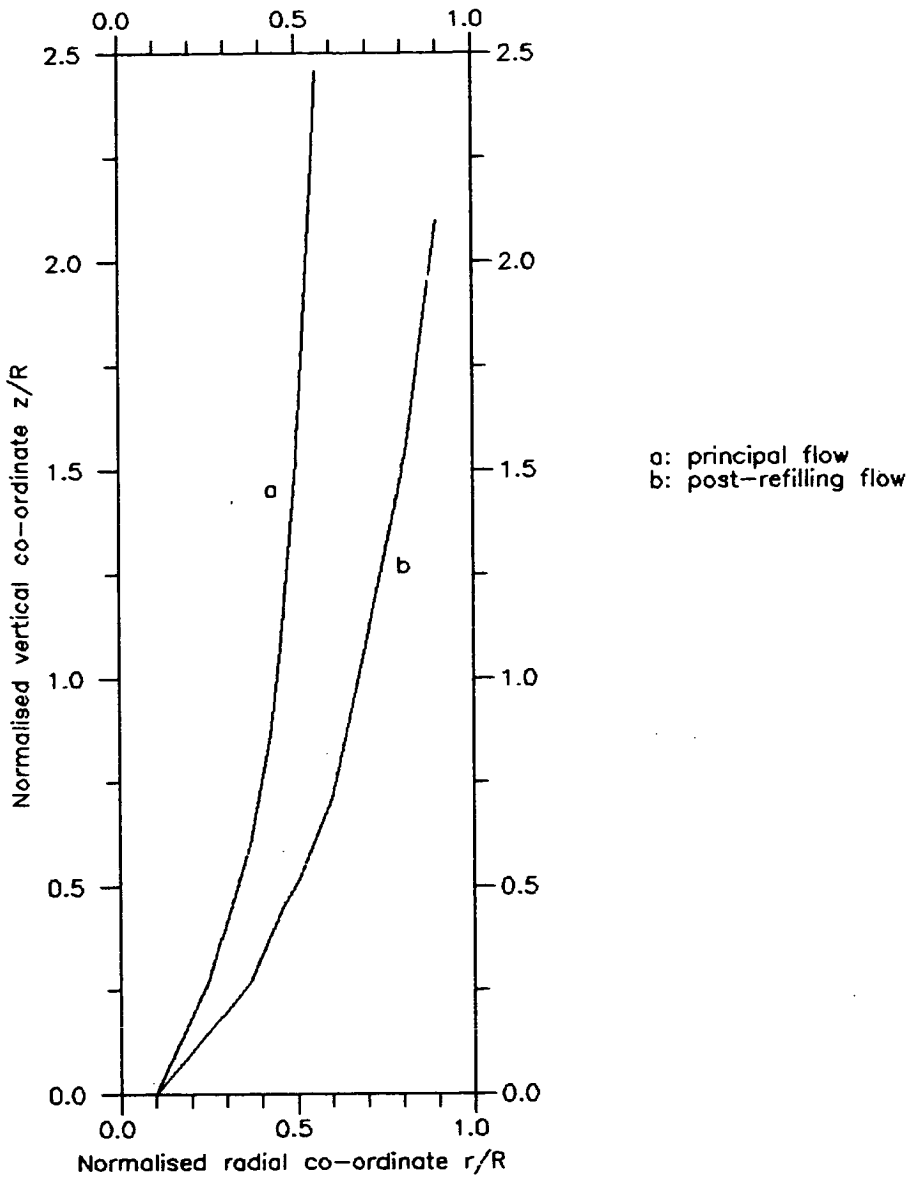

Fig. 6.16 Flow channel boundaries for sand using Method (a)

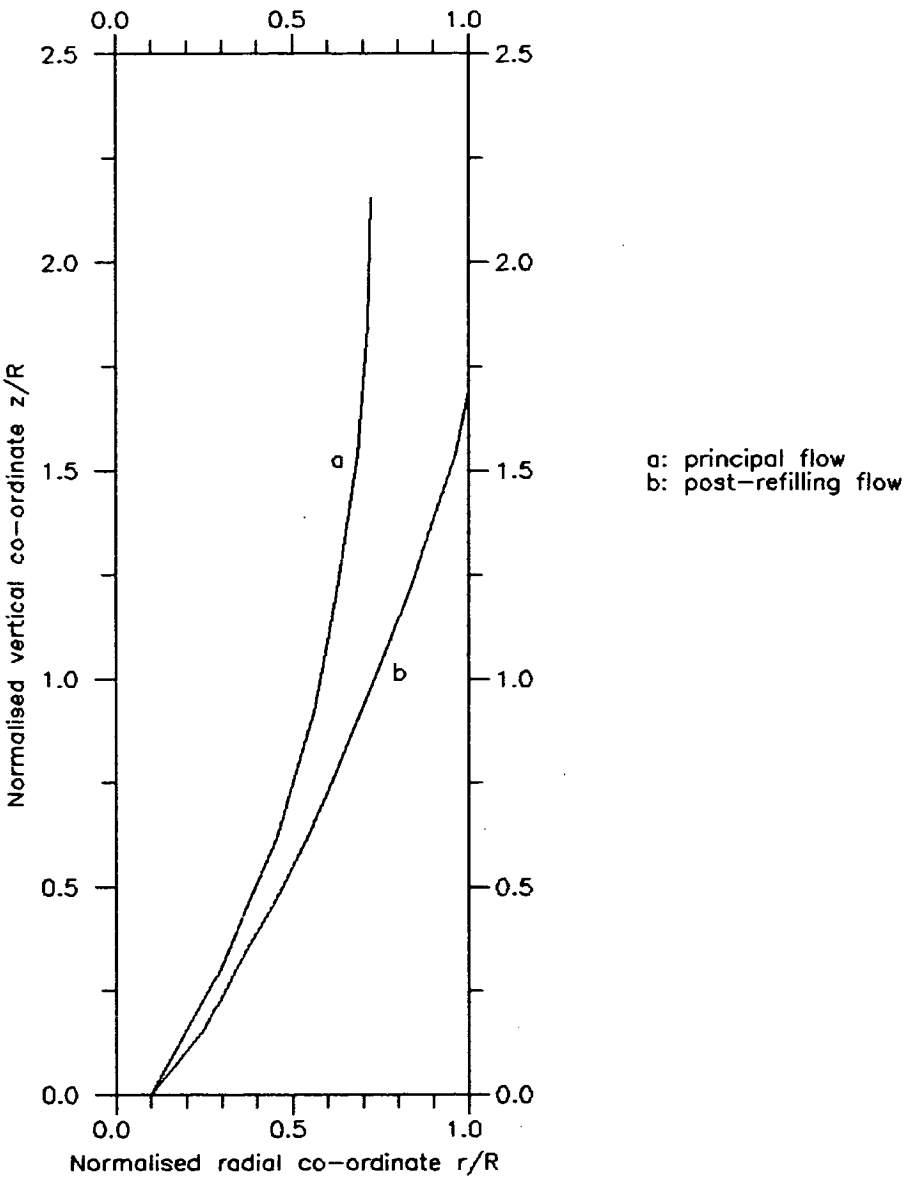

Fig. 6.17 Flow channel boundaries for polypropylene pellets using Method (a)

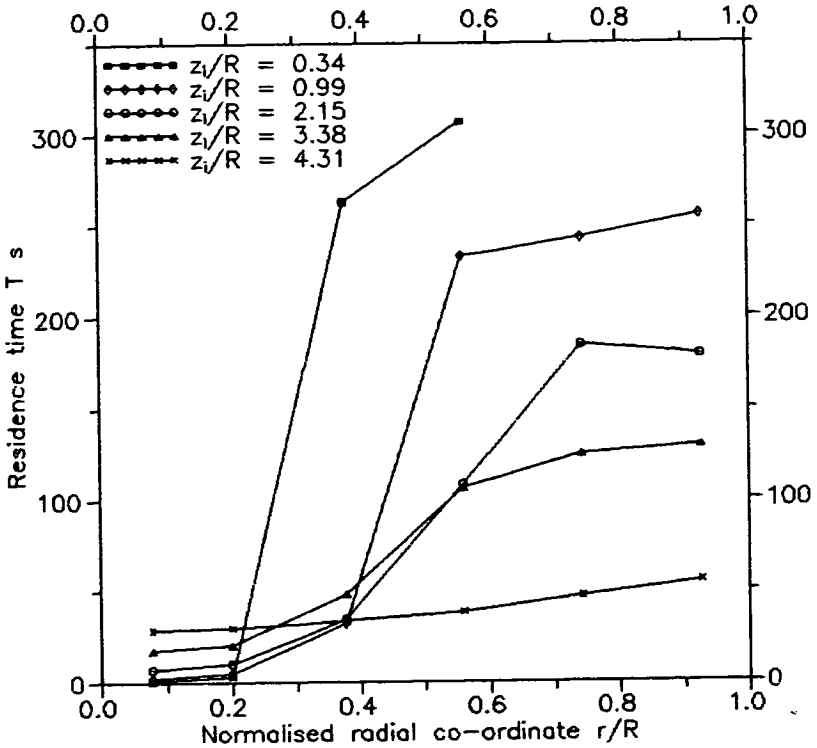

Fig. 6.18 Variation of residence time with radial co-ordinate for sand

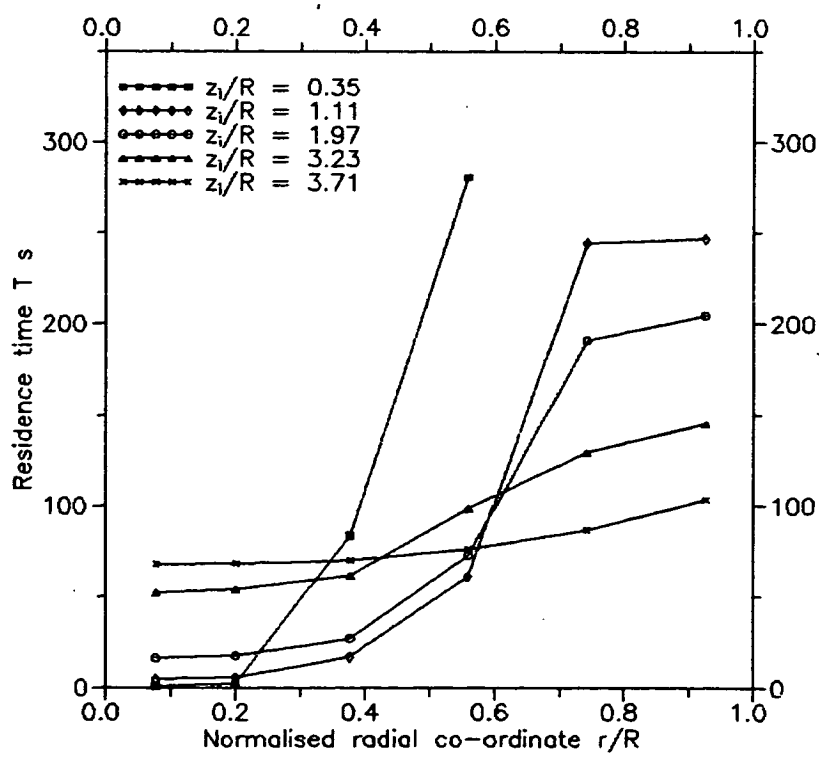

Fig. 6.19 Variation of residence time with radial co-ordinate for polypropylene pellets

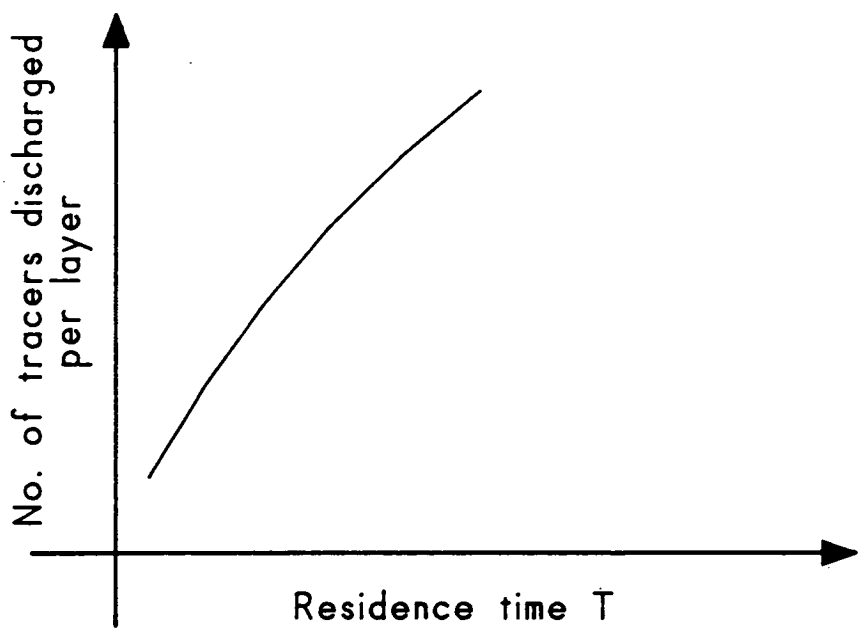

Fig. 6.20 Idealised variation between number of tracers discharged and residence time

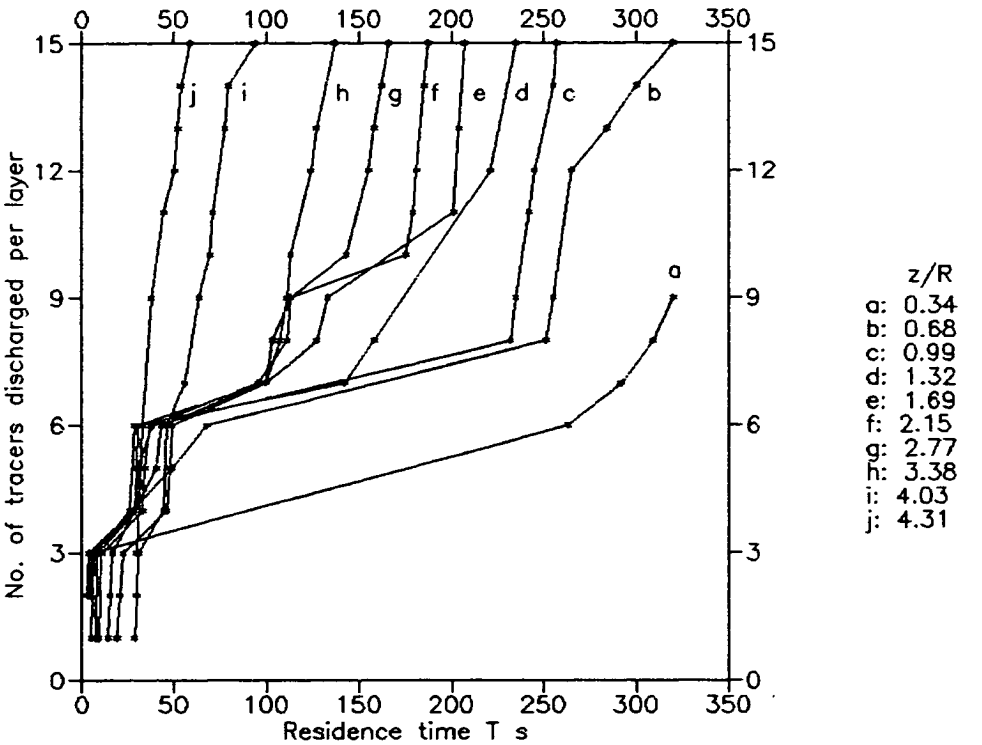

Fig. 6.21 Variation between number of tracers discharged and residence time for sand

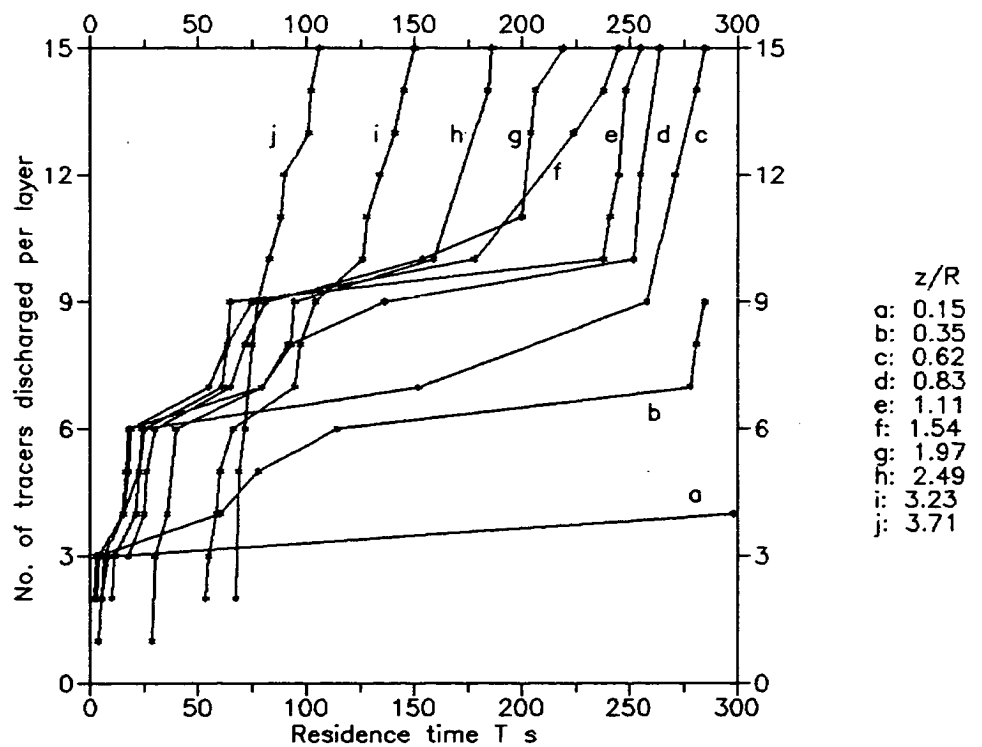

Fig. 6.22 Variation between number of tracers discharged and residence time for polypropylene pellets

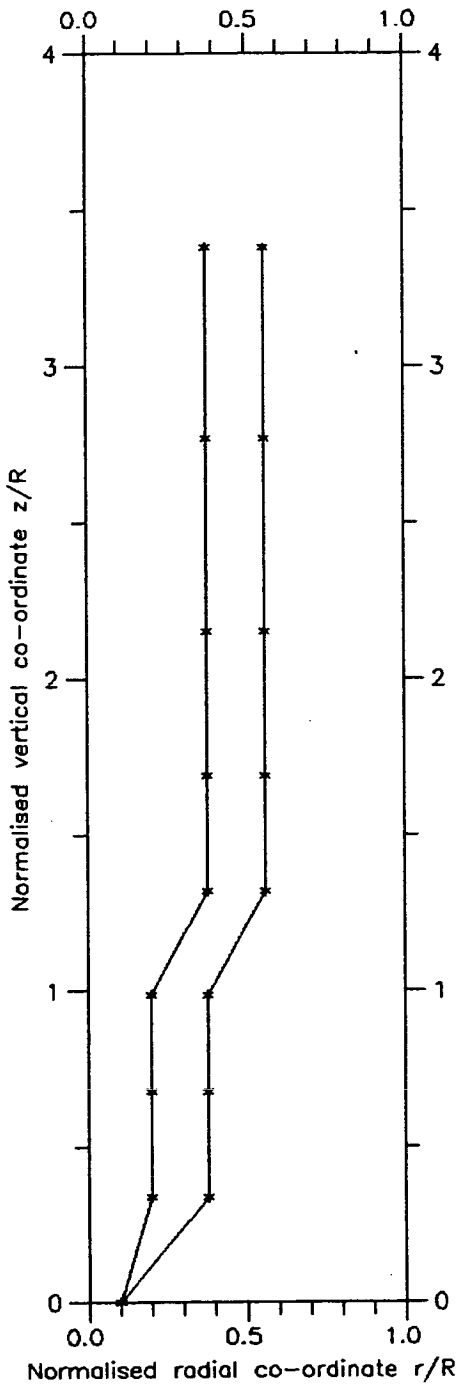

Fig. 6.23 Flow channel boundaries for sand using Method (b)

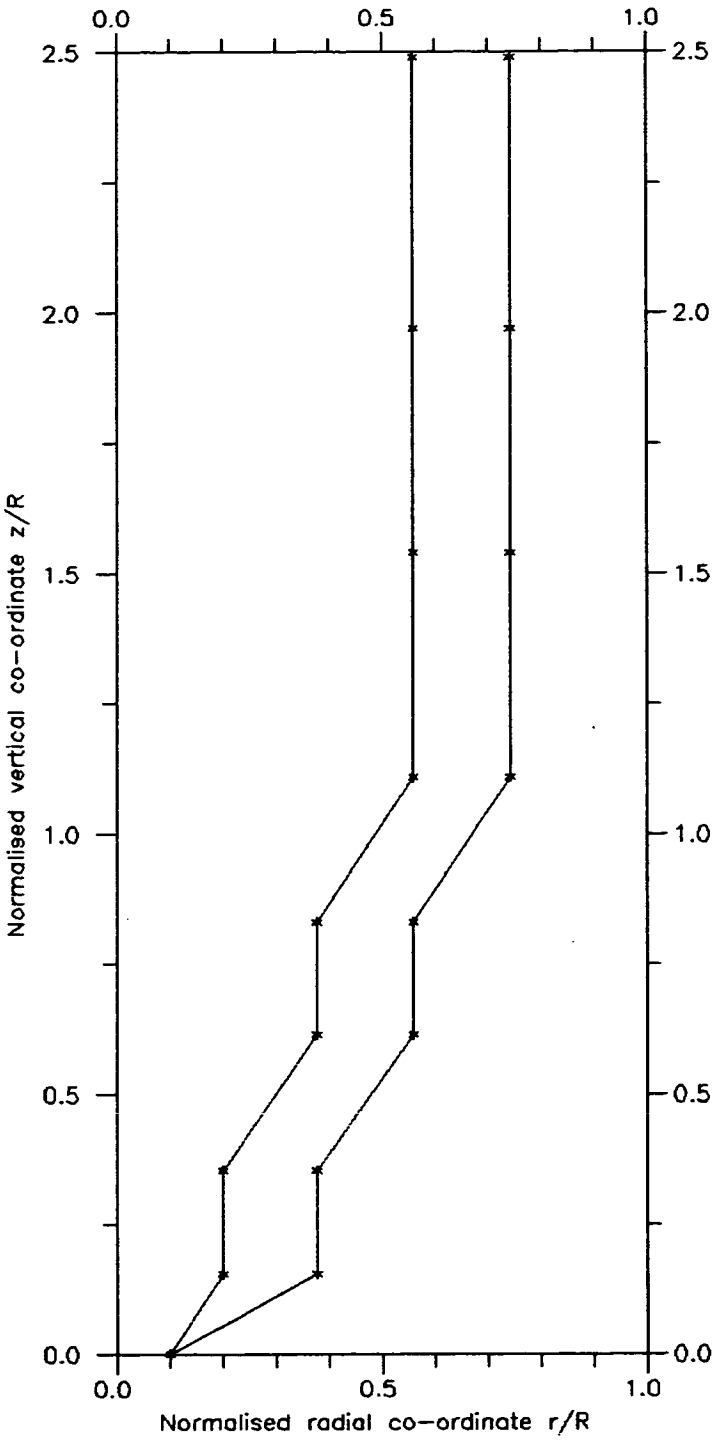

Fig. 6.24 Flow channel boundaries for polypropylene pellets using Method (b)

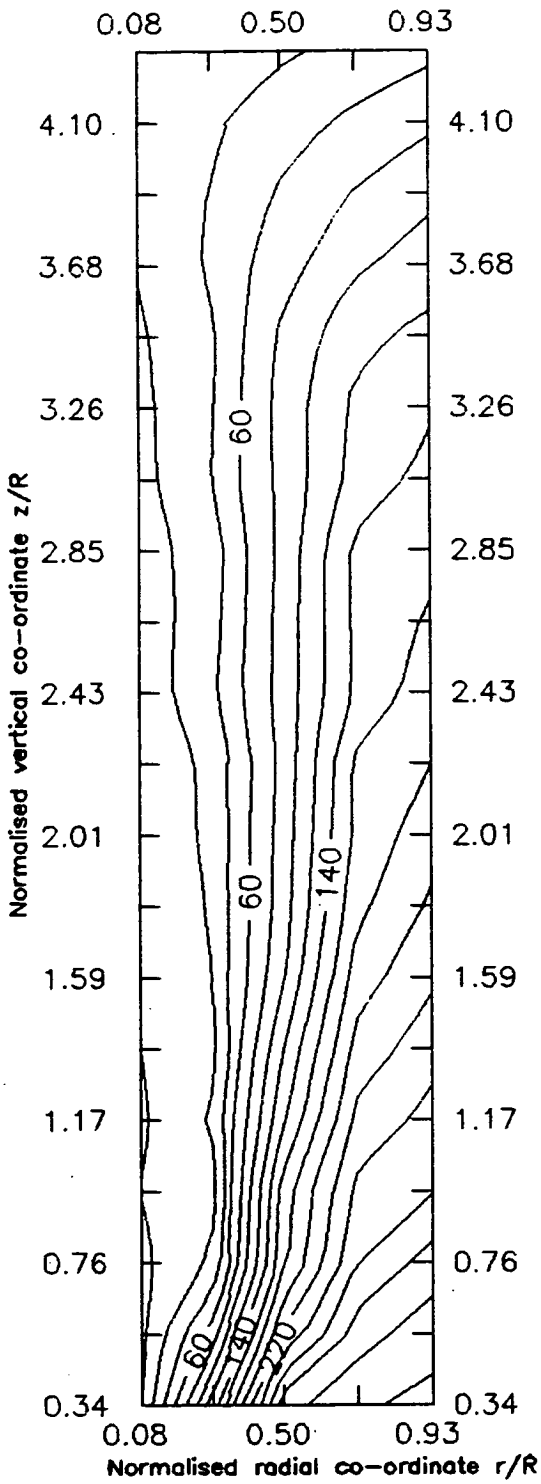

Fig. 6.25 Isochrone map for sand

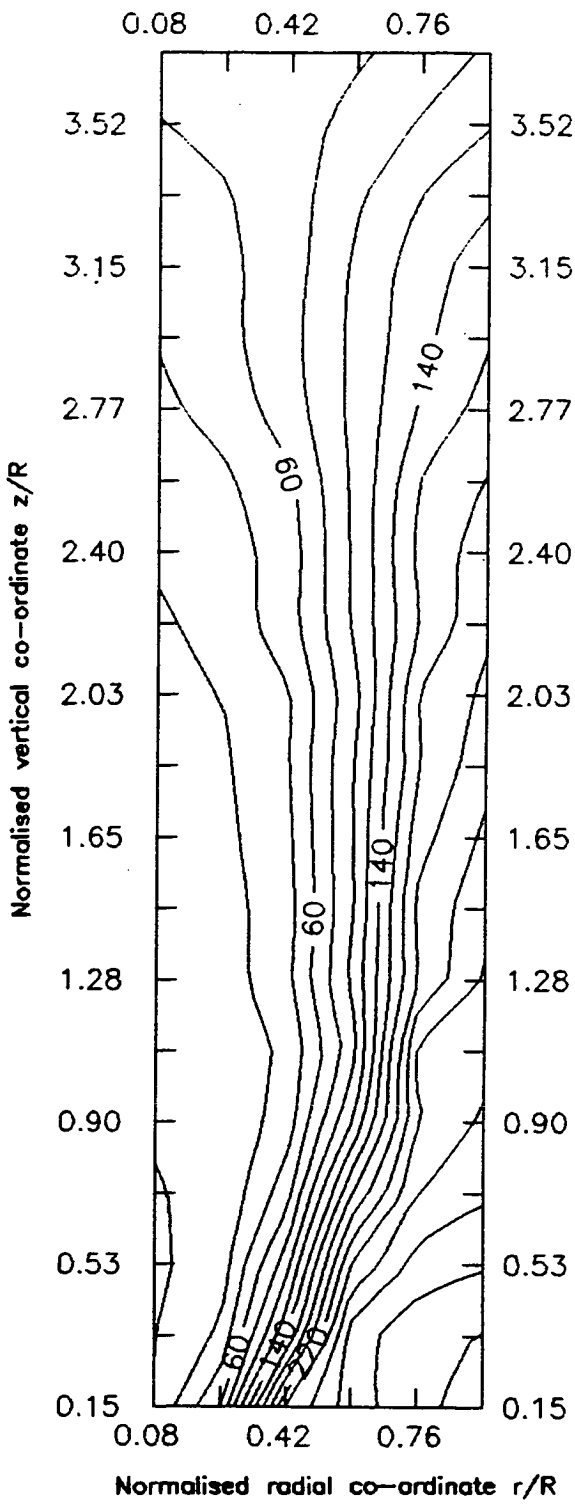

Fig. 6.26 Isochrone map for polypropylene pellets

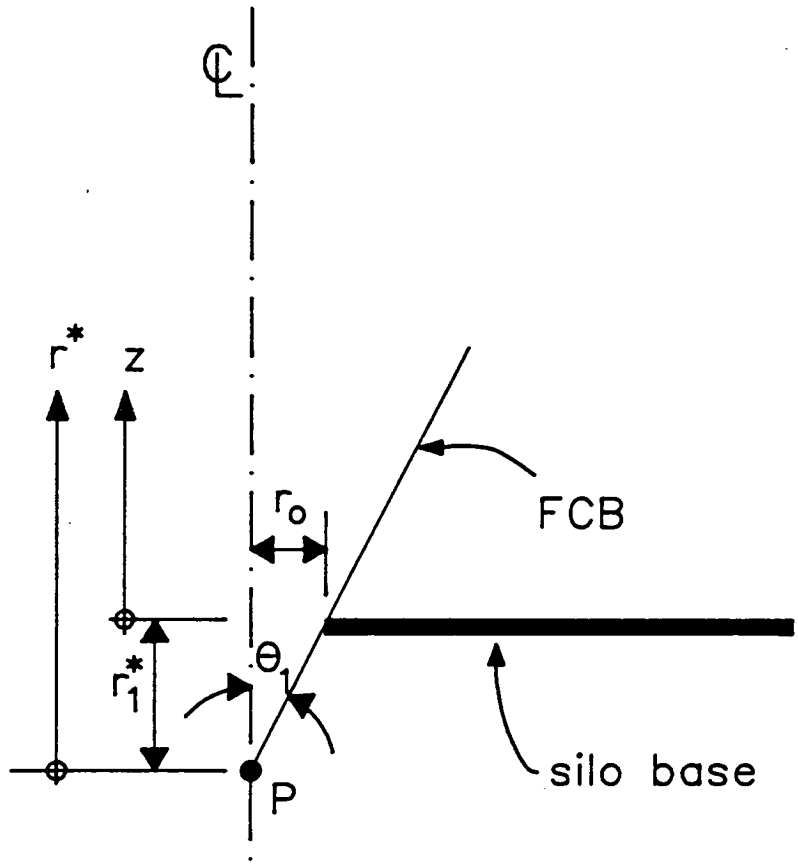

Fig. 6.27 Co-ordinate system used for Method (d)

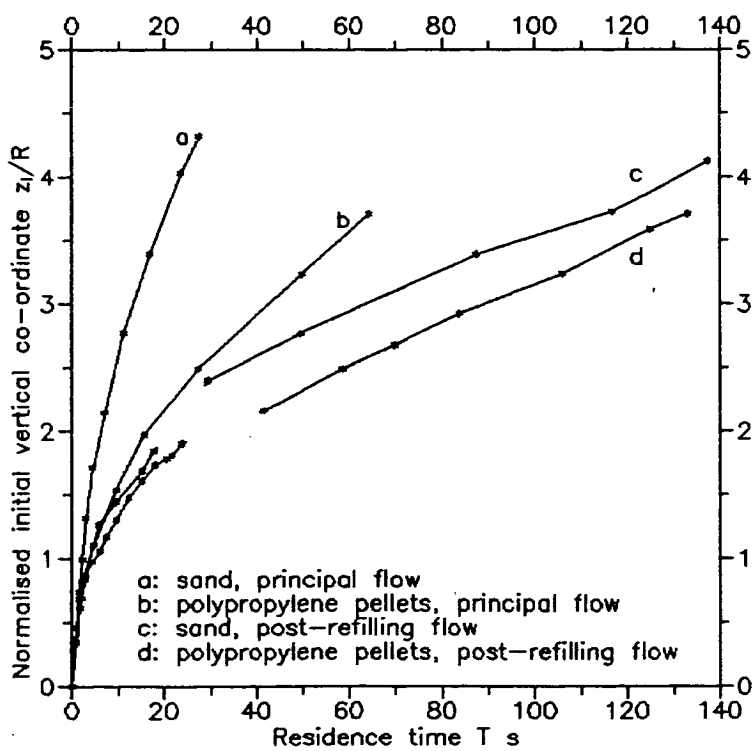

Fig. 6.28 Variation of initial height on centreline with residence time

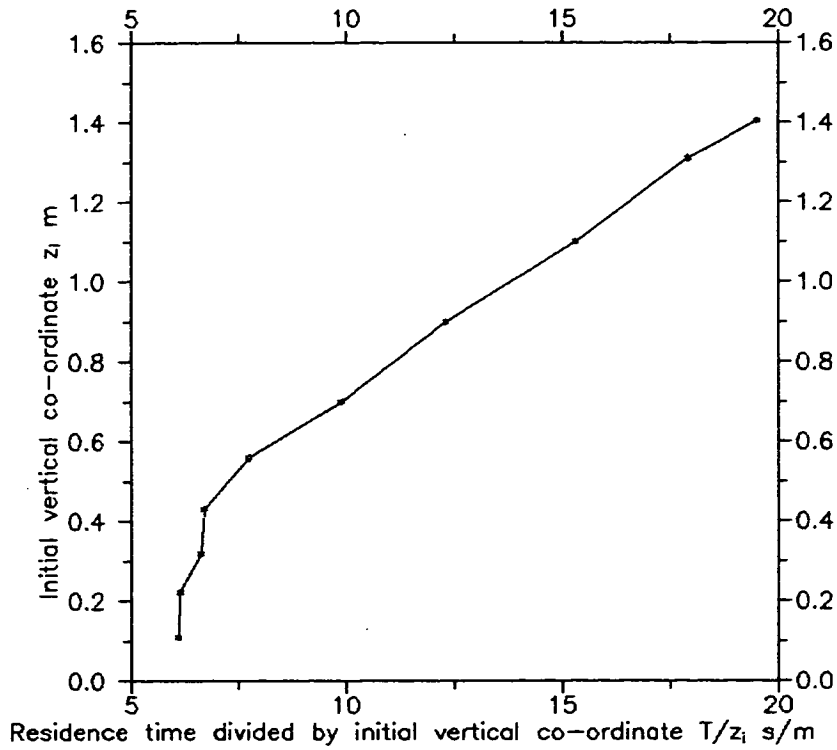

Fig. 6.29 First iteration stage for sand during principal flow (whole silo)

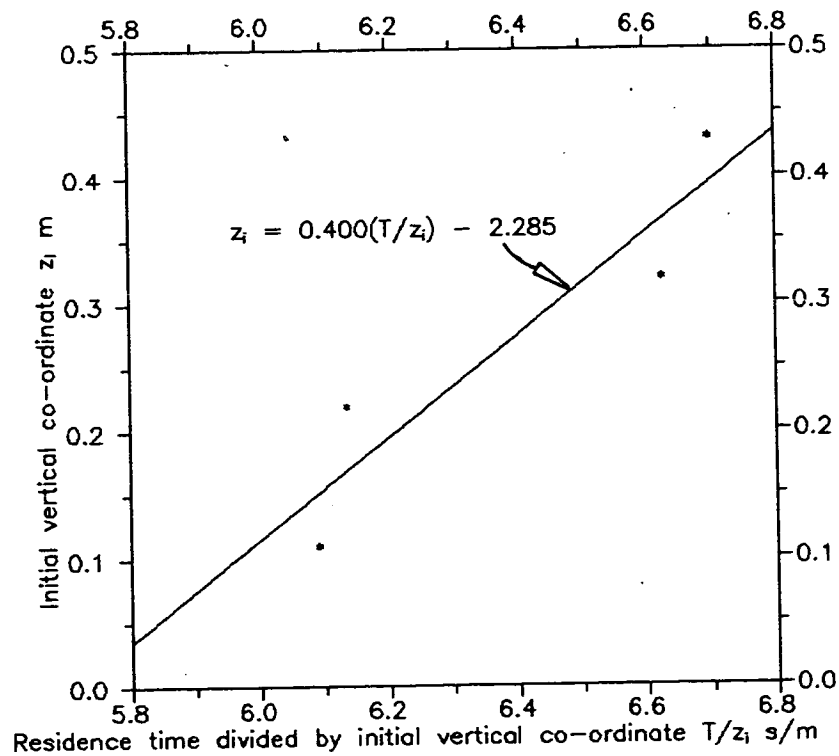

Fig. 6.30 First iteration stage for sand during principal flow (lower section)

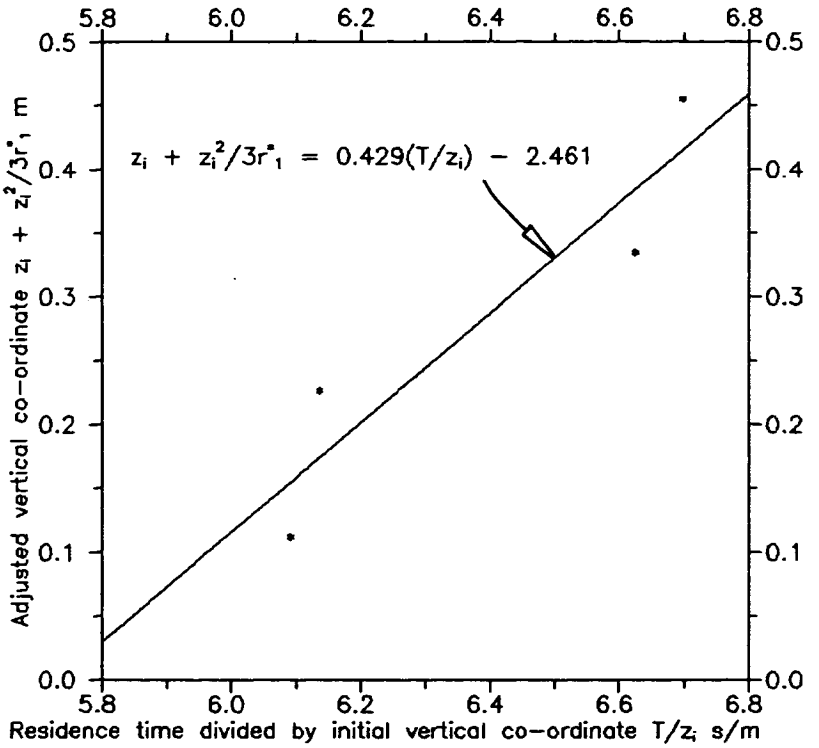

Fig. 6.31 Final iteration stage for sand during principal flow (lower section)

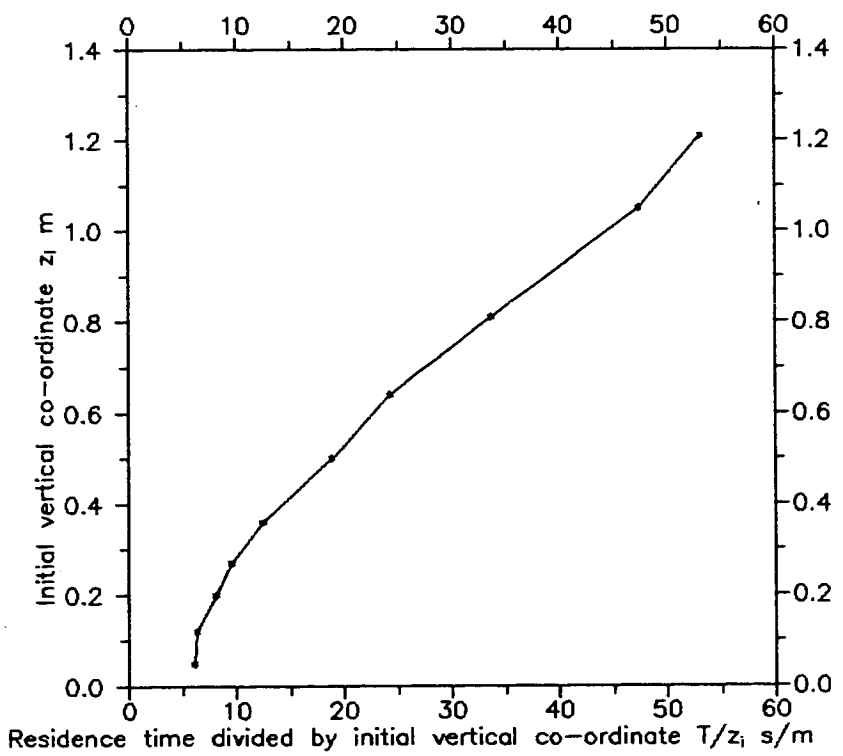

Fig. 6.32 First iteration stage for polypropylene pellets during principal flow (whole silo)

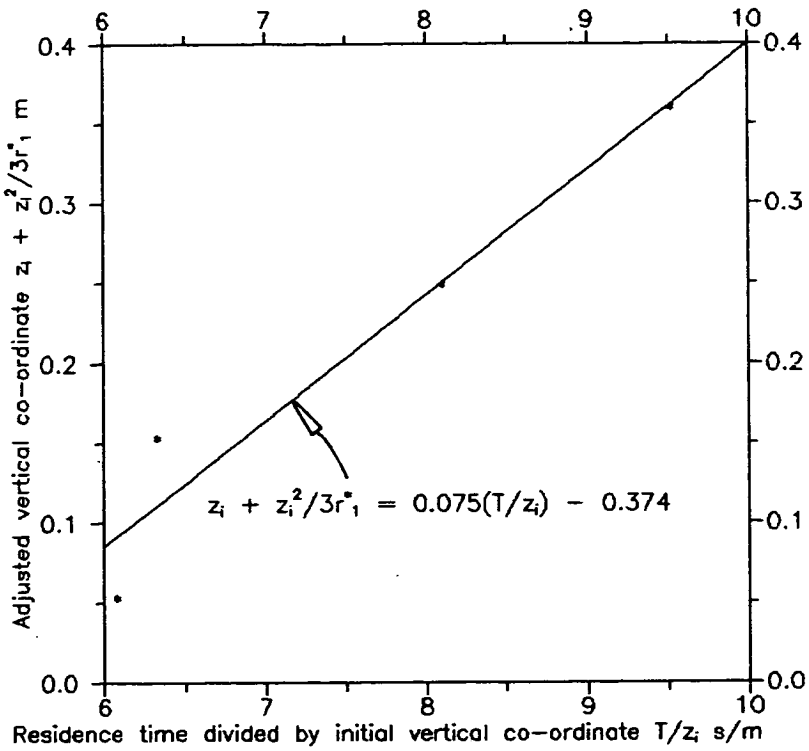

Fig. 6.33 Final iteration stage for polypropylene pellets during principal flow (lower section)

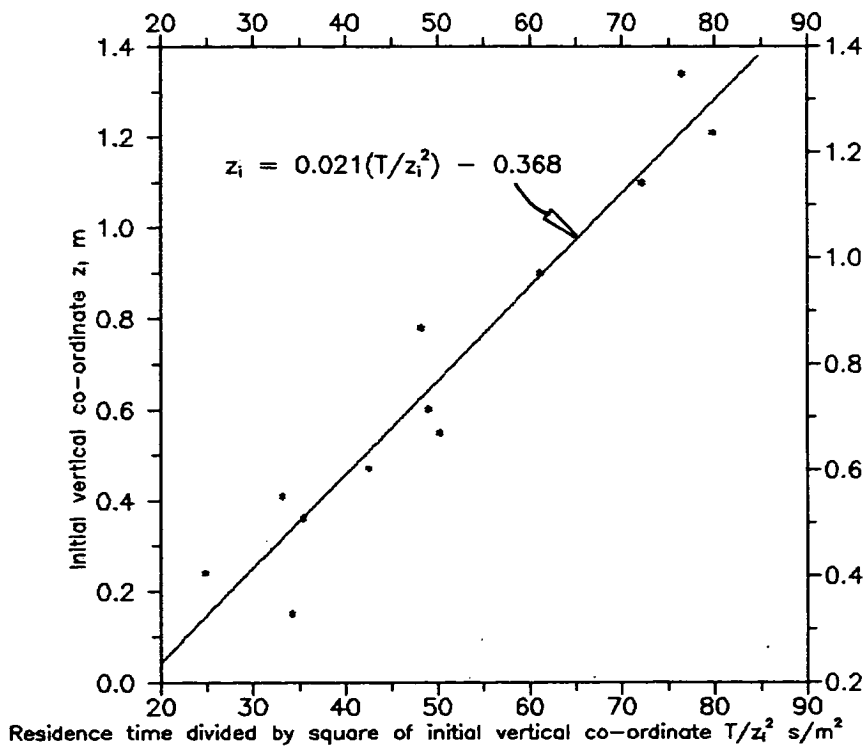

Fig. 6.34 First iteration stage for sand during post-refilling flow

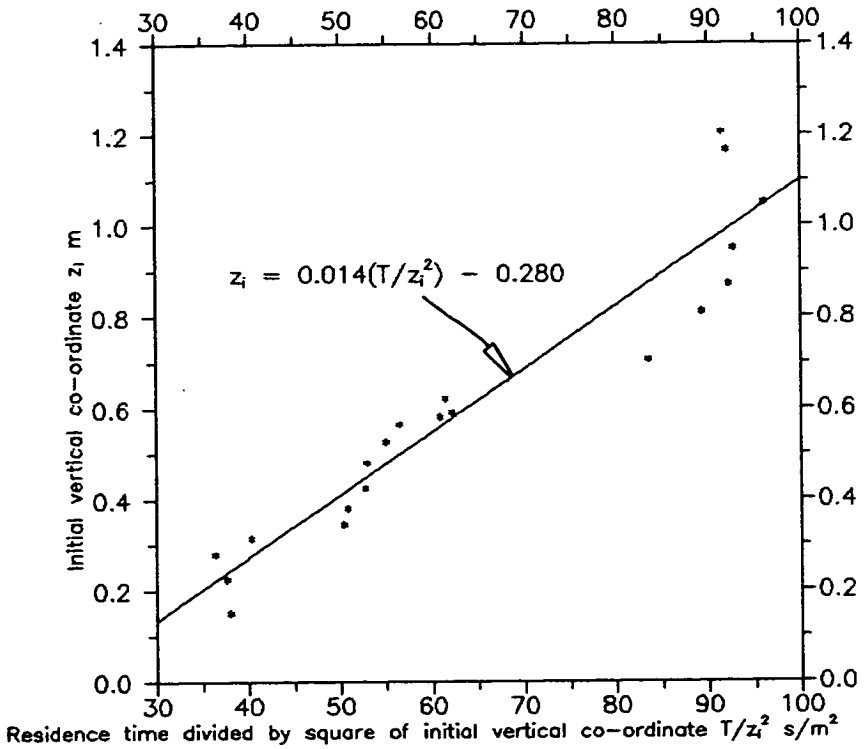

Fig. 6.35 First iteration stage for polypropylene pellets during post-refilling flow

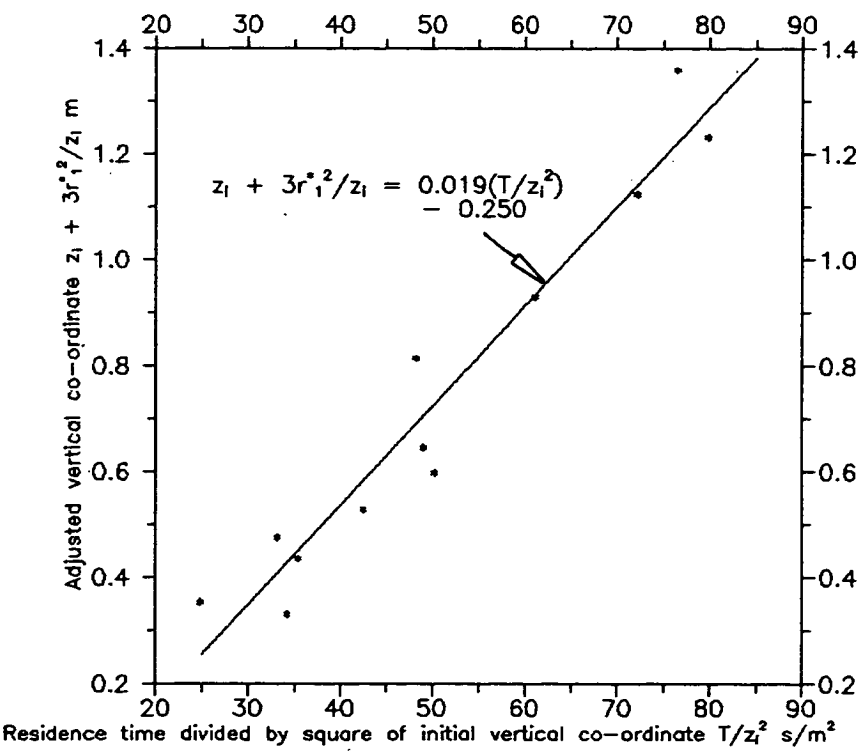

Fig. 6.36 Final iteration stage for sand during post-refilling flow

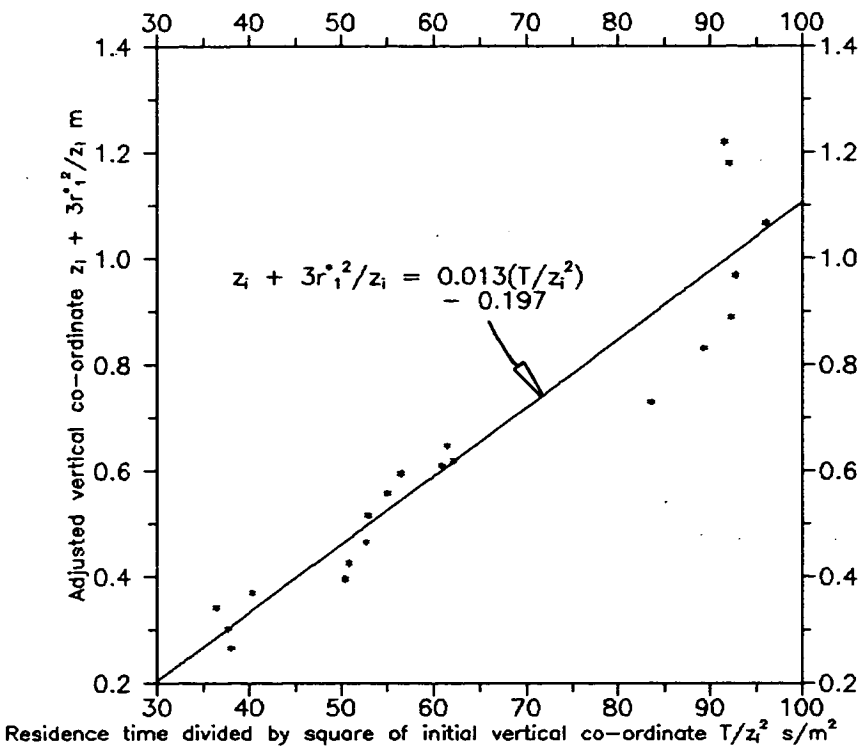

Fig. 6.37 Final iteration stage for polypropylene pellets during post-refilling flow

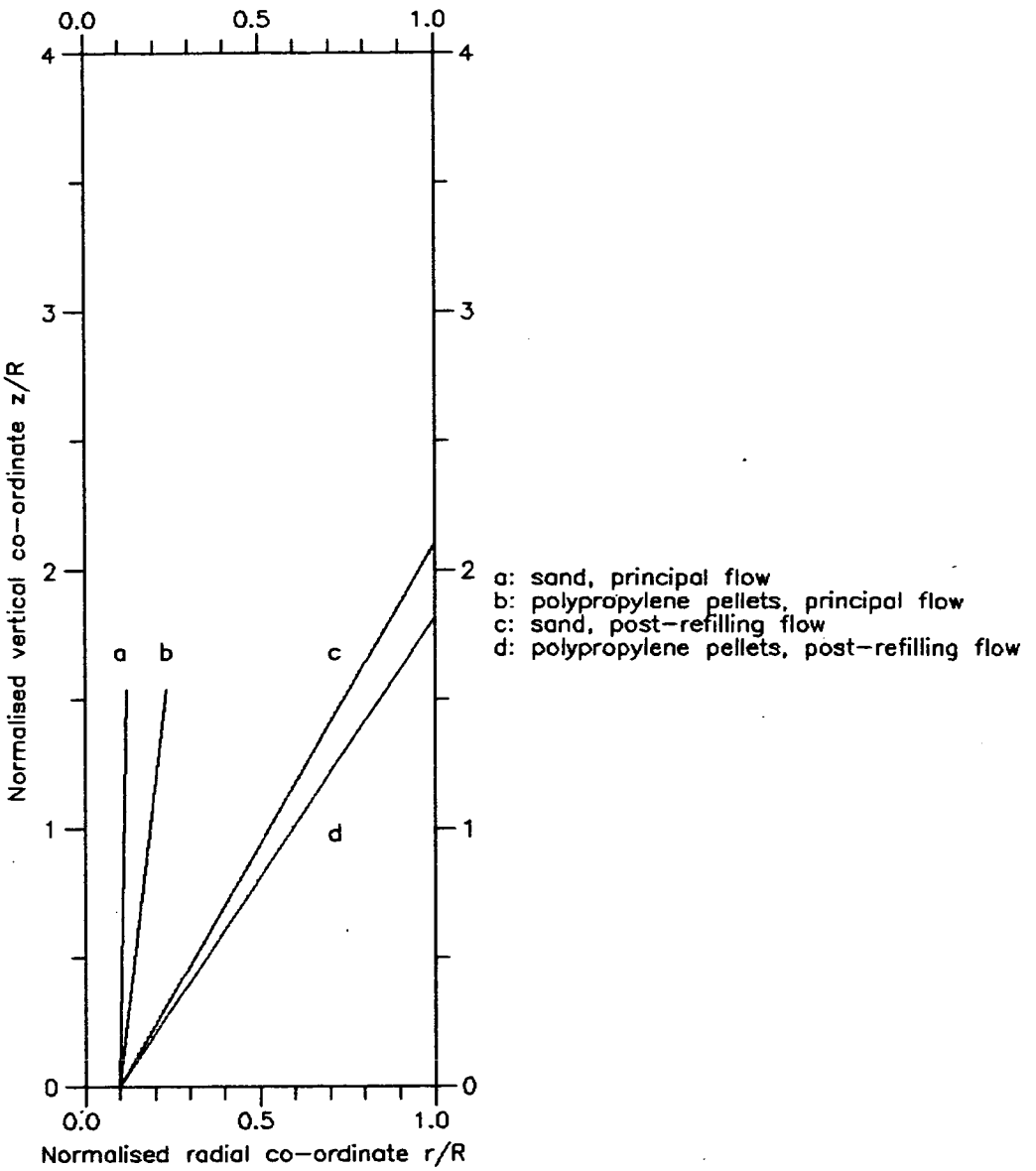

Fig. 6.38 Flow channel boundaries using Method (d)

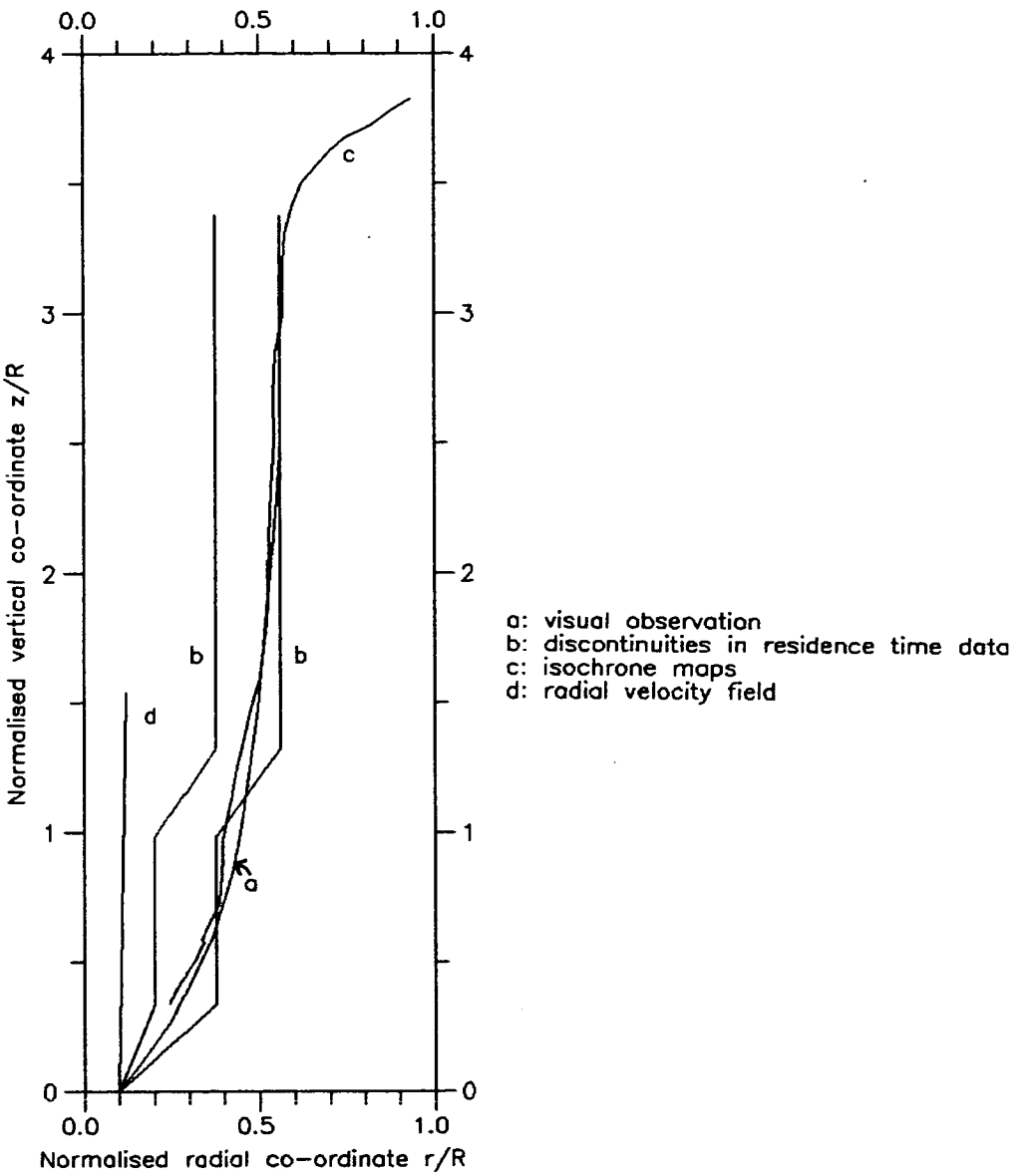

Fig. 6.39 Comparison of flow channel boundaries for sand during principal flow

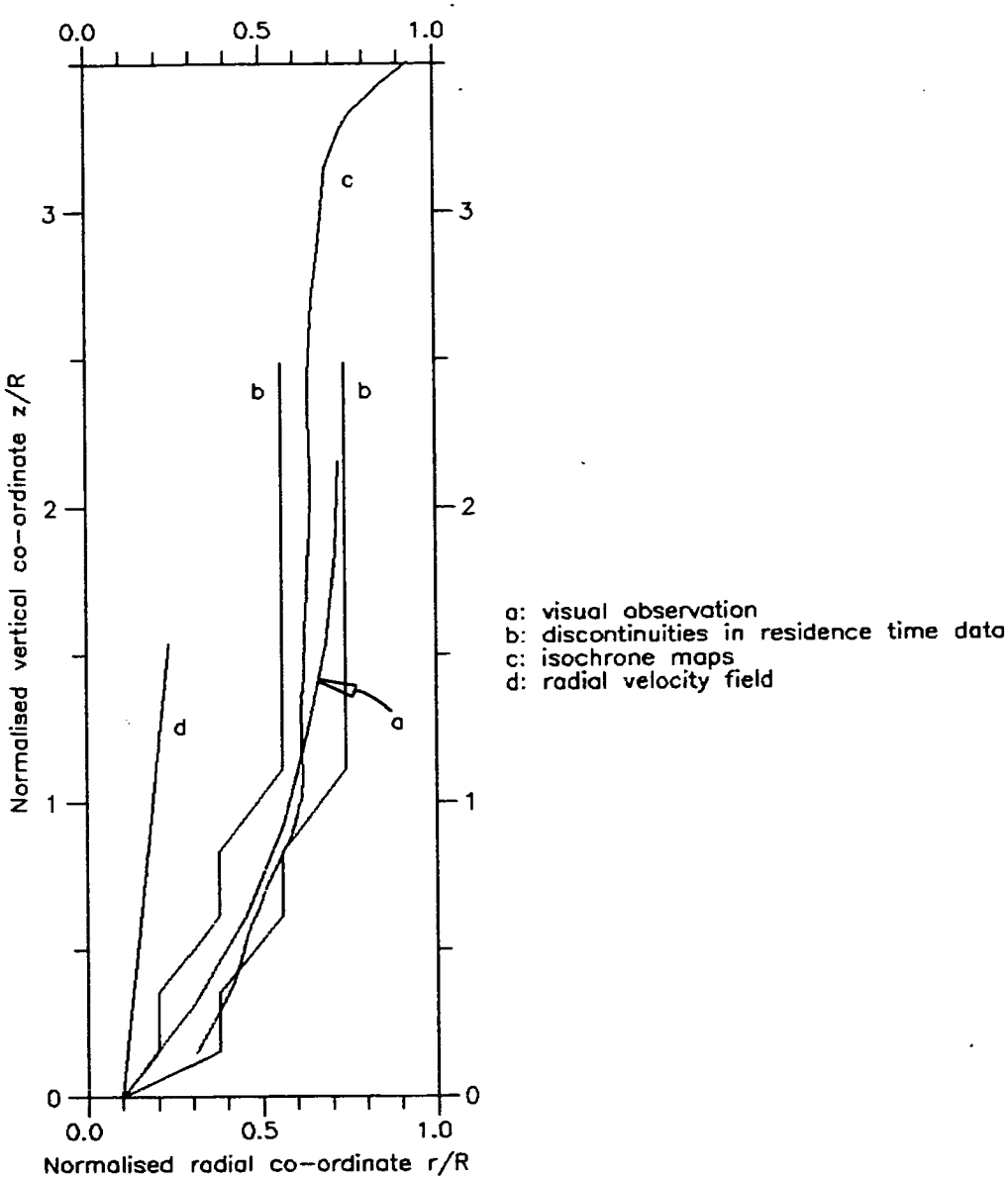

Fig. 6.40 Comparison of flow channel boundaries for polypropylene pellets during principal flow

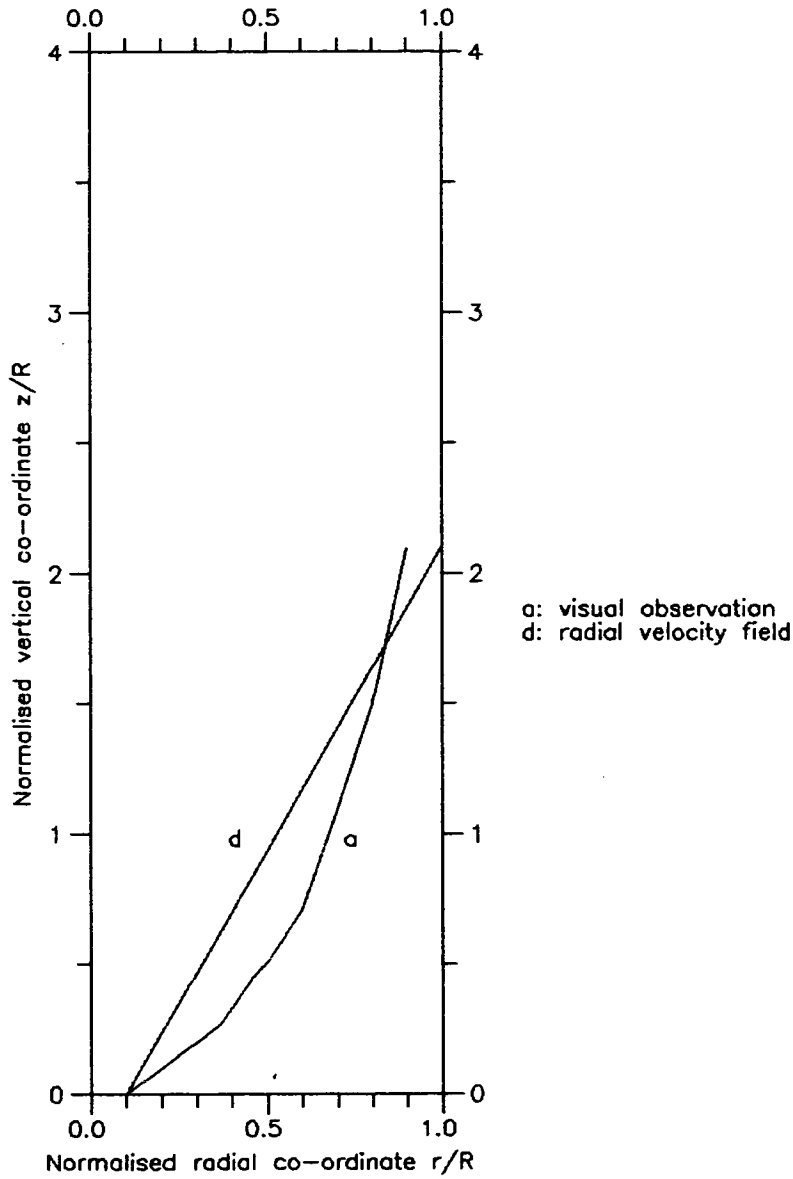

Fig. 6.41 Comparison of flow channel boundaries for sand during post-refilling flow

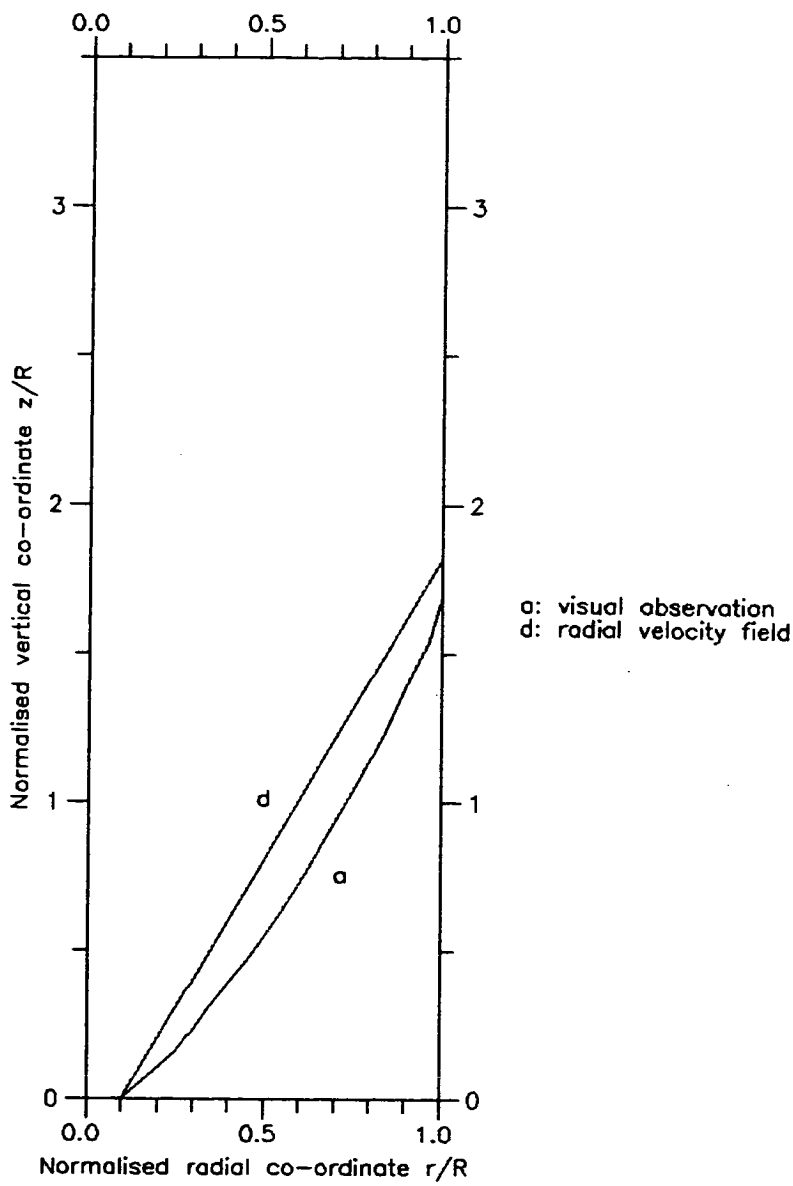

Fig. 6.42 Comparison of flow channel boundaries for polypropylene pellets during post-refilling flow

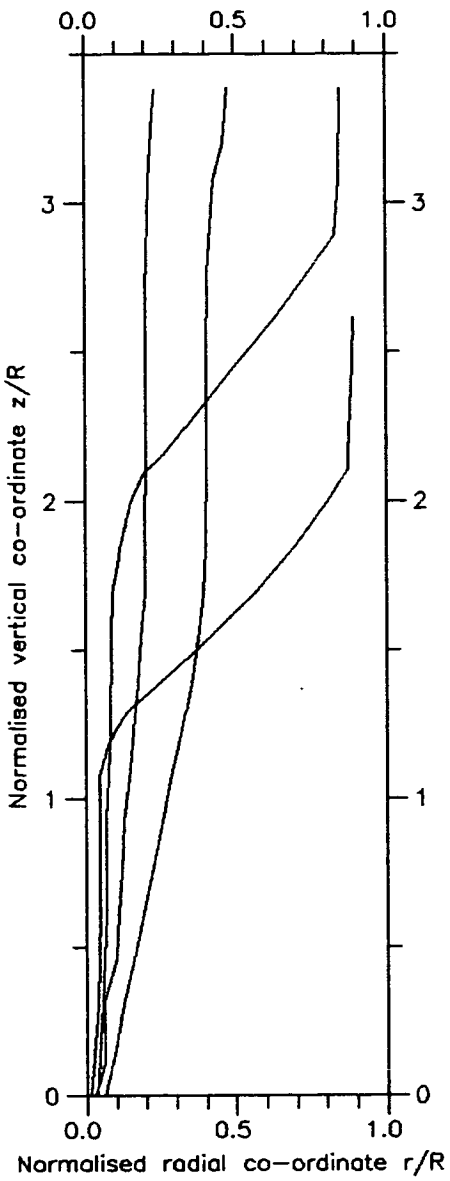

Fig. 6.43 Particle trajectories used for comparison with finite element method

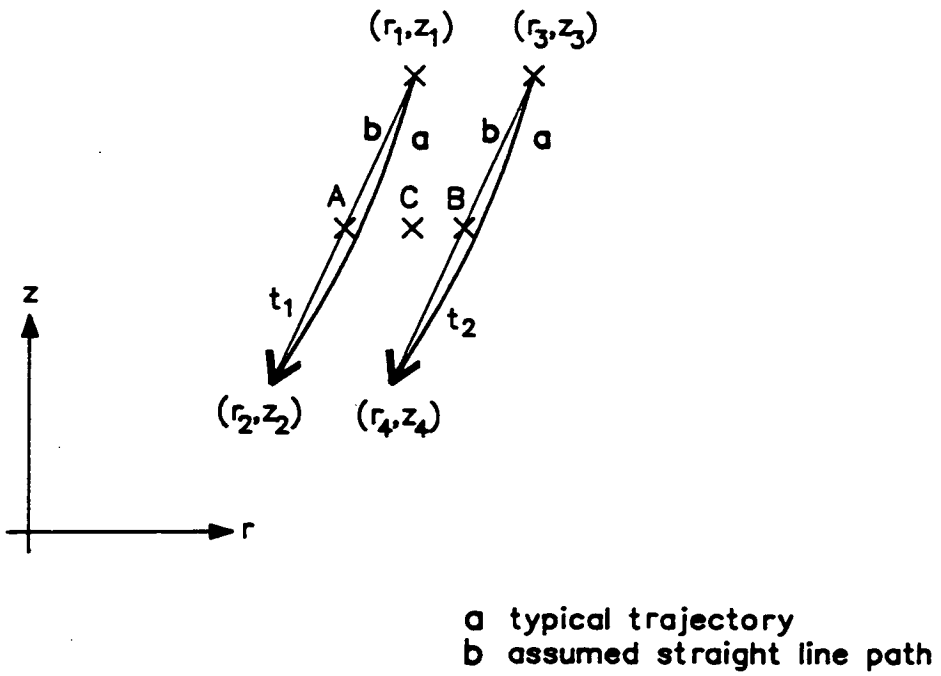

Fig. 6.44 Particle trajectories used for estimating the kinematic parameter

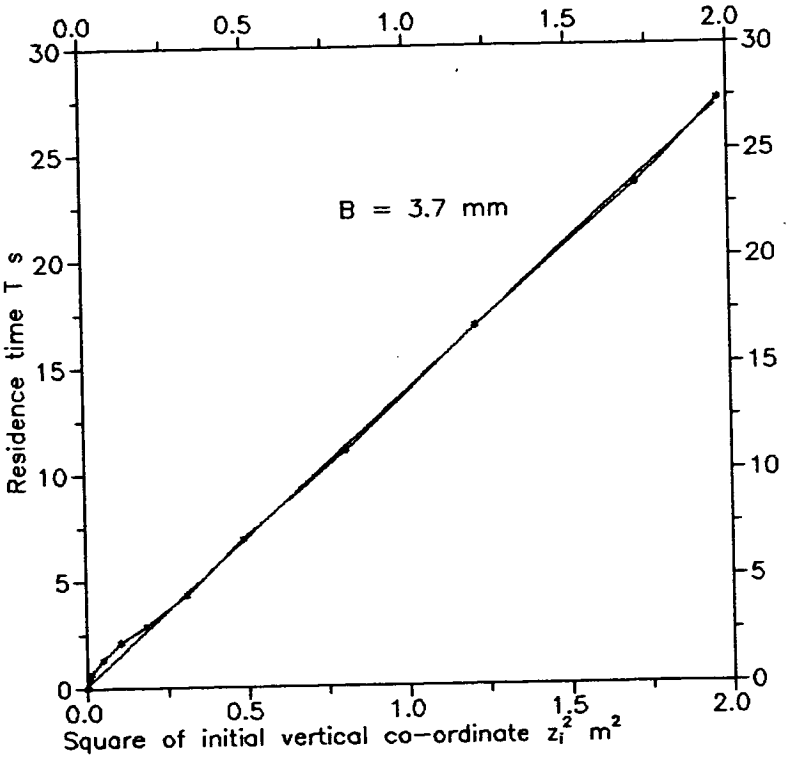

Fig. 6.45 Estimating the kinematic constant for sand during principal flow after Mullins (1974)

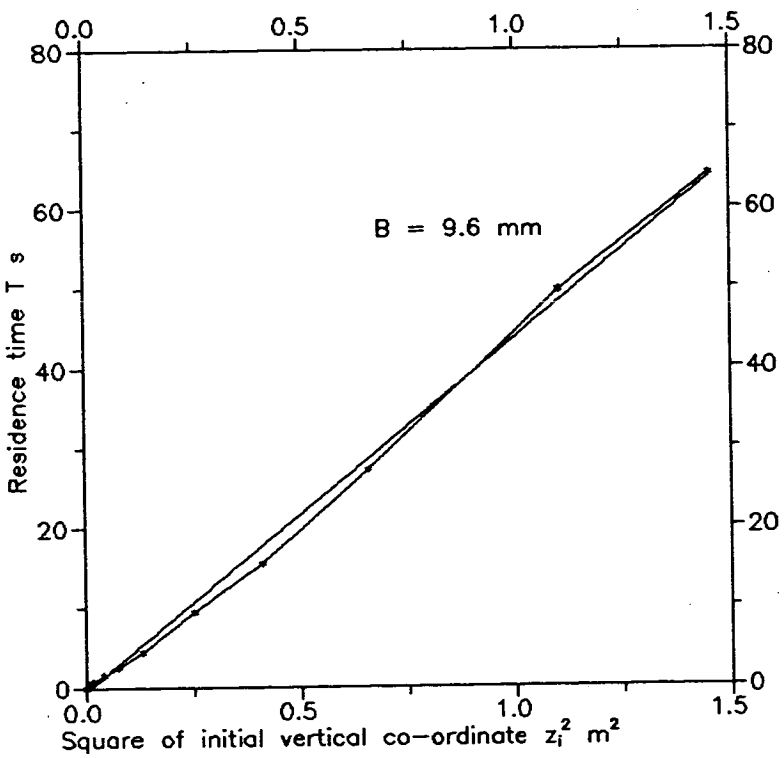

Fig. 6.46 Estimating the kinematic constant for polypropylene pellets during principal flow after Mullins (1974)

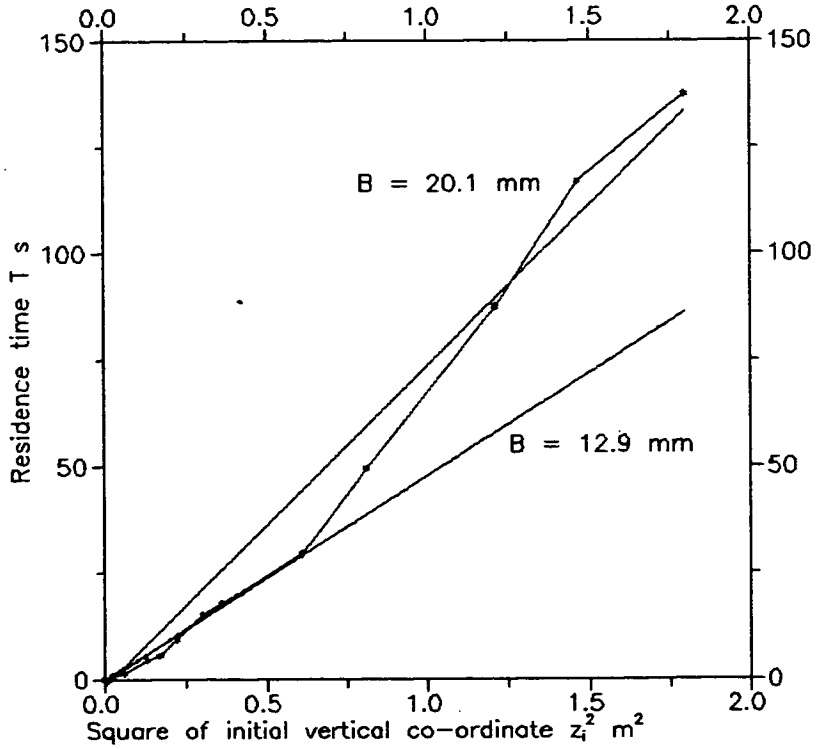

Fig. 6.47 Estimating the kinematic constant for sand during post-refilling flow after Mullins (1974)

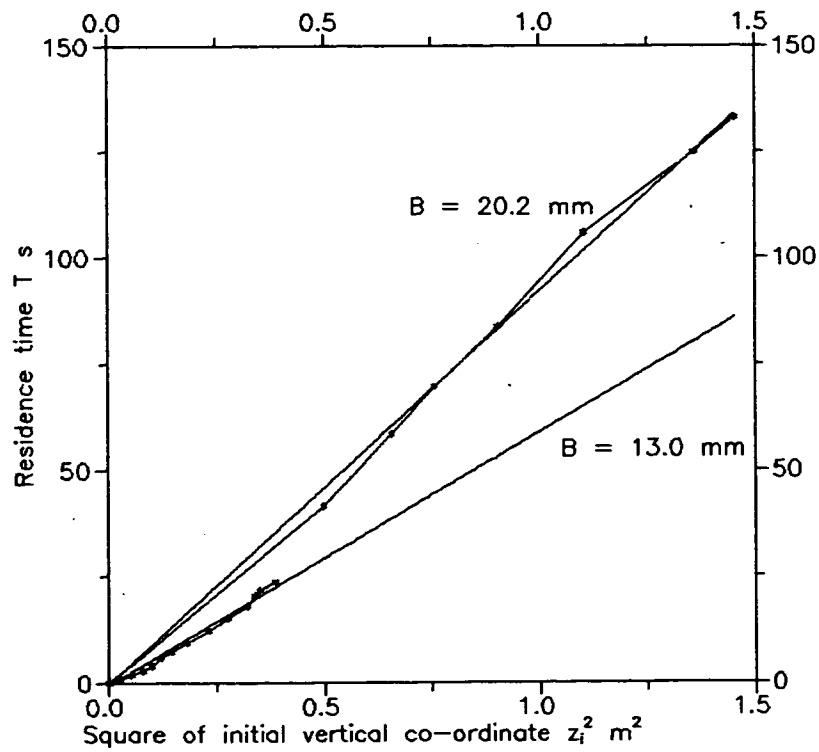

Fig. 6.48 Estimating the kinematic constant for polypropylene pellets during post-refilling flow after Mullins (1974)

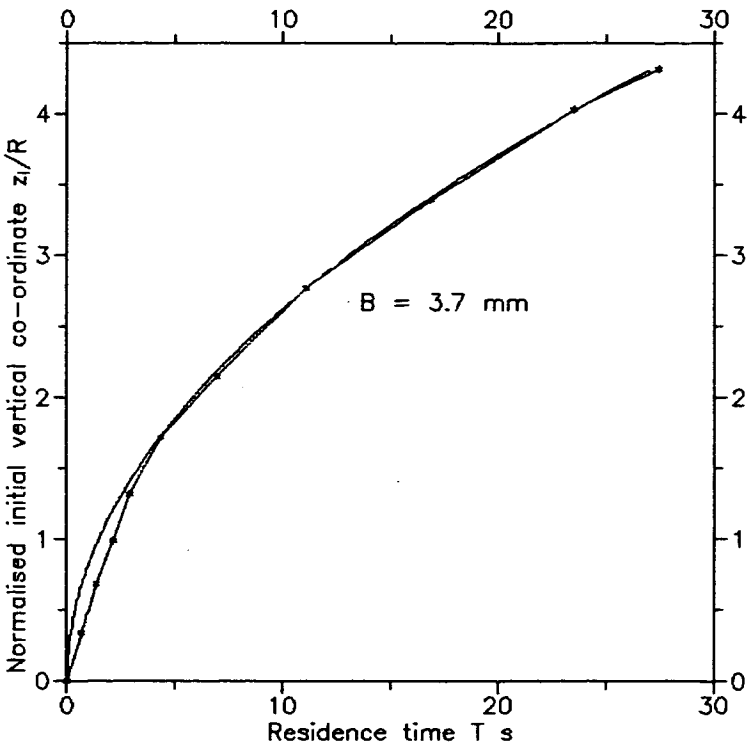

Fig. 6.49 Fitting the theory of Mullins (1974) to experimental data for sand during principal flow

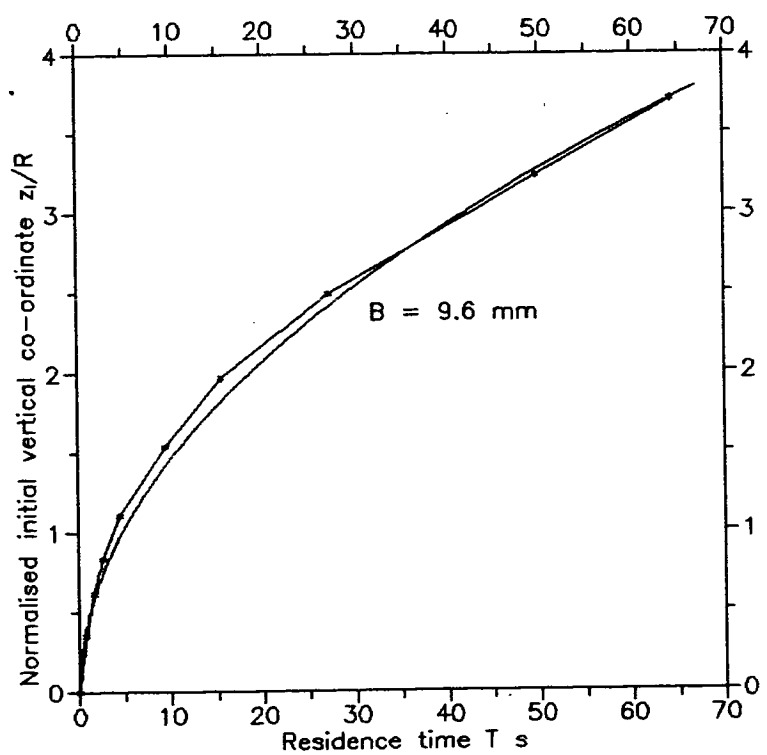

Fig. 6.50 Fitting the theory of Mullins (1974) to experimental data for polypropylene pellets during principal flow

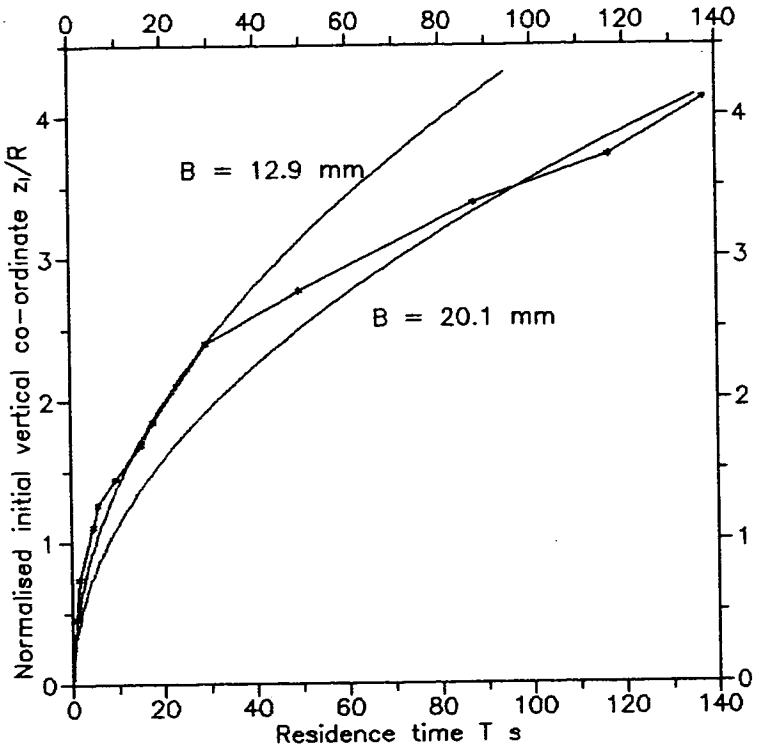

Fig. 6.51 Fitting the theory of Mullins (1974) to experimental data for sand during post-refilling flow

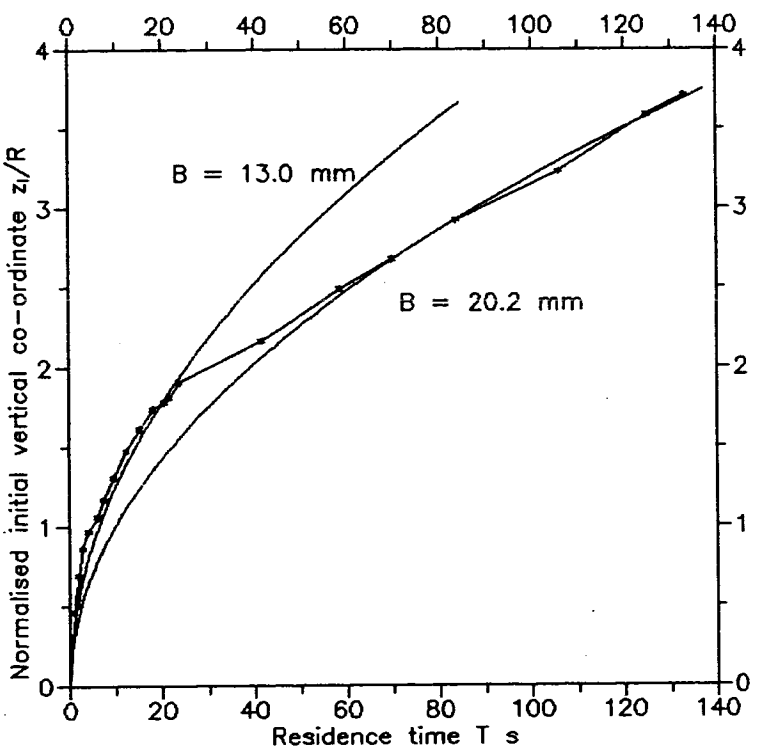

Fig. 6.52 Fitting the theory of Mullins (1974) to experimental data for polypropylene pellets during post-refilling flow

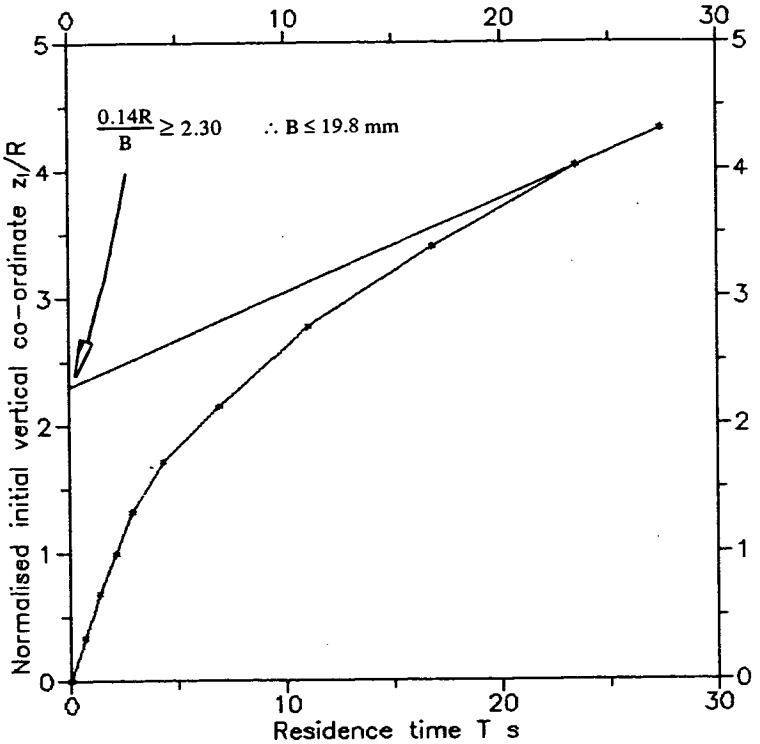

Fig. 6.53 Estimating the kinematic constant for sand during principal flow after Graham *et al* (1987)

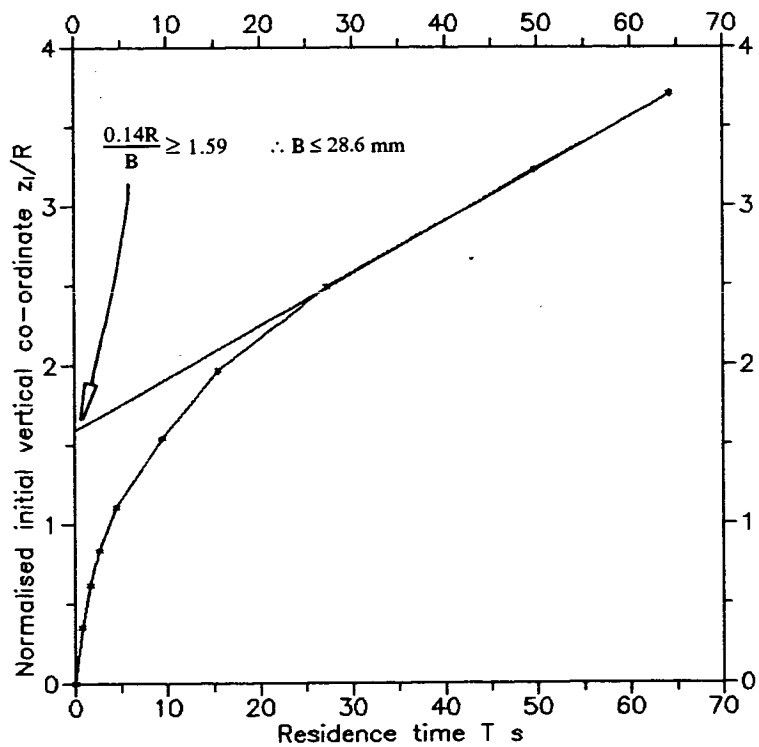

Fig. 6.54 Estimating the kinematic constant for polypropylene pellets during principal flow after Graham *et al* (1987)

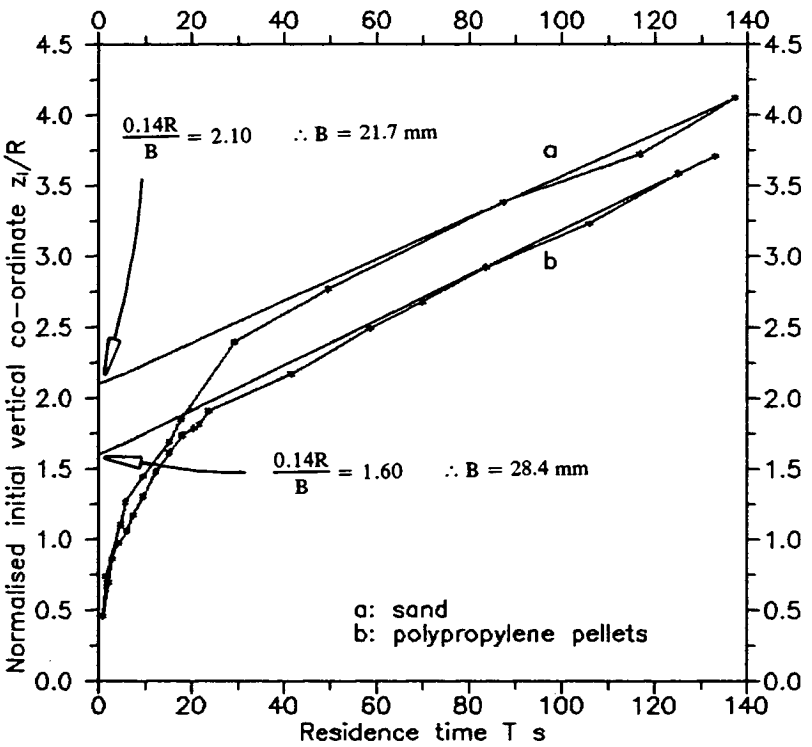

Fig. 6.55 Estimating the kinematic constant for sand and polypropylene pellets during post-refilling flow after Graham *et al* (1987)

CHAPTER 7

COMPARISON OF EXPERIMENTAL RESULTS WITH PREDICTIONS OF THE KINEMATIC THEORY

7.1 Introduction

In this chapter, the experimental findings described in the previous chapter are compared with the predictions of the axisymmetric version of the kinematic theory described in Chapter 4. Three comparisons are made. These are between the experimental and theoretical predictions of:

(1) flow channel boundaries (FCBs);
(2) residence times; and
(3) particle trajectories.

The comparisons were used to produce a qualitative assessment of the validity of the numerical model.

Comparisons (1) and (2) are used to estimate the kinematic parameter B that best fits the experimental data. It will be seen that the spatial variation of B in the silo can also be estimated. In Chapter 6, five methods for estimating B were described and three of them were presented. The two comparisons (1) and (2) constitute the remaining two methods. These comparisons are used to estimate values of B for both solids in both flow regimes. These values of B are then compared with the values that were obtained from the other three methods in Chapter 6 (the analytical methods of Mullins (1974) and Graham *et al* (1987) and the method of direct velocity measurement).

Comparison (3), between experimental and theoretical particle trajectories, cannot be used to assess the value of B since it was found in Chapter 5 that the particle trajectories are relatively independent of the value of B even though the velocity down the trajectory is not. Comparison (3) does, however, provide an interesting

qualitative comparison between the experimental and theoretically-predicted particle trajectories.

7.2 Comparison between the experimental and theoretically-predicted FCBs

7.2.1 General

In the experiments described in Chapter 6, the FCB was traced on the front wall using a water-soluble pen. In this chapter, these direct observations are compared with the theoretical 1% FCBs predicted from the numerical model for different values of B. Four such FCBs are compared (two solids, each with two flow regimes).

In all comparisons, initial attempts were made at matching the experimentally-measured FCBs with theoretical predictions using a constant value of B throughout the whole silo. A good match was deemed to be one which minimised the discrepancies between the experimental and theoretical FCBs as judged by eye. To reduce the discrepancies further, spatial variations of B were then explored. Because the FCB has a locus in r,z space, variations of B with the radial co-ordinate, the vertical co-ordinate or combinations of both the radial and vertical co-ordinates could be explored. Only variations of B with vertical co-ordinate were examined for the following reasons. Tuzun and Nedderman (1979a) reported that B increased with height. The method of estimating B using the theory of Mullins (1974) (see Section 6.3.5.5) also predicted that B may increase with height. By restricting the variation of B to the vertical co-ordinate in this section, these findings can be examined. The method of estimating B from the measured residence times of tracers close to the centreline, discussed in Section 7.3, also only explores variations of B with the vertical co-ordinate. Comparisons between all the methods used to estimate B (see Section 7.5) are facilitated by concentrating on the variation of B only with vertical co-ordinate. Since only a vertical variation in B is examined, the resulting pattern that leads to minimum discrepancies between the experimental and the theoretically-predicted FCB may not be the only or the optimum solution.

7.2.2 Comparisons

Each comparison between the experimental and the theoretically-predicted FCBs is now discussed in turn.

Polypropylene pellets during the principal flow regime

It was found that when B = 2.0 mm, the numerical model predicted a flow channel that was too narrow (Fig. 7.1). When B = 10.0 mm, the model predicted a flow channel that was too wide. When B took the value of 5.0 mm, a reasonable match to the experimental data was achieved. However, the predicted boundary became too narrow in the middle section of the curve and diverged quite markedly towards the top. An alternative prediction was sought using a spatial variation in B to minimise these discrepancies.

In general, as the value of B is decreased the predicted FCB becomes narrower and the channel boundary approaches the vertical at lower heights. Since the experimental FCB becomes almost vertical towards the top of the section used in tracing the boundary on the front wall (Fig. 7.1), a kinematic parameter that decreased with height was adopted. It was found that a linear variation that prescribed B = 6.0 mm on z/R = 0 (the silo floor) and B = 0.1 mm on z/R = 4.31 (the free surface) (*i.e.* B = 6.0 - 1.4z/R mm) provided a good predictive match to the experimental FCB (Fig. 7.1). However, this predicted FCB still began to diverge from the experimental FCB towards the top. A more complex variation in B was thus sought. Through successive refinements the variation shown in Fig. 7.2 was arrived at. This provided an accurate match to the experimental FCB for the entire height that the boundary was traced on the front wall. However, such a variation appears to be too complicated to be justified by any rational explanation. Thus, the linear variation of B = 6.0 - 1.4(z/R) mm is adopted as the kinematic parameter that provides an adequate fit to the experimental data. This kinematic parameter produces a prediction that differs only by a maximum of 12 mm from the experimental FCB.

Only simple linear variations in B with height are explored in the following three flow permutations. It is possible that higher-order variations would produce a better match, but these were deemed beyond the scope of this thesis. It will be seen that the linear variations lead to predicted FCBs that are never more than 10 mm from the experimentally-measured FCB.

Sand during principal flow

The experimental FCB for sand during the principal flow regime is shown in Fig. 7.3 together with some theoretical predictions. A kinematic parameter of 2.0 mm led to a FCB that was too narrow, whilst B = 5.0 mm led to a FCB that was too wide at all heights at which the boundary was traced. When B = 3.0 mm a reasonable global fit to the experimental data was achieved but local discrepancies of over 30 mm were present. The experimental FCB for this flow regime again became almost vertical towards the top of the studied section (Fig. 7.3). Therefore, variations in B that decrease with height were again explored. It was found that when B is taken to decrease from 3.5 mm on z/R = 0 to 0.1 mm on z/R = 4.31 (the free surface), a very satisfactory match is produced (Fig. 7.3).

Polypropylene pellets during post-refilling flow

The experimental FCB for polypropylene pellets during the post-refilling flow regime is shown in Fig. 7.4. This boundary intersected the silo wall at a height of z/R = 1.57 and was almost linear, displaying little curvature. When B = 5.0 mm, the predicted FCB is very close to the experimental FCB below z/R = 0.25. The prediction then rapidly becomes too narrow. When B = 8.0 or 10.0 mm, the predicted FCBs display too much curvature to afford an accurate fit to the experimental data. However, when B = 10.0 mm, the predicted FCB strikes the wall at z/R = 1.65, only 4.8% higher than the position where the experimental FCB struck the wall. Kinematic parameters that linearly increased from 5.0 mm at z/R = 0 were examined. Two such cases are shown in Fig. 7.4: the curve labelled (c) has B increasing to 30.0 mm on z/R = 4.31 and the curve labelled (e) has B increasing to 40.0 mm on z/R = 4.31. It is seen that the latter variation provides an excellent fit to the experimental data.

Sand during post-refilling flow

It was found that with B = 5.0 mm in the numerical model, the predicted FCB lay inside the experimental FCB for the entire height that the boundary was traced on the front wall (see Fig. 7.5). Conversely, with B = 10.0 mm, the predicted FCB lay outside the experimental FCB throughout the entire height. When B = 8.0 mm, a good fit to the experimental data was achieved up to a height of z/R = 1.0. Above this height, the predicted FCB became too wide and intersected the wall (Fig. 7.5). Therefore, kinematic parameters that started at 8.0 mm on the silo floor and decreased with height were examined. In Fig. 7.5, B = 8.0 - 1.6(z/R) mm

represents a kinematic parameter that decreases from 8.0 mm to 1.0 mm on the free surface and B = 8.0 - 1.4(z/R) represents a kinematic parameter that decreases from 8.0 mm to 2.0 mm on the free surface. The latter of these variations provides a very good fit to the experimental data.

7.2.3 Summary

The spatial variations in B that have been estimated by fitting predictions from the kinematic model to the experimental FCB as traced through the front wall are shown in Table 7.1. It is seen from this table that all predictions estimate a kinematic parameter that decreases with height except for the case of polypropylene pellets during the post-refilling flow regime. For this flow permutation, the FCB strikes the wall. For the other three flow permutations, the FCB becomes almost vertical in the upper section, requiring a very low value of B to model the behaviour in these regions. Were the silo much wider, it is expected that the FCB for polypropylene pellets during the post-refilling flow regime would start to curve upwards and tend towards the vertical. In this case, a kinematic parameter that decreased with height would perhaps provide the best fit to the experimental data.

The spatial variations in B predicted by this method provide accurate matches to the experimental data in all four flow permutations. As mentioned above, these spatial variations in B are not necessarily the only variations that could be used to achieve such accuracy to the experimental data. Further work could be undertaken to achieve a rigorous and statistically-based fit, but this was deemed to be beyond the scope of the present work.

7.3 Comparison between the experimental and theoretically-predicted residence times

7.3.1 General

In this section two comparisons are made. These are between the variation of the residence time with height close to the centreline and between the variation of the residence time with radial co-ordinate. In Chapter 6, the initial height z_i/R of tracers originally positioned close to the centreline was plotted against the residence

time T for sand and polypropylene pellets in both the principal and post-refilling flow regimes (Fig. 6.28). These tracers began to move almost immediately after the orifice was opened. As a result, the residence time of each tracer accurately represents the time it was in motion. As has been mentioned before, these tracers were retarded to a small extent by being close to the front wall. To take account of this, their residence times were corrected from an examination of the other tracers in the silo (see Section 6.3.2.3).

Also in Chapter 6, a plot of the residence time T against the normalised radial co-ordinate r/R was produced for polypropylene pellets during the principal flow regime (Fig. 6.15). These residence times were corrected by taking into account the time taken for the FCB to reach their position (see Section 6.3.2.4).

In this section, these plots are compared with theoretical predictions from the finite element formulation of Chapter 4. In this way, the spatial variation of the kinematic parameter can be estimated.

The process of matching observed and predicted residence times was as follows: first, it was necessary to estimate the centreline exit velocity, since this must be specified in the numerical analysis. One way of estimating this velocity is to consider the gradient of the relationship between initial vertical height of tracers close to the centreline and their residence times (Fig. 6.28). This gradient is the modulus of the vertical velocity close to the centreline (factored by the silo radius R). The value of this gradient at $z_i/R = 0$ should therefore provide a measure of the vertical exit velocity close to the centreline. This value could be used to estimate the vertical velocity at the centre of the orifice (*i.e.* the centreline exit velocity). However, since the data in Fig. 6.28 represent the transient flow conditions which occur only immediately after opening the orifice, the gradient at $z_i/R = 0$ does not provide the required steady-state vertical velocity. Even if residence times were measured during steady-state conditions (for example, by positioning tracers during discharge *via* placing tubes), the gradient at $z_i/R = 0$ would still be hard to measure accurately for the following reason. At small heights above the orifice, this gradient would become very steep and would depend strongly on the residence times of the tracers positioned in this region. The experimental errors involved in measuring these very small residence times would be great. The vertical exit velocity close to the centreline obtained from this gradient would therefore not be reliable.

An alternative method of finding the centreline exit velocity was therefore employed, in which the form of the exit velocity distribution was assumed. From the assumed distribution, and the known volumetric flow rate (assumed constant), a value for the centreline exit velocity was obtained.

The exit vertical velocity distribution was not constant with radial co-ordinate, since it was observed that the velocity of the granular solid was high in the centre of the orifice and zero at its edge. Across the orifice, two variations of vertical velocity with radius were considered: a conical exit velocity distribution and a cubically-varying exit velocity distribution (Fig. 7.6). It is shown in Appendix 7.1 that these two exit velocity distributions result in centreline vertical velocities that differ by only 10%. The choice between them is therefore not critical. From a close examination of the exit velocities during the experiments, the cubic variation was deemed to provide the most accurate modelling. Using the known volumetric flow rate for each solid, the vertical velocity at the centre of the orifice was calculated as -1.69 m/s for sand and -1.38 m/s for polypropylene pellets during the period where the flow was stable. These velocities are negative because they are directed vertically downwards, in the negative z-direction.

In these comparisons, the challenge was to find the spatial variation of B which gives an accurate fit to the test data. This was judged by eye to be the curve that provides the best approximation to the experimental data over the whole range that data was collected. The process of finding the best choice is a little complicated and was undertaken as follows. First, a constant value of B was adopted throughout the silo and the value of B which provides the best fit to the experimental data was deduced. Next, a spatial variation of B was explored, to reduce the discrepancies. A vertical variation was adopted for the plots of z_i/R against T and a horizontal variation was adopted for the plot of T against r/R. By successive refinements, a spatial variation of the kinematic parameter was arrived at which provided a close fit to the experimental residence times. It was found that a simple linear variation is adequate to produce an accurate modelling of the experimental data.

7.3.2 Comparisons and discussion for plots of z_i/R against T

Each of the four flow permutations (two solids, each with two flow regimes) are now discussed in turn. The analytical best fits using the theory of Mullins (1974), which were previously shown in Figs 6.49-6.52, are included for comparison in the final plots for each flow permutation (Figs 7.7, 7.8, 7.12 and 7.16). The values of B established by this numerical fitting technique are shown in the figures and in Table 7.2.

Sand during principal flow

It was found that in the principal flow regime for sand (Fig. 7.7), an excellent fit to the experimental data was obtained using a homogeneous value of B of 3.5 mm throughout the silo. The match is extremely good above $z_i/R = 1.5$. Below this height, the theoretical prediction and the experimental data diverge very slightly. Since the residence times are under 3 seconds in this region, the divergence is not significant. In Fig. 7.7, theoretical relationships between the initial vertical co-ordinate z_i/R and the residence time T for control values of B of 2.0, 3.0, 4.0 and 5.0 mm are also shown to illustrate the accuracy of the theoretical fit of B = 3.5 mm. The theory of Mullins (1974) also provides a good fit, with B = 3.7 mm.

Polypropylene pellets during principal flow

During the principal flow regime for polypropylene pellets (Fig. 7.8), the experimental relationship between z_i/R and T is again matched very well using a constant value of B throughout the silo, this time of 9.0 mm. The match is not quite as good as the previous one for the principal flow regime of sand (Fig. 7.7), but it was not necessary to search for a spatial variation which provided an even more accurate match since the discrepancy at all heights was less than 2.5 s. Again, the theory of Mullins (1974) provides a reasonable fit to the experimental data, this time with B = 9.6 mm.

Sand during post-refilling flow

The experimental plot of z_i/R against T during the post-refilling flow regime of sand (Fig. 7.9) is now examined. It was found in Section 6.3.5.5, that the theory of Mullins (1974) could not be used with a constant value of B to provide a good fit to this experimental relationship. It was also found that numerical predictions using a constant value of B also did not provide a good match to the data set (see Fig. 7.9).

The theory of Mullins (1974) predicted two different values of B, one value suitable for the lower section of the silo and a higher value suitable for the upper section. This is in keeping with the findings of Tuzun and Nedderman (1979a), who experimentally measured a kinematic parameter that increased with height. For these reasons, spatial variations of B that increase with height are explored here. In Fig. 7.10, four spatial variations in B are shown that all start with B = 2.0 mm on the silo floor and increase with height. It is seen that when B increases to 70.0 mm on the free surface (*i.e.* B = 2.0 + 15.8z/R mm), a good match to the experimental data, as judged by eye, is achieved at all heights. In Fig. 7.11, alternative variations of B are explored. These variations start at 5.0 mm on the silo floor and increase with height. It is seen from this figure that when B increases from 5.0 mm on the silo floor to 60.0 mm on the free surface (*i.e.* B = 5.0 + 12.8z/R mm), a satisfactory fit is produced.

Thus, two alternative spatial variations of B have been found that both provide good fits to the experimental data. These are shown in Fig. 7.12 along with the predictions from the theory of Mullins (1974). Of the two numerically-predicted fits, the B = 2.0 + 15.8z/R mm variation was judged to provide a marginally better fit.

Polypropylene pellets during post-refilling flow

The experimental relationship between the initial height of tracers z_i/R and the residence time T for the post-refilling flow regime for polypropylene pellets could not be modelled by using a constant value of B throughout the silo (Fig. 7.13). Spatial variations in B that increased with height were again explored. The kinematic parameter was set to increase from 2.0 mm to a range of higher values in Fig. 7.14 and from 5.0 mm to a range of higher values in Fig. 7.15. From these figures, the variations of B increasing from 2.0 mm to 80.0 mm (B = 2.0 + 18.1z/R mm) and from 5.0 mm to 70.0 mm (B = 5.0 + 15.1z/R mm) both provide accurate fits to the experimental data. These two variations are shown along with the predictions using the theory of Mullins (1974) in Fig. 7.16. The two spatial variations both provide accurate fits to the experimental data. The former spatial variation (B = 2.0 + 18.1z/R mm) was judged to be slightly more accurate and is adopted from comparison with the values of B obtained from the other methods. This comparison is carried out in Section 7.5.

7.3.3 Comparisons and discussion for plot of T against r/R

In Fig. 7.17, the experimental plot for polypropylene pellets during the principal flow regime of T against r/R at a height of z/R = 1.54 is shown together with some theoretical predictions. The relationship between T and r/R at this height proved to be characteristic, so relationships at other heights are not presented. It can be seen that when B = 5.0 mm, the predicted residence times close to the centreline are too low, but quickly become too high at increasing horizontal co-ordinates. When B = 10.0 mm, the predicted residence times are higher than the experimental residence times at all co-ordinates. A kinematic parameter that increased from 5.0 mm on the centreline to 20.0 mm at the side wall was used to try to improve the match. However, this variation still did not provide a reasonable match to the experimental data. The reasons for this are now examined.

The residence times represented in Fig. 7.17 were corrected by subtracting the approximate time the FCB took to reach the tracer's position from the residence time that was measured during the experiment (Section 6.3.2.4). The effect of the slight inward curvature of the FCB at the front wall (Fig. 6.11) was ignored. This curvature would have the effect of causing an over-estimation of the time taken for the FCB to reach a particular tracer. Therefore, the corrected residence time would be too low. For this reason, it was not possible to match the experimental plot of the corrected residence time against the radial co-ordinate, even with a spatial variation in B.

7.3.4 Summary

The values of B estimated from the method of matching the residence times of tracers positioned close to the centreline with predictions of the present finite element formulation are presented in Table 7.2. It seems that in the principal flow regime, these residence times can be accurately modelled using a constant value of B for both solids (Figs 7.7 and 7.8). However, in the post-refilling flow regime a spatial variation in the kinematic parameter is needed (Figs 7.12 and 7.16). Because the analytical treatment of Mullins (1974) cannot accommodate a spatial variation of B, the match between the current experimental data and his theory is not good in the post-refilling flow regime. The numerical predictions in post-

refilling flow yield a kinematic parameter that increases with height. This finding is in agreement with the experimental observations of Tuzun and Nedderman (1979a).

7.4 Comparison between experimental and theoretically-predicted particle trajectories

In Chapter 6, the method of direct observation of particle trajectories by tracing on the front wall was described. In this section, these experimental trajectories are compared with theoretically-simulated trajectories. To obtain a theoretical simulation, a value of B was needed. However, in Chapter 5 it was found that theoretically-predicted particle trajectories are very nearly independent of the value of B, especially when the trajectory is close to the centreline. The choice of which value of B to use is therefore not critical. However, a value that relates to the flow conditions and granular solid is desirable.

In Chapter 6, five methods for the evaluation of B were described. Three of these methods were implemented in Chapter 6 and the remaining two methods have been implemented in the preceding two sections of this chapter. The results are shown in Table 7.3 and are discussed later in Section 7.5. In Chapter 6, it was found that the trajectories traced for sand and polypropylene pellets were very similar. The trajectories during principal flow were also found to show little curvature. For these reasons, only trajectories in the post-refilling flow regime of polypropylene pellets are theoretically-simulated. Since the choice of which value of B to use from Table 7.3 is not critical, an approximate mean value was adopted. This was 40 mm for polypropylene pellets during the post-refilling flow regime.

Two experimental and theoretical particle trajectories for polypropylene pellets during the post-refilling flow regime are shown in Fig. 7.18. The scale of the horizontal axis has been blown up with respect to that of the vertical axis to highlight the differences between the experimental and theoretically-simulated trajectories. It is seen that the match is satisfactory for the entire length of the trajectory. The maximum deviation between the experimental and theoretical trajectories is only 0.046 R or 15.1 mm. This comparison demonstrates that the finite element method described in Chapter 4 predicts the trajectories of particles discharging in steady-state conditions quite accurately.

7.5 Comparison of methods for determining B

7.5.1 Introduction

Five different methods of finding a value for the kinematic parameter B were described in Chapter 6. These were from:

(a) a fit to the experimentally-determined FCB using the finite element theory of Chapter 4;

(b) a fit to the relationship between initial height z_i/R and residence time T for tracers close to the axis using the finite element theory of Chapter 4;

(c) direct measurements of velocity through the front wall;

(d) a fit to the relationship between the residence time T and the square of the initial height z_i^2 using the theory of Mullins (1974); and

(e) the asymptotic intercept in the plot of initial height z_i against residence time T using the theory of Graham *et al* (1987).

Methods (c), (d) and (e) were implemented in Chapter 6 and Methods (a) and (b) have been implemented above. The values of B estimated using the five methods are summarised in Table 7.3.

7.5.2 Critique of methods

In this section, each of the five methods for estimating B are considered in turn. The relative accuracy of each method and its merits and drawbacks are discussed.

Method (a)

Method (a) involved matching the FCB as traced through the front wall to the predictions of the kinematic theory formulated in Chapter 4. In this thesis, the FCB was somewhat arbitrarily defined as the locus of points where the vertical velocity fell to 1% of that at the centreline at the same height. In Chapter 5, it was shown that this simple criterion is equivalent to the trajectory of a very slow particle. If a higher percentage criterion had been used in the numerical model, the value of B predicted using Method (a) would be slightly higher. Conversely, if a lower criterion had been used the predicted value of B would be slightly lower. The

subjectivity of the choice of 1% is therefore a small source of error. As discussed in Chapter 3, 1% was selected because it was judged to be a realistic value.

The tracing of the FCB on the front wall, as described in Section 6.3.3.2, was not a clear-cut affair, particularly during the principal flow regime where this boundary becomes only quasi-stable. For these reasons, the value of B estimated using Method (a) is expected to provide only a rough approximation to the true value.

Method (b)

Method (b) involved fitting the predictions of the kinematic theory to the measured residence times of tracers positioned at different heights 25 mm from the centreline. For principal flow, most of these tracers discharged before the quasi-stable FCB had been fully attained. For this reason, the value of B derived from the residence times of these tracers during principal flow was expected to give a slightly low estimate and to produce a predicted FCB that was slightly too narrow. In fitting the theory to the experimental data, a value of the centreline exit velocity was required. This was calculated from an assumed exit vertical velocity distribution, as described in Section 7.3.1 above. The theory of Mullins (1974) was used in Section 6.3.5.5 to predict values of B. These assumptions were based only on the volumetric flow rate and not the shape of the exit velocity distribution. It may be seen from Figs 7.7 and 7.8 that the predictions using the theory of Mullins (1974) are very similar to those of the present finite element formulation. It is concluded, therefore, that the adopted cubic exit velocity distribution is reasonably accurate.

Method (c)

A value of B was estimated from measured velocities in Method (c). Trajectory pairs were traced on the front wall and estimates of the mean horizontal velocity and the mean horizontal gradient of the vertical velocity were made at the point midway between the trajectories. A large degree of measuring of distances and of time intervals was required for this method and this was a source of experimental error. This would affect the subsequent calculations leading to the estimate of B. For this reason, the values of B using Method (c) were considered to be only guiding approximations. However, Method (c) is the only (current) method that can be directly used to estimate the spatial variation of B with both the radial and vertical co-ordinates.

Method (d)

In Method (d), the analytical theory of Mullins (1974) was used to estimate a homogeneous value of B for the whole silo. This theory assumes that the solid forms a semi-infinite bed and discharges through a point orifice. It is expected that the predictions from this theory will only be reliable at large distances from the orifice and the silo walls and in a flow regime where the value of B does not vary spatially.

Method (e)

Method (e) uses the theory of Graham *et al* (1987) to estimate a constant value of B for the whole silo. An asymptote is drawn on the plot of initial vertical height z_i/R of tracers on the silo axis against the residence time T. An estimate of B can be made from the point where this asymptote intercepts the vertical axis. If the silo has a high aspect ratio (say, $H/D > 5$, where D is the silo diameter), the asymptote will be easy to identify. In squat silos, the gradient of the relationship between z_i/R and T will not become constant, and an accurate asymptote cannot be drawn.

In the experiments of this thesis, described in Chapter 6, it was mentioned that the tracers could not be positioned exactly on the silo axis because of the presence of the front wall. The theory of Graham *et al* (1987) assumes the tracers to be on the axis, so errors will be incurred when using the residence times of tracers positioned only close to the axis. Because this method relies on uniform flow behaviour at large heights above the orifice, the errors are not very significant.

It was demonstrated in Chapter 5 that the kinematic theory using a constant value of B cannot accommodate the analysis of flow down an inclined boundary. Because this is one of the boundary conditions incorporated into the theory of Graham *et al* (1987), doubt is cast on the accuracy of their method for estimating B.

Summary

From the five methods for estimating B discussed above, Method (b) is considered to be the most accurate. This method can be used to predict a spatial variation of B with vertical co-ordinate and relies on measured residence times which generally involve only small experimental errors. Tracers close to the centreline were used. The retarding effect of these tracers was taken into account (see Section 6.3.2.3) and the small distance the tracers lay from the axis (25 mm) was incorporated into the numerical analysis when predicting their residence times.

7.5.3 Discussion of results

The results from the five methods used to estimate a value for the kinematic parameter B are presented in Table 7.3. It can be seen that there is no entry for the value of B for the principal flow regimes of both solids as calculated from Method (c). In this method, the value of B was determined from estimates of the mean horizontal gradient of the vertical velocity and the mean horizontal velocity. During the principal flow regime, the flow channel was narrow and the trajectories of particles were almost vertical. The calculation of the mean horizontal velocity for these trajectories was therefore prone to large errors. For this reason, Method (c) was not used during the principal flow regime.

A number of observations can be made concerning the values of B shown in Table 7.3. Each flow permutation is considered in turn.

Principal flow regime for sand

Methods (b) and (d) predict values of B of 3.5 mm and 3.7 mm respectively. Method (a) predicts a spatial variation of B of 3.5 mm at the bottom of the silo decreasing linearly to 0.1 mm at the top of the silo. It is seen that all these three methods predict very low values of B relative to the other values in Table 7.3. In Method (e), the value of the asymptotic intercept in the plot of initial vertical co-ordinate z_i/R against residence time T (Fig. 6.53) was used to estimate a value for B. Since it was not easy to identify this asymptote, only an upper-bound value (19.8 mm) can be estimated. When this value was used in the finite element formulation, a flow channel that was far too wide was predicted. For Method (e) to give a value of B of 3.5 mm (in line with Method b), the intercept would have to be $z_i/R = 13.0$. From an examination of Fig. 6.53, this intercept would not be reached even if the gradient had stabilised and the asymptote was clearly defined. If the silo had been much taller, a maximum intercept of perhaps $z_i/R = 4.0$ might have been reached. This would yield a value of B = 11.4 mm. The theory behind Method (e) uses the residence times of tracers on the centreline. In the experiments described in Chapter 6, the tracers could not be positioned exactly on the centreline because a half-cylindrical silo was used. The tracers were positioned 25 mm from the centreline. As such, Method (e) will only provide an approximation of the value of B. Even so, the prediction is much higher than the values of B estimated

using the other methods. This casts doubt on the method of Graham *et al* (1987) for estimating a value for B. For the principal flow regime of sand, a constant value of B = 3.5 mm seems to provide a good description of the behaviour of the granular solid.

Principal flow regime for polypropylene pellets

The principal flow regime of polypropylene pellets is now discussed. The trend here is similar to that for the principal flow regime of sand, discussed in the preceding paragraph. Again, the values of B obtained using Methods (b) and (d) are very similar. That from Method (a) is slightly lower. The value of B using Method (e) again provides a very high upper bound. This value is, in fact, higher than that predicted using the same method during the post-refilling flow regime for polypropylene pellets. This suggests that the real value of B for the principal flow regime of polypropylene pellets is much lower than 28.6 mm. It is also not clear whether the gradient of z_i/R against T for this flow condition (Fig. 6.54) has reached its constant value. However, even if the height of the silo were dramatically increased, a value of B using Method (e) comparable to the values obtained using Methods (a), (b) and (d) would not be attained. It is concluded, therefore, that a constant value of about B = 7.0 mm provides a good approximation to the prevalent flow conditions during the principal flow regime of polypropylene pellets. Method (e) is again inaccurate in its prediction.

Post-refilling flow regime for sand

In the post-refilling flow regime for sand, a linear spatial variation in B is predicted using Methods (a)-(c). Method (d) predicts one value of B pertaining to the lower section of the silo and a higher value pertaining to the upper section. Method (e) can only be used to predict a single value for B. In Fig. 7.19, the values of B on the silo axis (r/R = 0), estimated from the five methods, are plotted against the vertical co-ordinate z/R. In Methods (b), (d) and (e) the results close to the centreline are again taken to approximate closely the behaviour on the centreline. In Method (c), the linear regression has been interpolated to r/R = 0. Although this is outside the range over which the data was taken, it still provides a guiding approximation to the value of B on the centreline obtained using Method (c).

As can be seen from this figure, Method (c) predicts negative values of B on the silo axis for $0 \leq z/R \leq 1.95$. A negative value of B is clearly incorrect in terms of the kinematic model expressed in Eq. 3.1. In the region above the orifice, the

particles started to free-fall under gravity, so the kinematic model cannot be applied to this region. An attempt to do so may well yield negative values of B. However, this free-fall region extended only a few centimetres up into the silo so this effect cannot explain the range of negative values predicted by Method (c). In this method, a linear regression analysis was used to determine the spatial variation of B from a limited number of estimated values of B at known points. All the values used were positive (see, for example, Table 6.3). The negative values of B arose only as a result of the regression analysis. This casts doubt on the validity of using a linear regression analysis to predict values of B throughout the whole silo. A non-linear regression analysis may give more sensible predictions on the centreline but, as mentioned in Section 6.3.5.4, the data is insufficient to support such an analysis.

Methods (b)-(d) predict that B increases with height. In addition, Method (c) also predicts that B increases with radial co-ordinate. These trends are here related to the initial packing density. In Chapter 5, a hypothesised relationship between B and the initial density was put forward. It was proposed that in regions of high initial density, a low value of B may be expected whilst in regions of lower initial density, a higher value of B may be expected. In the experiments carried out in this thesis, initial density gradients were expected. During the first stages of filling the silo, the granular solid fell from the reservoir tank through a greater distance than in the final stages. Once the silo was full, the solids near the silo floor had a greater 'head' of solids above them than those solids nearer the top of the silo. For these reasons, it was expected that the density of the granular solid would be relatively high near the silo floor and would decrease with height. In terms of the proposed relationship made in Chapter 5, this conjectured density gradient should lead to low values of B in the bottom of the silo and higher values in the top of the silo. This, in fact, is the trend predicted by Methods (b)-(d). Method (c) predicts that B also increases slightly with radial co-ordinate. The density gradients should not have been significant across a horizontal plane because a distributed filling technique was used. This slight variation of B with radial co-ordinate may be independent of the initial density, but may depend on some other undiscovered physical mechanism. The variation with radial co-ordinate is small compared with the variation in the vertical direction. Method (a) predicts a kinematic parameter that decreases with height. This is in disagreement with the initial-density hypothesis of Chapter 5. It was mentioned previously that the prediction made using Method (a) was only one of a range of possible solutions. It may be possible that an alternative solution

would have predicted that B increases with height, but decreases with radial co-ordinate.

For the post-refilling flow regime using Method (e), the value of B is much more in line with the values obtained from the other four methods than it is for the principal flow regime (Table 7.3). This is because the asymptote in the plot of z_i/R against T (Fig. 6.55) is clearly defined and steady-state flow conditions have been attained.

The spatial variation predicted by Method (b) indicates much higher values of B in the upper section of the silo than the other methods. From Fig. 7.12, it can be seen that the alternative variation of $B = 5.0 + 12.8(z/R)$ also gave a good fit to the experimental data. The relationship between z/R and T is therefore not very sensitive to the final value of B attained at the top of the silo. The values of B obtained from Methods (d) and (e) are close to the mean of this alternative variation.

Post-refilling flow regime for polypropylene pellets

The trends in the values of B predicted from the five methods for this flow condition are similar in many ways to the trends for the post-refilling flow regime for sand, which was discussed above. Again, Method (c) predicts negative values of B in the lower section of the silo; and the value of B using Method (e) is close to the values predicted by the other methods. The extension of the linear regression to the whole silo may be the cause of the negative values predicted using Method (c). Also, only three values of B were used to calculate this regression (Table 6.4). This has led to large errors when the regression is extended to encompass the entire height of the silo. Method (e) provides a constant value of B that is approximately the mean of the spatial variation provided by Method (b).

Summary

It can be seen from Table 7.3 that the value of B is generally higher in polypropylene pellets than in sand and higher in the post-refilling flow regime than in the principal flow regime. This implies that the flow channel is wider in polypropylene pellets than in sand and wider in post-refilling flow than in principal flow. Naturally, this rather elementary observation does match what was observed in the experiments.

The spatial variation of B estimated using Method (b) was considered the most accurate for the reasons given above. The constant value of B estimated using Method (e) gives a value close to the mean of the variation predicted using Method (b) provided that the asymptote is easy to identify.

The value of B obtained for post-refilling flow using Method (a) is lower than the values obtained using the other methods (Table 7.3). Method (a) involves fitting the theoretical 1% FCB to the FCB observed through the front wall. If a higher percentage criterion had been used in the numerical model, the value of B estimated using Method (a) would have been slightly higher. This higher value of B from Method (a) would be more in line with the values of B from Methods (b), (c) and (d). The value of B from Method (a) is, however, not significantly different from the values of B from Methods (b), (c) and (d). From this argument, it is concluded that the 1% criterion provides an satisfactorily accurate representation of the FCB.

7.6 Summary and concluding remarks

In this chapter, the results of the experiments described in Chapter 6 have been compared with theoretical predictions from the numerical model described in Chapter 4. Flow channel boundaries, kinematic parameters and particle trajectories have been compared. Where possible, comparisons were made for both the principal and post-refilling flow regimes for both tested solids. It has been demonstrated above that the finite element model can predict the FCB observed through the front wall quite accurately. The theoretical particle trajectories also closely resemble the experimental trajectories that were traced on the front wall. It has been argued that the method of fitting the predictions of the numerical model to the residence times of tracers positioned close to the centreline at different heights (Method (b) above) is the most accurate method of estimating a value for the kinematic parameter.

Appendix 7.1 Comparing two different possible exit velocity distributions

The aim of this appendix is to gauge how sensitive the centreline vertical velocity is to the assumed exit velocity profile for the same volumetric flow rate. The two different exit vertical velocity distributions shown in Fig. 7.6 are considered. The

vertical velocity in the centre of the orifice is denoted $v_o{}^a$ when a conical exit velocity distribution is used and $v_o{}^b$ when a cubic exit velocity distribution is used. It is assumed that both exit velocity distributions produce the same total volumetric flow rate Q (*i.e.* the volumes underneath the two exit velocity distributions are equal). The relationship between $v_o{}^a$ and $v_o{}^b$ is investigated in this appendix. For clarity, only the right-hand half of the silo is considered.

For the conical exit velocity profile, the vertical velocity distribution is given as

$$v_{exit} = v_o{}^a \left(1 - \frac{r}{r_o} \right) \tag{A7.1}$$

Equation A7.1 can be integrated to find the volumetric flow rate:

$$\frac{Q}{2} = \frac{1}{6} \pi r_o{}^2 v_o{}^a \tag{A7.2}$$

For the cubic exit velocity profile, the vertical velocity distribution was given in Eq. 4.15 as

$$v_{exit} = 2v_o{}^b \left(\frac{r}{r_o} \right)^3 - 3v_o{}^b \left(\frac{r}{r_o} \right)^2 + v_o{}^b \tag{A7.3}$$

Integrating this to find the volumetric flow rate gives

$$\frac{Q}{2} = \frac{3}{20} \pi r_o{}^2 v_o{}^b \tag{A7.4}$$

Therefore

$$\frac{v_o{}^a}{v_o{}^b} = 0.90 \tag{A7.5}$$

Thus the two different exit velocity distributions result in centreline exit velocities that differ only by 10.0%.

Table 7.1 Values of B estimated from the FCB (mm)

	principal flow	post-refilling flow
sand	3.5 - 0.8(z/R)	8.0 - 1.4(z/R)
polypropylene pellets	6.0 - 1.4(z/R)	5.0 + 8.1(z/R)

Table 7.2 Values of B estimated from residence times of tracers close to the centreline (mm)

	principal flow	post-refilling flow
sand	3.5	2.0 + 15.8(z/R)
polypropylene pellets	9.0	2.0 + 18.1(z/R)

Table 7.3 Values of B estimated from the five methods (mm)

	principal flow	post-refilling flow
sand	(a) 3.5 - 0.8(z/R)	(a) 8.0 - 1.4(z/R)
	(b) 3.5	(b) 2.0 + 15.8(z/R)
	(c) -	(c) -24.5 + 8.1(r/R) + 13.0(z/R)
	(d) 3.7	(d) 12.9 $0<z/R<2.4$
		20.1 $2.4<z/R<4.2$
	(e) ≤ 19.8	(e) 21.7
polypropylene pellets	(a) 6.0 - 1.4(z/R)	(a) 5.0 + 8.1(z/R)
	(b) 9.0	(b) 2.0 + 18.1(z/R)
	(c) -	(c) -17.5 + 4.9(r/R) + 28.9(z/R)
	(d) 9.6	(d) 13.0 $0<z/R<1.8$
		20.2 $1.8<z/R<3.7$
	(e) ≤ 28.6	(e) 28.4

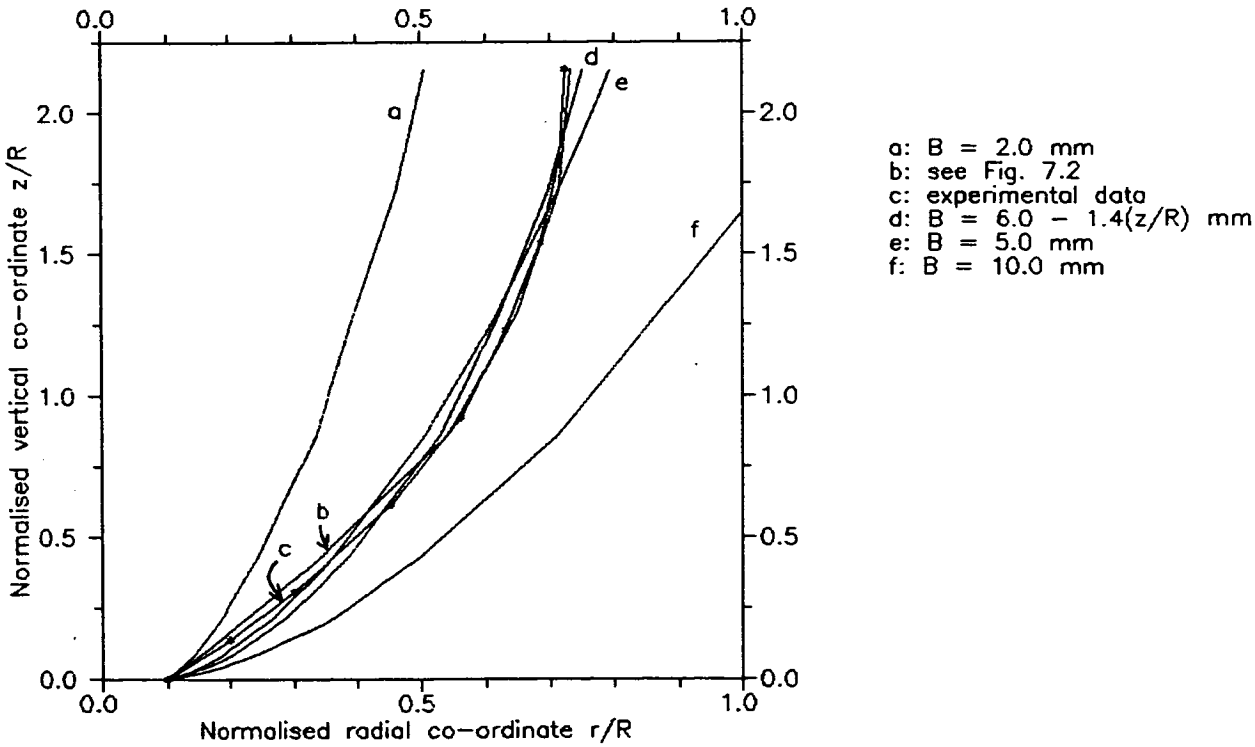

Fig. 7.1 FCB for polypropylene pellets during principal flow

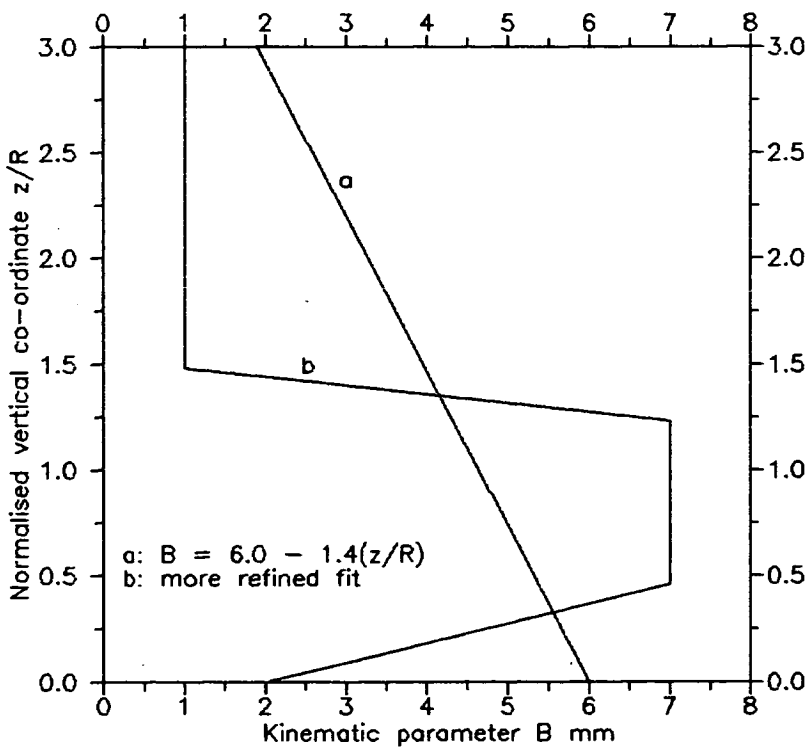

Fig. 7.2 Spatial variations of B

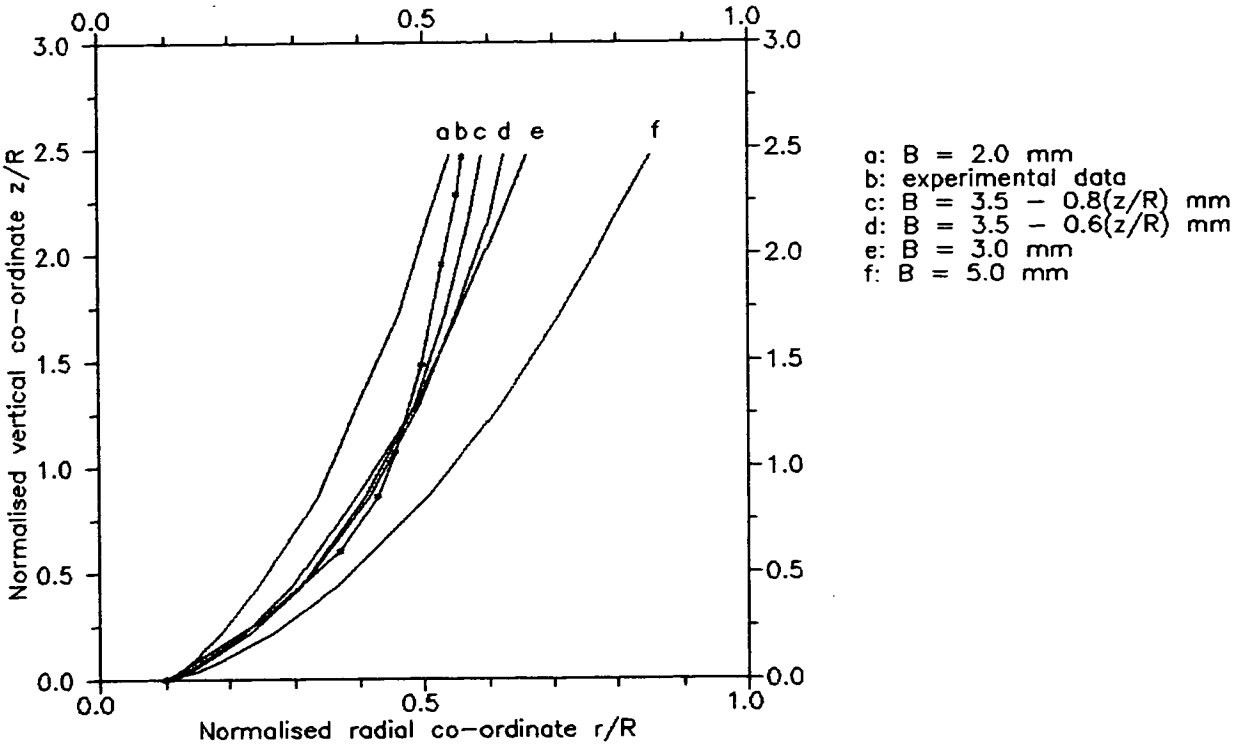

Fig. 7.3 FCB for sand during principal flow

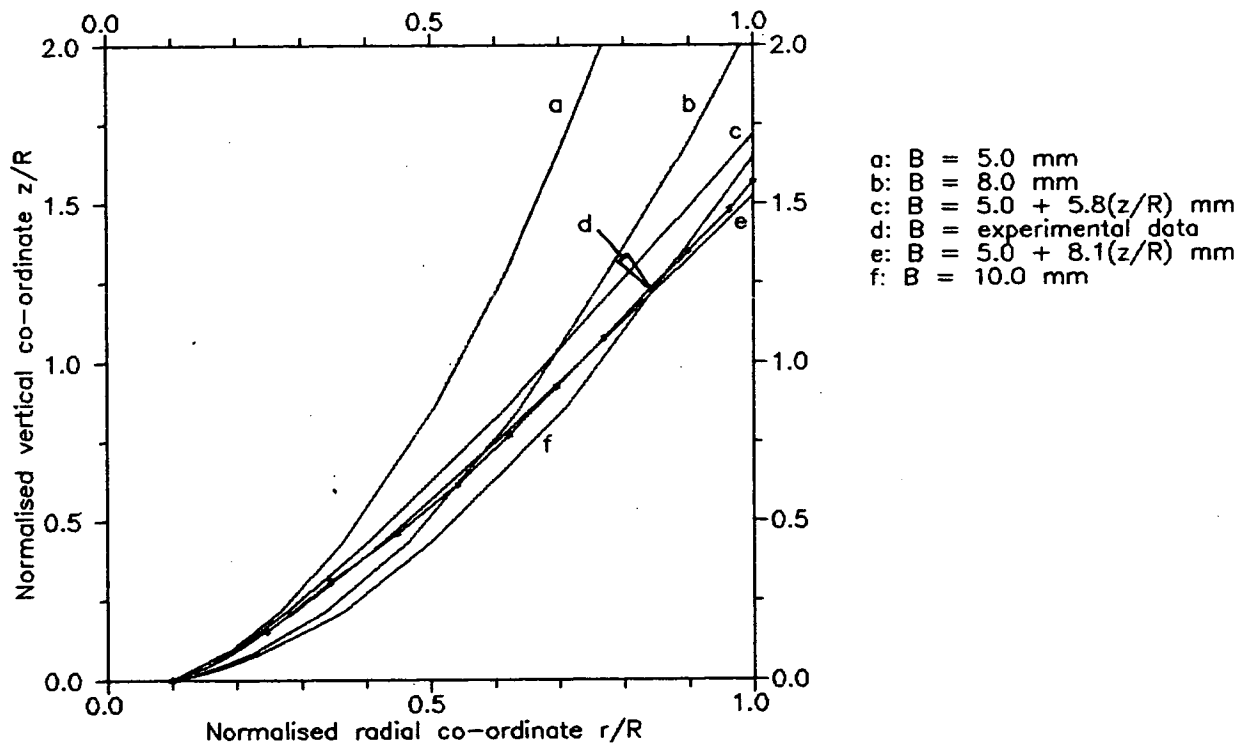

Fig. 7.4 FCB for polypropylene pellets during post-refilling flow

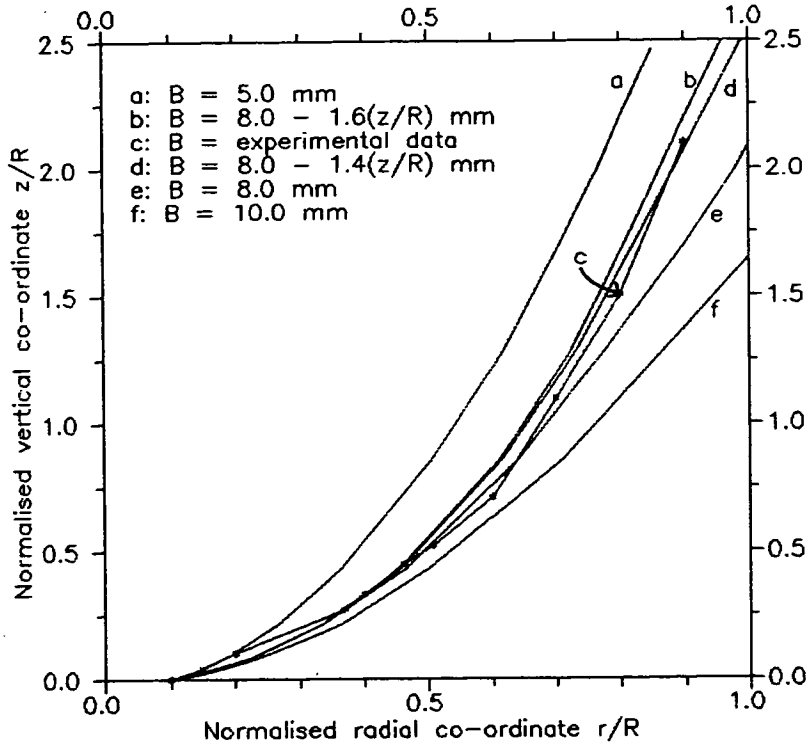

Fig. 7.5 FCB for sand during post-refilling flow

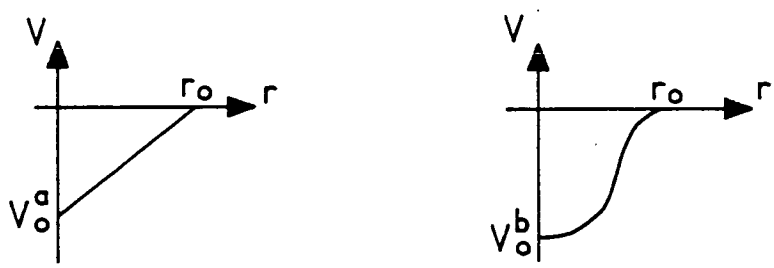

Fig. 7.6 Alternative exit velocity distributions

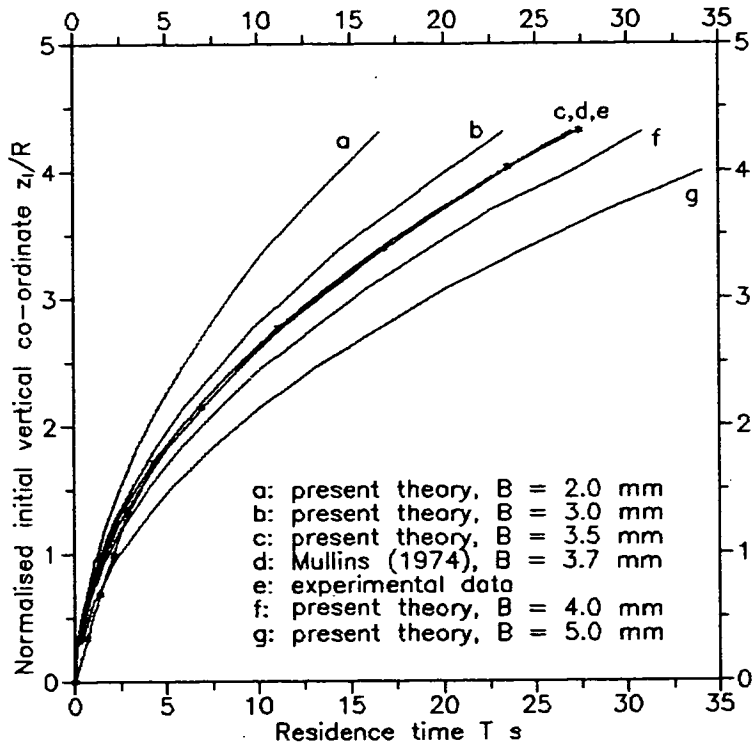

Fig. 7.7 Residence times of tracers close to centreline for sand during principal flow

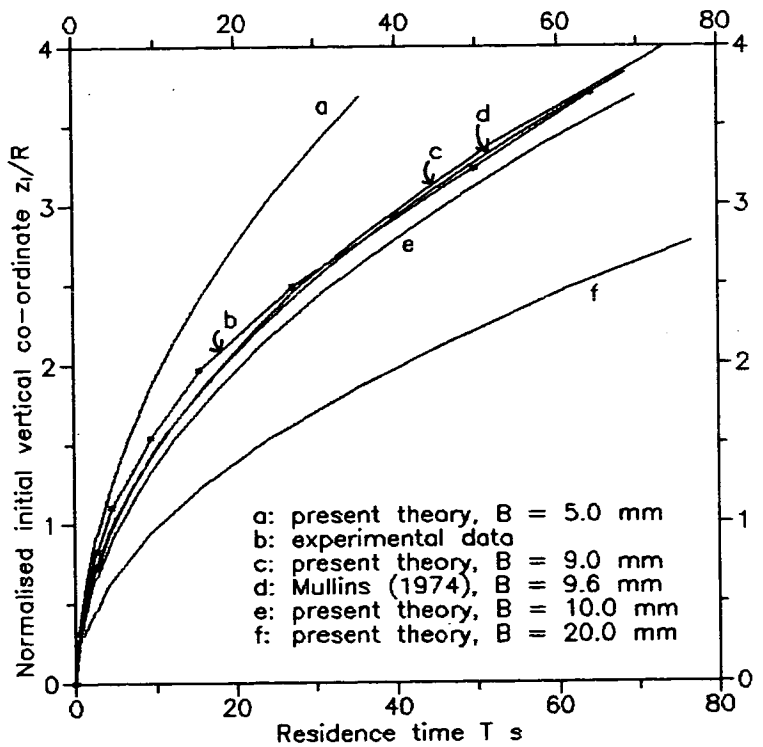

Fig. 7.8 Residence times of tracers close to centreline for polypropylene pellets during principal flow

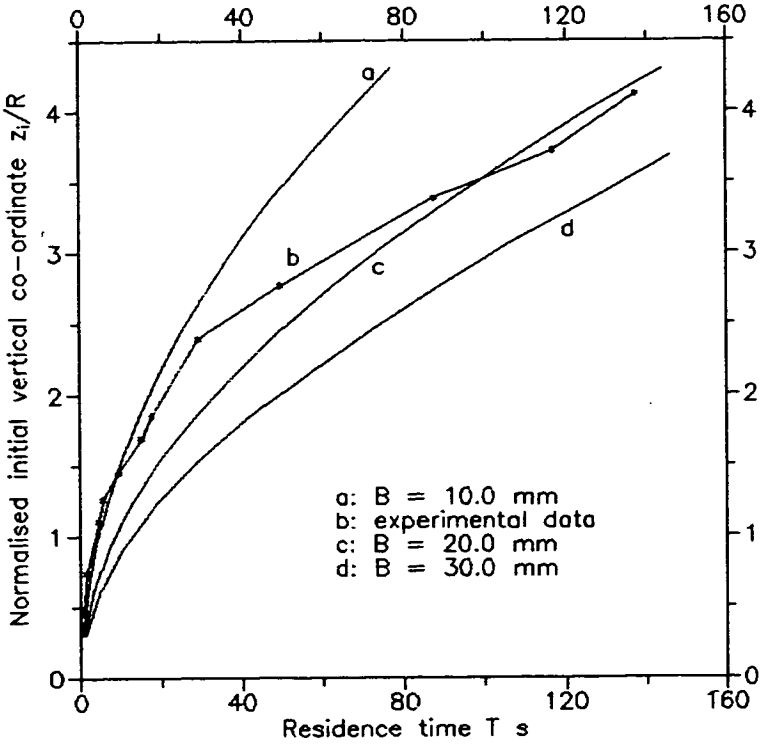

Fig. 7.9 Residence times of tracers close to centreline for sand during post-refilling flow (fit 1)

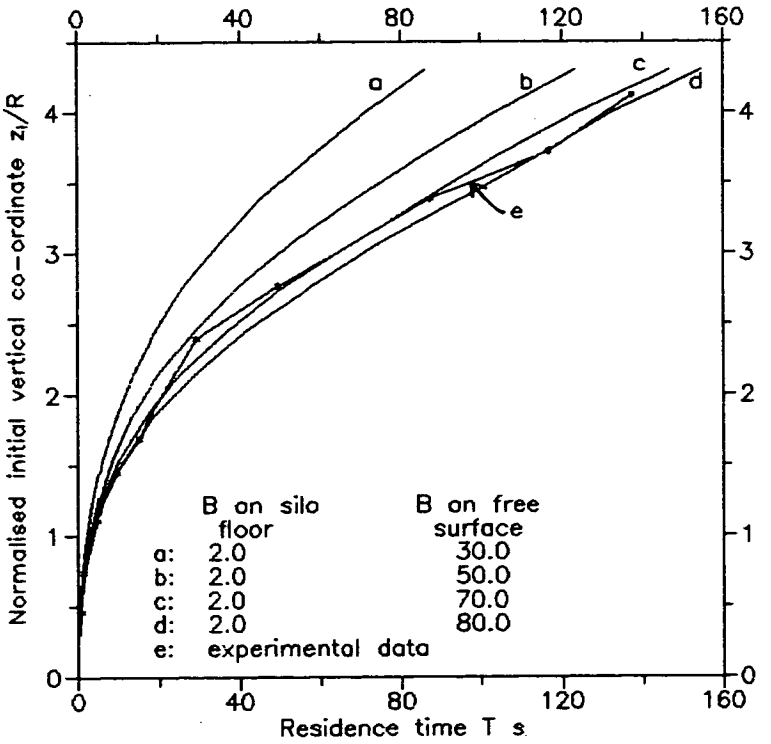

Fig. 7.10 Residence times of tracers close to centreline for sand during post-refilling flow (fit 2)

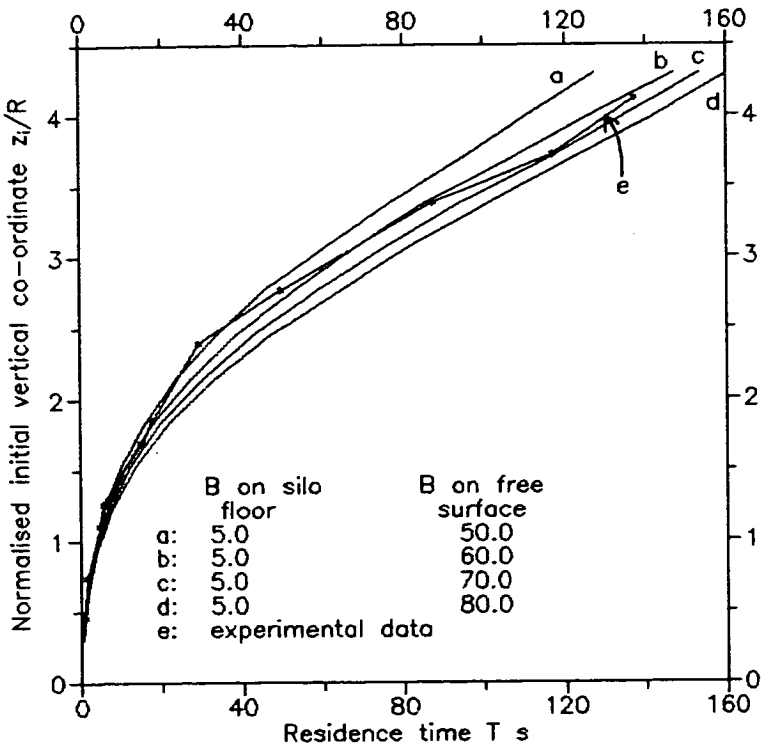

Fig. 7.11 Residence times of tracers close to centreline for sand during post-refilling flow (fit 3)

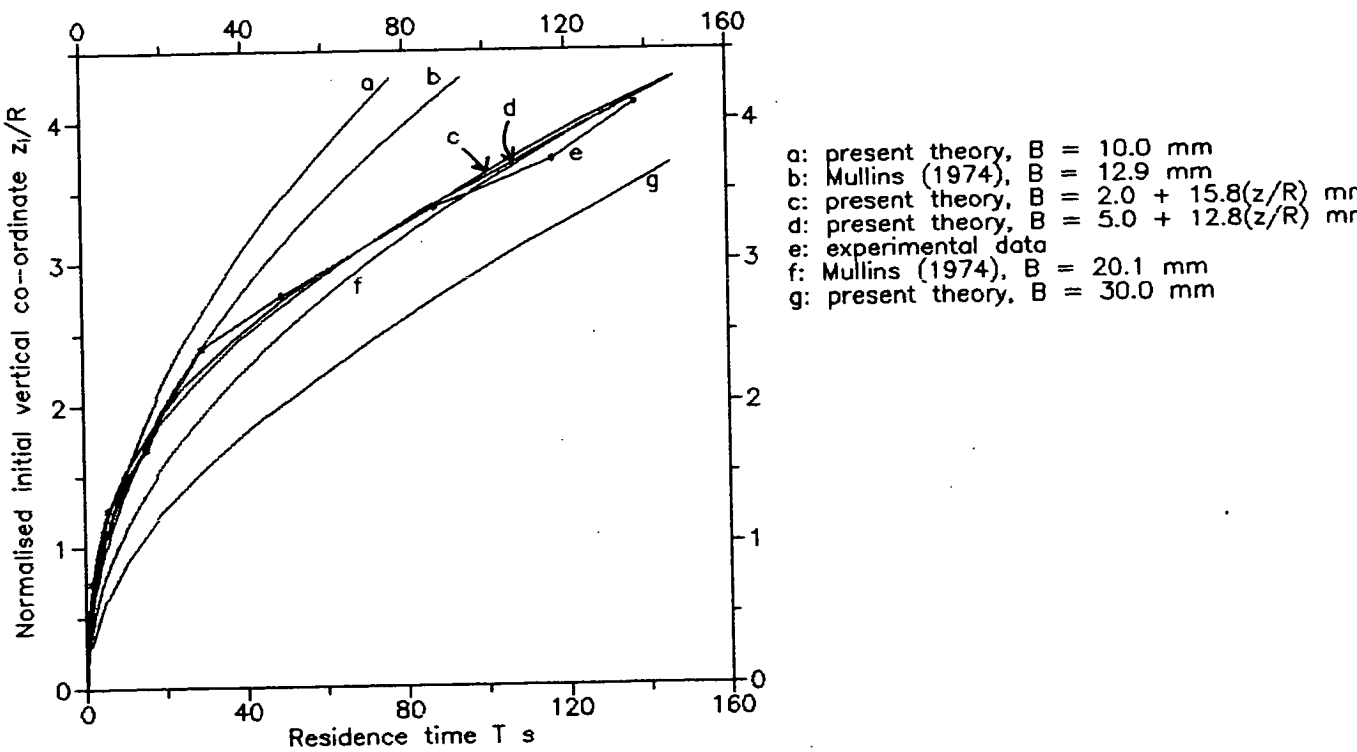

Fig. 7.12 Residence times of tracers close to centreline for sand during post-refilling flow (fit 4)

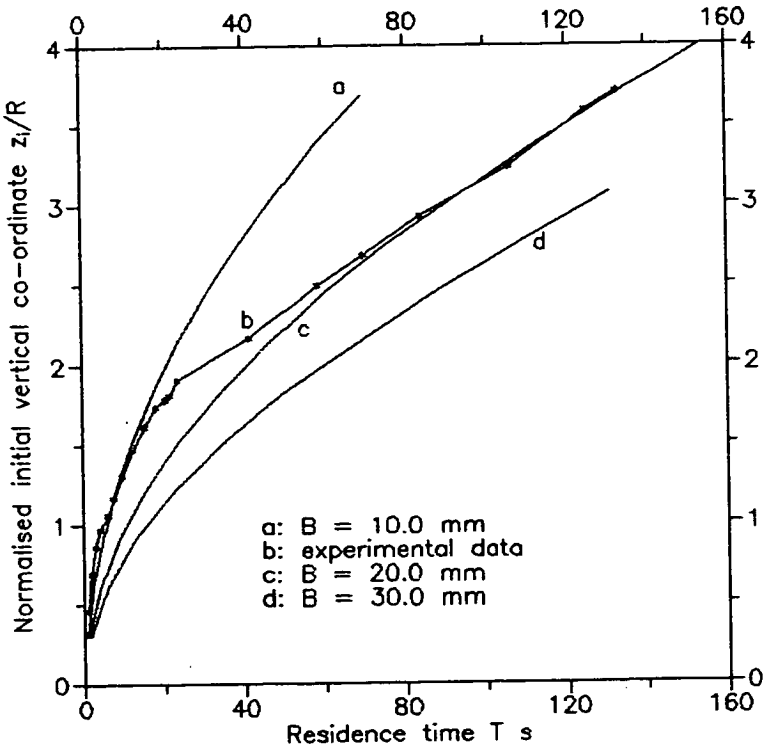

Fig. 7.13 Residence times of tracers close to centreline for polypropylene pellets during post-refilling flow (fit 1)

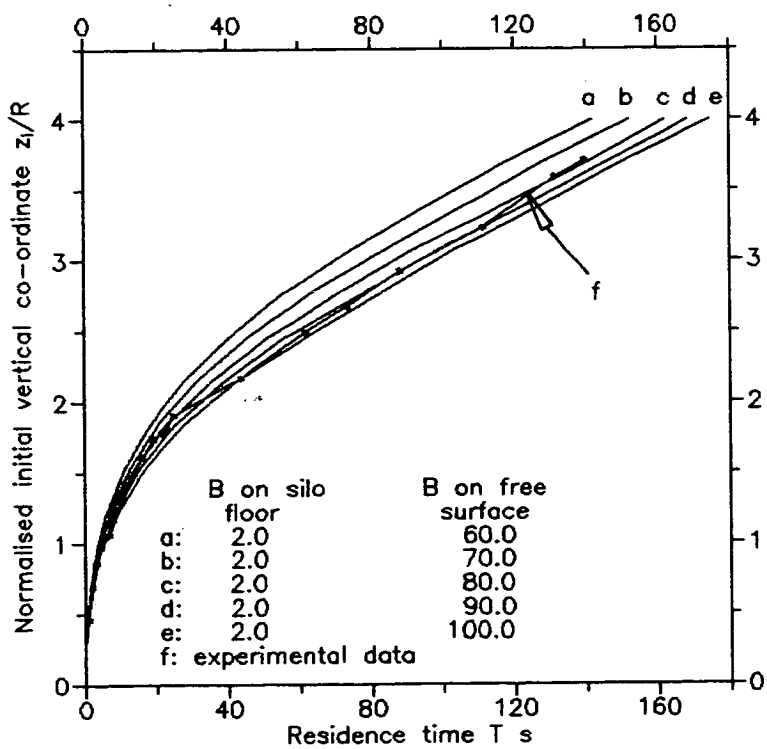

Fig. 7.14 Residence times of tracers close to centreline for polypropylene pellets during post-refilling flow (fit 2)

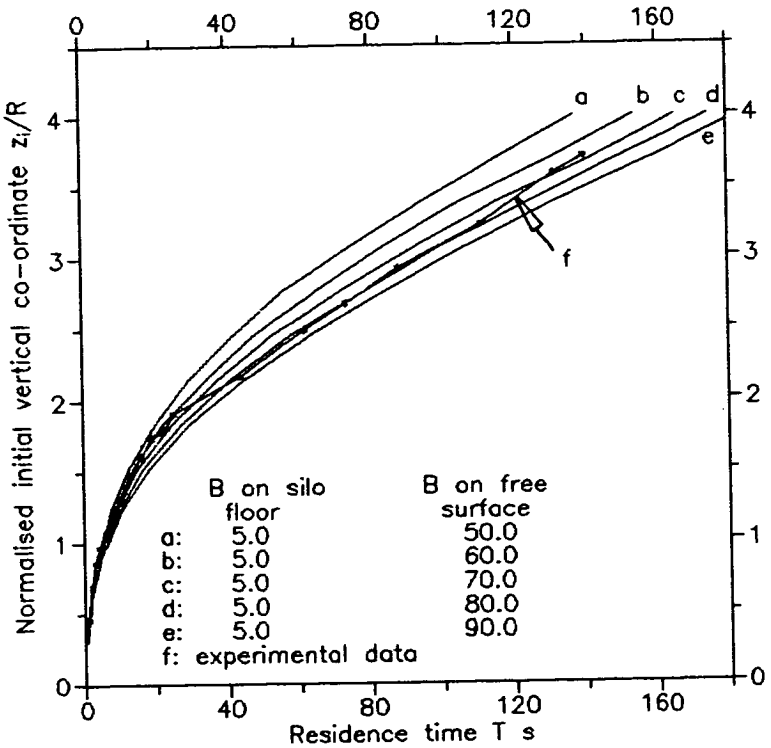

Fig. 7.15 Residence times of tracers close to centreline for polypropylene pellets during post-refilling flow (fit 3)

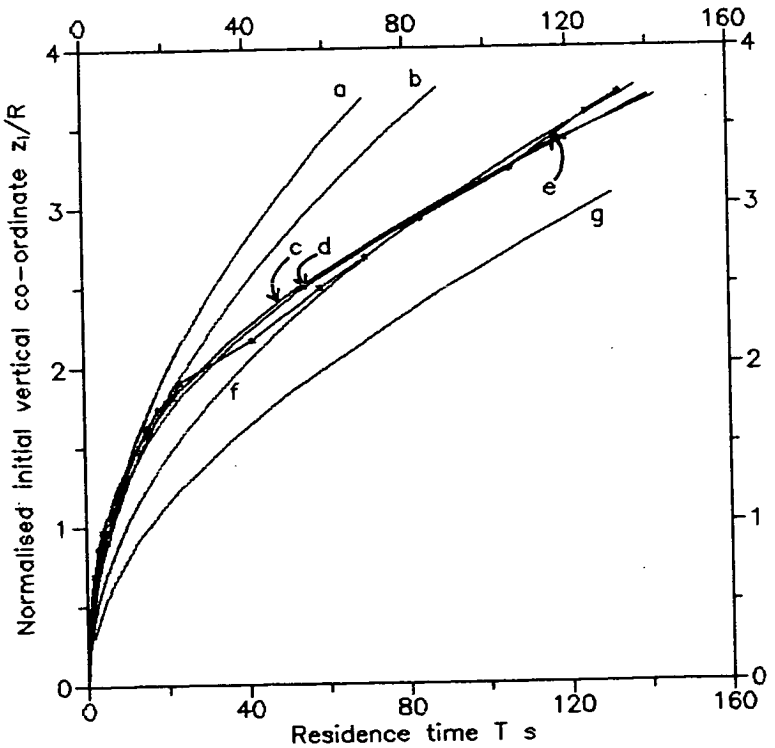

a: present theory, B = 10.0 mm
b: Mullins (1974), B = 13.0 mm
c: present theory, B = 2.0 + 18.1(z/R) mm
d: present theory, B = 5.0 + 15.1(z/R) mm
e: experimental data
f: Mullins (1974), B = 20.2 mm
g: present theory, B = 30.0 mm

Fig. 7.16 Residence times of tracers close to centreline for polypropylene pellets during post-refilling flow (fit 4)

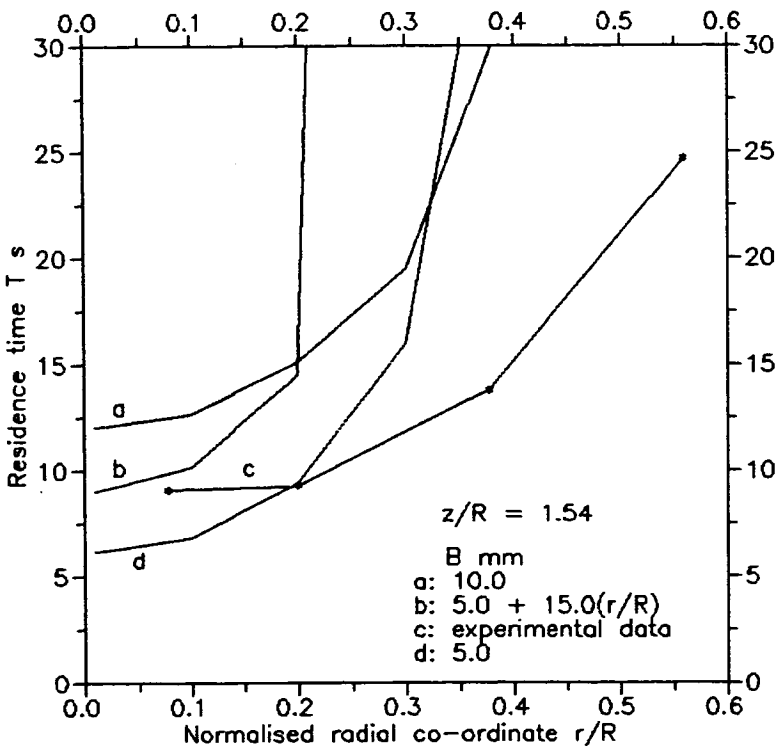

Fig. 7.17 Variation of residence time with radial co-ordinate for polypropylene pellets during principal flow

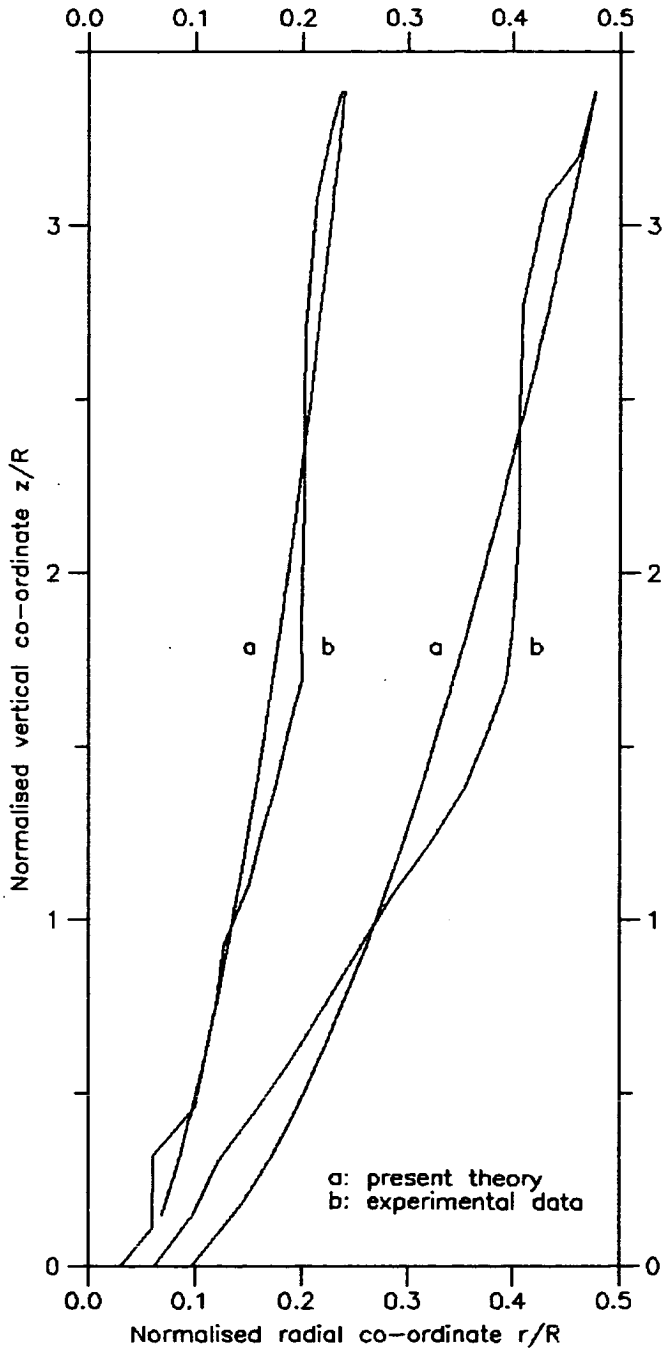

Fig. 7.18 Experimental and theoretical particle trajectories

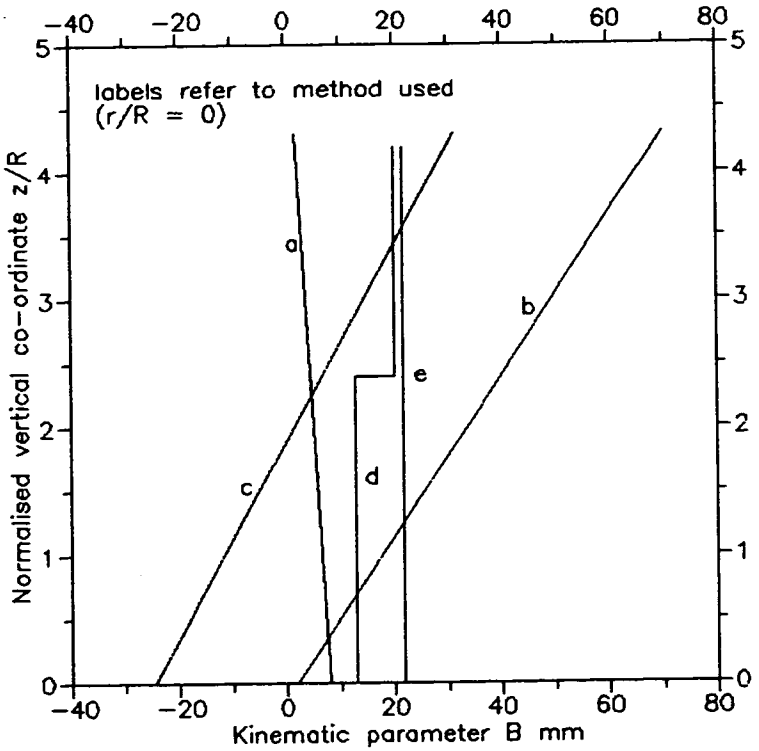

Fig. 7.19 Values of B from the five methods for sand during post-refilling flow

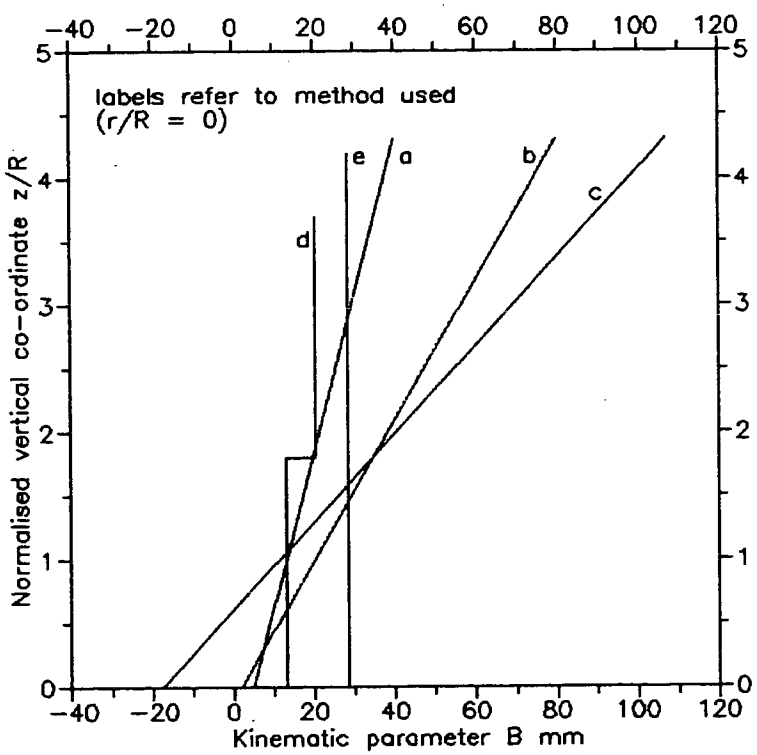

Fig. 7.20 Values of B from the five methods for polypropylene pellets during post-refilling flow

CHAPTER 8

CONCLUSIONS

8.1 Introduction

In this thesis, the discharge of dry bulk granular solids from containment structures, such as bins and silos, has been investigated. A numerical theory has been formulated and implemented based on the method of finite elements. This theory is founded on the kinematics of granular solids and takes the analytical work of Tuzun and Nedderman (1979a) as its starting point. The numerical theory has been formulated for both planar and axisymmetric geometries. The formulations are two-dimensional and have been applied to both concentrically- and eccentrically-discharging planar silos. In axisymmetric silos, only the analysis of concentric discharge was possible since eccentric discharge is a fully three-dimensional phenomenon. The kinematic theory hinges on the value of a parameter which Tuzun and Nedderman (1979a) termed 'the kinematic constant'. It is believed that this constant may be thought of as a material parameter, but it may also depend on the local value of the initial filling density. Experimental evidence exists (Tuzun and Nedderman, 1979a and the present work) that demonstrates that it is not constant within a silo. Exploiting the inherent flexibility of the finite element method, a spatial variation of the kinematic constant (here termed the 'kinematic parameter') has been created and employed. Variable boundary conditions can also be easily accommodated.

Experiments have been conducted in a concentrically-discharging half-cylindrical silo. Two experimental techniques have been employed. These were residence time measurements and visual observation through the transparent front wall. Measurements of the flow channel boundary, the kinematic parameter, and particle trajectories were made. Comparisons between the experimental results and predictions from the numerical formulation were also carried out.

8.2 Conclusions

8.2.1 Conclusions from numerical work

The numerical work was presented in Chapters 3, 4 and 5 of this thesis and was also applied, in conjunction with the experimental results, in Chapter 7. Several new contributions were made in applying the numerical formulations. The most significant are possibly the application to eccentric discharge, the analysis of multiple-outlet silos and time-stepping to investigate changing solids geometry.

As far as is known, the kinematic theory was applied, for the first time, to eccentrically-discharging planar silos. The rigorous analysis of this flow situation yielded some interesting results. It was found, for instance, that the FCB is not symmetrical about the orifice centre. The centre of the crater in the free surface is also seen to move towards the wall as the height above the orifice is increased. This phenomenon has been observed many times in the field.

The analysis of silos with more than one outlet was also made possible by the present numerical formulation. The velocity fields above each outlet were predicted to be unaffected by the presence of the other outlet.

The generality of the finite element discretisation allowed the solution to be stepped forward in time. Changing surface profiles and particle movements could therefore be calculated, at least for a limited time range.

8.2.2 Conclusions from experimental work

The experimental work was described in Chapter 6 and the results were analysed in Chapters 6 and 7. Two distinct flow regimes were identified: principal flow and post-refilling flow. The flow regime which occurs was found to depend upon the way the silo had been filled. The FCBs and velocity fields depended upon which flow regime was manifested. It was found that a different value of the kinematic parameter B was required to model the FCB in each of the two flow regimes. This is direct evidence that B is not simply a material property.

Four methods for the determination of the FCB have been described. Apart from the method of radial velocity fields applied during principal flow, all methods produce FCBs that are very similar. It was found that the front wall slightly retarded the flow, but the retarding effect could be estimated and appropriate corrections made. It was demonstrated that axisymmetric flow occurred in the silo except for a slight retardation of the tracers adjacent to the front wall. The FCBs determined from isochrone maps and from discontinuities in the residence time data matched up well with the FCB traced on the front wall. It was concluded that the quasi-stable FCB which formed during principal flow can be most reliably found from a study of discontinuities in the residence time data. This method can also be applied to full circular silos where direct flow observation is not possible. The stable FCB formed during the post-refilling flow regime can be estimated from the residence times of tracers close to the centreline.

Five methods have been described for the determination of B. Apart from the analytical method of Graham *et al* (1987), all methods yield values of B that are quite similar, even though some of the methods are clearly more approximate than others. It is proposed that the most reliable and easily extracted value of B can be obtained from comparing the residence times of tracers on the centreline with the present numerical formulation.

8.3 Recommendations for further work

The numerical formulations could be developed further. Several possibilities are open. The steady-state analysis could be extended into a third spatial dimension. It is not thought that this step would require extensive re-writing of the equations, although the computational times are expected to burgeon drastically. This extension would allow the eccentric discharge from axisymmetric silos to be analysed. The unit thickness assumption, necessary in the planar analysis, could also be abandoned.

It has been noted that the founding kinematic equations are parabolic in nature. As such, they cannot predict a discontinuity. If the founding equations were modified in such a way so as to render them hyperbolic, discontinuities could then be predicted. In this way, a precise locus for the FCB could be obtained. Some work

towards this goal was undertaken during the course of the present study, but it remained incomplete and has therefore not been presented.

Another possible extension of the numerical method would be the introduction of time-dependence. This is viewed as an ambitious goal but would yield many useful results. The modelling of the complete discharge, from the instant the orifice door was opened until the instant the last particle trickled out, could then, in theory, be modelled. The occurrence of compressible flow could also be accommodated. This would allow the bulk solids density in the model to vary spatially and temporally.

It has been shown that the kinematic equations of Tuzun and Nedderman (1979a) cannot accommodate radial flow. Radial flow is the flow pattern that is expected to be manifested in hoppers. It is thought that if the present finite element formulation was modified to accommodate mixed boundary conditions then, with the spatially-varying nature of the kinematic parameter, the analysis of flow through hoppers would be possible.

More experiments are needed to investigate the kinematic parameter B for a wide range of solids and flow configurations. Tuzun and Nedderman's (1979b) suggestion that B depends on particle diameter requires further exploration. Simple material tests to measure B must also be devised.

This thesis has been concerned only with the prediction and measurement of flow patterns in silos. It is appreciated that these flow patterns cause wall pressures which in turn induce stress states in the silo structure. By utilising an appropriate flow rule and by invoking equilibrium, it should be possible to convert the predicted velocity fields into wall pressures.

REFERENCES

ARNOLD, P.C., McLEAN, A.G. and ROBERTS, A.W. (1980) 'Bulk Solids: Storage, Flow and Handling', Tunra Bulk Solids Handling Associates, University of Newcastle, Australia, Sept.

ARTEAGA, P. and TUZUN, U. (1990) 'Flow of Binary Mixtures of Equal-Density Granules in Hoppers - Size Segregation, Flowing Density and Discharge Rates', Chemical Engineering Science, Vol. 45, No. 1, pp. 205-223.

BAGNOLD, R.A. (1954) 'Experiments on a Gravity-free Dispersion of Large Solid Spheres in a Newtonian Fluid under Shear', Proc. R. Soc. London, A225, pp. 49-63.

BAKER, A.J. and PEPPER, D.W. (1991) 'Finite Elements 1-2-3', McGraw-Hill, New York, U.S.A.

BISHARA, A.G. and MAHMOUD, M.H. (1976), 'Using Finite Elements to Analyse Silo Pressure', Agricultural Engineering, Vol. 57, No. 6, pp.12-15.

BLAIR-FISH, P.M. and BRANSBY, P.L. (1973) 'Flow Patterns and Wall Stresses in a Mass Flow Bunker', Journal of Engineering for Industry, ASME, Vol. 95, No. 1, pp. 17-26.

BOSLEY, J., SCHOFIELD, C. and SHOOK, C.A. (1969) 'An Experimental Study of Granule Discharge from Model Hoppers', Transactions of the Institute of Chemical Engineers, Vol. 47, pp. T147-T153.

BRANSBY, P.L., BLAIR-FISH, P.M. and JAMES, R.G. (1973) 'An Investigation of the Flow of Granular Materials', Powder Technology, Vol. 8, No. 5-6, pp. 197-206, Nov-Dec.

BROWN, R.L. and RICHARDS, J.C. (1965) 'Kinematics of the Flow of Dry Powders and Bulk Solids', Rheologica Acta, Band 4, Heft 3, pp. 153-165, Oct.

CARSON, J.W., GOODWILL, D.J. and BENGTSON, K.E. (1991) 'Predicting the Shape of Flow Channels in Funnel Flow Bins and Silos', presented at the American Concrete Institute Convention, Boston, Massachusetts, U.S.A, March.

CHATLYNNE, C.J. and RESNICK, W. (1973) 'Determination of Flow Patterns for Unsteady-State Flow of Granular Materials', Powder Technology, Vol. 8, No. 3-4, pp. 177-182.

CLEAVER, J.A.S. (1991) 'Velocity Distributions in Conical Hoppers', PhD thesis, Department of Chemical Engineering, University of Cambridge, May.

COUSENS, T.W. and JAMES, R.G. (1983) 'Gravity Flow of Particulate Materials in Bunkers', Cambridge University Engineering Department Technical Report, CUED/D-Soils, Vol. 133, pp. 116.

CUNDELL, P.A. and STRACK, O.D.L. (1979) 'A Discrete Numerical Model for Granular Assemblies', Geotechnique, Vol. 29, No. 1, pp. 47-65.

CUTRESS, J.O. and PULFER, R.F. (1967) 'X-ray Investigaions of Flowing Powders', Powder Technology, Vol. 1, No. 1, pp. 213-220.

DEUTSCH, G.P. and CLYDE, D.H. (1967) 'Flow and Pressure of Granular Materials in Silos', Journal of Engineering Mechanics, ASCE, Vol. 93, No. 6, pp. 103-125, Dec.

DEUTSCH, G.P. and SCHMIDT, L.C. (1969) 'Pressures on Silo Walls', Journal of Engineering for Industry, ASME, Vol. 91, Ser. B, No. 2, pp. 450-459.

DOUGLAS, J.F., GASIOREK, J.M. and SWAFFIELD, J.A. (1986) 'Fluid Mechanics', Second edition, Longman Scientific and Technical, Harlow, Essex, England.

DRESCHER, A. (1991) 'Analytical Methods in Bin Load Analysis', Developments in Civil Engineering, Vol. 36, Elsevier, Amsterdam, Netherlands.

DRESCHER, A., COUSENS, T.W., BRANSBY, P.L. (1978) 'Kinematics of the Mass Flow of Granular Material through a Plane Hopper', Geotechnique, Vol. 28, No. 1, pp. 27-42.

EIBL, J. and ROMBACH, G. (1987a) 'Stress and Velocity Fields at Discharging of Silos', Proc. of NUMETA Conference, Swansea, pp. D1-D12.

EIBL, J. and ROMBACH, G. (1987b) 'Numerical Computation of Velocity and Stress Fields in Silos - Theory and Applications', Scientific Papers of the Institute of Building Engineering of the Technical University of Wroclaw.

EIBL, J. and ROMBACH, G. (1988) 'Numerical Investigations on Discharging Silos', ICONMIG, Innsbruck, pp. unknown, Apr.

GARDNER, G.C. (1964) 'The Axisymmetric "Best" Hopper, its Relevance to the Plane "Best" Hopper and "Best" Hoppers Integrated with Bins', Chemical Engineering Science, Vol. 19, No. 3, pp. 283-288.

GARDNER, G.C. (1966) 'The Region of Flow when Discharging Granular Materials from Bin-Hopper Systems', Chemical Engineering Science, Vol. 21, No. 3, pp. 261-273.

GIUNTA, J.S. (1969) 'Flow Patterns of Granular Materials in Flat-Bottom Bins', Journal of Engineering for Industry, ASME, Vol. 91, No. 2, pp. 406-413, May.

GRAHAM, D.P., TAIT, A.R. and WADMORE, R.S. (1987) 'Measurement and Prediction of Flow Patterns of Granular Solids in Cylindrical Vessels', Powder Technology, Vol. 50, No. 1, pp. 65-76, Mar.

HAFF, P.K. (1983) 'Grain Flow as a Fluid-Mechanical Phenomenon', Journal of Fluid Mechanics, Vol. 134, pp. 401-430, Sept.

HANDLEY, M.F. and PERRY, M.G. (1965) 'Measurements of Stresses in Flowing Granular Materials', Rheological Acta, 4, Heft 3, pp. 225-235.

HANDLEY, M.F. and PERRY, M.G. (1967) 'Stresses in Granular Materials in Converging Hopper Sections', Powder Technology, Vol. 1, pp. 245-251.

HAUSSLER, U. and EIBL, J. (1984) 'Numerical Investigations on Discharging Silos', Journal of Engineering Mechanics, ASCE, Vol. 110(1), No. 6, pp. 957-971, June.

HUI, K. and HAFF, P.K. (1986) 'Kinetic Grain Flow in a Vertical Channel', International Journal of Multiphase Flow', Vol. 12, No. 2, pp. 289-298, Mar-Apr.

JANSSEN, H.A. (1895) 'Versuche uber Getreidedruck in Silozellen', Zeitschrift des Vereines Deutscher Ingenieure, Vol. 39, pp. 1045-1049.

JENIKE, A.W. (1964) 'Steady Gravity Flow of Frictional-Cohesive Solids in Converging Channels', Journal of Applied Mechanics, ASME, Vol. 31, Ser. E, No. 1, pp. 5-11, Mar.

JENIKE, A.W. and JOHANSON, J.R. (1962) 'Stress and Velocity Fields in Gravity Flow of Bulk Solids', Bulletin No. 116 of the Utah Engineering Experiment Station, May.

JENIKE, A.W., JOHANSON, J.R. and CARSON, J.W. (1973a) 'Bin Loads - Part 2: Concepts', Journal of Engineering for Industry, ASME, Vol. 95, Ser. B, No. 1, pp. 1-5.

JENIKE, A.W., JOHANSON, J.R. and CARSON, J.W. (1973b) 'Bin Loads - Part 4: Funnel-Flow Bins', Journal of Engineering for Industry, ASME, Vol. 95, Ser. B, No. 1, pp. 13-16.

JENIKE, A.W. and SHIELD, R.T. (1959) 'On the Plastic Flow of Coloumb Solids Beyond Original Failure', Journal of Applied Mechanics, ASME, Vol. 26, Ser. E, No. 4, pp. 599-602, Dec.

JOHANSON, J.R. (1964) 'Stress and Velocity Fields in the Gravity Flow of Bulk Solids', Journal of Applied Mechanics, ASME, Vol. 31, Ser. E, No. 3, pp. 499-506, Sept.

KUZNETSOV, A.S. (1984) 'Gravity Flow of a Granular Medium from a Hopper, with Stagnation Zones', Izvestia AN SSSR, Mekhanika Tverdogo Tela, Vol. 19, No. 2, Mechanics of Solids, pp. 148-152.

LAOHAKUL, C. (1979) 'Velocity Distributions in the Wall Region of Flowing Granular Materials', Ph. D. Thesis, University of Cambridge, Feb.

LEE, J., COWIN, S..C. and TEMPLETON, J.S. (1974) 'An Experimental Study of the Kinematics of Flow through Hoppers', Trans. Soc. Rheology, 18:2, pp. 247-269.

LENCZNER, D. (1963) 'An Investigation into the Behaviour of Sand in a Model Silo', The Structural Engineer, Vol. 41, No. 12, pp. 389-398, Dec.

LINK, R.A. and ELWI, A.E. (1987) 'Incipient Flow in Silos: A Numerical Approach', Structural Engineering Report No. 147, Dept. of Civil Engineering, University of Alberta, May.

LITWINISZYN (1963) 'The Model of a Random Walk of Particles Adapted to Researches on Problems of Mechanics of Loose Media', Bulletin de L'Academie Polonaise des Sciences, Series des Sciences Techniques, Vol. 11, No. 10, pp. 61[593]-70[602].

McCABE, R.P. (1974) 'Flow Patterns in Granular Material in Circular Silos', Geotechnique, Vol. 24, No. 1, pp. 45-62.

MAHMOUD, A.A. and ABDEL-SAYED, G. (1981) 'Loading on Shallow Cylindrical Flexible Grain Bins', Journal of Powder and Bulk Solids Tech., Vol. 5, No. 3, pp. 12-19.

MORRISON, H.L. (1977) 'A One-Dimensional Analysis of Granular Flow in Bunkers', Chemical Engineering Science, Vol. 33, pp. 241-251.

MULLINS, W.W. (1972) 'Stochastic Theory of Particle Flow Under Gravity', Journal of Applied Physics, Vol. 43, No. 2, pp. 665-678, Feb.

MULLINS, W.W. (1974) 'Experimental Evidence for the Stochastic Theory of Particle Flow under Gravity', Powder Technology, Vol. 9, pp. 29-37.

MULLINS, W.W. (1979) 'Critique and Comparison of Two Stochastic Theories of Gravity-Induced Particle Flow', Powder Technology, Vol. 23, No. 1, pp. 115-119.

MUNCH-ANDERSEN, J. and NIELSEN, J. (1990) 'Pressures in Slender Grain Silos - Measurements in Three Silos of Different Sizes', presented at CHISA 1990, Praha, second European Symposium on the Mechanics of Particulate Solids, 26-31 Aug., 9 pp.

MURFITT, P.G. (1980) 'Flow Patterns and Wall Stresses in Core Flow Hoppers', Ph. D. Thesis, University of London.

NEDDERMAN, R.M. (1988) 'The Measurement of the Velocity Profile in a Granular Material Discharging from a Conical Hopper', Chemical Engineering Science, Vol. 43, No. 7, pp. 1507-1516.

NGUYEN, T.V., BRENNEN, C.E. and SABERSKY, R.H. (1980) 'Funnel Flow in Hoppers', Journal of Applied Mechanics, ASME, Vol. 47, No. 4, pp. 729-735, Dec.

NOVOSAD, K. and SURAPATI, K. (1968) 'Flow of Granular Materials: Determination and Interpretation of Flow Patterns', Powder Technology, Vol. 2, No. 2, pp. 82-86.

OOI, J.Y. (1990) 'Bulk Solids Behaviour and Silo Wall Pressures', Ph. D. Thesis, University of Sydney.

OOI, J.Y., ROTTER, J.M. and PHAM, L. (1990) 'Systematic and Random Features of Measured Pressures on Full-Scale Silo Walls', Engineering Structures, Vol. 12, No. 2, pp. 74-87, April.

OOI, J.Y. and ROTTER, J.M. (1991) 'Measured Pressures in Full Scale Silos: A New Understanding', Proc., International Conference: Bulk Materials - Towards the Year 2000, Institution of Mechanical Engineers, October 29-31, London, pp. 195-200.

PARISEAU, W.G. (1970) 'Discontinuous Velocity Fields in Gravity Flows of Granular Materials through Slots', Powder Technology, Vol. 3, No. 4, pp. 218-226.

PERRY, M.G., ROTHWELL, E. and WOODFIN, W.T. (1975) 'Model Studies of Mass Flow Bunkers, 1 - Development of the Radio Pill Technique for Dynamic Pressure and Velocity Measurements', Powder Technology, Vol. 12, No. 12, pp. 51-56.

PERRY, M.G., ROTHWELL, E. and WOODFIN, W.T. (1976) 'Model Studies of Mass Flow Bunkers, 2 - Velocity Distributions in the Discharge of Solids from Mass Flow Bunkers', Powder Technology, Vol. 14, No. 1, pp. 81-92.

PIEPER, K. (1969) 'Investigations of Silo Loads in Measuring Models', Journal of Engineering for Industry, ASME, Vol. 91, Ser. B, No. 2, pp. 365-372.

RAO, V. LAKSHMAN and VENKATESWARLU, D. (1973) 'Determination of Velocities and Flow Patterns of Particles in Mass Flow Hoppers, Powder Technology, Vol. 7, No. 5, pp. 263-265.

RICHARDS, P.C. (1977) 'Bunker Design - Part 1: Bunker Outlet Design and Initial Measurements of Wall Pressures', Journal of Engineering for Industry, ASME, Vol. 99, No. 4, pp. 809-813.

RUNESSON, K. and NILSSON, L. (1986) 'Finite Element Modelling of the Gravitational Flow of a Granular Material', Bulk Solids Handling, Vol. 6, No. 5, pp. 877-884.

SAVAGE, S.B. (1979) 'Gravity Flow of Cohesionless Granular Materials in Chutes and Channels', Journal of Fluid Mechanics, Vol. 92, Part 1, pp. 53-96.

SCHMIDT, L.C. and WU, Y.H. (1989) 'Prediction of Dynamic Wall Pressures on Silos', Bulk Solids Handling, Vol. 9, No. 3, pp. 333-338, Aug.

SMALLWOOD and THORPE (1980) 'Flow of Granular Media', Chemical Engineering Tripos, Undergraduate final year dissertation, University of Cambridge.

SUGDEN, M.B. (1980) 'Effect of Initial Density on Flow Patterns in Circular Flat-Bottomed Silos', 'International conference on the design of silos for strength and flow', Lancaster, England.

TAKAHASHI, H. and YANAI, H. (1973) 'Flow Profile and Void Fraction of Granular Solids in a Moving Bed', Powder Technology, Vol. 7, No. 4, pp. 205-214.

TAKAHASHI, H. and YANAI, H. (1974) 'On the Converging Flow of Granular Solids Discharged from a Moving Bed System - Predictions of Dead Zone and some Considerations', Kagaku Kogaku, Vol. 38, pp. 746-51.

THORNTON, C. (1979) 'The Conditions for Failure of a Face-Centered Cubic Array of Uniform Rigid Spheres', Geotechnique, Vol. 29, No. 4, pp. 441-459.

TUZUN, U. and NEDDERMAN, R.M. (1979a) 'A Kinematic Model for the Flow of Granular Materials', Powder Technology, Vol. 22, No. 2, pp. 243-253, Mar-Apr.

TUZUN, U. and NEDDERMAN, R.M. (1979b) 'Experimental Evidence Supporting Kinematic Modelling of the Flow of Granular Media in the Absence of Air Drag', Powder Technology, Vol. 24, No. 2, pp. 257-266, Jan-Feb.

TUZUN, U. and NEDDERMAN, R.M. (1982) 'An Investigation of the Flow Boundary during Steady-State Discharge from a Funnel Flow Bunker', Powder Technology, Vol. 31, No. 1, pp. 27-43, Jan-Feb.

TUZUN, U., HOULSBY, G.T., NEDDERMAN, R.M. and SAVAGE, S.B. (1982) 'The Flow of Granular Materials - 2: Velocity Distributions in Slow Flow', Review Article Number 11, Chemical Engineering Science, Vol. 37, No. 12, pp. 1691-1709.

WALKER, D.M. (1966) 'An Approximate Theory for Pressures and Arching in Hoppers', Chemical Engineering Science, Vol. 21, No. 11, pp. 975-997.

WALKER, D.M. and BLANCHARD, M.H. (1967) 'Pressures in Experimental Coal Hoppers', Chemical Engineering Science, Vol. 22, No. 8, pp. 1713-1745.

WU, Y.H. (1990) 'Static and Dynamic Analysis of the Flow of Bulk Materials through Silos', PhD thesis, Department of Civil and Mining Engineering, The University of Wollongong, Australia, Feb.

VAN ZANTEN, D.C. and MOOIJ, A. (1977) 'Bunker Design - Part 2: Wall Pressures in Mass Flow', Journal of Engineering for Industry, ASME, Vol. 99, Ser. B, No. 4, pp. 814-818.

VAN ZANTEN, D.C., RICHARDS, P.C. and MOOIJ, A. (1977) 'Bunker Design - Part 3: Wall Pressures and Flow Patterns in Funnel Flow', Journal of Engineering for Industry, ASME, Vol. 99, Ser. B, No. 4, pp. 819-823.

ZIENKIEWICZ, O.C. (1971) 'The Finite Element Method in Engineering Science', McGraw-Hill, Maidenhead, England.